

# West African Monsoon dynamics and its control on stable oxygen isotopic composition of precipitation in the Late Cenozoic

DANIEL BOATENG<sup>1</sup>, Jeffrey Nii Armah Aryee<sup>2</sup>, Michael Baidu<sup>3</sup>, Frank Arthur<sup>4</sup>, and Sebastian Gerhard Mutz<sup>1</sup>

<sup>1</sup>University of Tübingen

<sup>2</sup>Kwame Nkrumah University of Science and Technology

<sup>3</sup>Institute for Climate and Atmospheric Science, School of Earth and Environment, University of Leeds

<sup>4</sup>Department of Natural Sciences and Environmental Health, University of South-Eastern Norway

January 18, 2024

## Abstract

This study presents an overview of the Late Cenozoic evolution of the West African Monsoon (WAM), and the associated changes in atmospheric dynamics and oxygen isotopic composition of precipitation ( $\delta^{18}\text{O}_p$ ). This evolution is established by using the high-resolution isotope-enabled GCM ECHAM5-wiso to simulate the climatic responses to paleoenvironmental changes during the Mid-Holocene (MH), Last Glacial Maximum (LGM), and Mid-Pliocene (MP). The simulated responses are compared to a set of GCM outputs from Paleoclimate Model Intercomparison Project phase 4 (PMIP4) to assess the added value of a high resolution and model consistency across different time periods. Results show WAM magnitudes and pattern changes that are consistent with PMIP4 models and proxy reconstructions. ECHAM5-wiso estimates the highest WAM intensification in the MH, with a precipitation increase of up to 150 mm/month reaching 25°N during the monsoon season. The WAM intensification in the MP estimated by ECHAM5-wiso (up to 80 mm/month) aligns with the mid-range of the PMIP4 estimates, while the LGM dryness magnitude matches most of the models. Despite an enhanced hydrological cycle in MP, MH simulations indicate a ~50% precipitation increase and a greater northward extent of WAM than the MP simulations. Strengthened conditions of the WAM in the MH and MP result from a pronounced meridional temperature gradient driving low-level westerly, Sahel-Sahara vegetation expansion, and a northward shift of the Africa Easterly Jet. The simulated  $\delta^{18}\text{O}_p$  values patterns and their relationship with temperature and precipitation are non-stationarity over time, emphasising the implications of assuming stationarity in proxy reconstruction transfer functions.

1           **West African Monsoon dynamics and its control on stable oxygen isotopic**  
2           **composition of precipitation in the Late Cenozoic**

3   **Daniel Boateng<sup>1\*</sup>, Jeffrey N. A. Aryee<sup>2</sup>, Michael Baidu<sup>3</sup>, Frank Arthur<sup>4</sup>, Sebastian G. Mutz<sup>5</sup>**

4   <sup>1</sup>Department of Geosciences, University of Tübingen, Tübingen, Germany

5   <sup>2</sup>Department of Meteorology and Climate Science, Kwame Nkrumah University of Science and  
6   Technology, Kumasi, Ghana

7   <sup>3</sup>Institute for Climate and Atmospheric Science, School of Earth and Environment, University of  
8   Leeds, UK

9   <sup>4</sup>Department of Natural Sciences and Environmental Health, University of South-Eastern  
10   Norway, Bo, Norway

11   <sup>5</sup>School of Geographical and Earth Sciences, University of Glasgow, Scotland, UK

12  
13   Corresponding author: Daniel Boateng ([daniel.boateng@uni-tuebingen.de](mailto:daniel.boateng@uni-tuebingen.de))

14   **Key Points:**

- 15       • We simulate the Late Cenozoic evolution of the West African Monsoon and the isotopic  
16       composition of rainwater.
- 17       • Using a high-resolution model setup and realistic vegetation cover increases the intensity  
18       of the West African Monsoon in the Mid-Holocene.
- 19       • Strengthened conditions of the West African Monsoon in the Mid-Holocene and Mid-  
20       Pliocene result from the pronounced meridional temperature gradient
- 21       • The relationship between precipitation and the simulated isotopes is non-stationary in  
22       time, which complicates proxy climate reconstructions.

23  
24

## 25 **Abstract**

26 This study presents an overview of the Late Cenozoic evolution of the West African Monsoon  
27 (WAM), and the associated changes in atmospheric dynamics and oxygen isotopic composition  
28 of precipitation ( $\delta^{18}\text{O}_p$ ). This evolution is established by using the high-resolution isotope-  
29 enabled GCM ECHAM5-wiso to simulate the climatic responses to paleoenvironmental changes  
30 during the Mid-Holocene (MH), Last Glacial Maximum (LGM), and Mid-Pliocene (MP). The  
31 simulated responses are compared to a set of GCM outputs from Paleoclimate Model  
32 Intercomparison Project phase 4 (PMIP4) to assess the added value of a high resolution and  
33 model consistency across different time periods. Results show WAM magnitudes and pattern  
34 changes that are consistent with PMIP4 models and proxy reconstructions. ECHAM5-wiso  
35 estimates the highest WAM intensification in the MH, with a precipitation increase of up to 150  
36 mm/month reaching 25°N during the monsoon season. The WAM intensification in the MP  
37 estimated by ECHAM5-wiso (up to 80 mm/month) aligns with the mid-range of the PMIP4  
38 estimates, while the LGM dryness magnitude matches most of the models. Despite an enhanced  
39 hydrological cycle in MP, MH simulations indicate a ~50% precipitation increase and a greater  
40 northward extent of WAM than the MP simulations. Strengthened conditions of the WAM in the  
41 MH and MP result from a pronounced meridional temperature gradient driving low-level  
42 westerly, Sahel-Sahara vegetation expansion, and a northward shift of the Africa Easterly Jet.  
43 The simulated  $\delta^{18}\text{O}_p$  values patterns and their relationship with temperature and precipitation are  
44 non-stationarity over time, emphasising the implications of assuming stationarity in proxy  
45 reconstruction transfer functions.

## 46 **Plain Language Summary**

47 We use a global climate model to simulate how the West African Monsoon and related climate  
48 elements changed over the Late Cenozoic (from ca. 3 million years ago to now). We use a single,  
49 high-resolution model to calculate these changes for the Mid-Holocene, Last Glacial Maximum  
50 and Mid-Pliocene time periods. We then compare our results to already existing simulations to  
51 find out if there are any benefits to using a single, high-resolution model set-up. Overall, our  
52 simulations are similar to previous simulations and other climate reconstructions. However, our  
53 results also yield two important new findings: 1) our simulations reproduce some aspects of the  
54 monsoon better than previous simulations; 2) the chemical composition of rainwater, which is  
55 used by geologists to reconstruct climate, is impacted by more factors than previously assumed.  
56 This makes it more challenging to create reliable reconstructions of climate from geological  
57 records of rainwater composition.

## 58 **1 Introduction**

59 Understanding the complex climate dynamics and variability over West Africa has been a  
60 pertinent concern due to its strong environmental and socio-economic impacts. This is especially  
61 important since most West African countries rely on a rainfed agriculture economy (Sultan et al.,  
62 2005). Most importantly, the long-lasting multidecadal wet and dry periods during the 20th  
63 century emphasise the need to understand the long-term and future variability of the West  
64 African Monsoon (WAM) system. This requires knowledge about the response of the WAM  
65 dynamics to changes in internal feedbacks and external forcings, such as orbital parameters,  
66 atmospheric greenhouse gases, and vegetation distribution. Considering past climate change  
67 outside the recent observational period can provide valuable insights into that. More specifically,  
68 time periods with atmospheric  $\text{CO}_2$  concentrations ( $p\text{CO}_2$ ) and palaeogeography similar to the

69 present day can serve as analogue for a possible future climate in which all forcings have had  
70 their full effect. This would require looking back 3 million years in Earth's history (Burke et al.,  
71 2018). Therefore, this study focuses on a model-based exploration of the evolution of the WAM  
72 from the Mid-Pliocene (MP: ~3 Ma) to the present-day, considering the Last Glacial Maximum  
73 (LGM: ~21 ka), and Mid-Holocene (MH: ~6 ka) as important intermediate time steps.

74 Due to the complicated dynamics and teleconnections of the WAM, state-of-art General  
75 Circulation Models (GCMs) still fall short in accurately reproducing its past variability and  
76 providing consistent future projections (Biasutti, 2013; Pausata et al., 2016; Tierney et al., 2017).  
77 Improving the representation of the WAM system in climate models requires knowledge about  
78 its sensitivity to various global and regional paleoenvironment forcings and feedbacks. This  
79 knowledge can help identify the elements that need improvement in GCMs to ensure more  
80 reliable predictions of the WAM in the future. For instance, the response of the WAM dynamics  
81 to orbitally driven seasonal and latitudinal distribution of incoming solar radiation can be  
82 evaluated under MH conditions (Joussaume et al., 1999; Kutzbach & Liu, 1997). The LGM  
83 provides an opportunity to study the response of the WAM to the most recent global cold  
84 extreme, characterised by extensive ice sheet coverage and low  $p\text{CO}_2$  concentrations (e.g.,  
85 Bereiter et al., 2015). The long-term sensitivity of the WAM to  $p\text{CO}_2$  concentrations similar to  
86 the present, along with a less arid Sahara and a globally enhanced hydrological cycle, can also be  
87 assessed under MP paleoenvironment conditions (Corvec & Fletcher, 2017; H. Dowsett et al.,  
88 2010; Alan M. Haywood et al., 2020; U. Salzmann et al., 2008).

89 Despite the challenges in replicating the entirety of past climate changes with GCMs  
90 under appropriate paleoenvironmental conditions (Pascale Braconnot et al., 2012; Harrison et al.,  
91 2015), comparing the simulated responses from different climate models would shed more light  
92 on the inadequate representation of feedbacks and model biases that can be improved for future  
93 climate predictions (e.g., Zheng & Braconnot, 2013). Furthermore, such inter-model comparison  
94 across multiple past climates would help determine if the systematic model biases affect the  
95 overall strength of the responses and feedbacks in the different climates and help evaluate if such  
96 biases are GCM-specific or exist independently of the GCM that is used.

97 Numerous modelling studies have simulated the precipitation changes associated with the  
98 WAM in response to multiple forcings and climate states during the Late Cenozoic (e.g., Berntell  
99 et al., 2021; Weldeab et al., 2011; Zheng & Braconnot, 2013). However, the differences between  
100 the simulations, such as spatial resolution, boundary conditions, and the complexity of the GCM,  
101 make it difficult to identify the predominant atmospheric dynamics behind the WAM  
102 precipitation changes. For instance, model-dependent uncertainties of the individual GCMs that  
103 simulated these climates in previous studies may not fully capture certain components of the  
104 WAM system, which can amplify the systematic biases related to the sensitivity to various  
105 forcings or external perturbations across different climates. Moreover, GCMs with varied spatial  
106 resolutions and parameterisations of clouds, atmospheric dynamics, hydrological cycles, and  
107 atmosphere-land surface interactions would simulate distinct responses of the WAM to different  
108 forcings, leading to inconsistent patterns of WAM dynamics. Aside from these, only a few  
109 studies have comprehensively delved into atmospheric dynamics and teleconnections behind the  
110 changes in precipitation patterns and magnitudes under different paleoenvironmental conditions  
111 throughout the Late Cenozoic (e.g., Bosmans et al., 2012; Gaetani et al., 2017; Patricola & Cook,  
112 2007; Su & Neelin, 2005). Furthermore, previous studies have highlighted that monsoons and  
113 related circulations, such as the Inter Tropical Convergence Zone (ITCZ), are better resolved at

114 higher resolutions, including improved topographical representation and model parameterisation  
115 (Bosmans et al., 2012; Gao et al., 2006; Jungandreas et al., 2021). This study addresses the  
116 points above by providing details about the WAM atmospheric dynamics across these past  
117 climates using a consistent modelling framework with a high-resolution isotope-enabled GCM.

118 Geological archives can record information about various paleoenvironmental changes in  
119 the climate system over time. They can therefore be used for model-data comparisons and as a  
120 benchmark for climate models (Pascale Braconnot et al., 2012; I. Harris et al., 2014; Harrison et  
121 al., 2015). However, the scarcity of palaeohydrological records over Africa and the spatial  
122 resolution of climate models preclude the robust model-data comparison necessary for improving  
123 climate models (e.g., Salzmann et al., 2008, 2013). Several problems for data-model persist in  
124 this region. For instance, proxy-based reconstructions using pollen, past lake levels, leaf wax  
125 isotopes, and other records have suggested significantly wetter conditions across the Sahel and  
126 Sahara during the MH (e.g., Bartlein et al., 2011; Tierney et al., 2017). However, most climate  
127 models struggle to replicate the extent and magnitude of precipitation changes indicated by these  
128 proxy records despite accounting for factors like increased insolation, altered land surface  
129 condition (e.g., vegetation, lakes, orography, soil moisture), reduced dust emissions,  
130 atmospheric-ocean interactions, and atmospheric dynamics (P. deMenocal et al., 2000; Harrison  
131 et al., 2014; Hopcroft & Valdes, 2019; Pausata et al., 2016; Tierney et al., 2017).

132 While proxy records point to varying increases in precipitation levels over North Africa's  
133 higher latitudes, climate models estimate a more moderate WAM intensification,  
134 underestimating both the northward extent and magnitude of precipitation increase suggested by  
135 the proxies. If the proxy data is a well-collected, representative sample, there are two possible  
136 model-related reasons for this mismatch: (1) The climate models simply do not capture the  
137 atmospheric processes in the region well enough to accurately model said hydroclimate changes.  
138 (2) Proxy system models, which allow the conversion of the proxy signal to a paleoclimate  
139 signal, are flawed. Proxy system models rely on calibrations based on modern-day observations,  
140 such as the spatial correlation between water isotopes and precipitation. These are used to  
141 establish a transfer function that allows a proxy-to-climate signal conversion. This signal  
142 transformation assumes that the transfer functions are stationary in time, i.e. that modern  
143 correlations are equally valid for past climates. This study uses an isotope-enabled GCM to  
144 decipher atmospheric dynamics driving WAM changes and to explore their impacts on water  
145 isotopologues under various past global changes. This allows for the testing of this assumption of  
146 the stationarity of the transfer function. Furthermore, such an analysis facilitates a direct model-  
147 isotope proxy comparison and contributes to understanding the general causal mechanisms  
148 behind the variability in different proxy materials (Bühler et al., 2022; Phipps et al., 2013; Risi et  
149 al., 2012; Werner et al., 2000).

150 This study provides the first overview of the changes of the WAM and its associated  
151 atmospheric dynamics in response to multiple forcings and feedbacks during the Late Cenozoic,  
152 using the high-resolution isotope-enabled GCM ECHAM5-wiso. More specifically, the study  
153 addresses the following specific objectives: (1) systematically simulating the responses of the  
154 WAM patterns and magnitude to the various paleoenvironment conditions, including changes in  
155 vegetation, orbital forcings, ice sheet extent, and atmospheric CO<sub>2</sub> concentrations; (2)  
156 investigating the atmospheric dynamics driving the simulated WAM changes, such as moisture  
157 transport (e.g., low-level southwesterlies), Africa Easterly Jet (AEJ), Tropical Easterly Jet (TEJ),  
158 Sahara Heat Low (SHL) and surface heat fluxes; and (3) exploring the simulated  $\delta^{18}\text{O}_p$  values

159 and how they are influenced by near-surface temperature and precipitation in response to the  
160 different boundary conditions. We further compare the simulated changes of the WAM to some  
161 of the state-of-the-art models that participated in the Paleoclimate Model Intercomparison  
162 Project (PMIP4) phase 4 to evaluate the added values of using a consistent, high-resolution  
163 modelling framework to understand the complex climate system over West Africa and improve  
164 its representation in Earth system models.

## 165 **2 Background**

### 166 2.1 On the intensification and northward extent of the West African Monsoon during the 167 Mid-Holocene

168 During the early-to-middle Holocene, spanning from 11,000 to 5,000 years before the  
169 present, the arid landscapes of the Sahel and Sahara regions transformed into shrubs, grasslands,  
170 and water bodies like rivers and lakes (Armitage et al., 2015; Claussen et al., 1999; P. deMenocal  
171 et al., 2000; Holmes, 2008; Kohfeld & Harrison, 2000). The development of this “Green Sahara”  
172 was attributed to changes in the insolation cycle, which intensified the equator-to-pole gradient  
173 and land-sea thermal contrasts and ultimately lead to an increase in rainfall across the Sahel-  
174 Sahara. The associated pressure gradient facilitated the moisture transport from the equatorial  
175 Atlantic into the continent. Overall, the changes in the orbital cycles and expansion of vegetation  
176 across the Sahel-Sahara caused the strengthening of the WAM and its northward extent (Gaetani  
177 et al., 2017; Patricola & Cook, 2007). This WAM intensification and northward migration have  
178 been reflected in many proxy systems such as paleo-lake levels (Hoelzmann et al., 1998; Prentice  
179 et al., 2000), leaf wax, and aeolian deposits in sedimentary cores from the Eastern Atlantic (P.  
180 deMenocal et al., 2000; Tierney et al., 2017) and archaeological findings that indicate human  
181 habitation (Cremaschi & Di Lernia, 1999; Dunne et al., 2012; Gabriel, 1987; Hoelzmann et al.,  
182 2001; Manning & Timpson, 2014; Sereno et al., 2008). However, state-of-art climate models still  
183 struggle to replicate the level of intensification and the northward reach as suggested by the  
184 different proxies, even when appropriate boundary conditions are prescribed (P. deMenocal et  
185 al., 2000; Harrison et al., 2014; Hopcroft & Valdes, 2019; Kutzbach & Liu, 1997; Pausata et al.,  
186 2016; Tierney et al., 2017). For instance, MH simulations in PMIP3-CMIP5 experiments  
187 estimate a precipitation increase of  $\sim 400$  mm/year over West Africa, with a northward shift that  
188 is underestimated by  $20^\circ\text{N}$  when compared to proxy reconstructions (Perez-Sanz et al., 2014).  
189 Thompson et al. (2021) utilised a water isotope-enabled Earth system model (iCESM1) that  
190 exhibited enhanced MH precipitation compared to PI conditions, and a northernmost WAM shift  
191 of approximately  $24^\circ\text{N}$ , which aligns with reconstructions from pollen and dust records ( $23$ -  
192  $28^\circ\text{N}$ ). Most of these models, however, lack vegetation feedback or appropriate prescribed MH  
193 vegetation reconstruction, which is crucial for sustaining the WAM's northward extension  
194 through vegetation-precipitation feedback (Otto-Bliesner et al., 2017; Pausata et al., 2016;  
195 Tierney et al., 2017). Rachmayani et al. (2015) demonstrated that using dynamic vegetation-  
196 coupled GCMs enhances the orbitally-induced precipitation increase by 20% over West Africa  
197 compared to fixed vegetation GCMs.

198 Recent studies have also highlighted that accounting for dust feedbacks related to the  
199 Green Sahara during the MH can further intensify and expand the WAM, aligning it more with  
200 proxy reconstructions (e.g., Egerer et al., 2018; Hopcroft & Valdes, 2019; Pausata et al., 2016;  
201 Thompson et al., 2019). These findings indicate that the discrepancies between the model and  
202 proxy reconstructions are due to the inadequate representation of certain atmospheric physics,

203 such as inaccurate cloud representation, energy fluxes, subgrid-scale convection, and surface  
204 conditions in the GCMs. Moreover, the coarse spatial resolution of GCMs fails to capture meso-  
205 to-local-scale processes like mesoscale convective systems (e.g., Baidu et al., 2022; Crook et al.,  
206 2019; Marsham et al., 2013), potentially contributing to further biases. Thus, understanding the  
207 mechanics and dynamics underlying vegetation feedback and natural variability in insolation  
208 cycles driving the WAM's northward migration during the MH is crucial for evaluating GCM  
209 performance in future projections. While these forcing mechanisms are not linked to  
210 anthropogenic emissions, evaluating and improving the GCMs' representation of climate system  
211 dynamics and feedbacks is vital for future climate change projections.

## 212 2.2 Large-scale feature of the Last Glacial Maximum and its influence on the West 213 African Monsoon

214 The LGM (~21,000 years BP) is a time period that is suitable for assessing the  
215 capabilities of state-of-the-art models due to its starkly different conditions from the present,  
216 such as lower atmospheric CO<sub>2</sub> levels (~185 ppm) and eustatic sea levels (~115 to 130 m below  
217 present) (Lambeck et al., 2014; Peltier & Fairbanks, 2006). The extensive continental ice sheets  
218 led to significant perturbations in atmospheric radiative forcing and circulation patterns,  
219 contributing to alterations in precipitation and temperature that were generally drier and colder  
220 than pre-industrial conditions (Clark et al., 2009; D'Agostino et al., 2019, 2020). Since the LGM,  
221 the Earth's global mean temperature has risen by approximately 4 to 6 °C (Annan & Hargreaves,  
222 2013, 2015; Friedrich et al., 2016), which is of the same order of magnitude increase projected  
223 under moderate to high emission scenarios for near-future climate change. Due to this similarity  
224 in global forcing and temperature response from the LGM to the present, and the present to the  
225 near future, the LGM is a relevant period to examine (e.g., Brady et al., 2013; Yoshimori et al.,  
226 2009). Furthermore, the interactions between temperature-driven and circulation-driven regional  
227 precipitation patterns in response to LGM conditions would help evaluate the ability of climate  
228 models to project precipitation under future scenarios, where both thermodynamic and dynamic  
229 phenomena contribute to changes in the magnitude and seasonality of precipitation patterns (e.g.,  
230 Boos, 2012; Lora, 2018; Scheff & Frierson, 2012).

231 Prior studies have indicated a high sensitivity of Africa's climate to rapid recurring ice  
232 sheet instabilities during the last glacial period (Adegbie et al., 2003; Stager et al., 2002, 2011;  
233 Weldeab et al., 2011). For example, the cold air temperatures over Greenland (Dansgaard-  
234 Oeschger stadials) and the influx of meltwater into the North Atlantic during Heinrich events  
235 correlated with the rapid decline in precipitation across much of Africa (Blunier & Brook, 2001;  
236 Dansgaard et al., 1993; McManus et al., 2004). Previous modelling studies of PMIP phases 1 to  
237 4 indicated weakened atmospheric circulation and associated decreased precipitation over West  
238 Africa (Kageyama et al., 2021). However, a good understanding of the dynamics leading to the  
239 dryness across the WAM region is still lacking.

240 Pollen-based reconstructions across the WAM and nearby offshore regions generally  
241 depict colder and drier conditions than the present (Bartlein et al., 2011). Although fully coupled  
242 atmosphere-ocean models can reasonably reproduce large-scale features of the LGM, several  
243 challenges remain with regard to the reconstruction of LGM topography and the assessment of  
244 inter-model biases for various climate feedbacks (Kageyama et al., 2021; Werner et al., 2018).  
245 Additionally, the spatial resolution of simulations has been identified as a crucial factor for the  
246 inter-model variabilities in LGM simulations, primarily due to the representation of ice sheet

247 topography (Kim et al., 2008; Shi et al., 2020). Overall, the complexity and diverse  
248 paleoenvironment of LGM conditions offers the opportunity to decipher the relative  
249 contributions of individual climate factors that influence precipitation changes across West  
250 Africa.

### 251 2.3 Changes of the WAM in the Mid-Pliocene

252 The MP (~3 Ma) is an important warm period for understanding the atmospheric  
253 dynamics of near-future climate change, because the Earth's geography was similar to the present  
254 and  $p\text{CO}_2$  approached present-day values (~400 ppm) (Badger et al., 2013; Bartoli et al., 2011;  
255 Harry Dowsett et al., 2016; Alan M. Haywood et al., 2020; Ulrich Salzmann et al., 2013; de la  
256 Vega et al., 2020). Additionally, the MP provides useful insights into climate feedbacks through  
257 the impact of the carbon cycle on geological times and is often considered an analogue for a  
258 near-future climate (Burke et al., 2018; Jiang et al., 2005). Climate models that participated in  
259 the PlioMIP (Pliocene Modelling Intercomparison Project) phases 1 and 2 indicate an increase of  
260 1.4 to 4.7 °C in global mean near-surface anomalies above the pre-industrial levels, along with  
261 an enhanced hydrological cycle and strengthened global monsoons (Haywood et al., 2013, 2020;  
262 Zhang et al., 2016).

263 Proxy reconstructions suggest warm and humid conditions, and fewer deserts during the  
264 MP. Boreal forests and grasslands expanded into high northern latitude regions that are currently  
265 covered by tundra (Salzmann et al., 2008). Dust records along the coast of West Africa indicate a  
266 strengthened WAM and wetter conditions over the Sahara (Kuechler et al., 2018; Salzmann et  
267 al., 2008). Palynological records also suggest an expansion of vegetation over the WAM region,  
268 with high tree cover density and widespread woodland and savanna over the Sahara (Bonnefille,  
269 2010; Salzmann et al., 2008).

270 Although previous modelling studies indicated that high-latitude warming could lead to a  
271 decreased meridional temperature gradient and a weakened tropical circulation, the warming  
272 experienced in the Sahara region, along with the corresponding Sahara heat low, actually caused  
273 an increased influx of moisture from the tropical Atlantic Ocean, strengthening WAM (Corvec &  
274 Fletcher, 2017; Alan M. Haywood et al., 2020). More specifically, the PlioMIP2 models estimate  
275 an increase in precipitation anomalies in the range of 60-120 mm/month (Berntell et al., 2021),  
276 compared to a lesser increase of 30-60 mm/month from the PlioMIP1 (Ran Zhang et al., 2016).  
277 Even though similar magnitude of changes are predicted for the future, models are still limited in  
278 capturing rainfall variability over West Africa, and future projections of it are referenced with  
279 less confidence (Biasutti, 2013; Cook, 2008; Roehrig et al., 2013). Further work and model  
280 development is needed to understand climate feedback over West Africa under high atmospheric  
281  $\text{CO}_2$  conditions.

### 282 2.4 Stable oxygen isotopic signal as proxy for reconstructing the West African Monsoon

283 Stable water isotopes serve as integrated tracers for diverse climate processes, and reflect  
284 changes in the water cycle (Craig & Gordon, 1965; Dansgaard et al., 1993). Consequently, they  
285 have been extensively used to investigate historical climate changes and characterise the current  
286 hydrological cycle. Reconstructions of the water cycle from proxy materials typically rely on  
287 modern calibrations. The modern spatial correlation between water isotopes and climate  
288 variables, such as precipitation amount or surface temperature, is used as a transfer function for  
289 reconstructing past climatic variations from proxies. For example, the oxygen isotopic

290 composition of precipitation ( $\delta^{18}\text{O}_p$ ) reconstructed from calcite in speleothems from (sub)tropical  
291 regions is interpreted to reflect past monsoon dynamics due to its relationship with precipitation  
292 amount, commonly known as the "amount effect" (e.g., Wang et al., 2001). However, these  
293 paleoclimate reconstructions from isotopic archives are compromised by changes in the transfer  
294 functions due to various non-linear climatic processes influencing the spatiotemporal variability  
295 of water isotopes, such as evaporative recycling, moisture transport pathways, source variation,  
296 vapour mixing, and precipitation dynamics (Bony et al., 2008; Risi et al., 2008, 2013). Hence,  
297 GCMs with explicit diagnostics of stable water isotopes can contribute to understanding their  
298 controlling mechanisms under different climatic conditions to ensure accurate paleoclimate  
299 reconstructions. Additionally, modelling the spatial representation of water isotopes in response  
300 to distinct past climate states aids in identifying potential non-stationarities in their relationships  
301 with climate elements like monsoon characteristics or precipitation amounts. While previous  
302 studies have employed water isotopes to understand present precipitation seasonality in West  
303 Africa (e.g., Risi et al., 2010) and even during the MH (Shi et al., 2023; Thompson et al., 2021),  
304 none have explored  $\delta^{18}\text{O}_p$  changes in response to Late Cenozoic paleoenvironmental conditions  
305 or assessed how water isotopes correspond to the spatial variability of precipitation and  
306 temperature during the WAM season.

307

308

### 309 **3 Data and Methods**

#### 310 **3.1 ECHAM5-wiso General Circulation Model**

311 Global climate changes in response to late Cenozoic paleoenvironmental conditions (i.e.,  
312 PI, MH, LGM, and MP) and present-day (PD) conditions were simulated using the isotope-  
313 tracking climate model ECHAM5-wiso. ECHAM5 is the fifth generation of the well-established  
314 atmospheric general circulation model developed by the Max Planck Institute for Meteorology  
315 (Roeckner et al., 2003). It is based on the spectral forecast model of the European Centre of  
316 Medium Range Weather Forecast (ECMWF) (Simmons et al., 1989) and represents the climate  
317 system with prognostic equations and parameterisations. Compared to its previous version, the  
318 fifth version has improved the representation of land surfaces, shortwave radiation, cumulus  
319 convection, and other factors relevant to atmospheric dynamics across the monsoon region.  
320 Specifically, the model employs an implicit scheme for the coupling of land surfaces and the  
321 atmosphere, enabling synchronous calculation of surface fluxes due to unconditional stability  
322 (Roeckner et al., 2003). It also employs land surface parameters that effectively portray the  
323 global distribution of major ecosystem types (Hagemann, 2002). Furthermore, the model  
324 simulates clouds using prognostic equations for all water phases (vapour, liquid, and solid), bulk  
325 microphysics, and statistical cloud cover parameterisation (U. Lohmann & Roeckner, 1996;  
326 Tompkins, 2002). The version employed in this study has been expanded to include isotope  
327 tracking capabilities, enabling the simulation of the water's isotopic composition as part of the  
328 hydrological cycle (Werner et al., 2011). The incorporated water isotopologues (i.e.,  $\text{H}_2^{16}\text{O}$ ,  
329  $\text{H}_2^{18}\text{O}$ , and HDO) function as independent tracers that undergo both kinetic and equilibrium  
330 fractionation during phase transitions in the atmosphere. It has been demonstrated that the model  
331 adequately represents the global hydrological cycle and stable isotopic composition (Hagemann  
332 et al., 2006; Werner et al., 2011). In this study, we compare the model's present-day simulations

333 with observed and reanalysis precipitation and near-surface temperature datasets across West  
334 Africa to assess its capability in representing WAM patterns and their seasonality.

### 335 3.2 Model Experiments and Boundary Conditions

336 Previous simulations of Late Cenozoic climate were conducted with different models and  
337 model setups. Varied parameterisation schemes, spatial resolution, and prescribed boundary  
338 conditions complicate the comparison of the regional climates across the considered time  
339 periods. We therefore conducted (paleo)climate simulations for PD, PI, MH, LGM, and MP  
340 boundary conditions using only ECHAM5-wiso, while maintaining the same spatial resolution.  
341 All climate simulation experiments were performed using a high T159 spectral resolution (~80 x  
342 80 km around the equator) and 31 vertical levels up to 10 hPa. The model uses prescribed sea  
343 surface temperature (SST) as the interface between the ocean and atmosphere and, therefore,  
344 requires less time to reach dynamic equilibrium than fully coupled atmosphere-ocean models.  
345 However, the prescribed SSTs disregard oceanic decadal variability, making the simulated  
346 response inevitably biased by the specific SST reconstructions used. The paleoclimate  
347 experiments were run for 18 years with a 6-hour model output and only considered the last 15  
348 years for the analysis. The first 3 years of the model serve as the spin-up period, which is the  
349 time required for the model to reach dynamic equilibrium. Given the study's aim to understand  
350 the WAM response to the diverse paleoenvironmental conditions, the different experimental set-  
351 ups accounting for variations in orbital parameters, greenhouse gases concentration, SSTs, sea  
352 ice concentrations (SICs), and land surface cover (e.g., ice sheet and vegetation) were devised for  
353 the different climates. The prescribed boundary conditions for the experiments are similar to the  
354 Late Cenozoic simulations presented by Mutz et al. (2018) and Botsyun et al. (2022). We build  
355 on those by simulating and analysing the isotopic compositions for all paleoclimates.

356 To validate the model's ability to represent WAM dynamics, we compared the present-  
357 day (PD) simulation conducted by Boateng et al. (2023) with observed and reanalysis  
358 precipitation and near-surface temperature datasets. The PD simulation setup follows the  
359 Atmospheric Model Intercomparison Project (AMIP) protocol, using prescribed annual means of  
360 SST and SIC from 1979 to 2014. The pre-industrial simulation (the reference year 1850) was  
361 also obtained from Boateng et al. (2023). The model was simulated with prescribed SST and SIC  
362 from a transient coupled ocean-atmosphere model (Lorenz & Lohmann, 2004). It used an  
363 atmospheric CO<sub>2</sub> concentration of 280 ppm in accordance with Dietrich et al. (2013), which was  
364 derived from the ice-core record (Etheridge et al., 1996, 1998). Land surface parameters were  
365 taken from Hagemann (2002). The initial isotopic composition of the atmosphere was adopted  
366 from global gridded data of <sup>18</sup>O composition of seawater provided by LeGrande & Schmidt  
367 (2006). In this study, the climate change signals are defined as deviations from the PI estimates.  
368 Therefore, all reported anomalies (e.g., MH-PI) throughout the paper, described as either  
369 "increases" or "decreases", use the simulated PI values as a reference. We also represent the  
370 H<sub>2</sub><sup>18</sup>O composition using the  $\delta$ -notation and calculate it as precipitation-weighted means using  
371 the Vienna Standard Mean Ocean Water (V-SNOW).

372 The SST and SIC boundary conditions prescribed for the MH experiments were derived  
373 from transient MH simulation of a low-resolution ocean-atmosphere coupled model (Etheridge et  
374 al., 1996, 1998)(G. Lohmann et al., 2013; Wei & Lohmann, 2012). The GHG concentrations  
375 (e.g., CO<sub>2</sub> of 280 ppm) are based on ice-core reconstructions (Etheridge et al., 1996, 1998), and  
376 the orbital forcing parameters are taken from Dietrich et al. (2013). On the other hand, the LGM

377 simulation was forced with sea surface variables from reconstructions for the Atlantic, Pacific,  
 378 and Indian oceans based on the GLAMAP (Sarnthein et al., 2003) and CLIMAP (1981) projects.  
 379 Moreover, the GHG concentrations (CO<sub>2</sub> of 185 ppm) and orbital parameters follow Otto-  
 380 Bliessner et al. (2006). The palaeogeography and ice sheet extent and thickness are based on the  
 381 PMIP3 experimental protocol (Abe-Ouchi et al., 2015). The vegetation distribution maps for  
 382 both the LGM and MH are based on the reconstruction of plant functional types from BIOME  
 383 6000 of the paleovegetation mapping project (Bigelow et al., 2003; Harrison et al., 2001; Pickett  
 384 et al., 2004; Prentice et al., 2000). The MP paleoenvironment conditions prescribed in the  
 385 ECHAM5 model were based on the Pliocene Research, Interpretation, and Synoptic Mapping  
 386 (PRISM) project (Dowsett et al., 2010; Haywood et al., 2016). More specifically, GHG  
 387 concentration (e.g., CO<sub>2</sub> of 405 ppm), orbital parameters, land surface variables (e.g.,  
 388 topography, ice cover, and land-sea mask), and sea surface variables (SST, and SIC) were  
 389 derived from PRISM3D. The vegetation distribution map was regenerated with JSBACH plant  
 390 functional types using the PRISM reconstruction (C. Stepanek & Lohmann, 2012). A summary  
 391 of the major boundary conditions used in this study is presented in Table 1.

392 Due to the sparse availability of isotopic composition records for the past climates, all the  
 393 initial conditions of the ocean and the atmosphere were kept the same. The H<sub>2</sub><sup>18</sup>O and HDO  
 394 starting conditions for the ocean were taken from the equilibrium 3000-year run with MPI-OM-  
 395 wiso (Xu et al., 2012), and the atmosphere was initialised with δ<sup>18</sup>O and δD of -10 and -80 ‰,  
 396 respectively, similar to previous studies (e.g., Cauquoin et al., 2019; Werner et al., 2011).

397

398

399

400 **Table 1.** Summary of boundary conditions for the ECHAM5-wiso experiments (this study) and  
 401 the list of PMIP4 models that simulated the coeval climates. e stands for eccentricity, o for  
 402 obliquity, and lop for longitude of perihelion.

403

Experiment name	Greenhouse gas concentrations	Orbital forcing parameters	Surface conditions	PMIP4 models considered
Pre-industrial (PI): year 1850	CO <sub>2</sub> : 280 ppm, CH <sub>4</sub> : 760 ppb, N <sub>2</sub> O: 270 ppb.	e: 0.016804, o: 23.4725, lop: 278.734	The SST and SIC data are taken from a low-resolution coupled ocean-atmosphere simulation by Dietrich et al. (2013) and Lorenz & Lohmann (2004). Vegetation distribution data was adopted from Hagemann (2002).	All models
Mid-Holocene (MH): ~6 ka	CO <sub>2</sub> : 280 ppm, CH <sub>4</sub> : 650 ppb, N <sub>2</sub> O: 270 ppb.	e: 0.018682, o: 24.1048, lop: 180.918	SSTs and SICs are obtained from a transient, low-resolution coupled ocean-atmosphere simulation of the Mid-Holocene (Lohmann et al., 2013; Wei & Lohmann, 2012). Vegetation reconstructions from the BIOME 6000 dataset (Bigelow et al., 2003; Harrison et al., 2001; Pickett et al., 2004;	AWI-ESM-1-1-LR, CESM2, EC-Earth3-LR, GISS-E2-1-G, HadGEM3-GC31-LL, IPSL-CM6A-LR, MIROC-ES2L, NorESM1-F

			Prentice et al., 2000) converted into plant functional types.	
Last Glacial Maximum (LGM): ~21 ka	CO <sub>2</sub> : 185 ppm, CH <sub>4</sub> : 350 ppb, N <sub>2</sub> O: 200 ppb.	e: 0.018994, o: 22.949, lop: 294.42	SSTs and SICs were derived from GLAMAP reconstructions for the Atlantic Ocean (Sarnthein et al., 2003) and CLIMAP reconstructions for the Pacific and Indian Oceans (CLIMAP, 1981). Land-sea distribution, ice sheet extent, and thickness were based on PMIP3 data (Abe-Ouchi et al., 2015). Vegetation patterns were reconstructed using maps of plant functional types from the BIOME 6000 Paleovegetation Mapping Project (Bigelow et al., 2003; Harrison et al., 2001; Pickett et al., 2004; Prentice et al., 2000) and model predictions provided by Arnold et al. (2009).	AWI-ESM-1-1-LR, CESM2-WACCM-FV2, MIROC-ES2L, MPI-ESM1-2-LR, INM-CM4-8
Mid-Pliocene (MP): ~3 Ma	CO <sub>2</sub> : 405 ppm, CH <sub>4</sub> : 760 ppb, N <sub>2</sub> O: 270 ppb.	e: 0.016804, o: 23.4725, lop: 278.734	SSTs, SICs, land-sea mask, topography, and ice cover data were sourced from PRISM3D (Dowsett et al., 2010; Haywood et al., 2010; Sohl et al., 2009). The vegetation boundary condition was established by converting the PRISM vegetation reconstruction into JSBACH plant functional types, following the method outlined by Stepanek and Lohmann (2012).	CESM2, EC-Earth3-LR, GISS-E2-1-G, HadGEM3-GC31-LL, IPSL-CM6A-LR, NorESM1-F

404

### 3.3 Observed and Simulated Data Comparison

405

406 Reanalysis products are used as validation datasets to assess how ECHAM5-wiso  
407 simulates the climatologies and seasonality of precipitation and near-surface temperature across  
408 the WAM region. More specifically, the ERA5 climate reanalysis, produced and maintained by  
409 ECMWF, is compared to the simulated long-term seasonal means of the PD climate. ERA5  
410 consists of globally interpolated observations (e.g., ocean buoys, satellites, aircraft, weather  
411 stations, and other platforms) and numerical simulations using a four-dimensional variational  
412 (4D-var) data assimilation scheme (Hersbach et al., 2020). It has hourly output, an approximately  
413 31 km spatial resolution, and extends back to 1959 (Bell et al., 2021). We only extract the  
414 monthly long-term mean for the period 1979-2014 due to the simulated time range of the PD  
415 experiment. Moreover, the CRU (Climate Research Unit gridded Time series) high-resolution  
416 dataset (i.e., 0.5° x 0.5° over land regions except for Antarctica), maintained at the University of  
417 East Anglia, UK, was used to compare the PD precipitation simulation. CRU relies on the  
418 extensive network of global weather stations, which are interpolated using angular-distance  
419 weighting (ADW). This dataset extends back to 1901 (more details in Harris et al. 2014 and  
2020).

### 420 3.4 Observed and Simulated Data Comparison

421 Simulated model outputs from various climate models that participated in the fourth  
422 phase of the Paleoclimate Model Intercomparison Project (PMIP4), which is a component of the  
423 current Coupled Model Intercomparison Project (CMIP6) (Eyring et al., 2016), were analysed to  
424 further compare our simulated responses to paleoenvironmental conditions with the current state-  
425 of-the-art models. However, we emphasise that our analysis does not constitute a formal inter-  
426 model comparison since different experimental protocols were used for the simulations in this  
427 study. For instance, we rely on a high-resolution atmosphere-only model with prescribed  
428 forcings, in contrast to the fully coupled atmosphere-ocean GCMs used in the PMIP4  
429 experiments. Furthermore, the ECHAM5-wiso simulation time is shorter than that of the PMIP4  
430 models (>100 years) due to the longer period required for fully coupled ocean-atmosphere  
431 models to reach quasi-equilibrium and avoid drifts in climate variables. The boundary conditions  
432 and experimental setup protocols for the PMIP4 models simulating the MH, LGM, and MP are  
433 described in Kageyama et al. (2018) and Otto-Bliesner et al. (2017). We analysed the last 100  
434 years of monthly precipitation amounts for each model, with climate anomalies estimated using  
435 their respective PI control simulations. Moreover, we highlight that the individual PMIP4  
436 models' spatial resolutions were kept for our analysis to disentangle the impact of the model  
437 resolution in representing the WAM dynamics.

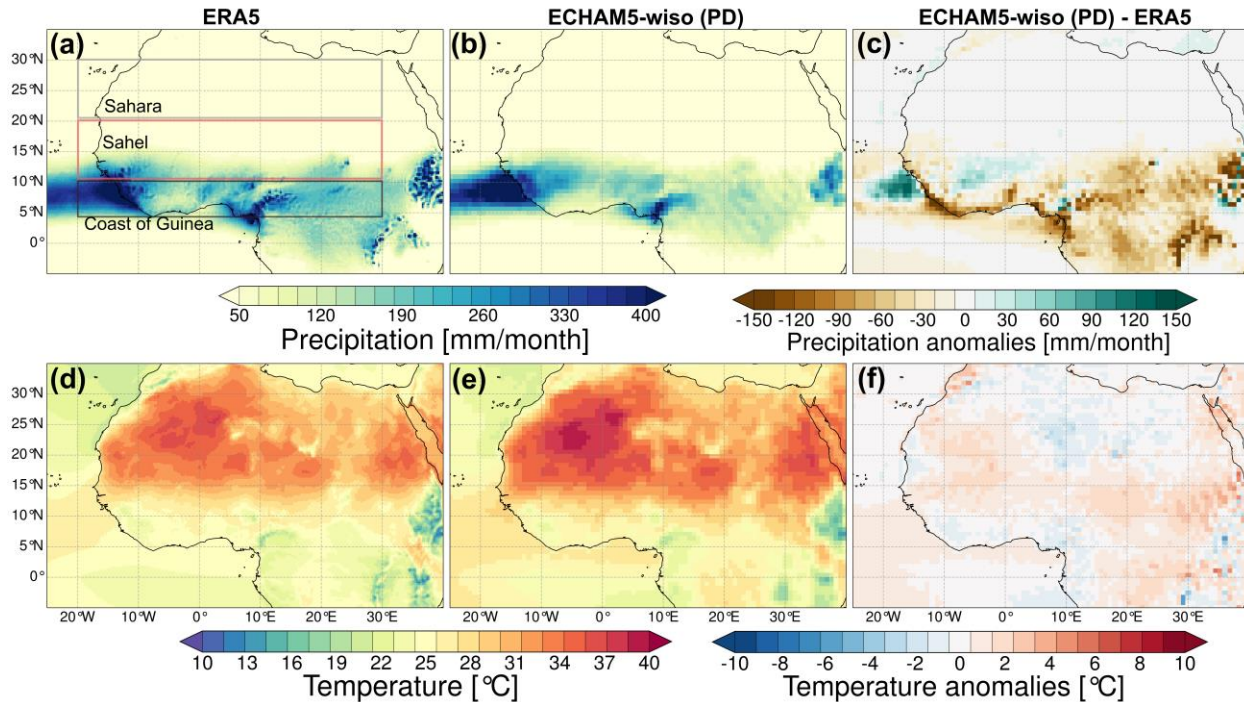
### 438 3.5 West African Monsoon Anomalies and Statistical Test

439 Long-term seasonal means of the WAM months (JJAS) were estimated using the 6-hour  
440 model output from the ECHAM5-wiso experiments and the monthly means from the PMIP4  
441 models. The statistical significance of the long-term anomalies is evaluated using a student t-test  
442 with a confidence interval threshold of 95%. It is important to note that the analysis is based on  
443 uncorrected time, even though orbits were modified in the time slice experiments. However, this  
444 does not influence the analysis since climatological means are considered. As the WAM  
445 seasonality is zonally distributed (Janicot et al., 2011; S. E. Nicholson & Palao, 1993), three  
446 different latitudinal transects were delineated for further analysis. Specifically, zonal averages  
447 over the Sahara (30-20°N, 20°W-30°E), Sahel (20-10°N, 20°W-30°E), and Guinea coast (10-  
448 5°N, 20°W-30°E) were used to understand the meridional variations of the simulated rain belt  
449 across the WAM region.

## 450 4 Results

### 451 4.1 Present-day simulation and comparison to observations

452 Comparisons of the simulated and the observed spatial patterns and seasonality of  
453 precipitation and near-surface temperature revealed that ECHAM5-wiso represents the climate  
454 across the WAM region well. More specifically, the simulated and observed precipitation in the  
455 monsoon season shows a similar rain belt, i.e., a latitudinal band of maximum precipitation of  
456 approximately 400 mm/month across Africa. There are only slight deviations in magnitude  
457 between ECHAM5-wiso and ERA5 (Fig. 1a-c): ERA5 shows a higher magnitude of  
458 precipitation, with ~40 mm/month more than predicted by the simulation. However, comparing  
459 the simulated patterns to the CRU datasets reduces these slight differences in precipitation  
460 patterns and magnitudes (Fig. S1). Moreover, the simulated near-surface temperature indicates  
461 similar spatial patterns with a pronounced meridional gradient, indicating high temperatures of  
462 up to 40 °C across the Sahara region (Fig. 1d-f).

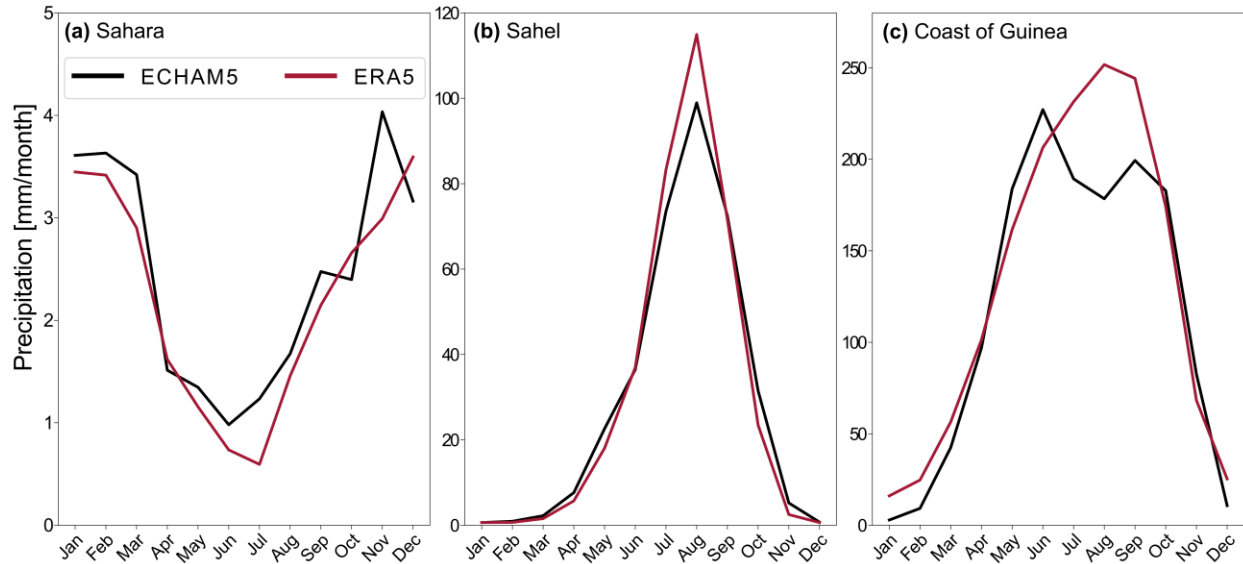


463

464 **Figure 1.** Long-term annual means (1979-2014) of ERA5 and ECHAM5-wiso precipitation (a  
 465 and b) and near-surface temperature (d and e) during the monsoon season (JJAS), and the  
 466 differences in precipitation and near-surface temperature between the datasets (c and f). The  
 467 green colour range in the precipitation difference indicates a wet bias, while the brown colours  
 468 indicate a dry bias in the model. The red colour range also represents a warm bias, and the blue  
 469 colours indicate a cold bias in the model. Overall, the simulated patterns of the rain belt and  
 470 meridional temperature gradient during the monsoon season demonstrate a reasonable model  
 471 performance. The demarcated regions in (a) are used for estimating the regional means.

472

473 The migration of the WAM drives different seasonal precipitation patterns across West  
 474 Africa. Consequently, we analyse the seasonal trends using regional monthly means across the  
 475 Sahara, Sahel, and the coast of Guinea. Overall, the model simulates an accurate seasonal  
 476 distribution and intensity across most of the transects (Fig. 2). Specifically, the observed and the  
 477 modelled seasonal cycle shows a precipitation increase of  $>3$  mm/month during the winter in the  
 478 Sahara region (Fig. 2a). Moreover, the model also simulates a realistic unimodal monthly  
 479 distribution across the Sahel, with maximum precipitation of  $\sim 100$  mm/month in August (Fig.  
 480 2b). However, ECHAM5-wiso predicts the expected bimodal precipitation seasonality across the  
 481 Guinea coast, with peak months in June ( $\sim 225$  mm/month) and September ( $\sim 200$  mm/month),  
 482 while ERA5 indicates wider unimodal patterns of maximum precipitation of  $\sim 250$  mm/month in  
 483 June (Fig. 2c). Despite the adequate precipitation representation of ERA5 over West Africa,  
 484 previous studies have indicated their underestimation over the coast of Guinea (e.g., Quagraine et  
 485 al., 2020). Overall, the present-day simulation results confirm ECHAM5-wiso's ability to  
 486 represent the hydroclimate of the WAM and its associated teleconnections, validating its use for  
 487 paleoclimate simulations.



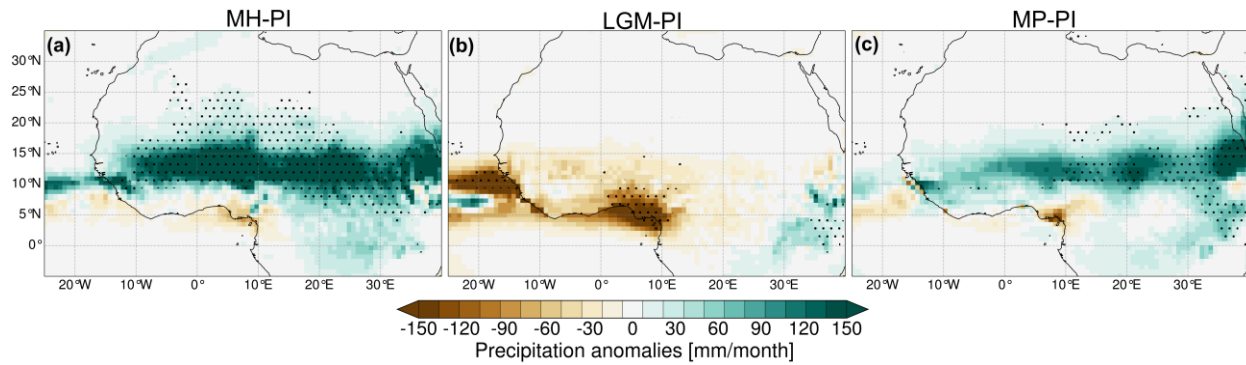
488

489 **Figure 2.** Comparison of ERA5 (red) and ECHAM5-wiso (black) monthly precipitation changes  
 490 across the (a) Sahara (30°–20°N, 20°W–30°E), (b) Sahel (20°–10°N, 20°W–30°E), and (c) Coast of  
 491 Guinea (10°–5°N, 20°W–30°E) (see Fig. 1a). For the Sahara and the Sahel, the modelled evolution  
 492 of the WAM is consistent with ERA5. However, the model produces the expected bimodal  
 493 precipitation seasonality across the Guinea coast, while ERA5 only shows a unimodal pattern.

494

#### 4.2 Simulated changes of the WAM in the late Cenozoic

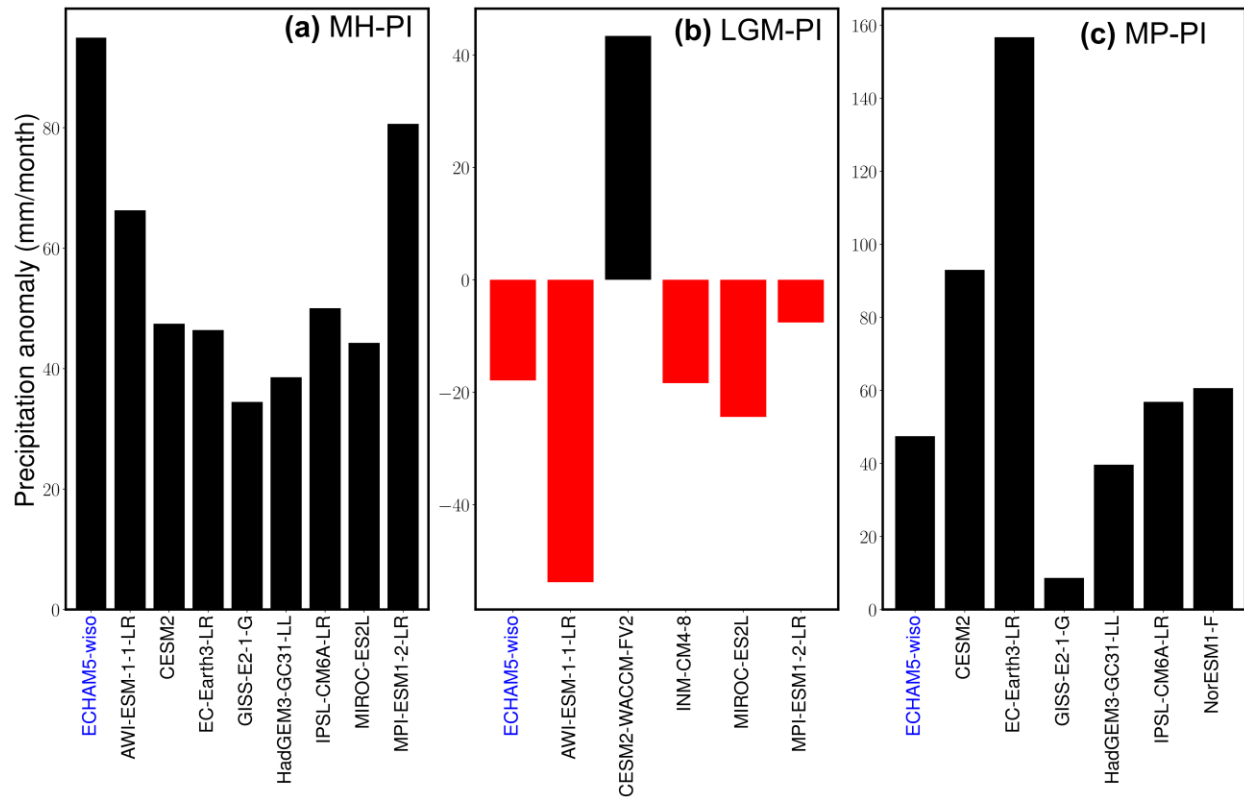
495 The simulated regional patterns of the WAM in the MH, LGM, and MP deviate  
 496 significantly from PI conditions. Overall, the model estimates an intensification of the WAM in  
 497 the MH and MP, with the MH showing a more significant intensification than the MP. On the  
 498 other hand, the model estimates a pattern of extensive dryness during the WAM season in the  
 499 LGM (Fig. 3). The estimated precipitation anomalies during the WAM season in the MH  
 500 indicate bidirectional latitudinal patterns. The MH experiment estimates an increase of ~150  
 501 mm/month from 7°N to 30°N, with statistical significance below 27°N. Conversely, the model  
 502 indicates a decrease of ~30 mm/month towards the coastal regions (2°–6°N) (Fig. 3a). Overall, the  
 503 LGM simulation indicates a precipitation decrease of up to 150 mm/month across the WAM  
 504 region, with significant anomalies along the coastal regions (Fig. 3b). Lastly, MP estimates an  
 505 increase of ~100 mm/month in precipitation anomalies during the WAM season, with patches of  
 506 a slight decrease in precipitation along the coast of Guinea, Nigeria, and Cameroon (Fig. 3c).  
 507 The simulated patterns of precipitation anomalies indicate a higher magnitude of the latitudinal  
 508 extent of the WAM towards the Sahara region in the MH compared to the MP. To assess the  
 509 relative importance and added value of using ECHAM5-wiso to simulate all the studied periods,  
 510 we compare our model estimates to those of other models from the CMIP6-PMIP4 experiments  
 511 (Table 1) that simulate the same periods. We focus our analysis on regional means of  
 512 precipitation anomalies across the Sahel and also evaluate the latitudinal distribution of the  
 513 WAM. The simulated WAM seasonal climatologies of the different climates (i.e., MH, LGM,  
 514 and MP) and their respective control means (PI) are presented in the supplementary material  
 515 (Fig. S2, S3, S4, and S5).



516

517 **Figure 3.** Precipitation anomalies during the WAM season (JJAS) for the (a) Mid-Holocene  
 518 (MH), (b) Last Glacial Maximum (LGM), and (c) Mid-Pliocene (MP), as simulated by  
 519 ECHAM5-wiso. The green colour range represents wetter conditions, while the brown colour  
 520 range represents drier conditions compared to the Pre-Industrial (PI) estimates. The black dot  
 521 stippling indicates regions with statistically significant differences, assuming a confidence  
 522 interval of 95% based on a student t-test analysis. The precipitation anomalies patterns indicate  
 523 the highest intensification of the WAM and its northward reach in the MH despite the enhanced  
 524 hydrological cycle in the MP.

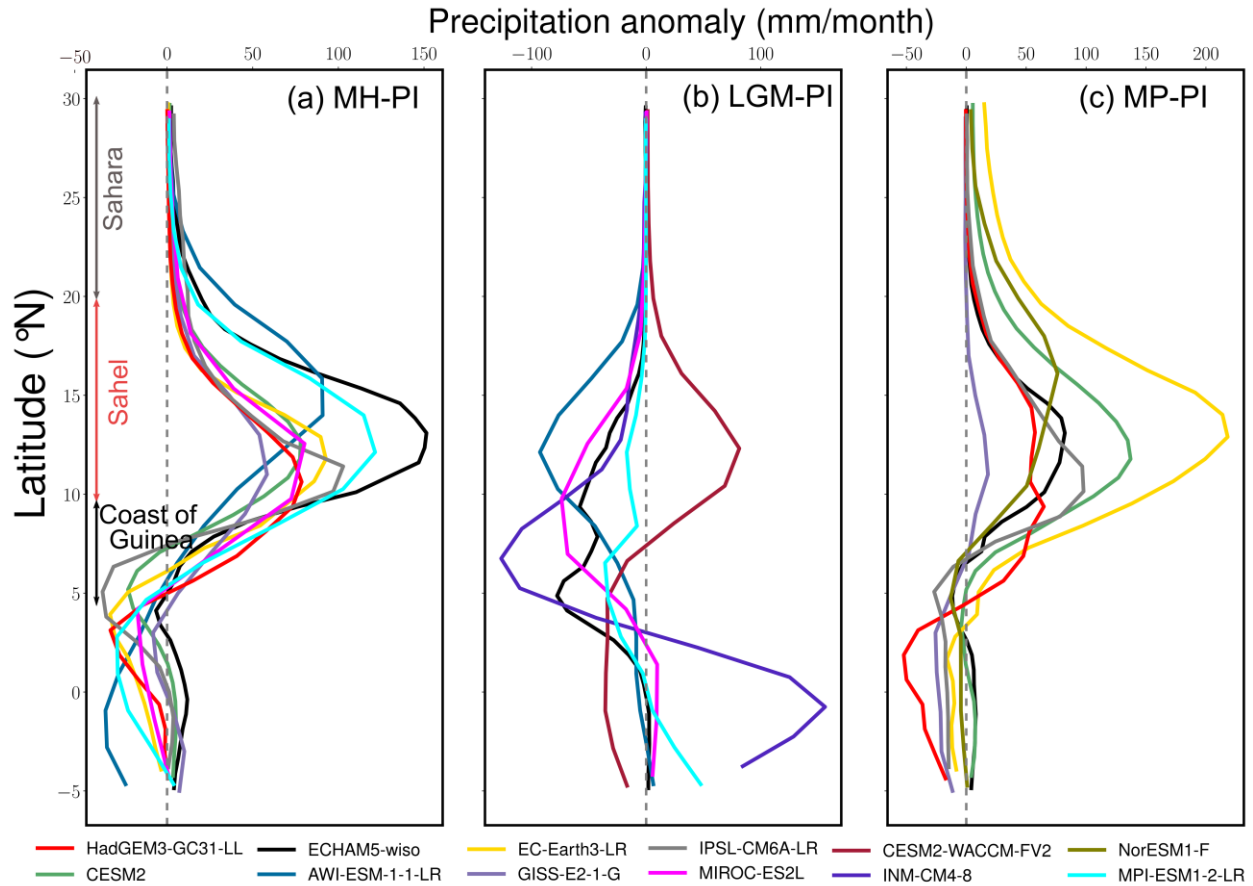
525 Overall, the inter-model comparison reveals consistent estimates in the direction and  
 526 magnitude of change in response to different paleoenvironmental conditions, with the exception  
 527 of CESM2-WCCM-FV2. Surprisingly, this model estimates an increase in precipitation  
 528 anomalies across the Sahel in the LGM. However, Zhu et al. (2021) have indicated that this  
 529 unrealistic sensitivity to colder climates may be attributed to exaggerated shortwave cloud  
 530 feedback or an unrepresented physical mechanism countering such cloud feedback. Specifically,  
 531 ECHAM5-wiso estimates the maximum increase in precipitation anomalies of ~90 mm/month  
 532 across the Sahel in the MH for the WAM season, followed by MPI-ESM1-2-LR (with ~80  
 533 mm/month), while GISS-E2-1-G shows the lowest precipitation anomalies of ~35 mm/month.  
 534 Alternatively, AWI-ESM-1-1-LR estimates a maximum precipitation decrease of 55 mm/month  
 535 across the Sahel in the LGM. The precipitation decreases (~20 mm/month) estimated by  
 536 ECHAM5-wiso is similar to the estimates by the INN-CM4-8 and MIROC-ES2L models. In the  
 537 MP, the WAM response across the Sahel exhibits a wider range of precipitation anomalies, with  
 538 EC-Earth3-LR, indicating the maximum increase of ~160 mm/month and GISS-E2-1-G showing  
 539 the lowest increase of ~10 mm/month. However, ECHAM5-wiso estimates fall within a mid-  
 540 range of ~50 mm/month, which is closer to the estimates by HadGEM3-GC31-LL, IPSL-CM6A-  
 541 LR, and NorESM1-F models. Even though ECHAM5-wiso indicates a maximum intensification  
 542 of the WAM across the Sahel in the MH rather than in the MP, other models (e.g., EC-Earth3-  
 543 LR) suggest the reverse trend. Consequently, the longitudinal regional means of the latitudinal  
 544 distribution of precipitation anomalies during the WAM season are evaluated to compare the  
 545 northward migration of the WAM in response to the different paleoenvironments.



546

547 **Figure 4.** Regional means of precipitation anomalies during the WAM season estimated for the  
 548 Sahel region (see Fig. 1a) using ECHAM5-wiso (labelled in blue) and the PMIP4 models  
 549 considered (Table 1) for the (a) Mid-Holocene (MH), (b) Last Glacial Maximum (LGM), and (c)  
 550 Mid-Pliocene (MP) paleoenvironmental conditions. The individual precipitation anomalies are  
 551 estimated based on their respective pre-industrial (PI) runs.

552 In total, most of the PMIP4 models suggest a higher meridional migration of the WAM in  
 553 the MP than in the MH, while the magnitude of changes in the latitudinal band of maximum  
 554 precipitation varies among the individual models. Specifically, EC-Earth3-LR estimates  
 555 maximum latitudinal precipitation of 200 mm/month with a greater northward extent in MP than  
 556 the ~100 mm/month rain belt in the MH. However, GISS-E2-1-G suggests a higher  
 557 intensification of the WAM with an increase in precipitation by 50 mm/month in the MH, and a  
 558 relatively modest increase of ~10 mm/month in the MP. The ECHAM5-wiso experiments  
 559 suggest a slight northward extent of the WAM in the MH and a higher intensification (~80  
 560 mm/month more) than in the MP. Despite the estimated differences, all the models, including  
 561 ECHAM5-wiso, indicate a similar meridional distribution in the MH and MP. However,  
 562 CESM2-WCCM-FV2 and INM-CM4-8 distinctively suggest an increased distribution of  
 563 meridional precipitation anomalies across the WAM areas and toward the equatorial Atlantic in  
 564 the LGM, respectively, despite the general decreasing trend estimated by the other models.



565

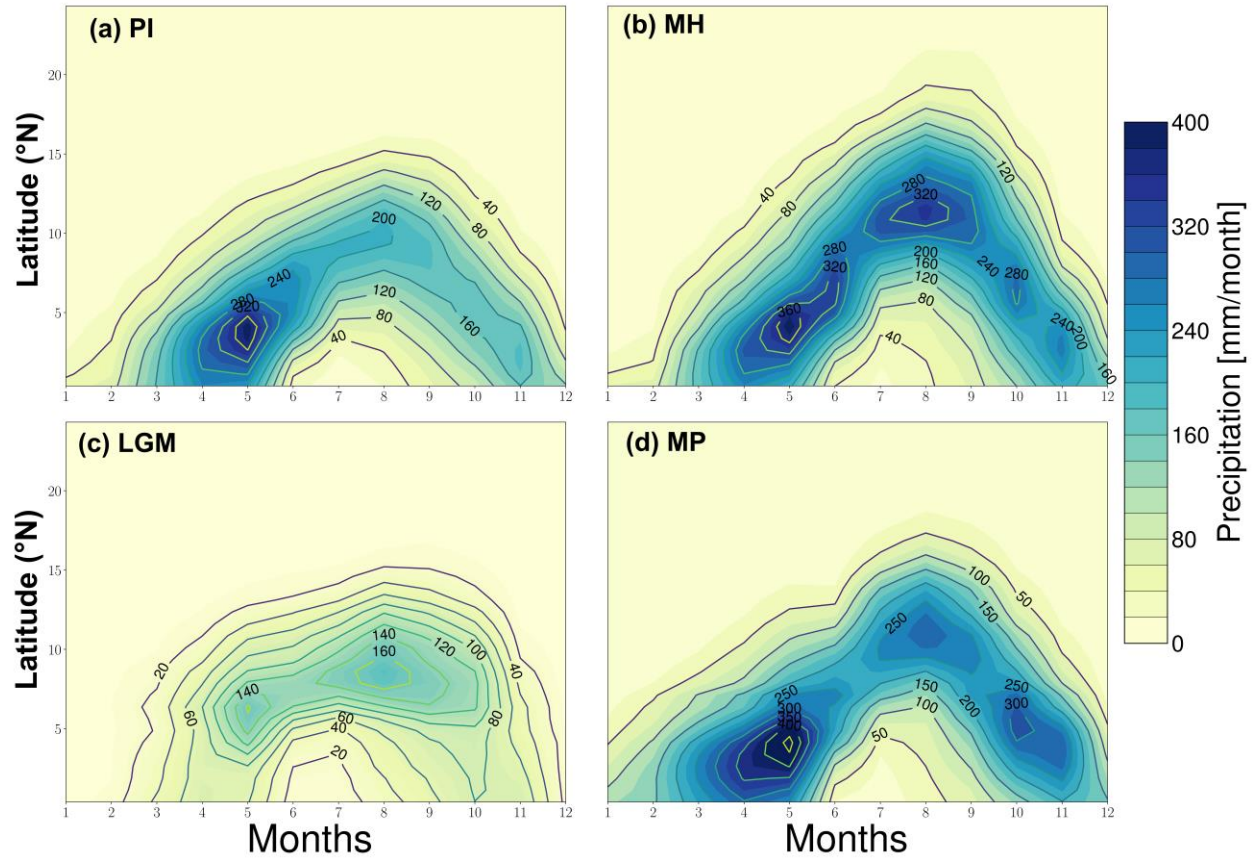
566 **Figure 5.** Latitudinal regional, seasonal means (JJAS) of precipitation anomalies across the  
 567 WAM region (averaged between 20°W and 30°E) estimated for the ECHAM5-wiso and PMIP4  
 568 models for (a) Mid-Holocene (MH), (b) Last Glacial Maximum (LGM), and (c) Mid-Pliocene  
 569 (MP) simulations. ECHAM5-wiso estimates show a latitudinal distribution that is consistent with  
 570 most of the PMIP4 models. ECHAM5-wiso estimates for LGM and MP fall into the PMIP4  
 571 model range, while ECHAM5-wiso estimates for the intensification of the WAM in the MH  
 572 exceed the PMIP4 model range.

573

#### 4.3 Seasonality of the simulated WAM in the late Cenozoic

574

575 The meridional migration of the WAM is investigated by analysing the evolution of  
 576 latitudinal regional means (Hovmöller diagram) (Fig. 6) and regional means over the coast of  
 577 Guinea, Sahel, and Sahara (Fig. 7). Generally, the seasonal cycle of the WAM progresses from  
 578 two rainy season regimes across the coastal areas to a single rainy event across higher latitudes  
 579 (Fig. 2). The progression of the WAM is classically defined in three phases: (1) the onset period  
 580 (March-May), driven by the low-level south-westerlies moist transport from the South Atlantic  
 581 towards the coastal regions up to 4°N and the abrupt shift of the ITCZ from the quasi-stationary  
 582 zone between 5-8°N to 8-10°N, (2) the high rain period (June-August), which abruptly shifts the  
 583 rain belt up to 10°N (also known as monsoon jump), marking the start of the high rainfall events  
 584 in the Sahel and the end of the first rainy regime across the coast, and (3) the southward retreat  
 585 (September-October), reflecting the last phase of the WAM annual cycle and the second rainfall  
 region across the coast (Barbé et al., 2002; Sultan et al., 2003; Sultan & Janicot, 2003).

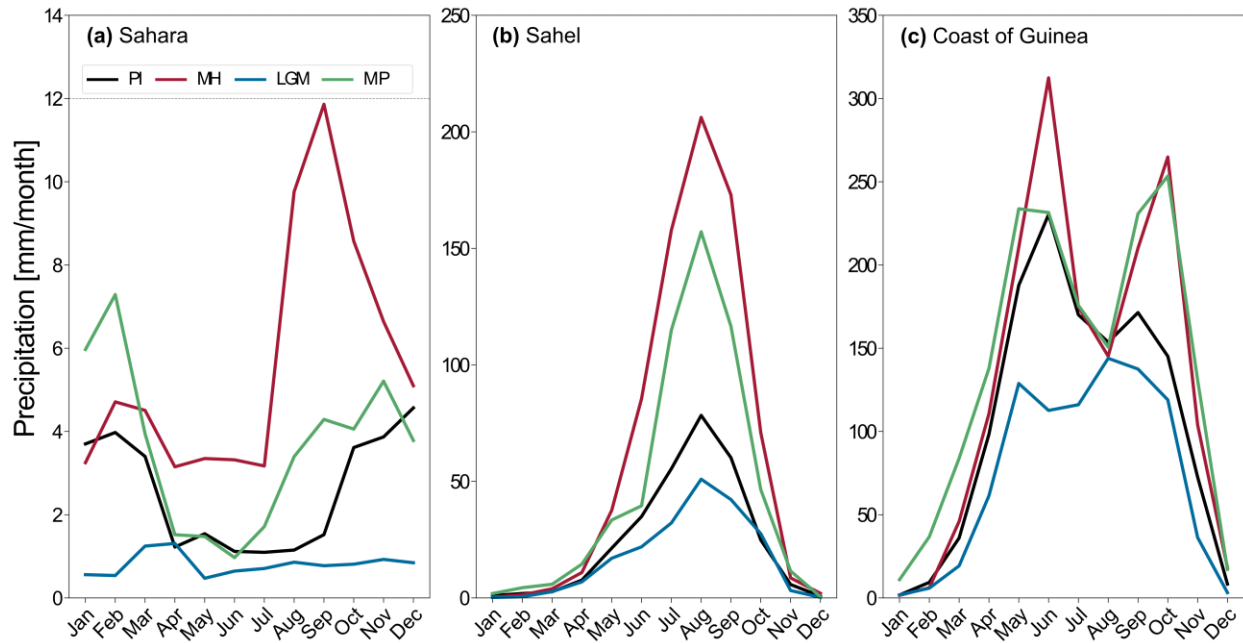


586

587 **Figure 6.** Hovmöller diagram (space-time) showing the latitudinal seasonal migration of  
 588 precipitation across the WAM region (averaged between  $20^\circ\text{W}$  and  $30^\circ\text{E}$ ) for the (a) Pre-  
 589 industrial (PI), (b) Mid-Holocene (MH), (c) Last Glacial Maximum (LGM), and (d) Mid-  
 590 Pliocene (MP) experiments using ECHAM5-wiso. The MH seasonal distribution indicates the  
 591 highest precipitation rate during the high-rainfall period (June-August), while the MP indicates  
 592 more precipitation in the onset (March-May) and southward retreat (September-October)  
 593 periods.

594 The latitudinal evolution of the WAM in the PI indicates maximum precipitation of up to  
 595 320 mm/month during the onset period (from March to May) along the coast, followed by a  
 596 monsoonal jump up to  $15^\circ\text{N}$  in the Sahel with  $\leq 40$  mm/month of precipitation (Fig. 6a).  
 597 Moreover, the southward retreat toward the coast at the end of the annual cycle records half of  
 598 the precipitation (i.e.,  $\sim 160$  mm/month) during the onset period. The MH evolution exhibits  
 599 similar phases, but with higher precipitation and a greater northward extent. Specifically, the  
 600 onset period records precipitation of  $\sim 360$  mm/month and a higher northward shift up to  $\sim 25^\circ\text{N}$   
 601 with higher precipitation rates of up to 320 mm/month across the Sahel (Fig. 6b). The southward  
 602 retreat phase in the MH is also characterised by higher precipitation rates of up to 240  
 603 mm/month. Overall, the MP seasonal trend shows an inverted V-shape distribution that is similar  
 604 to the MH pattern, but flatter and with a higher rainfall in the onset and southward retreat phases  
 605 along the coast. The onset and southward retreat phases are characterised by precipitation rates  
 606 of  $\sim 400$  mm/month and 300 mm/month across the coast of Guinea and the equatorial Atlantic,  
 607 respectively (Fig. 6d). However, the high-rainfall period is characterised by less rainfall ( $\sim 250$   
 608 mm/month) across the Sahel and a lower latitudinal extent ( $\leq 18^\circ\text{N}$ ) when compared to MH. On

609 the other hand, the LGM simulations predict drier conditions in all seasons, with a rainfall  
 610 increase of only up to 160 mm/month in the Sahel during the high-rain period (Fig. 6c).



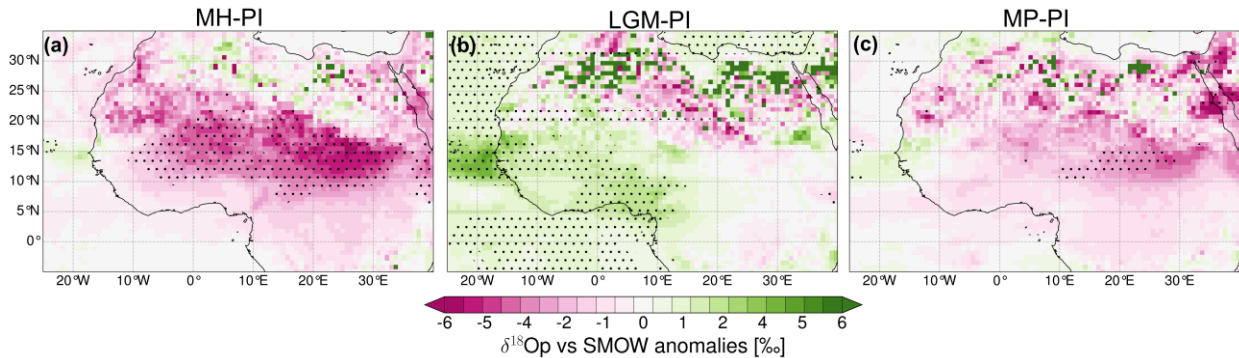
611  
 612 **Figure 7.** Seasonal cycle of precipitation across the (a) Sahara (30-20°N, 20°W-30°E), (b) Sahel  
 613 (20-10°N, 20°W-30°E), and (c) Guinea coast (10-5°N, 20°W-30°E) (See Fig. 1a) estimated for  
 614 the Pre-industrial (PI; black), Mid-Holocene (MH; red), (c) Last Glacial Maximum (LGM; blue),  
 615 and (d) Mid-Pliocene (MP; green) simulation using ECHAM5-wiso. The seasonal distribution of  
 616 precipitation across the Sahara shows different peak months for the different past climates, while  
 617 the Sahel and Coast of Guinea show a more consistent seasonality.

618 The seasonal cycle across the different climate zones is assessed through their regional  
 619 means. The seasonal precipitation cycle exhibits pronounced variations in magnitude, but few  
 620 changes in precipitation distribution. Among those few changes are variations in peak  
 621 precipitation months estimated for the Sahara. While the PI estimates indicate higher  
 622 precipitation (~4 mm/month) in November-February, the MH estimates suggest more  
 623 precipitation from July to October, with peak precipitation rates of 12 mm/month in September.  
 624 Overall, the LGM estimates indicate persistently drier conditions across all seasons in the  
 625 Sahara. The MP also indicates a higher precipitation record in the pre-onset period across the  
 626 Sahara, with a peak month in February (~7 mm/month). Regarding the bimodal monthly  
 627 distribution along the coastal regions, all climates show similar patterns. For the MH, the  
 628 precipitation peaks are highest, i.e. a ~300 mm/month peak in June and a ~260 mm/month peak  
 629 in October. The estimates across the Sahel also exhibit a unimodal distribution and precipitation  
 630 peak in August. The MH simulation produces the highest peak, with an increase of more than  
 631 100% relative to the PI.

#### 632 4.4 Changes of stable oxygen isotopic composition in precipitation associated with late 633 Cenozoic changes in the West African Monsoon

634 In this section, we explore the simulated seasonal climatological anomalies of the  
 635 precipitation-weighted stable oxygen isotopic composition of precipitation ( $\delta^{18}\text{O}_p$ ) during the

636 WAM season. Even though  $\delta^{18}\text{O}_p$  values are closely linked to precipitation due to the "amount  
 637 effect", the simulated spatial patterns of precipitation and  $\delta^{18}\text{O}_p$  values are different. Overall, the  
 638 warmer climates (i.e., MH and MP) estimate a decrease in  $\delta^{18}\text{O}_p$  values across the WAM region  
 639 when compared to the PI patterns during the monsoon season. In contrast, the  $\delta^{18}\text{O}_p$  anomalies  
 640 increase across many parts of the WAM region in response to the colder conditions in the LGM.  
 641 The MH is characterised by a significant decrease of  $\delta^{18}\text{O}_p$  values by  $\sim -5$  ‰ between 10-20 °N,  
 642 which spatially coincides with the region of the rain belt. The decrease becomes less pronounced  
 643 ( $\sim -1$  ‰) towards the Sahara region, and shows small areas that experience a slight increase ( $\sim 1$   
 644 ‰) towards the east. Moreover, the equatorial Atlantic region also experiences a slight  $\delta^{18}\text{O}_p$   
 645 decrease of about 1 ‰. The  $\delta^{18}\text{O}_p$  anomalies during the MP also decrease across the continent,  
 646 but show an increase of up to  $-6$  ‰ across the Sahara. Furthermore, the decrease of  $\delta^{18}\text{O}_p$  values  
 647 across the Sahel is less significant than the increase in precipitation anomalies in the MP. On the  
 648 other hand, the LGM simulation indicates a significant increase in  $\delta^{18}\text{O}_p$  values of  $\sim 3$  ‰ across  
 649 the Atlantic Ocean and the adjacent coastal regions.



650

651 **Figure 8.** Simulated changes in  $\delta^{18}\text{O}_p$  in the WAM season (JJAS) for the (a) Mid-Holocene  
 652 (MH), (b) Last Glacial Maximum (LGM), and (c) Mid-Pliocene (MP). The pink colour range  
 653 represents heavy isotope depletion, and the green colour range represents an enrichment in the  
 654 heavy isotopes in relation to Pre-industrial (PI) values. The black dot stippling indicates regions  
 655 with a statistically significant difference, assuming a confidence interval of 95%, using a student  
 656 t-test analysis.

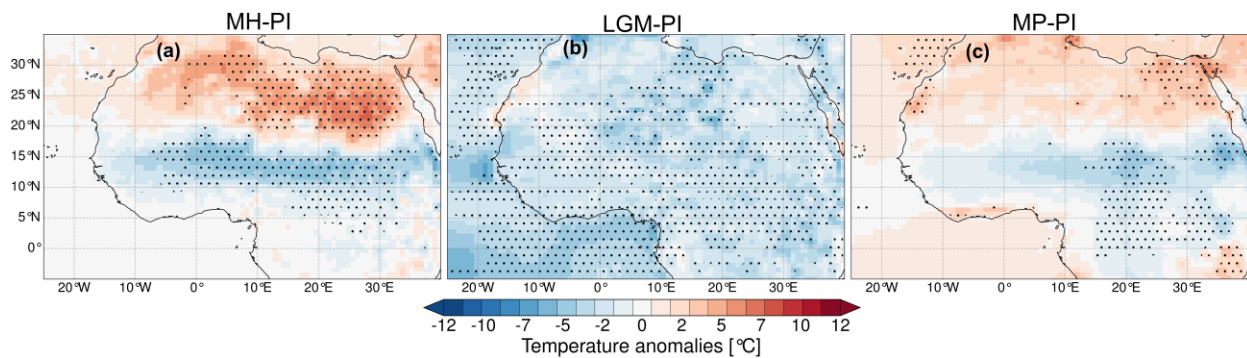
#### 657 4.5 Changes in the atmospheric dynamics behind the simulated WAM changes

658 Here, we analyse the atmospheric dynamics behind the simulated changes in the WAM.  
 659 Specifically, we use near-surface temperature, mean sea level pressure, wind patterns at different  
 660 atmospheric levels, and surface heat fluxes to investigate how these dynamics change in response  
 661 to different late Cenozoic boundary conditions. Due to our current understanding of WAM  
 662 dynamics (section 2.1), we focus on the spatial and intensification changes of the surface  
 663 temperature and pressure gradients, AEJ, TEJ, and the low-level south-westerly winds as the  
 664 dynamic feedback contributing to the simulated changes in the WAM. Additionally, we evaluate  
 665 the changes in the WAM due to land surface conditions (e.g., prescribed vegetation) in the  
 666 experiments through the responses of surface latent and sensible heat fluxes.

##### 667 4.5.1 Changes in near-surface temperature

668 The warmer climate experiments (i.e., MH and MP) produce a north-south near-surface  
 669 temperature gradient with an increase in the Sahara region, a decrease in the Sahel, and smaller

670 regions of increases (MP) or no (MH) changes at the southern coast (Fig. 9). Overall, the MH  
 671 indicates a pronounced meridional gradient with a significant increase in temperature anomaly of  
 672 up to 10 °C across the Sahara and a significant decrease of down to -8 °C towards the Guinea  
 673 coast. The MP anomalies indicate similar patterns, but with less pronounced gradients and  
 674 significant changes only toward Central and East Africa. More specifically, the MP shows an  
 675 increase of up to 5 °C across the Sahara and a decrease of about -3 °C across the Sahel,  
 676 transitioning into a slight increase of up to 2°C in the equatorial Atlantic. This spatial variability  
 677 is consistent with the precipitation patterns. Moreover, the mean sea level pressure patterns also  
 678 indicate the deepening of the low-pressure area across the Sahara in MH compared to the MP  
 679 (Fig. S6). However, comparing the cyclonic flow across the Sahara and the strengthened south-  
 680 westerlies moist transport from the equatorial Atlantic at 850 hPa between the MH and MP  
 681 reveals no noticeable changes (Fig. S6). Contrarily, the temperature anomalies in the LGM  
 682 indicate overall colder conditions across the continent with a significant decrease of up to -5 °C.



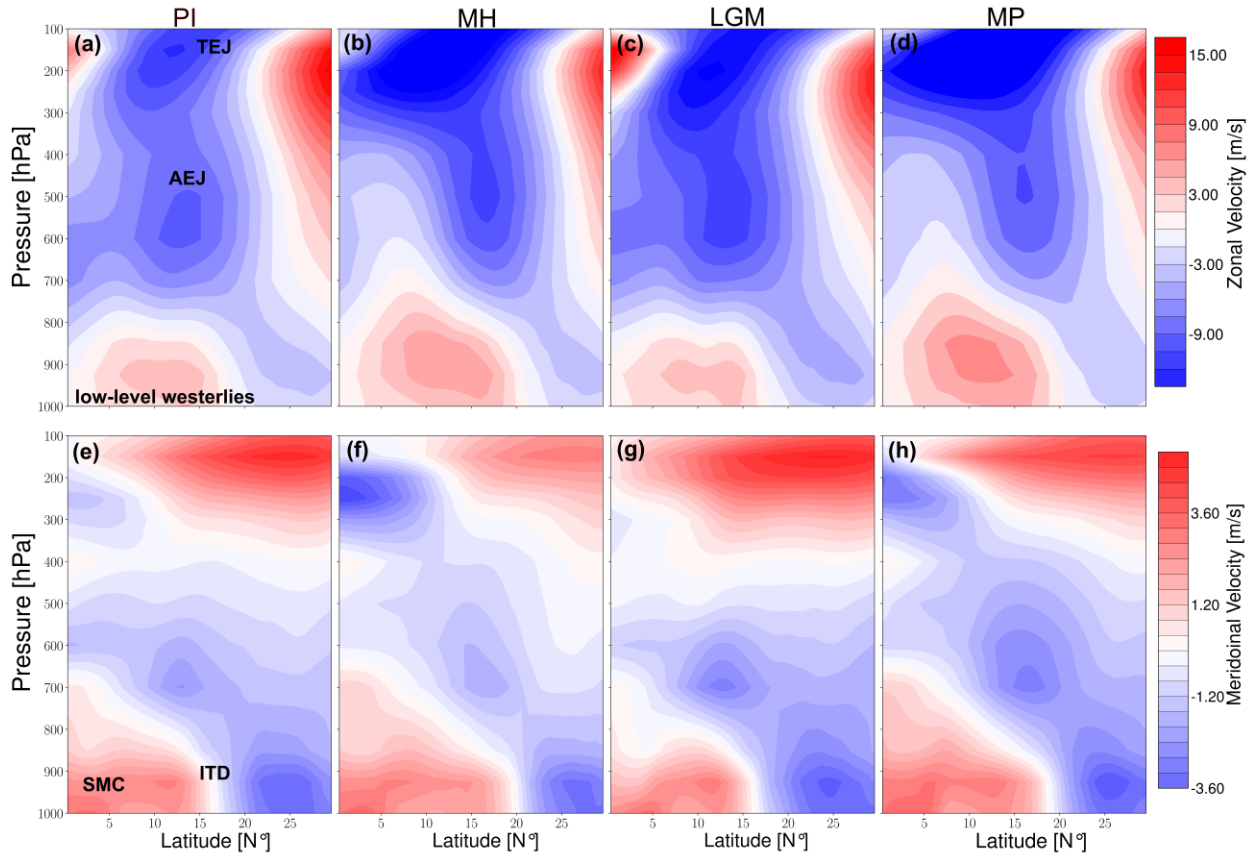
683

684 **Figure 9.** Simulated temperature anomalies of the WAM season (JJAS) estimated in response to  
 685 the (a) Mid-Holocene (MH), (b) Last Glacial Maximum (LGM), and (c) Mid-Pliocene (MP)  
 686 paleoenvironmental conditions using ECHAM5-wiso. The blue colour ranges represent colder  
 687 conditions, and the red colour ranges represent warmer conditions compared to the pre-industrial  
 688 estimates. The black dot stippling indicates regions with a statistically significant difference,  
 689 assuming a confidence interval of 95% using a student t-test analysis.

690

#### 4.5.2 Changes in the vertical structure of zonal and meridional wind speeds

691 We analysed the latitudinal-altitude cross-sections of zonal and meridional wind speeds  
 692 across the WAM region to understand the atmospheric circulation associated with the simulated  
 693 precipitation dynamics. The zonal wind patterns reveal a higher altitudinal reach of the low-level  
 694 southwesterlies and a greater northward propagation in the MH and MP when compared to the PI  
 695 and LGM (Fig. 10). The westerlies reach a latitudinal extent of 17°N and stay below 800 hPa  
 696 atmospheric level in the PI and LGM, while in the MH and MP, the flows extend over 20°N and  
 697 up to the 700 hPa level (Fig. 10 a-d). The MH and MP simulations estimate a higher northward  
 698 reach of the winds, but the latter predicts slightly higher wind shear at the core of the low-level  
 699 flow. Consistently, the AEJ is located between 10-15 °N at approximately 600 hPa in the PI and  
 700 LGM. However, the LGM indicates a more intense AEJ than the PI despite overall drier  
 701 conditions. In the MH and MP, the AEJ experiences a greater northward shift between 15-20 °N,  
 702 and its core shifts to a higher altitude than in the PI. In contrast to the LGM and PI, the AEJ in  
 703 the MH indicates higher intensification than the MP.



704

705 **Figure 10.** Latitudinal vertical cross-sectional for zonal (top panel) patterns, where positive  
 706 (negative) values indicate westerly (easterly) winds, and for meridional patterns (bottom panel),  
 707 where positive (negative) values indicate southerly (northerly) wind speeds estimated for the  
 708 WAM season (JJAS) in response to (a) Pre-industrial (PI), (b) Mid-Holocene (MH), (c) Last  
 709 Glacial Maximum (LGM), and (d) Mid-Pliocene (MP) paleoenvironmental conditions. The  
 710 approximate locations of the African Easterly Jet (AEJ), Tropical Easterly Jet (TEJ), Intertropical  
 711 Discontinuity (ITD), low-level westerlies and Shallow Meridional Cell (SMC) are shown in a  
 712 and e. The low-level westerlies reach the highest latitude and altitude in the MH. The  
 713 strengthened WAM conditions are more associated with the northward position of the Africa  
 714 Easterly Jet (AEJ) than its intensity.

715

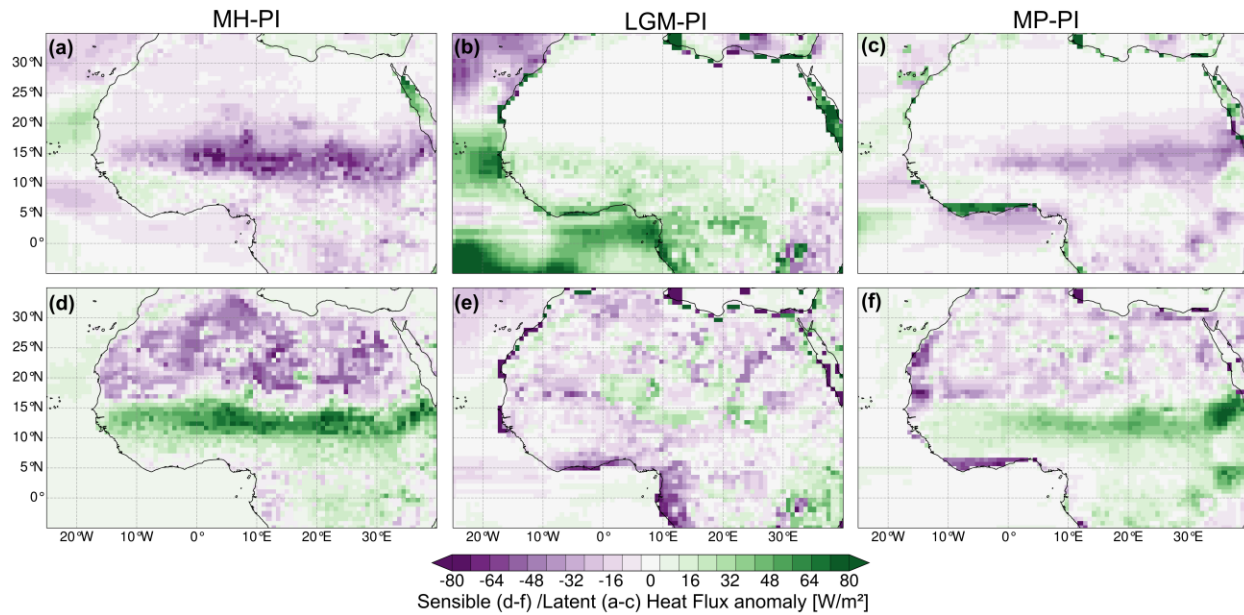
The latitudinal-altitude cross-section of winds also indicates higher vertical wind shear  
 716 (inferred from the transition from the low-level westerlies to the mid-level easterlies) in the MH  
 717 and MP compared to the PI. Stronger southwesterlies (and, therefore, a deeper monsoon depth)  
 718 are also identified in the MH and MP. The monsoon depth defines the altitudinal reach of  
 719 moisture transport from the equatorial Atlantic into the continent. In contrast, the LGM  
 720 experiment estimates a shallow monsoon depth compared to the PI. More specifically, the  
 721 monsoon depth reaches an altitude of 600 hPa in the MH and MP, and only up to 700 hPa in the  
 722 PI and LGM (Fig. 10 e-h). Moreover, the patterns in the MH and MP indicate a more northward  
 723 location of the ITD (i.e., the location where the moist southwesterlies deflect the dry  
 724 northeasterlies from the Sahara) at approximately 20 °N and 19 °N, respectively. For the PI and  
 725 LGM, the ITD is located further south (<17°N). The intensity of the low-level moisture  
 726 transport, TEJ, AEJ, and the location of the ITD coincide with the latitudinal band of negative

727 omega values (wind directions away from the ground; updraft) up to 200 hPa and the associated  
728 subsidence (positive omega values) across the Sahara (Fig. S7). Overall, the tropospheric  
729 structure of the winds reveals stronger southwesterlies moisture transport from the tropical  
730 Atlantic, a higher monsoon depth, the northward position of the AEJ, and the intensification of  
731 the TEJ, consistent with the increased intensity of the WAM and its northward migration in the  
732 MH and MP.

#### 733 4.5.3 Changes in sensible and latent heat fluxes

734 Generally, high vegetation cover yields more water availability through  
735 evapotranspiration, which increases latent heat (LH) flux. Moreover, moisture availability due to  
736 the increased LH flux leads to a rainfall-induced cooling effect, reducing sensible heat (SH) flux  
737 into the atmosphere. Specifically, for the WAM region, the recycling of water vapour through  
738 evaporative fluxes also contributes to the northward extent of precipitation. Therefore, the  
739 response of the WAM to different surface conditions is described here through the analysis of  
740 SH and LH fluxes.

741 The paleoclimate experiments indicate varied responses to the surface heat fluxes (Fig.  
742 11). In the MH experiment, the results indicate pronounced negative LH anomalies (i.e., upward  
743 flux) of up to  $-80 \text{ Wm}^{-2}$  across the Sahel, gradually reducing in magnitude towards the Sahara  
744 (Fig. 11a). Regions with more upward LH fluxes coincide with regions of a significant increase  
745 in precipitation the MH. The LGM reveals overall positive (downward) LH flux anomalies  
746 across the Sahel and coastal regions, with no changes towards the Sahara due to colder and drier  
747 conditions (Fig. 11b). In the MP, the estimated patterns reveal a slight increase in upward fluxes  
748 with negative LH anomalies down to  $-30 \text{ Wm}^{-2}$  across the Sahel, and no changes in the Sahara  
749 (Fig. 11c). Such simulated patterns of releasing LH are consistent with higher enhanced  
750 evaporation over vegetated surfaces through radiative forcing (Fig. S8) in the MH. The SH flux  
751 anomalies also show consistent results with more downward fluxes and colder surface conditions  
752 associated with increased precipitation. The MH experiment estimates negative SH anomalies  
753 down to  $-60 \text{ Wm}^{-2}$  across the Sahara, reaching  $15^\circ\text{N}$  and positive SH anomalies across the Sahel  
754 towards the coastal regions (Fig. 11d). The zonal band of the downward SH anomalies is also  
755 consistent with the simulated rain belt in both the MH and MP. The MP experiment estimates a  
756 similar, albeit less pronounced, north-south gradient of SH. The LGM experiment estimates  
757 negative SH anomalies across most regions on the continent, which is consistent with less  
758 availability of water to evaporate. The simulated SH flux patterns are consistent with the near-  
759 surface temperature anomalies, with a more pronounced meridional gradient in the MH relative  
760 to the MP.



761

762 **Figure 11.** Latent (top panel) and Sensible (bottom panel) heat flux anomalies during the WAM  
 763 months (JJAS) for the (a) Mid-Holocene (MH), (b) Last Glacial Maximum (LGM), and (c) Mid-  
 764 Pliocene (MP). The purple ranges represent net upward fluxes, and the green colour ranges  
 765 represent downward fluxes.

766

## 767 5 Discussion

### 768 5.1 Simulated changes of the WAM in response to the large-scale forcings

#### 769 *Mid-Holocene (~6ka)*

770 Overall, the analysed climate model outputs consistently indicate the intensification and  
 771 expansion of the WAM during the MH, specifically during the boreal summer. These simulated  
 772 patterns align with findings from previous modelling studies (e.g., Bosmans et al., 2012; Gaetani  
 773 et al., 2017; Patricola & Cook, 2007; Zhao & Harrison, 2012) and proxy reconstructions (e.g.,  
 774 Bartlein et al., 2011). The increase in precipitation during the WAM season is not surprising,  
 775 given that the orbital configurations of the MH lead to stronger insolation during the boreal  
 776 summer and autumn, and to weaker insolation during the winter when compared to PI forcings  
 777 (Joussaume et al., 1999; Kutzbach & Liu, 1997). These orbital precision variations with stronger  
 778 seasonal thermal amplitudes also result in more pronounced equator-to-pole and land-sea thermal  
 779 gradients, contributing to moisture redistribution across the continents (Brierley et al., 2020).  
 780 Specifically, the stronger thermal gradients and associated continental warming during the WAM  
 781 season (JJAS) deepen the low-pressure cells over the Sahara. This intensifies the advection of  
 782 moist air masses from the equatorial Atlantic Ocean, thereby amplifying and expanding the  
 783 WAM. Moreover, the redistribution of moisture associated with the seasonal insolation  
 784 distribution can be observed as a weakening of the annual-scale range of precipitation over the  
 785 ocean and a strengthening over the continent, as suggested in previous studies (e.g., Braconnot et  
 786 al., 2004). The MH precipitation anomalies in the inter-annual scale are less pronounced than the  
 787 seasonal changes. These changes reflect that the seasonal variations in insolation primarily drive

788 the MH global climate changes (Kageyama et al., 2013). The ECHAM5-wiso model estimates  
789 global warming of approximately  $\sim 0.3$  °C compared to the PI control run (Fig. S9 in the  
790 supplemental material). The bidirectional precipitation anomalies, with drier conditions toward  
791 the coastal regions, are also consistent with the rainfall dipole patterns of the African Humid  
792 Period (AHP). This phenomenon is explained by the northward shift of the ITCZ during the  
793 boreal summer in response to the insolation in the Northern Hemisphere (Braconnot et al., 2007;  
794 Coe & Harrison, 2002; deMenocal et al., 2000).

795 Compared to the model outputs from the PMIP4-CMIP6 experiments, ECHAM5-wiso  
796 predicts the highest intensification and greatest northward reach of the WAM. The precipitation  
797 anomalies estimated with ECHAM5-wiso indicate a maximum rain belt of approximately 150  
798 mm/month across the Sahel (10-20 °N) and less rainfall reaching 30 °N. Out of all considered  
799 models, ECHAM5-wiso estimates predict the highest regional precipitation means ( $\sim 95$   
800 mm/month), followed by the MPI-ESM-LR, which has a similar atmospheric model component  
801 (i.e., ECHAM6). This also further validates the ability of models in the ECHAM family to  
802 reproduce the atmospheric dynamics and hydrological cycle across the African continent. The  
803 relatively high precipitation rates predicted by our ECHAM5-wiso simulations might be partly  
804 due to the following:

805 (1) The representation of MH vegetation feedbacks. The experimental design for the  
806 PMIP4-CMIP6 MH simulation keeps vegetation from the PI, using prescribed surface conditions  
807 or dynamic vegetation models. However, previous studies have suggested a “Green Sahara”,  
808 characterised by steppe, savanna, and shrub vegetation, and fewer deserts than today (Dallmeyer  
809 et al., 2020; Hoelzmann et al., 1998; Jolly et al., 1998). Such vegetation is required to sustain the  
810 enhancement and northward extent of the WAM during the MH. The simulation with ECHAM5-  
811 wiso used MH vegetation patterns provided by the BIOME6000 vegetation reconstructions  
812 (Bigelow et al., 2003; Harrison et al., 2001; Pickett et al., 2004; Prentice et al., 2000), where the  
813 Sahara desert was drastically reduced, and the Sahelian vegetation belt, consisting of steppe,  
814 tropical dry forest, and xerophytic woods/shrubs, was extended northward (Jolly et al., 1998;  
815 Prentice et al., 2000). Through positive feedback, vegetation has been suggested to increase  
816 orbitally driven precipitation across North Africa due to the warming effect caused by reduced  
817 albedo (Bonfils et al., 2001) and increased evapotranspiration as a result of increased latent heat  
818 fluxes (Levis et al., 2004; Texier et al., 2000). Overall, moisture recycling through  
819 evapotranspiration and induced surface warming increases convection and inland moisture flux  
820 and intensifies the WAM. However, previous studies have also indicated a plausible negative  
821 vegetation feedback on precipitation at the annual scale due to a larger contribution of soil  
822 evaporation than the albedo feedback under wetter conditions (Notaro et al., 2008; Y. Wang et  
823 al., 2008).

824 (2) The lower values of greenhouse gas (GHG) concentrations used for the PMIP4-  
825 CMIP6 MH experiments. Lower  $p\text{CO}_2$  would result in a slightly colder climate than that  
826 produced by the ECHAM5-wiso simulation. This has been shown for the PMIP3-CMIP5 MH  
827 experiments that used GHG concentrations that are similar to those used for our ECHAM5-wiso  
828 experiment. The differences between PMIP4-CMIP6 and PMIP3-CMIP5 were due to the  
829 simulated difference in effective radiative forcing of  $-0.3 \text{ Wm}^{-2}$  (Otto-Bliesner et al., 2017).  
830 Generally, the slightly colder climate would reduce the temperature meridional gradient across  
831 the African continent that drives low-level south-westerly moist air masses from the equatorial  
832 Atlantic Ocean.

833 (3) The use of the high spatial resolution for the ECHAM5-wiso simulation. Several  
834 studies have demonstrated that monsoons are better resolved when resolution is increased, even  
835 though the magnitude changes are more susceptible to the model's parameterisation (e.g., Gao et  
836 al., 2006; Sperber et al., 1994). The higher spatial resolution consequently reproduces the MH  
837 patterns through improved representation of important processes, such as large-scale  
838 condensation, land-sea interaction, and topographic forcings (Boyle & Klein, 2010). Bosmans et  
839 al. (2012) showed that using a high-resolution (T159) for EC-Earth GCM resulted in an  
840 increased intensity and a greater northward reach of the WAM in the MH when compared to the  
841 low-resolution PMIP2 ocean-atmosphere coupled models. The inter-model variabilities can also  
842 be attributed to the differences in complexities and the models' sensitivity to the parameterisation  
843 of clouds, atmospheric dynamics, and the hydrological cycle in general. We highlight that  
844 determining the influence of resolution and model parameterisation is beyond the scope of this  
845 manuscript. Overall, all the models estimate similar latitudinal precipitation patterns across the  
846 WAM region, but the predicted northward reach and regional precipitation amounts are too low  
847 to sustain the plant types that existed during the MH (Braconnot et al., 2007; Jousaume et al.,  
848 1999).

#### 849 *Last Glacial Maximum (~21 ka)*

850 Generally, the global climate during the LGM was characterised by large-scale cooling  
851 due to radiative perturbations linked to the extensive continental ice sheets and lower  
852 atmospheric greenhouse gas (GHG) concentrations (Clark et al., 2009). These large-scale drivers  
853 were further modified by internal feedbacks in the climate system involving factors like sea ice,  
854 snow, and water vapour (e.g., Braconnot et al., 2007). ECHAM5-wiso simulates realistic patterns  
855 of temperature anomalies, indicating maximum cooling of approximately  $-15\text{ }^{\circ}\text{C}$  across regions  
856 with ice sheets in the Northern Hemisphere, and moderate cooling ( $-2$  to  $-5\text{ }^{\circ}\text{C}$ ) over tropical  
857 areas (Fig. S9). These patterns are similar to the results of PMIP4-CMIP6 experiments and align  
858 with findings from previous modelling studies (e.g., Cao et al., 2019; Kageyama et al., 2021).  
859 The large perturbations in the atmospheric radiative balance due to albedo feedbacks also result  
860 in significant changes in atmospheric circulation patterns, contributing to comprehensive  
861 changes in precipitation patterns (e.g., Liakka et al., 2016; Liakka & Lofverstrom, 2018). Large  
862 ice sheets covering North America and Fennoscandia redirect low-level winds, which strongly  
863 influences moisture transport and regional precipitation. Additionally, the associated  
864 thermodynamics, as indicated through specific humidity, can contribute to regional precipitation  
865 changes (D'Agostino et al., 2019, 2020). Most of the precipitation on land was substantially  
866 decreased due to the large-scale cooling and its associated reduction in evapotranspiration (e.g.,  
867 Braconnot et al., 2007). The lower SSTs led to reduced evaporation over the oceans, which in  
868 turn reduced the surface's moisture flux into the atmosphere. This eventually led to a decreased  
869 inland moisture flux, leading to overall large-scale drying. Apart from surface cooling,  
870 tropospheric cooling also decreased the amount of atmospheric water vapour by limiting its  
871 water-holding capacity through the Clausius-Clapeyron relation. However, in both hemispheres,  
872 other regions across the mid-latitudes experienced an increase in precipitation, mainly in areas  
873 corresponding to the positions of the North Pacific, North Atlantic, and Southern Ocean storm  
874 tracks (Fig. S9). The simulated temperature patterns indicate overall cooling across the African  
875 continent, suggesting that the meridional temperature and pressure gradient that drives northward  
876 moisture flux from the Atlantic Ocean are suppressed, thereby reducing moisture availability  
877 across the WAM areas. Furthermore, the surface cooling over the oceans was more intense than

878 over land, indicating a decrease in the land-sea thermal contrast, which would result in an  
879 additional reduction in inland moisture transport.

880 *Mid-Pliocene (~3 Ma)*

881 Simulating the MP climate provides the opportunity to evaluate the long-term response of  
882 the climate system to currently raised atmospheric GHG concentrations. This period is often  
883 considered an analogue for future climate change (Burke et al., 2018) due to its similarities to  
884 modern palaeogeography and high  $p\text{CO}_2$  (400 ppm). As such, the modelling framework of the  
885 MP helps assess how important climatic components of the Earth system, such as the El Niño-  
886 Southern Oscillation, the global hydrological cycle and monsoon systems, respond to the  
887 ongoing rise in  $\text{CO}_2$  concentrations. The simulated temperature patterns predict a global mean  
888 near-surface temperature increase of approximately 3 °C, primarily due to direct  $\text{CO}_2$  forcing.  
889 The overall warming exhibits polar amplification, with temperature anomalies increasing by  
890 more than 10 °C due to associated changes in albedo at higher latitudes (Chandan & Peltier,  
891 2020; de Nooijer et al., 2020; Samakinwa et al., 2020; Tindall et al., 2022). The simulated global  
892 mean temperature increase predicted by ECHAM5-wiso falls within the range of model  
893 estimates (1.4 to 4.6 °C) from the PlioMIP phase 1 and 2 experiments (Haywood et al., 2013,  
894 2020). The significant warming in high latitudes reduces the meridional temperature gradient,  
895 weakening the tropical atmospheric circulation, specifically the Hadley circulation (Corvec &  
896 Fletcher, 2017; Haywood et al., 2013). Previous studies also indicated a poleward shift of mid-  
897 latitude westerly winds (Li et al., 2015), increased intensity of tropical cyclones (Yan et al.,  
898 2016), and strengthening and poleward extension of the global land monsoon system (Li et al.,  
899 2018). The enhanced hydrological cycle intensifies the East Asian and West African summer  
900 monsoons (R. Zhang et al., 2013, 2016). These changes resemble future climate projections (e.g.,  
901 Erfanian et al., 2016; Seth et al., 2019) and require detailed understanding from a modelling  
902 perspective.

903 Through sensitivity experiments, (Stepanek et al. (2020) determined that MP  
904 palaeogeography contributes to increased rainfall across the WAM areas. The closure of the  
905 Arctic gateway and enhanced topography have also been suggested to strengthen the Atlantic  
906 Meridional Overturning Circulation (AMOC), thereby warming the North Atlantic Ocean (Z.  
907 Zhang et al., 2021), which impacts the WAM (Mulitza et al., 2008). These findings highlight the  
908 importance of other boundary conditions in regulating the WAM. As mentioned earlier, land  
909 surface conditions, such as vegetation, contribute to the variability and spatial extent of the  
910 WAM through evaporative fluxes. Proxy reconstructions from previous studies suggest more  
911 humid conditions across northern Africa, which facilitates an expansion of vegetation. More  
912 specifically, palynological records suggest high tree cover density and broadening of woodlands  
913 and savannas at the expense of deserts across the Sahara (Bonnefille, 2010; Salzmann et al.,  
914 2008). ECHAM5-wiso was set up with converted PRISM3 vegetation reconstructions, which  
915 indicate the expansion of grass and forests across North Africa towards the Mediterranean (Fig.  
916 S10). Such patterns are also consistent with the COSMOS dynamic vegetation results presented  
917 in Stepanek et al. (2020), which estimated an increase in precipitation by 70 mm/month across  
918 the WAM region. The PlioMIP2 models with prescribed MP vegetation also indicate a  
919 strengthened WAM, with an ensemble mean of precipitation showing an increase by ~76 (60 -  
920 120) mm/month (Berntell et al., 2021). The previous modelling inter-comparison project (i.e.,  
921 PlioMIP1) estimates a lower magnitude of increase within a range of 30 to 60 mm/month (R.  
922 Zhang et al., 2016). The PlioMIP1 experimental protocol (Haywood et al., 2010) was similar to

923 the model setup used for the ECHAM5-wiso simulation. These findings suggest that ECHAM5-  
924 wiso simulates a higher magnitude of WAM precipitation in the MP than the PlioMIP1 models.  
925 This may be due to the higher spatial resolution used for ECHAM5-wiso, which improves  
926 representation of land surface conditions (e.g., orography and vegetation) and model  
927 parameterisation. Overall, PlioMIP1 and PlioMIP2 models suggest that the updated MP  
928 boundary conditions from PRISM3 to PRISM4 contribute to the strengthening of the WAM.  
929 Samakinwa et al. (2020) confirm this with a sensitivity experiment using COSMOS, which  
930 indicated that the updated palaeogeography was the main reason for the changes in the large-  
931 scale features between PlioMIP1 and PlioMIP2.

932 The precipitation simulated with ECHAM5-wiso shows an increase of up to 120  
933 mm/month and an intensification towards the east (Fig. 3). However, regional means of  
934 precipitation across the Sahel increase by only ~50 mm/month, which falls within the broader  
935 range of PMIP4-CMIP6 estimates (10-160 mm/month) (Fig. 4). The CESM2 and EC-Earth3-LR  
936 models estimate significant increases of 90 and 160 mm/month, respectively. The HadGEM3-  
937 GC31-LL, IPSL-CM6A-LR, and NorESM1-F estimate a moderate increase of ~50 mm/month,  
938 with GISS-E2-G estimating the lowest increase of only ~10 mm/month. The magnitude of the  
939 precipitation response simulated by the individual models across the WAM is consistent with the  
940 global response. For instance, GISS-E2-1-G indicates a low global response to the MP boundary  
941 conditions and consistently estimates the lowest WAM precipitation anomalies. On the contrary,  
942 models with large land-sea rainfall anomalies (e.g., EC-Earth3-LR and CESM2) also simulate a  
943 strengthened WAM. Even though the updated boundary conditions contributed to the inter-  
944 model variabilities, Haywood et al. (2020) suggested model parameterisation and initial  
945 conditions as the main factors for the varied predictions. Moreover, later model versions tend to  
946 have a higher sensitivity than earlier versions when used with the same boundary and initial  
947 conditions. These findings suggest that using ECHAM6-wiso (Cauquoin et al., 2019) and even  
948 updated PRISM4 reconstructions (Dowsett et al., 2016; Haywood et al., 2016) would increase  
949 the strengthening of the WAM in the model.

## 950 5.2 Control of the precipitation and temperature on stable oxygen isotope in the WAM 951 season in response to the different past climates

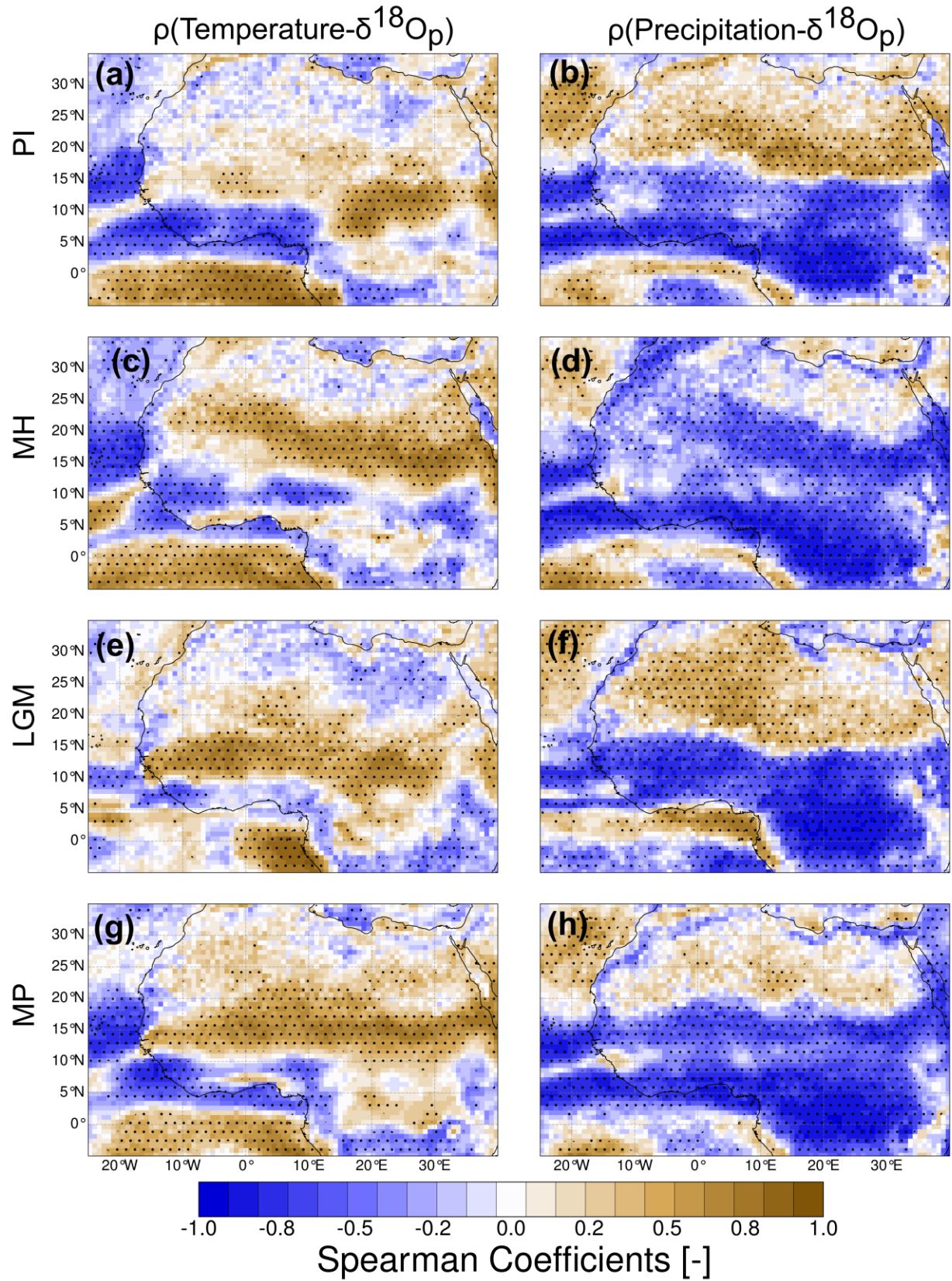
952 The stable oxygen isotopic composition of tropical precipitation provides information  
953 about the hydrological cycle and can be used to reconstruct past tropical climates. Several studies  
954 have employed stable isotopes to understand the intraseasonal water cycle variability in western  
955 Africa (e.g., Risi et al., 2008, 2010). These studies have revealed that the integrated convective  
956 activity in the monsoon season is spatially and temporally reflected in the  $\delta^{18}\text{O}$  values in  
957 precipitation and vapour records. On a broader scale, previous studies have used isotopic patterns  
958 to identify the strengthening of the Northern Hemisphere monsoon in response to warmer  
959 climates, both through modelling (e.g., Cauquoin et al., 2019; Shi et al., 2023; Thompson et al.,  
960 2021) and proxy records (Wang et al., 2008; Bartlein et al., 2011). Simulating the isotopic  
961 composition allows for a direct comparison of model simulations to isotopic archives and  
962 contributes to the understanding of the causal mechanisms behind various proxy archives (Bühler  
963 et al., 2022; Phipps et al., 2013; Risi et al., 2012; Werner et al., 2000). Here, we explore the  
964 response of simulated  $\delta^{18}\text{O}_p$  to varied paleoenvironmental conditions during the WAM season.  
965 The results suggest that meteoric water was more negative in past warmer climates and less  
966 negative in colder climates. Similar patterns have been reported in previous isotope-enabled  
967 GCM modelling studies (e.g., Risi et al., 2010; Cauquoin et al., 2019). Specifically, the oxygen

968 isotopes are most depleted during the MH, indicating the role of seasonal insolation distribution  
969 and associated precipitation dynamics in the isotopic patterns (Thompson et al., 2021).  
970 Importantly, the magnitude and spatial patterns, to some extent, are inconsistent with the  
971 simulated precipitation anomalies despite the expected dependence of the isotopic composition  
972 on convective activity, as suggested in previous studies (e.g., Bony et al., 2008; Lawrence et al.,  
973 2004). These changes reveal the plausibility of additional factors controlling  $\delta^{18}\text{O}_p$  in different  
974 climates. Therefore, we further explore the relative influence of precipitation and temperature on  
975 the simulated  $\delta^{18}\text{O}_p$  patterns to better understand what controls the oxygen isotopes during the  
976 monsoon season.

977 We evaluate the control of precipitation and temperature on  $\delta^{18}\text{O}_p$  values in different time  
978 periods by calculating their linear relationship during the WAM season using Spearman  
979 correlation analysis. The PI simulation yields north-south bidirectional correlation patterns  
980 between precipitation and  $\delta^{18}\text{O}_p$  values, with significant negative correlations ( $\geq -0.8$ ) over the  
981 Guinea Coast up to the Sahel (0-15 °N) and positive correlations ( $\geq 0.7$ ) across the Sahara (Fig.  
982 12). The strong negative relationship along the coastal region towards the Sahel indicates the  
983 amount effect, as is expected based on previous studies (Lawrence et al., 2004; Rozanski et al.,  
984 1993). Convective activity has been well established as the main factor driving the spatial and  
985 temporal patterns of the isotopic composition of precipitation and vapour (Lawrence et al., 2004;  
986 Risi et al., 2008; Bony et al., 2008). The reasons why an increase in precipitation amount results  
987 in the depletion of the heavy oxygen isotope across the WAM might be partially due to the fact  
988 that (1) the increase in rainfall amount moistens the atmosphere, which reduces rainfall re-  
989 evaporation and diffusive fluxes, and ultimately results in lower  $\delta^{18}\text{O}_p$  values in raindrops; (2)  
990 intense convective activity increases vertical mixing in the form of unsaturated downdrafts, so  
991 that the associated depletion of low-level vapour feeds into subsequent convective systems with  
992 lower  $\delta^{18}\text{O}_p$  values (Lawrence et al., 2004; Risi et al., 2008). The change in correlation direction  
993 over the Sahara indicates that the "amount effect" is limited across the Sahel region, where the  
994 maximum rain belt is situated during the monsoon season. These changes are unsurprising, as the  
995 rainout of the moisture transported from the equatorial Atlantic Ocean would deplete the  
996 remaining air masses of heavy oxygen isotopes. However, during the retreat of the WAM,  
997 evaporative recycling provides a moist air mass with relatively enriched heavy oxygen isotopes  
998 that condense to rainfall. These changes suggest the influence of continental recycling on the  
999 isotopic patterns across the Sahel. Surface evaporative fluxes through continental recycling result  
1000 in air masses that are less negative than oceanic fluxes (Risi et al., 2013). Moreover, the warmer  
1001 and drier conditions across the Sahara would contribute to more re-evaporation of falling vapour,  
1002 leading to an enrichment in the heavier isotope in relation to the source (Risi et al., 2008). The  
1003 LGM and MP simulations indicate similar correlation dipole patterns across the WAM, but the  
1004 positive relationship across the Sahara in the MP is less significant (Fig. 12). Nevertheless, the  
1005 correlation patterns in the MH indicate an overall negative link across the whole WAM region,  
1006 suggesting that the amount effect predominantly controls the oxygen isotopic patterns. The  
1007 changes in the correlation structure across different past climates suggest the non-stationarity of  
1008 the controlling mechanism across the WAM areas.

1009 The correlation analyses for  $\delta^{18}\text{O}_p$  and temperature yield fewer regions with significant  
1010 correlation due to the predominant influence of precipitation amount on  $\delta^{18}\text{O}_p$  during the WAM  
1011 season. The analysis indicates positive correlation patterns over the Sahara, which extends  
1012 further northward in the MP. The expanded area of positive correlation in the MP highlights the  
1013 importance of continental recycling during the retreat of the WAM. These patterns also validate

1014 the wider spread of precipitation during the retreat months in the MP (Fig. 6 d), which has also  
1015 been suggested in previous studies (Berntell et al., 2021). Although this analysis is limited to  
1016 empirical evidence that does not consider causal mechanisms, the results clearly indicate that  
1017 proxy reconstructions must efficiently understand the regional climatic influence on various  
1018 proxy records. This would help resolve the inaccuracies in paleoclimate and paleoenvironment  
1019 reconstructions that assume the stationarity of the calibrated transfer function (e.g., Kolstad &  
1020 Screen, 2019; Raible et al., 2014). The comparison of the simulated isotopic values to proxy  
1021 records and the investigation of the causal mechanisms leading to the available proxy records is  
1022 beyond the scope of this study.



1024 **Figure 12.** Spearman correlation coefficients for the relationship between the simulated monthly  
 1025  $\delta^{18}\text{O}_p$  and precipitation amount (right panel) and temperature (left panel) during the WAM  
 1026 months (JJAS). The dot stippling represents the regions with significant correlation coefficients  
 1027 with a 95% confidence interval. The correlations' magnitude and spatial patterns are not  
 1028 stationary in response to the different climates. For example, the bi-directional north-south  
 1029  $\delta^{18}\text{O}_p$ -precipitation relation transitions to an overall negative relationship in the Mid-Holocene  
 1030 (MH).

### 1031 5.3 Atmospheric dynamics driving the simulated WAM changes

1032 Overall, the response of the WAM to GHG forcing, vegetation changes, and orbital  
 1033 forcing is mostly associated with the changing meridional temperature gradient. A more  
 1034 pronounced gradient drives the increased intensity and higher altitude reach of the low-level  
 1035 southwesterlies and a more northward position of the ITD and AEJ. On the other hand, the  
 1036 weakening of the WAM in response to colder conditions can be attributed to the weak or non-  
 1037 existent meridional temperature and pressure gradient. This less pronounced gradient would lead  
 1038 to moisture transport into the continent and into the troposphere to suppress the wind shear of the  
 1039 AEJ. We discuss these simulated dynamics in the context of what has been suggested in previous  
 1040 studies, while also highlighting the new findings.

1041 The pronounced summer meridional temperature and pressure patterns in the MH and  
 1042 MP climates are consistent with the PMIP4 model results (e.g., Bertell et al., 2021; Brierley et  
 1043 al., 2020; Kageyama et al., 2021). These temperature anomalies reflect the patterns of increased  
 1044 precipitation, namely wetter conditions across the Sahel to coastal regions in the MH and MP.  
 1045 The warming over the high latitudes deepened the Sahara Heat Low, inducing low-level moisture  
 1046 convergence and strengthening the south-westerly flow that transports moisture from the  
 1047 equatorial Atlantic into the continent (Lavaysse et al., 2009). In the MH, the warming across the  
 1048 Sahara and the cooling over the Sahel are more intense than in the MP. The increased insolation  
 1049 across the Northern Hemisphere was the main driver of the intense warming across the Sahara.  
 1050 On the other hand, the cooling over the Sahel is partly due to the cloudiness associated with  
 1051 increased precipitation due to enhanced moisture flux into the Sahel areas. Another factor may  
 1052 be the increased evaporative fraction (Fig. S8) and upward latent heat flux (Fig. 11), which  
 1053 moisten the soil and reduce the energy available to heat the near-surface air through sensible heat  
 1054 flux. These mechanisms (a) cool the surface where precipitation increases and (b) further  
 1055 strengthen the north-south gradient to drive moisture advection into the WAM region. This  
 1056 feedback indicates that moisture advection strengthens the WAM more than local recycling does  
 1057 (Marzin & Braconnot, 2009; Y. Zhao et al., 2005). However, the internal feedback reinforces the  
 1058 pressure gradient and determines the northward migration of the WAM through evaporative  
 1059 recycling. In the MP, the seasonal precipitation distribution indicates a delayed WAM retreat  
 1060 with more precipitation during the southward retreat months than in the MH. Such precipitation  
 1061 seasonality highlights the role of internal feedback since the evaporative recycling supplies more  
 1062 moisture during the retreat months. Furthermore, cooling across the Sahel in the MP is more  
 1063 significant toward the east. These patterns coincide with the relative increase in upward latent  
 1064 heat flux toward the east, suggesting more moisture availability through local feedback to  
 1065 strengthen the cooling (Fig. 11). Even though the MP has higher atmospheric  $\text{CO}_2$  with an  
 1066 enhanced hydrological cycle, this study reveals that the orbital forcing and expanded vegetation  
 1067 in the MH produces the highest intensity of the WAM. These imply that GCMs must adequately  
 1068 represent these features to ensure accurate projections of the WAM in response to future climate

1069 change. In the LGM climate, the overall cooling and drying conditions prevent the initiation of a  
1070 meridional pressure gradient to drive moisture into the continent. This resulted in continuous  
1071 wind patterns from the Tropical Atlantic into the North Atlantic Ocean without diverging into the  
1072 continent, as suggested in previous studies (e.g., Jiang et al., 2015; Kageyama et al., 2021; Otto-  
1073 Bliesner et al., 2006). Overall, the strengthening of the meridional temperature and pressure  
1074 gradient determines the intensity of the southwesterlies, northward migration of the WAM, and  
1075 its altitudinal reach, which affects the location of the ITD and AEJ.

1076 The simulated intensity and location of the AEJ and its relationship to the strengthening  
1077 of the WAM suggest a complex causal mechanism. More specifically, the simulated core of the  
1078 AEJ is situated at higher latitudes (15-20°N) and altitudes (600-500 hPa) in summer during the  
1079 MH and MP than in the PI and LGM. These patterns are not surprising since the strengthened  
1080 WAM in these climates is associated with a more northward position of the ITD and deeper  
1081 monsoon depth (Janicot et al., 2011; Nicholson, 2009). Moreover, the surface temperature  
1082 gradient maintains the AEJ, along with two meridional circulations forced by the dry convection  
1083 of the Sahara Heat Low to the north and the moist convection driven by the ITCZ to the south  
1084 (Thorncroft & Blackburn, 1999; Wu et al., 2009). Usually, the monsoonal flow of the low-level  
1085 southwesterlies reaches far into the mid-troposphere to weaken the shear of the AEJ and shift it  
1086 to higher latitudes (Texier et al. 2000; Patricola and Cook 2007). However, the simulated intense  
1087 monsoonal flow due to the pronounced meridional temperature gradient in the MH induces high  
1088 AEJ intensity when compared to the MP. On the other hand, the reduced monsoonal flow  
1089 simulated in the LGM also results in an AEJ intensity that is higher than PI. These causal  
1090 relationship patterns indicate that the weakening of the AEJ is not entirely associated with the  
1091 strengthening of the WAM, especially when orbital forcings mainly control large-scale climatic  
1092 features. Therefore, the atmospheric dynamics response simulated in this study confirms that the  
1093 position of the AEJ is more important in strengthening the WAM than its intensity, as suggested  
1094 in previous studies (Jenkins et al., 2005; Nicholson, 2008; Nicholson & Grist, 2001; Nicholson &  
1095 Webster, 2007). These suggest that the intensity of the AEJ is an effect rather than a cause  
1096 (Newell & Kidson, 1984). The complexity of the causal relationship between AEJ and Sahel  
1097 rainfall and its varied feedback, as reported by some studies, might be due to its sensitivity to  
1098 localised conditions, which is represented differently in GCMs. For instance, Texier et al. 2000  
1099 and Patricola and Cook 2007 reveal that the decrease or even disappearance of the AEJ is  
1100 achieved when the GCM is coupled to a dynamic vegetation model. Contrarily, Texier et al.  
1101 2000 produced an increased AEJ located further north without dynamic vegetation feedback in  
1102 the model.

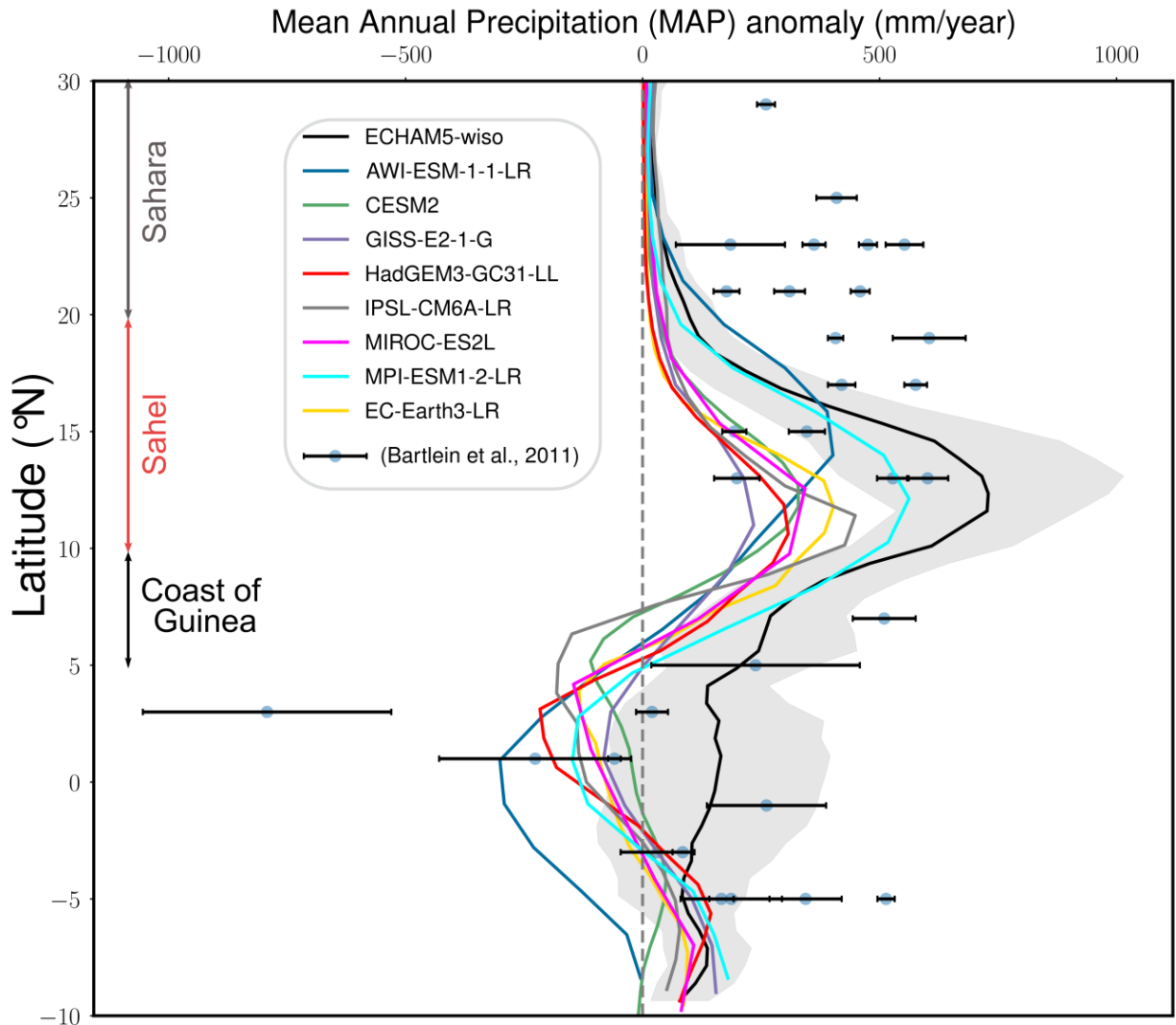
1103 The simulated TEJ intensity shows consistent patterns of increasing shear due to wetter  
1104 conditions, as indicated by previous studies (e.g., Nicholson and Klotter 2021). The simulated  
1105 intensity in the MH and MP revealed no significant changes, but was higher than LGM and PI  
1106 (Fig. 10). The TEJ is mostly driven by large-scale remote features such as convective heating  
1107 over the North Indian Ocean and the Himalayan-Tibetan plateau (Gill, 1980). However,  
1108 Redelsperger et al. (2002) indicate that the latent heat release through convection over the WAM  
1109 can enhance upper-level shear, thereby intensifying the TEJ. The causal mechanisms through  
1110 which the intensified TEJ increases the Sahel rainfall have been proposed in many studies  
1111 (Lemburg et al., 2019). These include upper-level divergence (Nicholson & Grist, 2003), vertical  
1112 and horizontal shear and how it affects dynamic instabilities (Grist, 2002; Nicholson, 2008), and  
1113 the modulation of the equatorial Rossby wave activity (Yang et al., 2018).

1114 The results reveal both the localised and large-scale impacts of vegetation on  
1115 precipitation over the WAM areas in response to different climates. Generally, vegetation  
1116 influences the exchange of mass and energy between the land surface and the atmosphere  
1117 through the modulation of (1) surface albedo, influencing surface radiation, and (2)  
1118 evapotranspiration, influencing the partitioning of net radiation into surface heat fluxes. These  
1119 imply that land cover does not only affect surface climate but also influences atmospheric  
1120 convection and large-scale circulations and moisture fluxes, which create further feedback and  
1121 influence soil moisture and vegetation (Charney et al., 1977; Sylla et al., 2016). In this study, we  
1122 focus on analysing the influence of surface conditions through surface heat flux anomalies.  
1123 Previous modelling studies have highlighted the role of soil moisture and evapotranspiration in  
1124 the vegetation-precipitation feedback due to their effect on low-level moist static energy,  
1125 convective instability, and surface latent heat flux anomalies (Patricola & Cook, 2007;  
1126 Rachmayani et al., 2015). These feedback mechanisms have been shown to strengthen the  
1127 response of the WAM to external forcing in past warmer climates (e.g., Messori et al., 2019).  
1128 The expanded vegetation over the Sahara in the MH resulted in a pronounced upward latent heat  
1129 flux, further strengthening the WAM and the moisture influx through the vegetation-albedo  
1130 feedback (e.g., Bonfils et al., 2001; Levis et al., 2004). The less expanded vegetation in the MP  
1131 also strengthened the WAM and contributed to the increased precipitation in the retreat months  
1132 of the WAM, even though the meridional pressure gradient was weaker than in the MH. Previous  
1133 studies have indicated wetter conditions and a northward migration of the WAM that is driven by  
1134 the cyclonic moisture flux anomaly over North Africa due to expanded vegetation into the  
1135 Sahara region (Chandan & Peltier, 2020; Pausata et al., 2020; Swann et al., 2014). Since the  
1136 various atmospheric dynamics and surface conditions had a unidirectional influence on the  
1137 WAM, isolating the impact of vegetation, a local amplifier forced by other large-scale features  
1138 (e.g., Klein et al., 2017; Messori et al., 2019), would require further sensitivity experiments.

#### 1139 5.4 Comparison of model estimates to proxies

1140 Comparing modelled paleoclimate to proxy reconstructions over Africa is often  
1141 challenging, because of the varying representation of relevant atmospheric processes in different  
1142 GCMs, and high spatial variability of proxy signals (e.g., deMenocal et al., 2000; Harrison et al.,  
1143 2014; Pausata et al., 2016; Tierney et al., 2017; Hopcroft and Valdes, 2019). Moreover, the  
1144 relatively low availability of paleohydrological records over Africa precludes a robust model-  
1145 data comparison (e.g., Salzmann et al., 2008, 2013). The sparsity of proxies also prevents the  
1146 merited direct comparison of simulated isotopic composition with past isotopic archives. Here,  
1147 we focus on the MH model-data comparison due to the relatively large number of proxy  
1148 reconstructions available and the ongoing debate about the northward migration and  
1149 intensification of the WAM during the African Humid Period (e.g., Pausata et al., 2020). The  
1150 sparse tropical African proxy records for the LGM reported in previous studies have shown  
1151 consistent cooling and drying conditions. It has been suggested that the dryness induced a  
1152 downward elevational shift of broadleaved evergreen or warm mixed forest and the enrichment  
1153 of steppe into regions now occupied by tropical forests (e.g., Elenga et al., 2000). The  
1154 reconstructed proxy records over North Africa during the MP consistently suggested more humid  
1155 conditions. More specifically, palynological data reveals denser tree cover and expanded  
1156 woodland and savanna at the expense of deserts over North Africa (Bonnefille, 2010; Salzmann  
1157 et al., 2008). Such vegetation expansion patterns are consistent with the only dynamic vegetation  
1158 GCM output participating in PlioMIP2 (Stepanek et al., 2020). Moreover, multi-proxy records,

1159 including plant wax and dust from marine sediment cores from offshore West Africa, suggest  
 1160 consistent wetter conditions in the MP (deMenocal, 2004; Kuechler et al., 2018). These  
 1161 reconstructed patterns are consistent with the more humid and dryness simulated for the LGM  
 1162 and MP.



1163  
 1164 **Figure 13.** Comparison of the mean annual precipitation (MAP) anomalies of the latitudinal  
 1165 extent of WAM in the Mid-Holocene for all models (ECHAM5-wiso (black) and PMIP4 models)  
 1166 to proxies reconstruction from Bartlein et al., (2011). The black shadings denote one standard  
 1167 deviation value from the regional means of the ECHAM5-wiso simulation. The error bars of the  
 1168 proxies represent the standard errors of the precipitation reconstructions.

1169 In the remainder of this section, we compare the simulated latitudinal variation of Mean  
 1170 Annual Precipitation (MAP) during the MH to pollen-based reconstructions by Bartlein et al.  
 1171 (2011). Overall, the simulated MAP magnitudes and latitudinal distribution by ECHAM5-wiso  
 1172 are closer to the proxy reconstructions than the PMIP4 models (Fig. 13). More specifically, the  
 1173 ECHAM5-wiso inter-annual means of the WAM's northward extent compare well to the lower  
 1174 latitudes pollen-based estimates over the Sahara with regards to the magnitude of changes and  
 1175 the patterns from the Sahel towards the tropical ocean. However, all models (i.e., PMIP4 models

1176 and ECHAM5-wiso) failed to match the magnitudes of the proxy-based MAP increase over the  
1177 high latitudes of the Sahara. The simulated MAP increase over the Sahara was 100-300 mm/year  
1178 less than the proxy reconstruction. It is important to note that the calculated MAP anomalies used  
1179 present-day CRU observation data as a reference period for the proxies, while the GCMs used  
1180 their PI simulations. Although the different reference periods can contribute slightly to the  
1181 discrepancies, the magnitude of the difference is large enough to acknowledge significant  
1182 deviations and thus potential limitations of either the GCMs or the proxy-based reconstructions.  
1183 The simulated ECHAM5-wiso anomalies during the monsoon season indicated wetter conditions  
1184 up to 25 °N, with increased precipitation anomalies of approximately 700 mm/year (Fig. 3). This  
1185 suggests a potential overestimation of precipitation anomalies from the pollen-based records on  
1186 the annual scale due to their potentially biased representation of the dry seasons across the  
1187 Sahara. In addition to the pollen-based reconstructions, other diverse archives over West Africa  
1188 estimate precipitation differences in the range of 300-500 mm/month, which are within the range  
1189 of our model estimates (Harrison et al., 2014; Kröpelin et al., 2008; Tierney et al., 2017). On the  
1190 other hand, recent reconstructions of leaf wax-alkane records off the coast of northern Africa  
1191 suggest MAP of higher than 700 mm/year as far north as 31°N, implying an expansion of the  
1192 WAM in the MH to 15-20° north of its present-day extent (Sultan & Janicot, 2003; Tierney et  
1193 al., 2017). Sha et al. (2019) interpreted their Moroccan speleothem at 31°N with high negative  
1194  $\delta^{18}\text{O}$  of carbonate records as a high rainfall signal created by the expansion of the WAM during  
1195 the MH. Paleoenvironment reconstructions also reflect wetter conditions in the MH with higher  
1196 lake levels and moisture-demanding biomes across North Africa (Kohfeld & Harrison, 2000;  
1197 Peyron et al., 2006; H. Wu et al., 2007). Vegetation reconstructions suggest a northward shift of  
1198 montane forest and a major extension of the tropical rainforest over North Africa (Jolly et al.  
1199 1998; Prentice et al. 2000).

1200 Overall, the model-proxy comparison reveals that all the adopted GCMs show limited  
1201 skill in reproducing the northward migration of the WAM and associated rainfall increase over  
1202 the Sahara. This suggests that the shortcomings leading to these discrepancies are shared by all  
1203 models and are not GCM-specific. The WAM dynamics are sensitive to the representation of  
1204 climate physics in the GCMs. Their limitations include inaccuracies in representing clouds,  
1205 surface conditions (e.g., lakes and wetlands), energy fluxes, and subgrid-scale convection  
1206 parameterisation. Additionally, the coarse spatial resolution of GCMs weakens their ability to  
1207 reproduce the mesoscale convection systems that are the main driver for the WAM. Previous  
1208 studies have also indicated that fully coupled models exhibit biases in reproducing the tropical  
1209 Atlantic dynamics, leading to elevated sea surface temperatures and a weakened monsoonal  
1210 circulation (Roehring et al., 2013). In this study, the high spatial resolution of the ECHAM5-  
1211 wiso experiment contributed to a better representation of surface conditions, such as orography.  
1212 Furthermore, the model was prescribed MH vegetation reconstruction. Contrarily, the PMIP4  
1213 models are fully coupled (atmosphere-ocean), incorporating ocean variability feedback, and  
1214 some consider dynamic vegetation feedback. Since all models, i.e. both ECHAM5-wiso and the  
1215 PMIP models, exhibit the above-mentioned deviations from proxy reconstructions, we propose  
1216 that the limitations are neither related solely to spatial resolution nor the use of fully coupled  
1217 models. Harrison et al. (2015) suggests the simulated biases of the PI control experiments of the  
1218 PMIP4-CMIP6, which indicate a more equatorward ensemble mean of the global monsoon when  
1219 compared to observations. Previous models have also shown that atmosphere-vegetation  
1220 feedback contributes to the northward extent of the WAM, but still underestimates the higher  
1221 latitude precipitation amount from the leaf wax n-alkanes (Dallmeyer et al., 2020; Pausata et al.,

1222 2016; Thompson et al., 2019). Rachmayani et al. (2015) demonstrated that dynamic vegetation  
1223 enhances the orbitally driven increase in precipitation anomalies over West Africa by 20% when  
1224 compared to models using fixed vegetation. However, their models with terrestrial and ocean  
1225 feedback still did not reach the level of vegetation coverage suggested by proxies.

1226 Recent studies have demonstrated that incorporating dust feedbacks associated with the  
1227 Green Sahara in the MH orbitally driven climate further enhances the northward reach and  
1228 intensification of the WAM (e.g., Thompson et al., 2019; Pausata et al., 2016; Hopcroft and  
1229 Valdes, 2019; Egerer et al., 2018) and better matches the paleoclimate reconstructions. This is  
1230 because the albedo-related feedback causes a reduction of dust concentration and changes in soil  
1231 properties over the vegetated Sahara, which induce an increase in incoming shortwave radiation  
1232 on the land surface, strengthening the warming over the Sahara. This further strengthens the  
1233 meridional temperature gradient and tropical circulation and then intensifies the WAM (Chandan  
1234 and Peltier, 2020; Pausata et al., 2016). Pausata et al. (2016) demonstrated the northward extent  
1235 of the WAM up to 31°N in the MH with a model forced with prescribed vegetation and reduced  
1236 dust concentrations, while the prescribed vegetation only reached ~26°N. These suggest that  
1237 simulating vegetation feedback with interactive dust dynamics on a high spatial resolution grid  
1238 would improve the representation of the MH. However, the state-of-art GCMs would require  
1239 improvement of their physical representation of dust dynamics, since they fail to reproduce dust  
1240 emission and transport (Evan et al., 2014; Kok, 2010; Leung et al., 2023; A. Zhao et al., 2022).  
1241 On the other hand, the plausible non-stationarity of the pollen-precipitation transfer function due  
1242 to changes in past climate dynamics from present conditions can also contribute to the mismatch  
1243 between climate simulation and paleoclimate reconstructions. Therefore, using a multi-proxy  
1244 system with varied causal mechanisms could ensure an accurate representation of the WAM  
1245 complex dynamics.

## 1246 **6 Conclusions**

1247 This study presents new and existing climate model simulations of the WAM and  
1248 associated features in the Late Cenozoic (i.e. the PI, MH, LGM and MP). More specifically, the  
1249 study presents an overview of the hydroclimate changes over West Africa and highlights the  
1250 components of the regional climate system that are important for generating accurate projections  
1251 of future climate. The paleoclimate experiments were conducted using the isotope-tracking  
1252 model (ECHAM5-wiso). The simulated results are similar to the CMIP6-PMIP4 experiments  
1253 and proxy reconstructions over West Africa. However, our simulations also show some  
1254 improvement over previous experiments, and yield new insights. We summarise the key results  
1255 as follows:

1256 1. A comparison between the present-day ECHAM5-wiso simulation and observation-  
1257 based datasets (i.e., ERA5 and CRU precipitation and temperature datasets) demonstrates the  
1258 model's ability to represent the atmospheric dynamics over West Africa reasonably well.

1259 2. The ECHAM5-wiso paleoclimate simulations produce the most intense WAM during  
1260 the MH, despite the MP's more enhanced hydrological cycle. In comparison, some of the  
1261 CMIP6-PMIP4 models suggest the highest intensification of the WAM in the MH (e.g., GISS-  
1262 E2-1-G), while others suggest the MP (e.g., EC-Earth3-LR).

1263 3. The intensification of the WAM is associated with a pronounced meridional gradient,  
1264 northward position of the ITD, northward reach of the core of the AEJ, higher altitudinal reach of

1265 the WAM (deeper monsoon depth), and higher moisture recycling through surface heat fluxes  
1266 due to vegetation across the Sahel-Sahara region. Most importantly, the AEJ is not entirely  
1267 responsible for the strengthening of the WAM, especially when large-scale features are  
1268 predominantly controlled by orbital forcings, as is the case in the MH. This needs to be well-  
1269 represented in GCMs to ensure realistic and accurate future projections.

1270 4. The simulation of the patterns and magnitude of  $\delta^{18}\text{O}_p$  values and associated regional  
1271 climate elements (e.g., temperature and precipitation) during the monsoon season reveal a non-  
1272 stationarity of their relationship throughout the late Cenozoic. Their changing relationships stress  
1273 the need to understand the causal mechanisms for each proxy system and refine their transfer  
1274 function to ensure accurate proxy-based reconstructions.

1275 5. ECHAM5-wiso simulates the higher precipitation rates over the WAM region in the  
1276 MH than the CMIP6-PMIP4 models. Since our model uses a more accurate vegetation  
1277 reconstruction and a higher resolution, we propose that a greater consideration of vegetation  
1278 feedbacks, and sub-grid processes will increase other models' representation of West African  
1279 climate during the MH.

1280 6. All models still underestimate the northward extent of the WAM, as reconstructed with  
1281 proxies. If proxy reconstructions are taken as accurate, this suggests that the representation of  
1282 additional climate processes, such as dust loading, interactive vegetation, and surface conditions,  
1283 such as lakes, will have to be improved to ensure a more realistic prediction of the WAM's  
1284 northward extent.

## 1285 **Acknowledgments**

1286 This research was supported by the German Science Foundation (DFG) grants EH329/19-1 and  
1287 EH329/23-1 (awarded to Todd A. Ehlers), MU4188/3-1 and MU4188/1-1 (awarded to Sebastian  
1288 G. Mutz). We acknowledge the World Climate Research Programme, which, through its  
1289 Working Group on Coupled Modeling, coordinated and promoted CMIP6. We thank the climate  
1290 modelling groups for producing and making their model output available, the Earth System Grid  
1291 Federation (ESGF) for archiving the data and providing access, and the multiple funding  
1292 agencies supporting CMIP and ESGF. Additionally, we thank the European Centre for Medium-  
1293 Range Weather Forecasts for providing ERA5 datasets and the University of East Anglia for  
1294 producing the CRU datasets.

1295

1296

1297

## 1298 **Open Research**

1299 Code availability statement:

1300 The ECHAM model code is available under a version of the MPI-M software license agreement  
1301 (<https://www.mpimet.mpg.de/en/science/models/license/>, last access: 03 January 2024). The  
1302 code of the isotopic version ECHAM5-wiso is available upon request on the Alfred Wegner  
1303 Institute's GitLab repository (<https://gitlab.awi.de/mwerner/mpi-esm-wiso>, last access: 03  
1304 January 2024). The scripts used for postprocessing, analysis, and visualisation are based on a  
1305 Python package (pyClimat) available at <https://doi.org/10.5281/zenodo.7143044> (Boateng, 2022)  
1306 and also on Github: <https://github.com/Dan-Boat/pyClimat> (last access: 03 January 2024)

1307

1308 Data availability statement:

1309 The postprocessed model output variables required to reproduce the figures of this study are  
 1310 available in NetCDF format at <https://doi.org/10.5281/zenodo.10455772> (Boateng, 2024). The  
 1311 CMIP6-PMIP4 (Eyring et al., 2016) models output are available at [https://esgf-  
 1312 node.llnl.gov/projects/esgf-llnl/](https://esgf-node.llnl.gov/projects/esgf-llnl/) (last access: 03 January 2024). The Climate Research Unit  
 1313 (CRUv4.01) (Harris et al., 2020) precipitation data were obtained from  
 1314 [https://crudata.uea.ac.uk/cru/data/hrg/cru\\_ts\\_4.01/](https://crudata.uea.ac.uk/cru/data/hrg/cru_ts_4.01/) (last access: 03 January 2024).  
 1315 The ERA5 reanalysis products (Hersbach et al., 2020) were obtained from the Copernicus  
 1316 Climate Data Store at <https://cds.climate.copernicus.eu/cdsapp#!/home> (last access: 03 January  
 1317 2024).

1318

1319 **References**

- 1320 Abe-Ouchi, A., Saito, F., Kageyama, M., Braconnot, P., Harrison, S. P., Lambeck, K., et al. (2015). Ice-sheet  
 1321 configuration in the CMIP5/PMIP3 Last Glacial Maximum experiments. *Geoscientific Model  
 1322 Development*, 8(11), 3621–3637. <https://doi.org/10.5194/gmd-8-3621-2015>
- 1323 Adegbe, A. T., Schneider, R. R., Röhl, U., & Wefer, G. (2003). Glacial millennial-scale fluctuations in central  
 1324 African precipitation recorded in terrigenous sediment supply and freshwater signals offshore Cameroon.  
 1325 *Palaeogeography, Palaeoclimatology, Palaeoecology*, 197(3), 323–333. [https://doi.org/10.1016/S0031-  
 1326 0182\(03\)00474-7](https://doi.org/10.1016/S0031-0182(03)00474-7)
- 1327 Annan, J. D., & Hargreaves, J. C. (2013). A new global reconstruction of temperature changes at the Last Glacial  
 1328 Maximum. *Climate of the Past*, 9(1), 367–376. <https://doi.org/10.5194/cp-9-367-2013>
- 1329 Annan, J. D., & Hargreaves, J. C. (2015). A perspective on model-data surface temperature comparison at the Last  
 1330 Glacial Maximum. *Quaternary Science Reviews*, 107, 1–10.  
 1331 <https://doi.org/10.1016/j.quascirev.2014.09.019>
- 1332 Armitage, S. J., Bristow, C. S., & Drake, N. A. (2015). West African monsoon dynamics inferred from abrupt  
 1333 fluctuations of Lake Mega-Chad. *Proceedings of the National Academy of Sciences*, 112(28), 8543–8548.  
 1334 <https://doi.org/10.1073/pnas.1417655112>
- 1335 Arnold, L., Bréon, F.-M., & Brewer, S. (2009). The Earth as an extrasolar planet: the vegetation spectral signature  
 1336 today and during the last Quaternary climatic extrema. *International Journal of Astrobiology*, 8(2), 81–94.  
 1337 <https://doi.org/10.1017/S1473550409004406>
- 1338 Badger, M. P. S., Schmidt, D. N., Mackensen, A., & Pancost, R. D. (2013). High-resolution alkenone  
 1339 palaeobarometry indicates relatively stable pCO<sub>2</sub> during the Pliocene (3.3–2.8 Ma). *Philosophical  
 1340 Transactions of the Royal Society A: Mathematical, Physical and Engineering Sciences*, 371(2001),  
 1341 20130094. <https://doi.org/10.1098/rsta.2013.0094>
- 1342 Baidu, M., Schwendike, J., Marsham, J. H., & Bain, C. (2022). Effects of vertical wind shear on intensities of  
 1343 mesoscale convective systems over West and Central Africa. *Atmospheric Science Letters*, 23(8), e1094.  
 1344 <https://doi.org/10.1002/asl.1094>
- 1345 Barbé, L. L., Lebel, T., & Tapsoba, D. (2002). Rainfall Variability in West Africa during the Years 1950–90.  
 1346 *Journal of Climate*, 15(2), 187–202. [https://doi.org/10.1175/1520-  
 1347 0442\(2002\)015<0187:RVIWAD>2.0.CO;2](https://doi.org/10.1175/1520-0442(2002)015<0187:RVIWAD>2.0.CO;2)
- 1348 Bartlein, P. J., Harrison, S. P., Brewer, S., Connor, S., Davis, B. A. S., Gajewski, K., et al. (2011). Pollen-based  
 1349 continental climate reconstructions at 6 and 21 ka: a global synthesis. *Climate Dynamics*, 37(3), 775–802.  
 1350 <https://doi.org/10.1007/s00382-010-0904-1>
- 1351 Bartoli, G., Hönisch, B., & Zeebe, R. E. (2011). Atmospheric CO<sub>2</sub> decline during the Pliocene intensification of  
 1352 Northern Hemisphere glaciations. *Paleoceanography*, 26(4). <https://doi.org/10.1029/2010PA002055>

- 1353 Bell, B., Hersbach, H., Simmons, A., Berrisford, P., Dahlgren, P., Horányi, A., et al. (2021). The ERA5 global  
 1354 reanalysis: Preliminary extension to 1950. *Quarterly Journal of the Royal Meteorological Society*,  
 1355 *147*(741), 4186–4227. <https://doi.org/10.1002/qj.4174>
- 1356 Bereiter, B., Eggleston, S., Schmitt, J., Nehrbass-Ahles, C., Stocker, T. F., Fischer, H., et al. (2015). Revision of the  
 1357 EPICA Dome C CO<sub>2</sub> record from 800 to 600 kyr before present. *Geophysical Research Letters*, *42*(2),  
 1358 542–549. <https://doi.org/10.1002/2014GL061957>
- 1359 Berntell, E., Zhang, Q., Li, Q., Haywood, A. M., Tindall, J. C., Hunter, S. J., et al. (2021). Mid-Pliocene West  
 1360 African Monsoon rainfall as simulated in the PlioMIP2 ensemble. *Climate of the Past*, *17*(4), 1777–1794.  
 1361 <https://doi.org/10.5194/cp-17-1777-2021>
- 1362 Biasutti, M. (2013). Forced Sahel rainfall trends in the CMIP5 archive. *Journal of Geophysical Research:*  
 1363 *Atmospheres*, *118*(4), 1613–1623. <https://doi.org/10.1002/jgrd.50206>
- 1364 Bigelow, N. H., Brubaker, L. B., Edwards, M. E., Harrison, S. P., Prentice, I. C., Anderson, P. M., et al. (2003).  
 1365 Climate change and Arctic ecosystems: 1. Vegetation changes north of 55°N between the last glacial  
 1366 maximum, mid-Holocene, and present. *Journal of Geophysical Research: Atmospheres*, *108*(D19).  
 1367 <https://doi.org/10.1029/2002JD002558>
- 1368 Blunier, T., & Brook, E. J. (2001). Timing of Millennial-Scale Climate Change in Antarctica and Greenland During  
 1369 the Last Glacial Period. *Science*, *291*(5501), 109–112. <https://doi.org/10.1126/science.291.5501.109>
- 1370 Boateng, D., Mutz, S. G., Ballian, A., Meijers, M. J. M., Methner, K., Botsyun, S., et al. (2023). The effects of  
 1371 diachronous surface uplift of the European Alps on regional climate and the oxygen isotopic composition  
 1372 of precipitation. *Earth System Dynamics*, *14*(6), 1183–1210. <https://doi.org/10.5194/esd-14-1183-2023>
- 1373 Bonfils, C., Noblet-Ducoudré, N. de, Braconnot, P., & Joussaume, S. (2001). Hot Desert Albedo and Climate  
 1374 Change: Mid-Holocene Monsoon in North Africa. *Journal of Climate*, *14*(17), 3724–3737.  
 1375 [https://doi.org/10.1175/1520-0442\(2001\)014<3724:HDAACC>2.0.CO;2](https://doi.org/10.1175/1520-0442(2001)014<3724:HDAACC>2.0.CO;2)
- 1376 Bonnefille, R. (2010). Cenozoic vegetation, climate changes and hominid evolution in tropical Africa. *Global and*  
 1377 *Planetary Change*, *72*(4), 390–411. <https://doi.org/10.1016/j.gloplacha.2010.01.015>
- 1378 Bony, S., Risi, C., & Vimeux, F. (2008). Influence of convective processes on the isotopic composition ( $\delta^{18}\text{O}$  and  
 1379  $\delta\text{D}$ ) of precipitation and water vapor in the tropics: 1. Radiative-convective equilibrium and Tropical  
 1380 Ocean–Global Atmosphere–Coupled Ocean–Atmosphere Response Experiment (TOGA-COARE)  
 1381 simulations. *Journal of Geophysical Research: Atmospheres*, *113*(D19).  
 1382 <https://doi.org/10.1029/2008JD009942>
- 1383 Boos, W. R. (2012). Thermodynamic Scaling of the Hydrological Cycle of the Last Glacial Maximum. *Journal of*  
 1384 *Climate*, *25*(3), 992–1006. <https://doi.org/10.1175/JCLI-D-11-00010.1>
- 1385 Bosmans, J. H. C., Drijfhout, S. S., Tuenter, E., Lourens, L. J., Hilgen, F. J., & Weber, S. L. (2012). Monsoonal  
 1386 response to mid-holocene orbital forcing in a high resolution GCM. *Climate of the Past*, *8*(2), 723–740.
- 1387 Botsyun, S., Mutz, S. G., Ehlers, T. A., Koptev, A., Wang, X., Schmidt, B., et al. (2022). Influence of Large-Scale  
 1388 Atmospheric Dynamics on Precipitation Seasonality of the Tibetan Plateau and Central Asia in Cold and  
 1389 Warm Climates During the Late Cenozoic. *Journal of Geophysical Research: Atmospheres*, *127*(12),  
 1390 e2021JD035810. <https://doi.org/10.1029/2021JD035810>
- 1391 Boyle, J., & Klein, S. A. (2010). Impact of horizontal resolution on climate model forecasts of tropical precipitation  
 1392 and diabatic heating for the TWP-ICE period. *Journal of Geophysical Research: Atmospheres*, *115*(D23).  
 1393 <https://doi.org/10.1029/2010JD014262>
- 1394 Braconnot, P., Otto-Bliesner, B., Harrison, S., Joussaume, S., Peterchmitt, J.-Y., Abe-Ouchi, A., et al. (2007).  
 1395 Results of PMIP2 coupled simulations of the Mid-Holocene and Last Glacial Maximum &ndash; Part 1:  
 1396 experiments and large-scale features. *Climate of the Past*, *3*(2), 261–277. [https://doi.org/10.5194/cp-3-261-](https://doi.org/10.5194/cp-3-261-2007)  
 1397 2007
- 1398 Braconnot, Pascale, Harrison, S. P., Joussaume, S., Hewitt, C. D., Kitoch, A., Kutzbach, J. E., et al. (2004).  
 1399 Evaluation of PMIP coupled ocean-atmosphere simulations of the Mid-Holocene. In R. W. Battarbee, F.  
 1400 Gasse, & C. E. Stickley (Eds.), *Past Climate Variability through Europe and Africa* (pp. 515–533).  
 1401 Dordrecht: Springer Netherlands. [https://doi.org/10.1007/978-1-4020-2121-3\\_24](https://doi.org/10.1007/978-1-4020-2121-3_24)

- 1402 Braconnot, Pascale, Harrison, S. P., Kageyama, M., Bartlein, P. J., Masson-Delmotte, V., Abe-Ouchi, A., et al.  
 1403 (2012). Evaluation of climate models using palaeoclimatic data. *Nature Climate Change*, 2(6), 417–424.  
 1404 <https://doi.org/10.1038/nclimate1456>
- 1405 Brady, E. C., Otto-Bliesner, B. L., Kay, J. E., & Rosenbloom, N. (2013). Sensitivity to Glacial Forcing in the  
 1406 CCSM4. *Journal of Climate*, 26(6), 1901–1925. <https://doi.org/10.1175/JCLI-D-11-00416.1>
- 1407 Brierley, C. M., Zhao, A., Harrison, S. P., Braconnot, P., Williams, C. J. R., Thornalley, D. J. R., et al. (2020).  
 1408 Large-scale features and evaluation of the PMIP4-CMIP6 *midHolocene* simulations. *Climate of the Past*,  
 1409 16(5), 1847–1872. <https://doi.org/10.5194/cp-16-1847-2020>
- 1410 Bühler, J. C., Axelsson, J., Lechleitner, F. A., Fohlmeister, J., LeGrande, A. N., Midhun, M., et al. (2022).  
 1411 Investigating stable oxygen and carbon isotopic variability in speleothem records over the last millennium  
 1412 using multiple isotope-enabled climate models. *Climate of the Past*, 18(7), 1625–1654.  
 1413 <https://doi.org/10.5194/cp-18-1625-2022>
- 1414 Burke, K. D., Williams, J. W., Chandler, M. A., Haywood, A. M., Lunt, D. J., & Otto-Bliesner, B. L. (2018).  
 1415 Pliocene and Eocene provide best analogs for near-future climates. *Proceedings of the National Academy of*  
 1416 *Sciences*, 115(52), 13288–13293. <https://doi.org/10.1073/pnas.1809600115>
- 1417 Cao, J., Wang, B., & Ma, L. (2019). Attribution of Global Monsoon Response to the Last Glacial Maximum  
 1418 Forcings. *Journal of Climate*, 32(19), 6589–6605. <https://doi.org/10.1175/JCLI-D-18-0871.1>
- 1419 Cauquoin, A., Werner, M., & Lohmann, G. (2019). Water isotopes – climate relationships for the mid-Holocene and  
 1420 preindustrial period simulated with an isotope-enabled version of MPI-ESM. *Climate of the Past*, 15(6),  
 1421 1913–1937. <https://doi.org/10.5194/cp-15-1913-2019>
- 1422 Chandan, D., & Peltier, W. R. (2020). African Humid Period Precipitation Sustained by Robust Vegetation, Soil,  
 1423 and Lake Feedbacks. *Geophysical Research Letters*, 47(21), e2020GL088728.  
 1424 <https://doi.org/10.1029/2020GL088728>
- 1425 Charney, J., Quirk, W. J., Chow, S., & Kornfield, J. (1977). A comparative study of the effects of albedo change on  
 1426 drought in semi-arid regions. *Journal of the Atmospheric Sciences*, 34(9), 1366–1385.  
 1427 [https://doi.org/10.1175/1520-0469\(1977\)034<1366:ACSOTE>2.0.CO;2](https://doi.org/10.1175/1520-0469(1977)034<1366:ACSOTE>2.0.CO;2)
- 1428 Clark, P. U., Dyke, A. S., Shakun, J. D., Carlson, A. E., Clark, J., Wohlfarth, B., et al. (2009). The Last Glacial  
 1429 Maximum. *Science*, 325(5941), 710–714. <https://doi.org/10.1126/science.1172873>
- 1430 Claussen, M., Kubatzki, C., Brovkin, V., Ganopolski, A., Hoelzmann, P., & Pachur, H.-J. (1999). Simulation of an  
 1431 abrupt change in Saharan vegetation in the Mid-Holocene. *Geophysical Research Letters*, 26(14), 2037–  
 1432 2040. <https://doi.org/10.1029/1999GL900494>
- 1433 CLIMAP, P. (1981). *Seasonal reconstructions of the Earth's surface at the last glacial maximum*. Geological  
 1434 Society of America.
- 1435 Coe, M., & Harrison, S. (2002). The water balance of northern Africa during the mid-Holocene: an evaluation of the  
 1436 6 ka BP PMIP simulations. *Climate Dynamics*, 19(2), 155–166. <https://doi.org/10.1007/s00382-001-0219-3>
- 1437 Cook, K. H. (2008). The mysteries of Sahel droughts. *Nature Geoscience*, 1(10), 647–648.  
 1438 <https://doi.org/10.1038/ngeo320>
- 1439 Corvec, S., & Fletcher, C. G. (2017). Changes to the tropical circulation in the mid-Pliocene and their implications  
 1440 for future climate. *Climate of the Past*, 13(2), 135–147. <https://doi.org/10.5194/cp-13-135-2017>
- 1441 Craig, H., & Gordon, L. I. (1965). Deuterium and oxygen 18 variations in the ocean and the marine atmosphere.
- 1442 Cremaschi, M., & Di Lernia, S. (1999). Holocene Climatic Changes and Cultural Dynamics in the Libyan Sahara.  
 1443 *African Archaeological Review*, 16(4), 211–238. <https://doi.org/10.1023/A:1021609623737>
- 1444 Crook, J., Klein, C., Folwell, S., Taylor, C. M., Parker, D. J., Stratton, R., & Stein, T. (2019). Assessment of the  
 1445 Representation of West African Storm Lifecycles in Convection-Permitting Simulations. *Earth and Space*  
 1446 *Science*, 6(5), 818–835. <https://doi.org/10.1029/2018EA000491>
- 1447 D'Agostino, R., Bader, J., Bordoni, S., Ferreira, D., & Jungclauss, J. (2019). Northern Hemisphere Monsoon  
 1448 Response to Mid-Holocene Orbital Forcing and Greenhouse Gas-Induced Global Warming. *Geophysical*  
 1449 *Research Letters*, 46(3), 1591–1601. <https://doi.org/10.1029/2018GL081589>

- 1450 D'Agostino, R., Brown, J. R., Moise, A., Nguyen, H., Dias, P. L. S., & Jungclaus, J. (2020). Contrasting Southern  
 1451 Hemisphere Monsoon Response: MidHolocene Orbital Forcing versus Future Greenhouse Gas–Induced  
 1452 Global Warming. *Journal of Climate*, *33*(22), 9595–9613. <https://doi.org/10.1175/JCLI-D-19-0672.1>
- 1453 Dallmeyer, A., Claussen, M., Lorenz, S. J., & Shanahan, T. (2020). The end of the African humid period as seen by  
 1454 a transient comprehensive Earth system model simulation of the last 8000&thinsp;years. *Climate of the*  
 1455 *Past*, *16*(1), 117–140. <https://doi.org/10.5194/cp-16-117-2020>
- 1456 Dansgaard, W., Johnsen, S. J., Clausen, H. B., Dahl-Jensen, D., Gundestrup, N. S., Hammer, C. U., et al. (1993).  
 1457 Evidence for general instability of past climate from a 250-kyr ice-core record. *Nature*, *364*(6434), 218–  
 1458 220. <https://doi.org/10.1038/364218a0>
- 1459 deMenocal, P., Ortiz, J., Guilderson, T., Adkins, J., Sarnthein, M., Baker, L., & Yarusinsky, M. (2000). Abrupt  
 1460 onset and termination of the African Humid Period:: rapid climate responses to gradual insolation forcing.  
 1461 *Quaternary Science Reviews*, *19*(1), 347–361. [https://doi.org/10.1016/S0277-3791\(99\)00081-5](https://doi.org/10.1016/S0277-3791(99)00081-5)
- 1462 deMenocal, P. B. (2004). African climate change and faunal evolution during the Pliocene–Pleistocene. *Earth and*  
 1463 *Planetary Science Letters*, *220*(1), 3–24. [https://doi.org/10.1016/S0012-821X\(04\)00003-2](https://doi.org/10.1016/S0012-821X(04)00003-2)
- 1464 Dietrich, S., Werner, M., Spanghel, T., & Lohmann, G. (2013). Influence of orbital forcing and solar activity on  
 1465 water isotopes in precipitation during the mid- and late Holocene. *Climate of the Past*, *9*(1), 13–26.  
 1466 <https://doi.org/10.5194/cp-9-13-2013>
- 1467 Dowsett, H., Robinson, M., Haywood, A. M., Salzmann, U., Hill, D., Sohl, L. E., et al. (2010). The PRISM3D  
 1468 paleoenvironmental reconstruction. *Stratigraphy*.
- 1469 Dowsett, Harry, Dolan, A., Rowley, D., Moucha, R., Forte, A. M., Mitrovica, J. X., et al. (2016). The PRISM4 (mid-  
 1470 Piacenzian) paleoenvironmental reconstruction. *Climate of the Past*, *12*(7), 1519–1538.  
 1471 <https://doi.org/10.5194/cp-12-1519-2016>
- 1472 Dunne, J., Evershed, R. P., Salque, M., Cramp, L., Bruni, S., Ryan, K., et al. (2012). First dairying in green Saharan  
 1473 Africa in the fifth millennium BC. *Nature*, *486*(7403), 390–394. <https://doi.org/10.1038/nature11186>
- 1474 Egerer, S., Claussen, M., & Reick, C. (2018). Rapid increase in simulated North Atlantic dust deposition due to fast  
 1475 change of northwest African landscape during the Holocene. *Climate of the Past*, *14*(7), 1051–1066.  
 1476 <https://doi.org/10.5194/cp-14-1051-2018>
- 1477 Erfanian, A., Wang, G., Yu, M., & Anyah, R. (2016). Multimodel ensemble simulations of present and future  
 1478 climates over West Africa: Impacts of vegetation dynamics. *Journal of Advances in Modeling Earth*  
 1479 *Systems*, *8*(3), 1411–1431. <https://doi.org/10.1002/2016MS000660>
- 1480 Etheridge, D. M., Steele, L. P., Langenfelds, R. L., Francey, R. J., Barnola, J.-M., & Morgan, V. I. (1996). Natural  
 1481 and anthropogenic changes in atmospheric CO<sub>2</sub> over the last 1000 years from air in Antarctic ice and firn.  
 1482 *Journal of Geophysical Research: Atmospheres*, *101*(D2), 4115–4128. <https://doi.org/10.1029/95JD03410>
- 1483 Etheridge, D. M., Steele, L. P., Francey, R. J., & Langenfelds, R. L. (1998). Atmospheric methane between 1000  
 1484 A.D. and present: Evidence of anthropogenic emissions and climatic variability. *Journal of Geophysical*  
 1485 *Research: Atmospheres*, *103*(D13), 15979–15993. <https://doi.org/10.1029/98JD00923>
- 1486 Evan, A. T., Flamant, C., Fiedler, S., & Doherty, O. (2014). An analysis of aeolian dust in climate models.  
 1487 *Geophysical Research Letters*, *41*(16), 5996–6001. <https://doi.org/10.1002/2014GL060545>
- 1488 Eyring, V., Bony, S., Meehl, G. A., Senior, C. A., Stevens, B., Stouffer, R. J., & Taylor, K. E. (2016). Overview of  
 1489 the Coupled Model Intercomparison Project Phase 6 (CMIP6) experimental design and organization.  
 1490 *Geoscientific Model Development*, *9*(5), 1937–1958. <https://doi.org/10.5194/gmd-9-1937-2016>
- 1491 Friedrich, T., Timmermann, A., Tigchelaar, M., Elison Timm, O., & Ganopolski, A. (2016). Nonlinear climate  
 1492 sensitivity and its implications for future greenhouse warming. *Science Advances*, *2*(11), e1501923.  
 1493 <https://doi.org/10.1126/sciadv.1501923>
- 1494 Gabriel, B. (1987). Palaeoecological evidence from neolithic fireplaces in the Sahara. *African Archaeological*  
 1495 *Review*, *5*(1), 93–103. <https://doi.org/10.1007/BF01117085>
- 1496 Gaetani, M., Messori, G., Zhang, Q., Flamant, C., & Pausata, F. S. R. (2017). Understanding the Mechanisms  
 1497 behind the Northward Extension of the West African Monsoon during the Mid-Holocene. *Journal of*  
 1498 *Climate*, *30*(19), 7621–7642. <https://doi.org/10.1175/JCLI-D-16-0299.1>

- 1499 Gao, X., Xu, Y., Zhao, Z., Pal, J. S., & Giorgi, F. (2006). On the role of resolution and topography in the simulation  
1500 of East Asia precipitation. *Theoretical and Applied Climatology*, 86(1), 173–185.  
1501 <https://doi.org/10.1007/s00704-005-0214-4>
- 1502 Gill, A. E. (1980). Some simple solutions for heat-induced tropical circulation. *Quarterly Journal of the Royal*  
1503 *Meteorological Society*, 106(449), 447–462. <https://doi.org/10.1002/qj.49710644905>
- 1504 Grist, J. P. (2002). Easterly Waves over Africa. Part I: The Seasonal Cycle and Contrasts between Wet and Dry  
1505 Years. *Monthly Weather Review*, 130(2), 197–211. [https://doi.org/10.1175/1520-  
1506 0493\(2002\)130<0197:EWOAPI>2.0.CO;2](https://doi.org/10.1175/1520-0493(2002)130<0197:EWOAPI>2.0.CO;2)
- 1507 Hagemann, S. (2002). Validierung des Niederschlags in globalen Klimamodellen. 5. *Workshop Zur Hydrologischen*  
1508 *Modellierung: Möglichkeiten Und Grenzen Für Den Einsatz Hydrologischer Modelle in Politik, Wirtschaft*  
1509 *Und Klimafolgenforschung*, 115-127 (2002).
- 1510 Hagemann, S., Arpe, K., & Roeckner, E. (2006). Evaluation of the Hydrological Cycle in the ECHAM5 Model.  
1511 *Journal of Climate*, 19(16), 3810–3827. <https://doi.org/10.1175/JCLI3831.1>
- 1512 Harris, I., Jones, P. d., Osborn, T. j., & Lister, D. h. (2014). Updated high-resolution grids of monthly climatic  
1513 observations – the CRU TS3.10 Dataset. *International Journal of Climatology*, 34(3), 623–642.  
1514 <https://doi.org/10.1002/joc.3711>
- 1515 Harris, Ian, Osborn, T. J., Jones, P., & Lister, D. (2020). Version 4 of the CRU TS monthly high-resolution gridded  
1516 multivariate climate dataset. *Scientific Data*, 7(1), 109. <https://doi.org/10.1038/s41597-020-0453-3>
- 1517 Harrison, S. P., Yu, G., Takahara, H., & Prentice, I. C. (2001). Diversity of temperate plants in east Asia. *Nature*,  
1518 413(6852), 129–130. <https://doi.org/10.1038/35093166>
- 1519 Harrison, S. P., Bartlein, P. J., Brewer, S., Prentice, I. C., Boyd, M., Hessler, I., et al. (2014). Climate model  
1520 benchmarking with glacial and mid-Holocene climates. *Climate Dynamics*, 43(3), 671–688.  
1521 <https://doi.org/10.1007/s00382-013-1922-6>
- 1522 Harrison, S. P., Bartlein, P. J., Izumi, K., Li, G., Annan, J., Hargreaves, J., et al. (2015). Evaluation of CMIP5  
1523 palaeo-simulations to improve climate projections. *Nature Climate Change*, 5(8), 735–743.  
1524 <https://doi.org/10.1038/nclimate2649>
- 1525 Haywood, A. M., Dowsett, H. J., Otto-Bliesner, B., Chandler, M. A., Dolan, A. M., Hill, D. J., et al. (2010).  
1526 Pliocene Model Intercomparison Project (PlioMIP): experimental design and boundary conditions  
1527 (Experiment 1). *Geoscientific Model Development*, 3(1), 227–242. <https://doi.org/10.5194/gmd-3-227-2010>
- 1528 Haywood, A. M., Hill, D. J., Dolan, A. M., Otto-Bliesner, B. L., Bragg, F., Chan, W.-L., et al. (2013). Large-scale  
1529 features of Pliocene climate: results from the Pliocene Model Intercomparison Project. *Climate of the Past*,  
1530 9(1), 191–209. <https://doi.org/10.5194/cp-9-191-2013>
- 1531 Haywood, Alan M., Dowsett, H. J., Dolan, A. M., Rowley, D., Abe-Ouchi, A., Otto-Bliesner, B., et al. (2016). The  
1532 Pliocene Model Intercomparison Project (PlioMIP) Phase 2: scientific objectives and experimental design.  
1533 *Climate of the Past*, 12(3), 663–675. <https://doi.org/10.5194/cp-12-663-2016>
- 1534 Haywood, Alan M., Tindall, J. C., Dowsett, H. J., Dolan, A. M., Foley, K. M., Hunter, S. J., et al. (2020). The  
1535 Pliocene Model Intercomparison Project Phase 2: large-scale climate features and climate sensitivity.  
1536 *Climate of the Past*, 16(6), 2095–2123. <https://doi.org/10.5194/cp-16-2095-2020>
- 1537 Hersbach, H., Bell, B., Berrisford, P., Hirahara, S., Horányi, A., Muñoz-Sabater, J., et al. (2020). The ERA5 global  
1538 reanalysis. *Quarterly Journal of the Royal Meteorological Society*, 146(730), 1999–2049.  
1539 <https://doi.org/10.1002/qj.3803>
- 1540 Hoelzmann, P., Jolly, D., Harrison, S. P., Laarif, F., Bonnefille, R., & Pachur, H.-J. (1998). Mid-Holocene land-  
1541 surface conditions in northern Africa and the Arabian Peninsula: A data set for the analysis of  
1542 biogeophysical feedbacks in the climate system. *Global Biogeochemical Cycles*, 12(1), 35–51.  
1543 <https://doi.org/10.1029/97GB02733>
- 1544 Hoelzmann, Philipp, Keding, B., Berke, H., Kröpelin, S., & Kruse, H.-J. (2001). Environmental change and  
1545 archaeology: lake evolution and human occupation in the Eastern Sahara during the Holocene.  
1546 *Palaeogeography, Palaeoclimatology, Palaeoecology*, 169(3), 193–217. [https://doi.org/10.1016/S0031-  
1547 0182\(01\)00211-5](https://doi.org/10.1016/S0031-0182(01)00211-5)

- 1548 Holmes, J. A. (2008). How the Sahara Became Dry. *Science*, 320(5877), 752–753.  
1549 <https://doi.org/10.1126/science.1158105>
- 1550 Hopcroft, P. O., & Valdes, P. J. (2019). On the Role of Dust-Climate Feedbacks During the Mid-Holocene.  
1551 *Geophysical Research Letters*, 46(3), 1612–1621. <https://doi.org/10.1029/2018GL080483>
- 1552 Janicot, S., Caniaux, G., Chauvin, F., de Coëtlogon, G., Fontaine, B., Hall, N., et al. (2011). Intraseasonal variability  
1553 of the West African monsoon. *Atmospheric Science Letters*, 12(1), 58–66. <https://doi.org/10.1002/asl.280>
- 1554 Jenkins, G. S., Gaye, A. T., & Sylla, B. (2005). Late 20th century attribution of drying trends in the Sahel from the  
1555 Regional Climate Model (RegCM3). *Geophysical Research Letters*, 32(22).  
1556 <https://doi.org/10.1029/2005GL024225>
- 1557 Jiang, D., Wang, H., Ding, Z., Lang, X., & Drange, H. (2005). Modeling the middle Pliocene climate with a global  
1558 atmospheric general circulation model. *Journal of Geophysical Research: Atmospheres*, 110(D14).  
1559 <https://doi.org/10.1029/2004JD005639>
- 1560 Jiang, D., Tian, Z., Lang, X., Kageyama, M., & Ramstein, G. (2015). The concept of global monsoon applied to the  
1561 last glacial maximum: A multi-model analysis. *Quaternary Science Reviews*, 126, 126–139.  
1562 <https://doi.org/10.1016/j.quascirev.2015.08.033>
- 1563 Jolly, D., Prentice, I. C., Bonnefille, R., Ballouche, A., Bengo, M., Brenac, P., et al. (1998). Biome reconstruction  
1564 from pollen and plant macrofossil data for Africa and the Arabian peninsula at 0 and 6000 years. *Journal of*  
1565 *Biogeography*, 25(6), 1007–1027. <https://doi.org/10.1046/j.1365-2699.1998.00238.x>
- 1566 Joussaume, S., Taylor, K. E., Braconnot, P., Mitchell, J. F. B., Kutzbach, J. E., Harrison, S. P., et al. (1999).  
1567 Monsoon changes for 6000 years ago: Results of 18 simulations from the Paleoclimate Modeling  
1568 Intercomparison Project (PMIP). *Geophysical Research Letters*, 26(7), 859–862.  
1569 <https://doi.org/10.1029/1999GL900126>
- 1570 Jungandreas, L., Hohenegger, C., & Claussen, M. (2021). Influence of the representation of convection on the mid-  
1571 Holocene West African Monsoon. *Climate of the Past*, 17(4), 1665–1684. <https://doi.org/10.5194/cp-17-1665-2021>
- 1573 Kageyama, M., Braconnot, P., Bopp, L., Caubel, A., Foujols, M.-A., Guilyardi, E., et al. (2013). Mid-Holocene and  
1574 Last Glacial Maximum climate simulations with the IPSL model—part I: comparing IPSL\_CM5A to  
1575 IPSL\_CM4. *Climate Dynamics*, 40(9), 2447–2468. <https://doi.org/10.1007/s00382-012-1488-8>
- 1576 Kageyama, M., Braconnot, P., Harrison, S. P., Haywood, A. M., Jungclaus, J. H., Otto-Bliesner, B. L., et al. (2018).  
1577 The PMIP4 contribution to CMIP6 – Part 1: Overview and over-arching analysis plan. *Geoscientific Model*  
1578 *Development*, 11(3), 1033–1057. <https://doi.org/10.5194/gmd-11-1033-2018>
- 1579 Kageyama, M., Harrison, S. P., Kapsch, M.-L., Lofverstrom, M., Lora, J. M., Mikolajewicz, U., et al. (2021). The  
1580 PMIP4 Last Glacial Maximum experiments: preliminary results and comparison with the PMIP3  
1581 simulations. *Climate of the Past*, 17(3), 1065–1089. <https://doi.org/10.5194/cp-17-1065-2021>
- 1582 Kim, S.-J., Crowley, T. J., Erickson, D. J., Govindasamy, B., Duffy, P. B., & Lee, B. Y. (2008). High-resolution  
1583 climate simulation of the last glacial maximum. *Climate Dynamics*, 31(1), 1–16.  
1584 <https://doi.org/10.1007/s00382-007-0332-z>
- 1585 Klein, C., Bliefernicht, J., Heinzler, D., Gessner, U., Klein, I., & Kunstmann, H. (2017). Feedback of observed  
1586 interannual vegetation change: a regional climate model analysis for the West African monsoon. *Climate*  
1587 *Dynamics*, 48(9), 2837–2858. <https://doi.org/10.1007/s00382-016-3237-x>
- 1588 Kohfeld, K. E., & Harrison, S. P. (2000). How well can we simulate past climates? Evaluating the models using  
1589 global palaeoenvironmental datasets. *Quaternary Science Reviews*, 19(1), 321–346.  
1590 [https://doi.org/10.1016/S0277-3791\(99\)00068-2](https://doi.org/10.1016/S0277-3791(99)00068-2)
- 1591 Kok, J. F. (2010). An improved parameterization of wind-blown sand flux on Mars that includes the effect of  
1592 hysteresis. *Geophysical Research Letters*, 37(12). <https://doi.org/10.1029/2010GL043646>
- 1593 Kolstad, E. W., & Screen, J. A. (2019). Nonstationary Relationship Between Autumn Arctic Sea Ice and the Winter  
1594 North Atlantic Oscillation. *Geophysical Research Letters*, 46(13), 7583–7591.  
1595 <https://doi.org/10.1029/2019GL083059>

- 1596 Kröpelin, S., Verschuren, D., Lézine, A.-M., Eggermont, H., Cocquyt, C., Francus, P., et al. (2008). Climate-Driven  
 1597 Ecosystem Succession in the Sahara: The Past 6000 Years. *Science*, *320*(5877), 765–768.  
 1598 <https://doi.org/10.1126/science.1154913>
- 1599 Kuechler, R. R., Dupont, L. M., & Schefuß, E. (2018). Hybrid insolation forcing of Pliocene monsoon dynamics in  
 1600 West Africa. *Climate of the Past*, *14*(1), 73–84. <https://doi.org/10.5194/cp-14-73-2018>
- 1601 Kutzbach, J. E., & Liu, Z. (1997). Response of the African Monsoon to Orbital Forcing and Ocean Feedbacks in the  
 1602 Middle Holocene. *Science*, *278*(5337), 440–443. <https://doi.org/10.1126/science.278.5337.440>
- 1603 Lambeck, K., Rouby, H., Purcell, A., Sun, Y., & Sambridge, M. (2014). Sea level and global ice volumes from the  
 1604 Last Glacial Maximum to the Holocene. *Proceedings of the National Academy of Sciences*, *111*(43),  
 1605 15296–15303. <https://doi.org/10.1073/pnas.1411762111>
- 1606 Lavaysse, C., Flamant, C., Janicot, S., Parker, D. J., Lafore, J.-P., Sultan, B., & Pelon, J. (2009). Seasonal evolution  
 1607 of the West African heat low: a climatological perspective. *Climate Dynamics*, *33*(2), 313–330.  
 1608 <https://doi.org/10.1007/s00382-009-0553-4>
- 1609 Lawrence, J. R., Gedzelman, S. D., Dexheimer, D., Cho, H.-K., Carrie, G. D., Gasparini, R., et al. (2004). Stable  
 1610 isotopic composition of water vapor in the tropics. *Journal of Geophysical Research: Atmospheres*,  
 1611 *109*(D6). <https://doi.org/10.1029/2003JD004046>
- 1612 LeGrande, A. N., & Schmidt, G. A. (2006). Global gridded data set of the oxygen isotopic composition in seawater.  
 1613 *Geophysical Research Letters*, *33*(12). <https://doi.org/10.1029/2006GL026011>
- 1614 Lemburg, A., Bader, J., & Claussen, M. (2019). Sahel Rainfall–Tropical Easterly Jet Relationship on Synoptic to  
 1615 Intraseasonal Time Scales. *Monthly Weather Review*, *147*(5), 1733–1752. [https://doi.org/10.1175/MWR-D-](https://doi.org/10.1175/MWR-D-18-0254.1)  
 1616 [18-0254.1](https://doi.org/10.1175/MWR-D-18-0254.1)
- 1617 Leung, D. M., Kok, J. F., Li, L., Okin, G. S., Prigent, C., Klose, M., et al. (2023). A new process-based and scale-  
 1618 aware desert dust emission scheme for global climate models – Part I: Description and evaluation against  
 1619 inverse modeling emissions. *Atmospheric Chemistry and Physics*, *23*(11), 6487–6523.  
 1620 <https://doi.org/10.5194/acp-23-6487-2023>
- 1621 Levis, S., Bonan, G. B., & Bonfils, C. (2004). Soil feedback drives the mid-Holocene North African monsoon  
 1622 northward in fully coupled CCSM2 simulations with a dynamic vegetation model. *Climate Dynamics*,  
 1623 *23*(7), 791–802. <https://doi.org/10.1007/s00382-004-0477-y>
- 1624 Li, X., Jiang, D., Zhang, Z., Zhang, R., Tian, Z., & Yan, Q. (2015). Mid-Pliocene westerlies from PlioMIP  
 1625 simulations. *Advances in Atmospheric Sciences*, *32*(7), 909–923. [https://doi.org/10.1007/s00376-014-4171-](https://doi.org/10.1007/s00376-014-4171-7)  
 1626 [7](https://doi.org/10.1007/s00376-014-4171-7)
- 1627 Li, X., Jiang, D., Tian, Z., & Yang, Y. (2018). Mid-Pliocene global land monsoon from PlioMIP1 simulations.  
 1628 *Palaeogeography, Palaeoclimatology, Palaeoecology*, *512*, 56–70.  
 1629 <https://doi.org/10.1016/j.palaeo.2018.06.027>
- 1630 Liakka, J., & Lofverstrom, M. (2018). Arctic warming induced by the Laurentide Ice Sheet topography. *Climate of*  
 1631 *the Past*, *14*(6), 887–900. <https://doi.org/10.5194/cp-14-887-2018>
- 1632 Liakka, J., Löfverström, M., & Colleoni, F. (2016). The impact of the North American glacial topography on the  
 1633 evolution of the Eurasian ice sheet over the last glacial cycle. *Climate of the Past*, *12*(5), 1225–1241.  
 1634 <https://doi.org/10.5194/cp-12-1225-2016>
- 1635 Lohmann, G., Pfeiffer, M., Laepple, T., Leduc, G., & Kim, J.-H. (2013). A model–data comparison of the  
 1636 Holocene global sea surface temperature evolution. *Climate of the Past*, *9*(4), 1807–1839.  
 1637 <https://doi.org/10.5194/cp-9-1807-2013>
- 1638 Lohmann, U., & Roeckner, E. (1996). Design and performance of a new cloud microphysics scheme developed for  
 1639 the ECHAM general circulation model. *Climate Dynamics*, *12*(8), 557–572.  
 1640 <https://doi.org/10.1007/BF00207939>
- 1641 Lora, J. M. (2018). Components and Mechanisms of Hydrologic Cycle Changes over North America at the Last  
 1642 Glacial Maximum. *Journal of Climate*, *31*(17), 7035–7051. <https://doi.org/10.1175/JCLI-D-17-0544.1>

- 1643 Lorenz, S. J., & Lohmann, G. (2004). Acceleration technique for Milankovitch type forcing in a coupled  
 1644 atmosphere-ocean circulation model: method and application for the Holocene. *Climate Dynamics*, 23(7–  
 1645 8), 727–743. <https://doi.org/10.1007/s00382-004-0469-y>
- 1646 Manning, K., & Timpson, A. (2014). The demographic response to Holocene climate change in the Sahara.  
 1647 *Quaternary Science Reviews*, 101, 28–35. <https://doi.org/10.1016/j.quascirev.2014.07.003>
- 1648 Marsham, J. H., Dixon, N. S., Garcia-Carreras, L., Lister, G. M. S., Parker, D. J., Knippertz, P., & Birch, C. E.  
 1649 (2013). The role of moist convection in the West African monsoon system: Insights from continental-scale  
 1650 convection-permitting simulations. *Geophysical Research Letters*, 40(9), 1843–1849.  
 1651 <https://doi.org/10.1002/grl.50347>
- 1652 Marzin, C., & Braconnot, P. (2009). Variations of Indian and African monsoons induced by insolation changes at 6  
 1653 and 9.5 kyr BP. *Climate Dynamics*, 33(2), 215–231. <https://doi.org/10.1007/s00382-009-0538-3>
- 1654 McManus, J. F., Francois, R., Gherardi, J.-M., Keigwin, L. D., & Brown-Leger, S. (2004). Collapse and rapid  
 1655 resumption of Atlantic meridional circulation linked to deglacial climate changes. *Nature*, 428(6985), 834–  
 1656 837. <https://doi.org/10.1038/nature02494>
- 1657 Messori, G., Gaetani, M., Zhang, Q., Zhang, Q., & Pausata, F. S. R. (2019). The water cycle of the mid-Holocene  
 1658 West African monsoon: The role of vegetation and dust emission changes. *International Journal of*  
 1659 *Climatology*, 39(4), 1927–1939. <https://doi.org/10.1002/joc.5924>
- 1660 Mulitza, S., Prange, M., Stuut, J.-B., Zabel, M., von Dobeneck, T., Itambi, A. C., et al. (2008). Sahel megadroughts  
 1661 triggered by glacial slowdowns of Atlantic meridional overturning. *Paleoceanography*, 23(4).  
 1662 <https://doi.org/10.1029/2008PA001637>
- 1663 Mutz, S. G., Ehlers, T. A., Werner, M., Lohmann, G., Stepanek, C., & Li, J. (2018). Estimates of late Cenozoic  
 1664 climate change relevant to Earth surface processes in tectonically active orogens. *Earth Surface Dynamics*,  
 1665 6(2), 271–301. <https://doi.org/10.5194/esurf-6-271-2018>
- 1666 Newell, R. E., & Kidson, J. W. (1984). African mean wind changes between sahelian wet and dry periods. *Journal*  
 1667 *of Climatology*, 4(1), 27–33. <https://doi.org/10.1002/joc.3370040103>
- 1668 Nicholson, S. E. (2008). The intensity, location and structure of the tropical rainbelt over west Africa as factors in  
 1669 interannual variability. *International Journal of Climatology*, 28(13), 1775–1785.  
 1670 <https://doi.org/10.1002/joc.1507>
- 1671 Nicholson, S. e., & Grist, J. p. (2001). A conceptual model for understanding rainfall variability in the West African  
 1672 Sahel on interannual and interdecadal timescales. *International Journal of Climatology*, 21(14), 1733–  
 1673 1757. <https://doi.org/10.1002/joc.648>
- 1674 Nicholson, S. E., & Grist, J. P. (2003). The Seasonal Evolution of the Atmospheric Circulation over West Africa and  
 1675 Equatorial Africa. *Journal of Climate*, 16(7), 1013–1030. [https://doi.org/10.1175/1520-0442\(2003\)016<1013:TSEOTA>2.0.CO;2](https://doi.org/10.1175/1520-0442(2003)016<1013:TSEOTA>2.0.CO;2)
- 1676 Nicholson, S. E., & Palao, I. M. (1993). A re-evaluation of rainfall variability in the sahel. Part I. Characteristics of  
 1677 rainfall fluctuations. *International Journal of Climatology*, 13(4), 371–389.  
 1678 <https://doi.org/10.1002/joc.3370130403>
- 1679 Nicholson, S. E., & Webster, P. J. (2007). A physical basis for the interannual variability of rainfall in the Sahel.  
 1680 *Quarterly Journal of the Royal Meteorological Society*, 133(629), 2065–2084.  
 1681 <https://doi.org/10.1002/qj.104>
- 1682 de Nooijer, W., Zhang, Q., Li, Q., Zhang, Q., Li, X., Zhang, Z., et al. (2020). Evaluation of Arctic warming in mid-  
 1683 Pliocene climate simulations. *Climate of the Past*, 16(6), 2325–2341. <https://doi.org/10.5194/cp-16-2325-2020>
- 1684 Notaro, M., Wang, Y., Liu, Z., Gallimore, R., & Levis, S. (2008). Combined statistical and dynamical assessment of  
 1685 simulated vegetation–rainfall interactions in North Africa during the mid-Holocene1. *Global Change*  
 1686 *Biology*, 14(2), 347–368. <https://doi.org/10.1111/j.1365-2486.2007.01495.x>
- 1687 Otto-Bliesner, B. L., Brady, E. C., Clauzet, G., Tomas, R., Levis, S., & Kothavala, Z. (2006). Last Glacial  
 1688 Maximum and Holocene Climate in CCSM3. *Journal of Climate*, 19(11), 2526–2544.  
 1689 <https://doi.org/10.1175/JCLI3748.1>

- 1692 Otto-Bliesner, B. L., Braconnot, P., Harrison, S. P., Lunt, D. J., Abe-Ouchi, A., Albani, S., et al. (2017). The PMIP4  
 1693 contribution to CMIP6 – Part 2: Two interglacials, scientific objective and experimental design for  
 1694 Holocene and Last Interglacial simulations. *Geoscientific Model Development*, *10*(11), 3979–4003.  
 1695 <https://doi.org/10.5194/gmd-10-3979-2017>
- 1696 Patricola, C. M., & Cook, K. H. (2007). Dynamics of the West African Monsoon under Mid-Holocene Precessional  
 1697 Forcing: Regional Climate Model Simulations. *Journal of Climate*, *20*(4), 694–716.  
 1698 <https://doi.org/10.1175/JCLI4013.1>
- 1699 Pausata, F. S. R., Messori, G., & Zhang, Q. (2016). Impacts of dust reduction on the northward expansion of the  
 1700 African monsoon during the Green Sahara period. *Earth and Planetary Science Letters*, *434*, 298–307.  
 1701 <https://doi.org/10.1016/j.epsl.2015.11.049>
- 1702 Pausata, F. S. R., Gaetani, M., Messori, G., Berg, A., Maia de Souza, D., Sage, R. F., & deMenocal, P. B. (2020).  
 1703 The Greening of the Sahara: Past Changes and Future Implications. *One Earth*, *2*(3), 235–250.  
 1704 <https://doi.org/10.1016/j.oneear.2020.03.002>
- 1705 Peltier, W. R., & Fairbanks, R. G. (2006). Global glacial ice volume and Last Glacial Maximum duration from an  
 1706 extended Barbados sea level record. *Quaternary Science Reviews*, *25*(23), 3322–3337.  
 1707 <https://doi.org/10.1016/j.quascirev.2006.04.010>
- 1708 Perez-Sanz, A., Li, G., González-Sampériz, P., & Harrison, S. P. (2014). Evaluation of modern and mid-Holocene  
 1709 seasonal precipitation of the Mediterranean and northern Africa in the CMIP5 simulations. *Climate of the  
 1710 Past*, *10*(2), 551–568. <https://doi.org/10.5194/cp-10-551-2014>
- 1711 Peyron, O., Jolly, D., Braconnot, P., Bonnefille, R., Guiot, J., Wirmann, D., & Chalié, F. (2006). Quantitative  
 1712 reconstructions of annual rainfall in Africa 6000 years ago: Model-data comparison. *Journal of  
 1713 Geophysical Research: Atmospheres*, *111*(D24). <https://doi.org/10.1029/2006JD007396>
- 1714 Phipps, S. J., McGregor, H. V., Gergis, J., Gallant, A. J. E., Neukom, R., Stevenson, S., et al. (2013). Paleoclimate  
 1715 Data–Model Comparison and the Role of Climate Forcings over the Past 1500 Years. *Journal of Climate*,  
 1716 *26*(18), 6915–6936. <https://doi.org/10.1175/JCLI-D-12-00108.1>
- 1717 Pickett, E. J., Harrison, S. P., Hope, G., Harle, K., Dodson, J. R., Peter Kershaw, A., et al. (2004). Pollen-based  
 1718 reconstructions of biome distributions for Australia, Southeast Asia and the Pacific (SEAPAC region) at 0,  
 1719 6000 and 18,000 14C yr BP. *Journal of Biogeography*, *31*(9), 1381–1444. <https://doi.org/10.1111/j.1365-2699.2004.01001.x>
- 1720
- 1721 Prentice, I. C., Jolly, D., & Participants, B. 6000. (2000). Mid-Holocene and glacial-maximum vegetation geography  
 1722 of the northern continents and Africa. *Journal of Biogeography*, *27*(3), 507–519.  
 1723 <https://doi.org/10.1046/j.1365-2699.2000.00425.x>
- 1724 Quagraine, K. A., Nkrumah, F., Klein, C., Klutse, N. A. B., & Quagraine, K. T. (2020). West African Summer  
 1725 Monsoon Precipitation Variability as Represented by Reanalysis Datasets. *Climate*, *8*(10), 111.  
 1726 <https://doi.org/10.3390/cli8100111>
- 1727 Rachmayani, R., Prange, M., & Schulz, M. (2015). North African vegetation–precipitation feedback in early and  
 1728 mid-Holocene climate simulations with CCSM3-DGVM. *Climate of the Past*, *11*(2), 175–185.  
 1729 <https://doi.org/10.5194/cp-11-175-2015>
- 1730 Raible, C. C., Lehner, F., González-Rouco, J. F., & Fernández-Donado, L. (2014). Changing correlation structures  
 1731 of the Northern Hemisphere atmospheric circulation from 1000 to 2100 AD. *Climate of the Past*, *10*(2),  
 1732 537–550. <https://doi.org/10.5194/cp-10-537-2014>
- 1733 Redelsperger, J.-L., Parsons, D. B., & Guichard, F. (2002). Recovery Processes and Factors Limiting Cloud-Top  
 1734 Height following the Arrival of a Dry Intrusion Observed during TOGA COARE. *Journal of the  
 1735 Atmospheric Sciences*, *59*(16), 2438–2457. [https://doi.org/10.1175/1520-0469\(2002\)059<2438:RPAFLC>2.0.CO;2](https://doi.org/10.1175/1520-0469(2002)059<2438:RPAFLC>2.0.CO;2)
- 1736
- 1737 Risi, C., Bony, S., Vimeux, F., Descroix, L., Ibrahim, B., Lebreton, E., et al. (2008). What controls the isotopic  
 1738 composition of the African monsoon precipitation? Insights from event-based precipitation collected during  
 1739 the 2006 AMMA field campaign. *Geophysical Research Letters*, *35*(24).  
 1740 <https://doi.org/10.1029/2008GL035920>

- 1741 Risi, C., Bony, S., Vimeux, F., Frankenberg, C., Noone, D., & Worden, J. (2010). Understanding the Sahelian water  
 1742 budget through the isotopic composition of water vapor and precipitation. *Journal of Geophysical*  
 1743 *Research: Atmospheres*, *115*(D24). <https://doi.org/10.1029/2010JD014690>
- 1744 Risi, C., Noone, D., Worden, J., Frankenberg, C., Stiller, G., Kiefer, M., et al. (2012). Process-evaluation of  
 1745 tropospheric humidity simulated by general circulation models using water vapor isotopologues: 1.  
 1746 Comparison between models and observations. *Journal of Geophysical Research: Atmospheres*, *117*(D5).  
 1747 <https://doi.org/10.1029/2011JD016621>
- 1748 Risi, C., Noone, D., Frankenberg, C., & Worden, J. (2013). Role of continental recycling in intraseasonal variations  
 1749 of continental moisture as deduced from model simulations and water vapor isotopic measurements:  
 1750 Continental Recycling and Water Isotopes. *Water Resources Research*, *49*(7), 4136–4156.  
 1751 <https://doi.org/10.1002/wrcr.20312>
- 1752 Roeckner, E., Bäuml, G., Bonaventura, L., Brokopf, R., Esch, M., Giorgetta, M., et al. (2003). The atmospheric  
 1753 general circulation model ECHAM 5. PART I: Model description. <https://doi.org/10.17617/2.995269>
- 1754 Roehrig, R., Bouniol, D., Guichard, F., Hourdin, F., & Redelsperger, J.-L. (2013). The Present and Future of the  
 1755 West African Monsoon: A Process-Oriented Assessment of CMIP5 Simulations along the AMMA  
 1756 Transect. *Journal of Climate*, *26*(17), 6471–6505. <https://doi.org/10.1175/JCLI-D-12-00505.1>
- 1757 Rozanski, K., Araguás-Araguás, L., & Gonfiantini, R. (1993). Climate change in continental isotopic records.  
 1758 Retrieved from [https://scholar.google.com/scholar\\_lookup?hl=en&publication\\_year=1993&pages=1-](https://scholar.google.com/scholar_lookup?hl=en&publication_year=1993&pages=1-36&author=K.+Rozanski&author=L.+Aragu%C3%A1s&author=R.+Gonfiantini&title=Climate+Change+in+Continental+Isotopic+Records)  
 1759 [36&author=K.+Rozanski&author=L.+Aragu%C3%A1s&author=R.+Gonfiantini&title=Climate+Change+in+Continental+Isotopic+Records](https://scholar.google.com/scholar_lookup?hl=en&publication_year=1993&pages=1-36&author=K.+Rozanski&author=L.+Aragu%C3%A1s&author=R.+Gonfiantini&title=Climate+Change+in+Continental+Isotopic+Records)
- 1760 Salzmann, U., Haywood, A. M., Lunt, D. J., Valdes, P. J., & Hill, D. J. (2008). A new global biome reconstruction  
 1761 and data-model comparison for the Middle Pliocene. *Global Ecology and Biogeography*, *17*(3), 432–447.  
 1762 <https://doi.org/10.1111/j.1466-8238.2008.00381.x>
- 1763 Salzmann, Ulrich, Dolan, A. M., Haywood, A. M., Chan, W.-L., Voss, J., Hill, D. J., et al. (2013). Challenges in  
 1764 quantifying Pliocene terrestrial warming revealed by data–model discord. *Nature Climate Change*, *3*(11),  
 1765 969–974. <https://doi.org/10.1038/nclimate2008>
- 1766 Samakinwa, E., Stepanek, C., & Lohmann, G. (2020). Sensitivity of mid-Pliocene climate to changes in orbital  
 1767 forcing and PlioMIP’s boundary conditions. *Climate of the Past*, *16*(4), 1643–1665.  
 1768 <https://doi.org/10.5194/cp-16-1643-2020>
- 1769 Sarnthein, M., Gersonde, R., Niebler, S., Pflaumann, U., Spielhagen, R., Thiede, J., et al. (2003). Overview of  
 1770 Glacial Atlantic Ocean Mapping (GLAMAP 2000). *Paleoceanography*, *18*(2).  
 1771 <https://doi.org/10.1029/2002PA000769>
- 1772 Scheff, J., & Frierson, D. M. W. (2012). Robust future precipitation declines in CMIP5 largely reflect the poleward  
 1773 expansion of model subtropical dry zones. *Geophysical Research Letters*, *39*(18).  
 1774 <https://doi.org/10.1029/2012GL052910>
- 1775 Sereno, P. C., Garcea, E. A. A., Jousse, H., Stojanowski, C. M., Saliège, J.-F., Maga, A., et al. (2008). Lakeside  
 1776 Cemeteries in the Sahara: 5000 Years of Holocene Population and Environmental Change. *PLOS ONE*,  
 1777 *3*(8), e2995. <https://doi.org/10.1371/journal.pone.0002995>
- 1778 Seth, A., Giannini, A., Rojas, M., Rauscher, S. A., Bordoni, S., Singh, D., & Camargo, S. J. (2019). Monsoon  
 1779 Responses to Climate Changes—Connecting Past, Present and Future. *Current Climate Change Reports*,  
 1780 *5*(2), 63–79. <https://doi.org/10.1007/s40641-019-00125-y>
- 1781 Sha, L., Ait Brahim, Y., Wassenburg, J. A., Yin, J., Peros, M., Cruz, F. W., et al. (2019). How Far North Did the  
 1782 African Monsoon Fringe Expand During the African Humid Period? Insights From Southwest Moroccan  
 1783 Speleothems. *Geophysical Research Letters*, *46*(23), 14093–14102. <https://doi.org/10.1029/2019GL084879>
- 1784 Shi, X., Lohmann, G., Sidorenko, D., & Yang, H. (2020). Early-Holocene simulations using different forcings and  
 1785 resolutions in AWI-ESM. *The Holocene*, *30*(7), 996–1015. <https://doi.org/10.1177/0959683620908634>
- 1786 Shi, X., Cauquoin, A., Lohmann, G., Jonkers, L., Wang, Q., Yang, H., et al. (2023). Simulated stable water isotopes  
 1787 during the mid-Holocene and pre-industrial using AWI-ESM-2.1-wiso. *Geoscientific Model Development*  
 1788 *Discussions*, 1–39. <https://doi.org/10.5194/gmd-2023-68>
- 1789

- 1790 Simmons, A. J., Burridge, D. M., Jarraud, M., Girard, C., & Wergen, W. (1989). The ECMWF medium-range  
 1791 prediction models development of the numerical formulations and the impact of increased resolution.  
 1792 *Meteorology and Atmospheric Physics*, 40(1), 28–60. <https://doi.org/10.1007/BF01027467>
- 1793 Sohl, L. E., Chandler, M. A., Schmunk, R. B., Mankoff, K., Jonas, J. A., Foley, K. M., & Dowsett, H. J. (2009).  
 1794 *PRISM3/GISS Topographic Reconstruction* (No. 419). *Data Series*. U.S. Geological Survey.  
 1795 <https://doi.org/10.3133/ds419>
- 1796 Sperber, K. R., Hameed, S., Potter, G. L., & Boyle, J. S. (1994). Simulation of the Northern Summer Monsoon in  
 1797 the ECMWF Model: Sensitivity to Horizontal Resolution. *Monthly Weather Review*, 122(11), 2461–2481.  
 1798 [https://doi.org/10.1175/1520-0493\(1994\)122<2461:SOTNSM>2.0.CO;2](https://doi.org/10.1175/1520-0493(1994)122<2461:SOTNSM>2.0.CO;2)
- 1799 Stager, J. C., Mayewski, P. A., & Meeker, L. D. (2002). Cooling cycles, Heinrich event 1, and the desiccation of  
 1800 Lake Victoria. *Palaeogeography, Palaeoclimatology, Palaeoecology*, 183(1), 169–178.  
 1801 [https://doi.org/10.1016/S0031-0182\(01\)00468-0](https://doi.org/10.1016/S0031-0182(01)00468-0)
- 1802 Stager, J. C., Ryves, D. B., Chase, B. M., & Pausata, F. S. R. (2011). Catastrophic Drought in the Afro-Asian  
 1803 Monsoon Region During Heinrich Event 1. *Science*, 331(6022), 1299–1302.  
 1804 <https://doi.org/10.1126/science.1198322>
- 1805 Stepanek, C., & Lohmann, G. (2012). Modelling mid-Pliocene climate with COSMOS. *Geoscientific Model*  
 1806 *Development*, 5(5), 1221–1243. <https://doi.org/10.5194/gmd-5-1221-2012>
- 1807 Stepanek, Christian, Samakinwa, E., Knorr, G., & Lohmann, G. (2020). Contribution of the coupled atmosphere–  
 1808 ocean–sea ice–vegetation model COSMOS to the PlioMIP2. *Climate of the Past*, 16(6), 2275–2323.  
 1809 <https://doi.org/10.5194/cp-16-2275-2020>
- 1810 Su, H., & Neelin, J. D. (2005). Dynamical mechanisms for African monsoon changes during the mid-Holocene.  
 1811 *Journal of Geophysical Research: Atmospheres*, 110(D19). <https://doi.org/10.1029/2005JD005806>
- 1812 Sultan, B., & Janicot, S. (2003). The West African monsoon dynamics. Part II: The “preonset” and “onset” of the  
 1813 summer monsoon. *Journal of Climate*, 16(21), 3407–3427.
- 1814 Sultan, B., Janicot, S., & Diedhiou, A. (2003). The West African monsoon dynamics. Part I: Documentation of  
 1815 intraseasonal variability. *Journal of Climate*, 16(21), 3389–3406.
- 1816 Sultan, B., Baron, C., Dingkuhn, M., Sarr, B., & Janicot, S. (2005). Agricultural impacts of large-scale variability of  
 1817 the West African monsoon. *Agricultural and Forest Meteorology*, 128(1), 93–110.  
 1818 <https://doi.org/10.1016/j.agrformet.2004.08.005>
- 1819 Swann, A. L. S., Fung, I. Y., Liu, Y., & Chiang, J. C. H. (2014). Remote Vegetation Feedbacks and the Mid-  
 1820 Holocene Green Sahara. *Journal of Climate*, 27(13), 4857–4870. <https://doi.org/10.1175/JCLI-D-13-00690.1>
- 1821
- 1822 Sylla, M. B., Nikiema, P. M., Gibba, P., Kebe, I., & Klutse, N. A. B. (2016). Climate Change over West Africa:  
 1823 Recent Trends and Future Projections. In J. A. Yaro & J. Hesselberg (Eds.), *Adaptation to Climate Change*  
 1824 *and Variability in Rural West Africa* (pp. 25–40). Cham: Springer International Publishing.  
 1825 [https://doi.org/10.1007/978-3-319-31499-0\\_3](https://doi.org/10.1007/978-3-319-31499-0_3)
- 1826 Texier, D., Noblet, N. de, & Braconnot, P. (2000). Sensitivity of the African and Asian Monsoons to Mid-Holocene  
 1827 Insolation and Data-Inferred Surface Changes. *Journal of Climate*, 13(1), 164–181.  
 1828 [https://doi.org/10.1175/1520-0442\(2000\)013<0164:SOTAAA>2.0.CO;2](https://doi.org/10.1175/1520-0442(2000)013<0164:SOTAAA>2.0.CO;2)
- 1829 Thompson, A. J., Skinner, C. B., Poulsen, C. J., & Zhu, J. (2019). Modulation of Mid-Holocene African Rainfall by  
 1830 Dust Aerosol Direct and Indirect Effects. *Geophysical Research Letters*, 46(7), 3917–3926.  
 1831 <https://doi.org/10.1029/2018GL081225>
- 1832 Thompson, A. J., Tabor, C. R., Poulsen, C. J., & Skinner, C. B. (2021). Water isotopic constraints on the  
 1833 enhancement of the mid-Holocene West African monsoon. *Earth and Planetary Science Letters*, 554,  
 1834 116677. <https://doi.org/10.1016/j.epsl.2020.116677>
- 1835 Thorncroft, C. D., & Blackburn, M. (1999). Maintenance of the African easterly jet. *Quarterly Journal of the Royal*  
 1836 *Meteorological Society*, 125(555), 763–786. <https://doi.org/10.1002/qj.49712555502>
- 1837 Tierney, J. E., Pausata, F. S. R., & deMenocal, P. B. (2017). Rainfall regimes of the Green Sahara. *Science*  
 1838 *Advances*, 3(1), e1601503. <https://doi.org/10.1126/sciadv.1601503>

- 1839 Tindall, J. C., Haywood, A. M., Salzmann, U., Dolan, A. M., & Fletcher, T. (2022). The warm winter paradox in the  
 1840 Pliocene northern high latitudes. *Climate of the Past*, 18(6), 1385–1405. [https://doi.org/10.5194/cp-18-](https://doi.org/10.5194/cp-18-1385-2022)  
 1841 1385-2022
- 1842 Tompkins, A. M. (2002). A Prognostic Parameterization for the Subgrid-Scale Variability of Water Vapor and  
 1843 Clouds in Large-Scale Models and Its Use to Diagnose Cloud Cover. *Journal of the Atmospheric Sciences*,  
 1844 59(12), 1917–1942. [https://doi.org/10.1175/1520-0469\(2002\)059<1917:APPFTS>2.0.CO;2](https://doi.org/10.1175/1520-0469(2002)059<1917:APPFTS>2.0.CO;2)
- 1845 de la Vega, E., Chalk, T. B., Wilson, P. A., Bysani, R. P., & Foster, G. L. (2020). Atmospheric CO<sub>2</sub> during the Mid-  
 1846 Piacenzian Warm Period and the M2 glaciation. *Scientific Reports*, 10(1), 11002.  
 1847 <https://doi.org/10.1038/s41598-020-67154-8>
- 1848 Wang, Y., Notaro, M., Liu, Z., Gallimore, R., Levis, S., & Kutzbach, J. E. (2008). Detecting vegetation-precipitation  
 1849 feedbacks in mid-Holocene North Africa from two climate models. *Climate of the Past*, 4(1), 59–67.  
 1850 <https://doi.org/10.5194/cp-4-59-2008>
- 1851 Wang, Y. J., Cheng, H., Edwards, R. L., An, Z. S., Wu, J. Y., Shen, C.-C., & Dorale, J. A. (2001). A High-  
 1852 Resolution Absolute-Dated Late Pleistocene Monsoon Record from Hulu Cave, China. *Science*, 294(5550),  
 1853 2345–2348. <https://doi.org/10.1126/science.1064618>
- 1854 Wei, W., & Lohmann, G. (2012). Simulated Atlantic Multidecadal Oscillation during the Holocene. *Journal of*  
 1855 *Climate*, 25(20), 6989–7002. <https://doi.org/10.1175/JCLI-D-11-00667.1>
- 1856 Weldeab, S., Frank, M., Stichel, T., Haley, B., & Sangen, M. (2011). Spatio-temporal evolution of the West African  
 1857 monsoon during the last deglaciation. *Geophysical Research Letters*, 38(13).  
 1858 <https://doi.org/10.1029/2011GL047805>
- 1859 Werner, M., Mikolajewicz, U., Heimann, M., & Hoffmann, G. (2000). Borehole versus isotope temperatures on  
 1860 Greenland: Seasonality does matter. *Geophysical Research Letters*, 27(5), 723–726.  
 1861 <https://doi.org/10.1029/1999GL006075>
- 1862 Werner, M., Langebroek, P. M., Carlsen, T., Herold, M., & Lohmann, G. (2011). Stable water isotopes in the  
 1863 ECHAM5 general circulation model: Toward high-resolution isotope modeling on a global scale. *Journal*  
 1864 *of Geophysical Research*, 116(D15), D15109. <https://doi.org/10.1029/2011JD015681>
- 1865 Werner, M., Jouzel, J., Masson-Delmotte, V., & Lohmann, G. (2018). Reconciling glacial Antarctic water stable  
 1866 isotopes with ice sheet topography and the isotopic paleothermometer. *Nature Communications*, 9(1), 3537.  
 1867 <https://doi.org/10.1038/s41467-018-05430-y>
- 1868 Wu, H., Guiot, J., Brewer, S., & Guo, Z. (2007). Climatic changes in Eurasia and Africa at the last glacial maximum  
 1869 and mid-Holocene: reconstruction from pollen data using inverse vegetation modelling. *Climate Dynamics*,  
 1870 29(2), 211–229. <https://doi.org/10.1007/s00382-007-0231-3>
- 1871 Wu, M.-L. C., Reale, O., Schubert, S. D., Suarez, M. J., Koster, R. D., & Pegion, P. J. (2009). African Easterly Jet:  
 1872 Structure and Maintenance. *Journal of Climate*, 22(17), 4459–4480.  
 1873 <https://doi.org/10.1175/2009JCLI2584.1>
- 1874 Xu, X., Werner, M., Butzin, M., & Lohmann, G. (2012). Water isotope variations in the global ocean model MPI-  
 1875 OM. *Geoscientific Model Development*, 5(3), 809–818. <https://doi.org/10.5194/gmd-5-809-2012>
- 1876 Yan, Q., Wei, T., Korty, R. L., Kossin, J. P., Zhang, Z., & Wang, H. (2016). Enhanced intensity of global tropical  
 1877 cyclones during the mid-Pliocene warm period. *Proceedings of the National Academy of Sciences*, 113(46),  
 1878 12963–12967. <https://doi.org/10.1073/pnas.1608950113>
- 1879 Yang, G.-Y., Methven, J., Woolnough, S., Hodges, K., & Hoskins, B. (2018). Linking African Easterly Wave  
 1880 Activity with Equatorial Waves and the Influence of Rossby Waves from the Southern Hemisphere.  
 1881 *Journal of the Atmospheric Sciences*, 75(6), 1783–1809. <https://doi.org/10.1175/JAS-D-17-0184.1>
- 1882 Yoshimori, M., Yokohata, T., & Abe-Ouchi, A. (2009). A Comparison of Climate Feedback Strength between CO<sub>2</sub>  
 1883 Doubling and LGM Experiments. *Journal of Climate*, 22(12), 3374–3395.  
 1884 <https://doi.org/10.1175/2009JCLI2801.1>
- 1885 Zhang, R., Yan, Q., Zhang, Z. S., Jiang, D., Otto-Bliesner, B. L., Haywood, A. M., et al. (2013). Mid-Pliocene East  
 1886 Asian monsoon climate simulated in the PlioMIP. *Climate of the Past*, 9(5), 2085–2099.  
 1887 <https://doi.org/10.5194/cp-9-2085-2013>

- 1888 Zhang, Ran, Zhang, Z., Jiang, D., Yan, Q., Zhou, X., & Cheng, Z. (2016). Strengthened African summer monsoon in  
1889 the mid-Piacenzian. *Advances in Atmospheric Sciences*, 33(9), 1061–1070. <https://doi.org/10.1007/s00376->  
1890 016-5215-y
- 1891 Zhang, Z., Li, X., Guo, C., Otterå, O. H., Nisancioglu, K. H., Tan, N., et al. (2021). Mid-Pliocene Atlantic  
1892 Meridional Overturning Circulation simulated in PlioMIP2. *Climate of the Past*, 17(1), 529–543.  
1893 <https://doi.org/10.5194/cp-17-529-2021>
- 1894 Zhao, A., Ryder, C. L., & Wilcox, L. J. (2022). How well do the CMIP6 models simulate dust aerosols?  
1895 *Atmospheric Chemistry and Physics*, 22(3), 2095–2119. <https://doi.org/10.5194/acp-22-2095-2022>
- 1896 Zhao, Y., & Harrison, S. P. (2012). Mid-Holocene monsoons: a multi-model analysis of the inter-hemispheric  
1897 differences in the responses to orbital forcing and ocean feedbacks. *Climate Dynamics*, 39(6), 1457–1487.  
1898 <https://doi.org/10.1007/s00382-011-1193-z>
- 1899 Zhao, Y., Braconnot, P., Marti, O., Harrison, S. P., Hewitt, C., Kitoh, A., et al. (2005). A multi-model analysis of the  
1900 role of the ocean on the African and Indian monsoon during the mid-Holocene. *Climate Dynamics*, 25(7),  
1901 777–800. <https://doi.org/10.1007/s00382-005-0075-7>
- 1902 Zheng, W., & Braconnot, P. (2013). Characterization of Model Spread in PMIP2 Mid-Holocene Simulations of the  
1903 African Monsoon. *Journal of Climate*, 26(4), 1192–1210. <https://doi.org/10.1175/JCLI-D-12-00071.1>
- 1904 Zhu, J., Otto-Bliesner, B. L., Brady, E. C., Poulsen, C. J., Tierney, J. E., Lofverstrom, M., & DiNezio, P. (2021).  
1905 Assessment of Equilibrium Climate Sensitivity of the Community Earth System Model Version 2 Through  
1906 Simulation of the Last Glacial Maximum. *Geophysical Research Letters*, 48(3), e2020GL091220.  
1907 <https://doi.org/10.1029/2020GL091220>  
1908  
1909

1           **West African Monsoon dynamics and its control on stable oxygen isotopic**  
2                           **composition of precipitation in the Late Cenozoic**

3   **Daniel Boateng<sup>1\*</sup>, Jeffrey N. A. Aryee<sup>2</sup>, Michael Baidu<sup>3</sup>, Frank Arthur<sup>4</sup>, Sebastian G. Mutz<sup>5</sup>**

4   <sup>1</sup>Department of Geosciences, University of Tübingen, Tübingen, Germany

5   <sup>2</sup>Department of Meteorology and Climate Science, Kwame Nkrumah University of Science and  
6   Technology, Kumasi, Ghana

7   <sup>3</sup>Institute for Climate and Atmospheric Science, School of Earth and Environment, University of  
8   Leeds, UK

9   <sup>4</sup>Department of Natural Sciences and Environmental Health, University of South-Eastern  
10   Norway, Bo, Norway

11   <sup>5</sup>School of Geographical and Earth Sciences, University of Glasgow, Scotland, UK

12  
13   Corresponding author: Daniel Boateng ([daniel.boateng@uni-tuebingen.de](mailto:daniel.boateng@uni-tuebingen.de))

14   **Key Points:**

- 15       • We simulate the Late Cenozoic evolution of the West African Monsoon and the isotopic  
16       composition of rainwater.
- 17       • Using a high-resolution model setup and realistic vegetation cover increases the intensity  
18       of the West African Monsoon in the Mid-Holocene.
- 19       • Strengthened conditions of the West African Monsoon in the Mid-Holocene and Mid-  
20       Pliocene result from the pronounced meridional temperature gradient
- 21       • The relationship between precipitation and the simulated isotopes is non-stationary in  
22       time, which complicates proxy climate reconstructions.

23  
24

## 25 **Abstract**

26 This study presents an overview of the Late Cenozoic evolution of the West African Monsoon  
27 (WAM), and the associated changes in atmospheric dynamics and oxygen isotopic composition  
28 of precipitation ( $\delta^{18}\text{O}_p$ ). This evolution is established by using the high-resolution isotope-  
29 enabled GCM ECHAM5-wiso to simulate the climatic responses to paleoenvironmental changes  
30 during the Mid-Holocene (MH), Last Glacial Maximum (LGM), and Mid-Pliocene (MP). The  
31 simulated responses are compared to a set of GCM outputs from Paleoclimate Model  
32 Intercomparison Project phase 4 (PMIP4) to assess the added value of a high resolution and  
33 model consistency across different time periods. Results show WAM magnitudes and pattern  
34 changes that are consistent with PMIP4 models and proxy reconstructions. ECHAM5-wiso  
35 estimates the highest WAM intensification in the MH, with a precipitation increase of up to 150  
36 mm/month reaching 25°N during the monsoon season. The WAM intensification in the MP  
37 estimated by ECHAM5-wiso (up to 80 mm/month) aligns with the mid-range of the PMIP4  
38 estimates, while the LGM dryness magnitude matches most of the models. Despite an enhanced  
39 hydrological cycle in MP, MH simulations indicate a ~50% precipitation increase and a greater  
40 northward extent of WAM than the MP simulations. Strengthened conditions of the WAM in the  
41 MH and MP result from a pronounced meridional temperature gradient driving low-level  
42 westerly, Sahel-Sahara vegetation expansion, and a northward shift of the Africa Easterly Jet.  
43 The simulated  $\delta^{18}\text{O}_p$  values patterns and their relationship with temperature and precipitation are  
44 non-stationarity over time, emphasising the implications of assuming stationarity in proxy  
45 reconstruction transfer functions.

## 46 **Plain Language Summary**

47 We use a global climate model to simulate how the West African Monsoon and related climate  
48 elements changed over the Late Cenozoic (from ca. 3 million years ago to now). We use a single,  
49 high-resolution model to calculate these changes for the Mid-Holocene, Last Glacial Maximum  
50 and Mid-Pliocene time periods. We then compare our results to already existing simulations to  
51 find out if there are any benefits to using a single, high-resolution model set-up. Overall, our  
52 simulations are similar to previous simulations and other climate reconstructions. However, our  
53 results also yield two important new findings: 1) our simulations reproduce some aspects of the  
54 monsoon better than previous simulations; 2) the chemical composition of rainwater, which is  
55 used by geologists to reconstruct climate, is impacted by more factors than previously assumed.  
56 This makes it more challenging to create reliable reconstructions of climate from geological  
57 records of rainwater composition.

## 58 **1 Introduction**

59 Understanding the complex climate dynamics and variability over West Africa has been a  
60 pertinent concern due to its strong environmental and socio-economic impacts. This is especially  
61 important since most West African countries rely on a rainfed agriculture economy (Sultan et al.,  
62 2005). Most importantly, the long-lasting multidecadal wet and dry periods during the 20th  
63 century emphasise the need to understand the long-term and future variability of the West  
64 African Monsoon (WAM) system. This requires knowledge about the response of the WAM  
65 dynamics to changes in internal feedbacks and external forcings, such as orbital parameters,  
66 atmospheric greenhouse gases, and vegetation distribution. Considering past climate change  
67 outside the recent observational period can provide valuable insights into that. More specifically,  
68 time periods with atmospheric  $\text{CO}_2$  concentrations ( $p\text{CO}_2$ ) and palaeogeography similar to the

69 present day can serve as analogue for a possible future climate in which all forcings have had  
70 their full effect. This would require looking back 3 million years in Earth's history (Burke et al.,  
71 2018). Therefore, this study focuses on a model-based exploration of the evolution of the WAM  
72 from the Mid-Pliocene (MP: ~3 Ma) to the present-day, considering the Last Glacial Maximum  
73 (LGM: ~21 ka), and Mid-Holocene (MH: ~6 ka) as important intermediate time steps.

74 Due to the complicated dynamics and teleconnections of the WAM, state-of-art General  
75 Circulation Models (GCMs) still fall short in accurately reproducing its past variability and  
76 providing consistent future projections (Biasutti, 2013; Pausata et al., 2016; Tierney et al., 2017).  
77 Improving the representation of the WAM system in climate models requires knowledge about  
78 its sensitivity to various global and regional paleoenvironment forcings and feedbacks. This  
79 knowledge can help identify the elements that need improvement in GCMs to ensure more  
80 reliable predictions of the WAM in the future. For instance, the response of the WAM dynamics  
81 to orbitally driven seasonal and latitudinal distribution of incoming solar radiation can be  
82 evaluated under MH conditions (Joussaume et al., 1999; Kutzbach & Liu, 1997). The LGM  
83 provides an opportunity to study the response of the WAM to the most recent global cold  
84 extreme, characterised by extensive ice sheet coverage and low  $p\text{CO}_2$  concentrations (e.g.,  
85 Bereiter et al., 2015). The long-term sensitivity of the WAM to  $p\text{CO}_2$  concentrations similar to  
86 the present, along with a less arid Sahara and a globally enhanced hydrological cycle, can also be  
87 assessed under MP paleoenvironment conditions (Corvec & Fletcher, 2017; H. Dowsett et al.,  
88 2010; Alan M. Haywood et al., 2020; U. Salzmann et al., 2008).

89 Despite the challenges in replicating the entirety of past climate changes with GCMs  
90 under appropriate paleoenvironmental conditions (Pascale Braconnot et al., 2012; Harrison et al.,  
91 2015), comparing the simulated responses from different climate models would shed more light  
92 on the inadequate representation of feedbacks and model biases that can be improved for future  
93 climate predictions (e.g., Zheng & Braconnot, 2013). Furthermore, such inter-model comparison  
94 across multiple past climates would help determine if the systematic model biases affect the  
95 overall strength of the responses and feedbacks in the different climates and help evaluate if such  
96 biases are GCM-specific or exist independently of the GCM that is used.

97 Numerous modelling studies have simulated the precipitation changes associated with the  
98 WAM in response to multiple forcings and climate states during the Late Cenozoic (e.g., Berntell  
99 et al., 2021; Weldeab et al., 2011; Zheng & Braconnot, 2013). However, the differences between  
100 the simulations, such as spatial resolution, boundary conditions, and the complexity of the GCM,  
101 make it difficult to identify the predominant atmospheric dynamics behind the WAM  
102 precipitation changes. For instance, model-dependent uncertainties of the individual GCMs that  
103 simulated these climates in previous studies may not fully capture certain components of the  
104 WAM system, which can amplify the systematic biases related to the sensitivity to various  
105 forcings or external perturbations across different climates. Moreover, GCMs with varied spatial  
106 resolutions and parameterisations of clouds, atmospheric dynamics, hydrological cycles, and  
107 atmosphere-land surface interactions would simulate distinct responses of the WAM to different  
108 forcings, leading to inconsistent patterns of WAM dynamics. Aside from these, only a few  
109 studies have comprehensively delved into atmospheric dynamics and teleconnections behind the  
110 changes in precipitation patterns and magnitudes under different paleoenvironmental conditions  
111 throughout the Late Cenozoic (e.g., Bosmans et al., 2012; Gaetani et al., 2017; Patricola & Cook,  
112 2007; Su & Neelin, 2005). Furthermore, previous studies have highlighted that monsoons and  
113 related circulations, such as the Inter Tropical Convergence Zone (ITCZ), are better resolved at

114 higher resolutions, including improved topographical representation and model parameterisation  
115 (Bosmans et al., 2012; Gao et al., 2006; Jungandreas et al., 2021). This study addresses the  
116 points above by providing details about the WAM atmospheric dynamics across these past  
117 climates using a consistent modelling framework with a high-resolution isotope-enabled GCM.

118 Geological archives can record information about various paleoenvironmental changes in  
119 the climate system over time. They can therefore be used for model-data comparisons and as a  
120 benchmark for climate models (Pascale Braconnot et al., 2012; I. Harris et al., 2014; Harrison et  
121 al., 2015). However, the scarcity of palaeohydrological records over Africa and the spatial  
122 resolution of climate models preclude the robust model-data comparison necessary for improving  
123 climate models (e.g., Salzmann et al., 2008, 2013). Several problems for data-model persist in  
124 this region. For instance, proxy-based reconstructions using pollen, past lake levels, leaf wax  
125 isotopes, and other records have suggested significantly wetter conditions across the Sahel and  
126 Sahara during the MH (e.g., Bartlein et al., 2011; Tierney et al., 2017). However, most climate  
127 models struggle to replicate the extent and magnitude of precipitation changes indicated by these  
128 proxy records despite accounting for factors like increased insolation, altered land surface  
129 condition (e.g., vegetation, lakes, orography, soil moisture), reduced dust emissions,  
130 atmospheric-ocean interactions, and atmospheric dynamics (P. deMenocal et al., 2000; Harrison  
131 et al., 2014; Hopcroft & Valdes, 2019; Pausata et al., 2016; Tierney et al., 2017).

132 While proxy records point to varying increases in precipitation levels over North Africa's  
133 higher latitudes, climate models estimate a more moderate WAM intensification,  
134 underestimating both the northward extent and magnitude of precipitation increase suggested by  
135 the proxies. If the proxy data is a well-collected, representative sample, there are two possible  
136 model-related reasons for this mismatch: (1) The climate models simply do not capture the  
137 atmospheric processes in the region well enough to accurately model said hydroclimate changes.  
138 (2) Proxy system models, which allow the conversion of the proxy signal to a paleoclimate  
139 signal, are flawed. Proxy system models rely on calibrations based on modern-day observations,  
140 such as the spatial correlation between water isotopes and precipitation. These are used to  
141 establish a transfer function that allows a proxy-to-climate signal conversion. This signal  
142 transformation assumes that the transfer functions are stationary in time, i.e. that modern  
143 correlations are equally valid for past climates. This study uses an isotope-enabled GCM to  
144 decipher atmospheric dynamics driving WAM changes and to explore their impacts on water  
145 isotopologues under various past global changes. This allows for the testing of this assumption of  
146 the stationarity of the transfer function. Furthermore, such an analysis facilitates a direct model-  
147 isotope proxy comparison and contributes to understanding the general causal mechanisms  
148 behind the variability in different proxy materials (Bühler et al., 2022; Phipps et al., 2013; Risi et  
149 al., 2012; Werner et al., 2000).

150 This study provides the first overview of the changes of the WAM and its associated  
151 atmospheric dynamics in response to multiple forcings and feedbacks during the Late Cenozoic,  
152 using the high-resolution isotope-enabled GCM ECHAM5-wiso. More specifically, the study  
153 addresses the following specific objectives: (1) systematically simulating the responses of the  
154 WAM patterns and magnitude to the various paleoenvironment conditions, including changes in  
155 vegetation, orbital forcings, ice sheet extent, and atmospheric CO<sub>2</sub> concentrations; (2)  
156 investigating the atmospheric dynamics driving the simulated WAM changes, such as moisture  
157 transport (e.g., low-level southwesterlies), Africa Easterly Jet (AEJ), Tropical Easterly Jet (TEJ),  
158 Sahara Heat Low (SHL) and surface heat fluxes; and (3) exploring the simulated  $\delta^{18}\text{O}_p$  values

159 and how they are influenced by near-surface temperature and precipitation in response to the  
160 different boundary conditions. We further compare the simulated changes of the WAM to some  
161 of the state-of-the-art models that participated in the Paleoclimate Model Intercomparison  
162 Project (PMIP4) phase 4 to evaluate the added values of using a consistent, high-resolution  
163 modelling framework to understand the complex climate system over West Africa and improve  
164 its representation in Earth system models.

## 165 **2 Background**

### 166 2.1 On the intensification and northward extent of the West African Monsoon during the 167 Mid-Holocene

168 During the early-to-middle Holocene, spanning from 11,000 to 5,000 years before the  
169 present, the arid landscapes of the Sahel and Sahara regions transformed into shrubs, grasslands,  
170 and water bodies like rivers and lakes (Armitage et al., 2015; Claussen et al., 1999; P. deMenocal  
171 et al., 2000; Holmes, 2008; Kohfeld & Harrison, 2000). The development of this “Green Sahara”  
172 was attributed to changes in the insolation cycle, which intensified the equator-to-pole gradient  
173 and land-sea thermal contrasts and ultimately lead to an increase in rainfall across the Sahel-  
174 Sahara. The associated pressure gradient facilitated the moisture transport from the equatorial  
175 Atlantic into the continent. Overall, the changes in the orbital cycles and expansion of vegetation  
176 across the Sahel-Sahara caused the strengthening of the WAM and its northward extent (Gaetani  
177 et al., 2017; Patricola & Cook, 2007). This WAM intensification and northward migration have  
178 been reflected in many proxy systems such as paleo-lake levels (Hoelzmann et al., 1998; Prentice  
179 et al., 2000), leaf wax, and aeolian deposits in sedimentary cores from the Eastern Atlantic (P.  
180 deMenocal et al., 2000; Tierney et al., 2017) and archaeological findings that indicate human  
181 habitation (Cremaschi & Di Lernia, 1999; Dunne et al., 2012; Gabriel, 1987; Hoelzmann et al.,  
182 2001; Manning & Timpson, 2014; Sereno et al., 2008). However, state-of-art climate models still  
183 struggle to replicate the level of intensification and the northward reach as suggested by the  
184 different proxies, even when appropriate boundary conditions are prescribed (P. deMenocal et  
185 al., 2000; Harrison et al., 2014; Hopcroft & Valdes, 2019; Kutzbach & Liu, 1997; Pausata et al.,  
186 2016; Tierney et al., 2017). For instance, MH simulations in PMIP3-CMIP5 experiments  
187 estimate a precipitation increase of  $\sim 400$  mm/year over West Africa, with a northward shift that  
188 is underestimated by  $20^\circ\text{N}$  when compared to proxy reconstructions (Perez-Sanz et al., 2014).  
189 Thompson et al. (2021) utilised a water isotope-enabled Earth system model (iCESM1) that  
190 exhibited enhanced MH precipitation compared to PI conditions, and a northernmost WAM shift  
191 of approximately  $24^\circ\text{N}$ , which aligns with reconstructions from pollen and dust records ( $23$ -  
192  $28^\circ\text{N}$ ). Most of these models, however, lack vegetation feedback or appropriate prescribed MH  
193 vegetation reconstruction, which is crucial for sustaining the WAM's northward extension  
194 through vegetation-precipitation feedback (Otto-Bliesner et al., 2017; Pausata et al., 2016;  
195 Tierney et al., 2017). Rachmayani et al. (2015) demonstrated that using dynamic vegetation-  
196 coupled GCMs enhances the orbitally-induced precipitation increase by 20% over West Africa  
197 compared to fixed vegetation GCMs.

198 Recent studies have also highlighted that accounting for dust feedbacks related to the  
199 Green Sahara during the MH can further intensify and expand the WAM, aligning it more with  
200 proxy reconstructions (e.g., Egerer et al., 2018; Hopcroft & Valdes, 2019; Pausata et al., 2016;  
201 Thompson et al., 2019). These findings indicate that the discrepancies between the model and  
202 proxy reconstructions are due to the inadequate representation of certain atmospheric physics,

203 such as inaccurate cloud representation, energy fluxes, subgrid-scale convection, and surface  
204 conditions in the GCMs. Moreover, the coarse spatial resolution of GCMs fails to capture meso-  
205 to-local-scale processes like mesoscale convective systems (e.g., Baidu et al., 2022; Crook et al.,  
206 2019; Marsham et al., 2013), potentially contributing to further biases. Thus, understanding the  
207 mechanics and dynamics underlying vegetation feedback and natural variability in insolation  
208 cycles driving the WAM's northward migration during the MH is crucial for evaluating GCM  
209 performance in future projections. While these forcing mechanisms are not linked to  
210 anthropogenic emissions, evaluating and improving the GCMs' representation of climate system  
211 dynamics and feedbacks is vital for future climate change projections.

## 212 2.2 Large-scale feature of the Last Glacial Maximum and its influence on the West 213 African Monsoon

214 The LGM (~21,000 years BP) is a time period that is suitable for assessing the  
215 capabilities of state-of-the-art models due to its starkly different conditions from the present,  
216 such as lower atmospheric CO<sub>2</sub> levels (~185 ppm) and eustatic sea levels (~115 to 130 m below  
217 present) (Lambeck et al., 2014; Peltier & Fairbanks, 2006). The extensive continental ice sheets  
218 led to significant perturbations in atmospheric radiative forcing and circulation patterns,  
219 contributing to alterations in precipitation and temperature that were generally drier and colder  
220 than pre-industrial conditions (Clark et al., 2009; D'Agostino et al., 2019, 2020). Since the LGM,  
221 the Earth's global mean temperature has risen by approximately 4 to 6 °C (Annan & Hargreaves,  
222 2013, 2015; Friedrich et al., 2016), which is of the same order of magnitude increase projected  
223 under moderate to high emission scenarios for near-future climate change. Due to this similarity  
224 in global forcing and temperature response from the LGM to the present, and the present to the  
225 near future, the LGM is a relevant period to examine (e.g., Brady et al., 2013; Yoshimori et al.,  
226 2009). Furthermore, the interactions between temperature-driven and circulation-driven regional  
227 precipitation patterns in response to LGM conditions would help evaluate the ability of climate  
228 models to project precipitation under future scenarios, where both thermodynamic and dynamic  
229 phenomena contribute to changes in the magnitude and seasonality of precipitation patterns (e.g.,  
230 Boos, 2012; Lora, 2018; Scheff & Frierson, 2012).

231 Prior studies have indicated a high sensitivity of Africa's climate to rapid recurring ice  
232 sheet instabilities during the last glacial period (Adegbie et al., 2003; Stager et al., 2002, 2011;  
233 Weldeab et al., 2011). For example, the cold air temperatures over Greenland (Dansgaard-  
234 Oeschger stadials) and the influx of meltwater into the North Atlantic during Heinrich events  
235 correlated with the rapid decline in precipitation across much of Africa (Blunier & Brook, 2001;  
236 Dansgaard et al., 1993; McManus et al., 2004). Previous modelling studies of PMIP phases 1 to  
237 4 indicated weakened atmospheric circulation and associated decreased precipitation over West  
238 Africa (Kageyama et al., 2021). However, a good understanding of the dynamics leading to the  
239 dryness across the WAM region is still lacking.

240 Pollen-based reconstructions across the WAM and nearby offshore regions generally  
241 depict colder and drier conditions than the present (Bartlein et al., 2011). Although fully coupled  
242 atmosphere-ocean models can reasonably reproduce large-scale features of the LGM, several  
243 challenges remain with regard to the reconstruction of LGM topography and the assessment of  
244 inter-model biases for various climate feedbacks (Kageyama et al., 2021; Werner et al., 2018).  
245 Additionally, the spatial resolution of simulations has been identified as a crucial factor for the  
246 inter-model variabilities in LGM simulations, primarily due to the representation of ice sheet

247 topography (Kim et al., 2008; Shi et al., 2020). Overall, the complexity and diverse  
248 paleoenvironment of LGM conditions offers the opportunity to decipher the relative  
249 contributions of individual climate factors that influence precipitation changes across West  
250 Africa.

### 251 2.3 Changes of the WAM in the Mid-Pliocene

252 The MP (~3 Ma) is an important warm period for understanding the atmospheric  
253 dynamics of near-future climate change, because the Earth's geography was similar to the present  
254 and  $p\text{CO}_2$  approached present-day values (~400 ppm) (Badger et al., 2013; Bartoli et al., 2011;  
255 Harry Dowsett et al., 2016; Alan M. Haywood et al., 2020; Ulrich Salzmann et al., 2013; de la  
256 Vega et al., 2020). Additionally, the MP provides useful insights into climate feedbacks through  
257 the impact of the carbon cycle on geological times and is often considered an analogue for a  
258 near-future climate (Burke et al., 2018; Jiang et al., 2005). Climate models that participated in  
259 the PlioMIP (Pliocene Modelling Intercomparison Project) phases 1 and 2 indicate an increase of  
260 1.4 to 4.7 °C in global mean near-surface anomalies above the pre-industrial levels, along with  
261 an enhanced hydrological cycle and strengthened global monsoons (Haywood et al., 2013, 2020;  
262 Zhang et al., 2016).

263 Proxy reconstructions suggest warm and humid conditions, and fewer deserts during the  
264 MP. Boreal forests and grasslands expanded into high northern latitude regions that are currently  
265 covered by tundra (Salzmann et al., 2008). Dust records along the coast of West Africa indicate a  
266 strengthened WAM and wetter conditions over the Sahara (Kuechler et al., 2018; Salzmann et  
267 al., 2008). Palynological records also suggest an expansion of vegetation over the WAM region,  
268 with high tree cover density and widespread woodland and savanna over the Sahara (Bonnefille,  
269 2010; Salzmann et al., 2008).

270 Although previous modelling studies indicated that high-latitude warming could lead to a  
271 decreased meridional temperature gradient and a weakened tropical circulation, the warming  
272 experienced in the Sahara region, along with the corresponding Sahara heat low, actually caused  
273 an increased influx of moisture from the tropical Atlantic Ocean, strengthening WAM (Corvec &  
274 Fletcher, 2017; Alan M. Haywood et al., 2020). More specifically, the PlioMIP2 models estimate  
275 an increase in precipitation anomalies in the range of 60-120 mm/month (Berntell et al., 2021),  
276 compared to a lesser increase of 30-60 mm/month from the PlioMIP1 (Ran Zhang et al., 2016).  
277 Even though similar magnitude of changes are predicted for the future, models are still limited in  
278 capturing rainfall variability over West Africa, and future projections of it are referenced with  
279 less confidence (Biasutti, 2013; Cook, 2008; Roehrig et al., 2013). Further work and model  
280 development is needed to understand climate feedback over West Africa under high atmospheric  
281  $\text{CO}_2$  conditions.

### 282 2.4 Stable oxygen isotopic signal as proxy for reconstructing the West African Monsoon

283 Stable water isotopes serve as integrated tracers for diverse climate processes, and reflect  
284 changes in the water cycle (Craig & Gordon, 1965; Dansgaard et al., 1993). Consequently, they  
285 have been extensively used to investigate historical climate changes and characterise the current  
286 hydrological cycle. Reconstructions of the water cycle from proxy materials typically rely on  
287 modern calibrations. The modern spatial correlation between water isotopes and climate  
288 variables, such as precipitation amount or surface temperature, is used as a transfer function for  
289 reconstructing past climatic variations from proxies. For example, the oxygen isotopic

290 composition of precipitation ( $\delta^{18}\text{O}_p$ ) reconstructed from calcite in speleothems from (sub)tropical  
291 regions is interpreted to reflect past monsoon dynamics due to its relationship with precipitation  
292 amount, commonly known as the "amount effect" (e.g., Wang et al., 2001). However, these  
293 paleoclimate reconstructions from isotopic archives are compromised by changes in the transfer  
294 functions due to various non-linear climatic processes influencing the spatiotemporal variability  
295 of water isotopes, such as evaporative recycling, moisture transport pathways, source variation,  
296 vapour mixing, and precipitation dynamics (Bony et al., 2008; Risi et al., 2008, 2013). Hence,  
297 GCMs with explicit diagnostics of stable water isotopes can contribute to understanding their  
298 controlling mechanisms under different climatic conditions to ensure accurate paleoclimate  
299 reconstructions. Additionally, modelling the spatial representation of water isotopes in response  
300 to distinct past climate states aids in identifying potential non-stationarities in their relationships  
301 with climate elements like monsoon characteristics or precipitation amounts. While previous  
302 studies have employed water isotopes to understand present precipitation seasonality in West  
303 Africa (e.g., Risi et al., 2010) and even during the MH (Shi et al., 2023; Thompson et al., 2021),  
304 none have explored  $\delta^{18}\text{O}_p$  changes in response to Late Cenozoic paleoenvironmental conditions  
305 or assessed how water isotopes correspond to the spatial variability of precipitation and  
306 temperature during the WAM season.

307

308

### 309 **3 Data and Methods**

#### 310 **3.1 ECHAM5-wiso General Circulation Model**

311 Global climate changes in response to late Cenozoic paleoenvironmental conditions (i.e.,  
312 PI, MH, LGM, and MP) and present-day (PD) conditions were simulated using the isotope-  
313 tracking climate model ECHAM5-wiso. ECHAM5 is the fifth generation of the well-established  
314 atmospheric general circulation model developed by the Max Planck Institute for Meteorology  
315 (Roeckner et al., 2003). It is based on the spectral forecast model of the European Centre of  
316 Medium Range Weather Forecast (ECMWF) (Simmons et al., 1989) and represents the climate  
317 system with prognostic equations and parameterisations. Compared to its previous version, the  
318 fifth version has improved the representation of land surfaces, shortwave radiation, cumulus  
319 convection, and other factors relevant to atmospheric dynamics across the monsoon region.  
320 Specifically, the model employs an implicit scheme for the coupling of land surfaces and the  
321 atmosphere, enabling synchronous calculation of surface fluxes due to unconditional stability  
322 (Roeckner et al., 2003). It also employs land surface parameters that effectively portray the  
323 global distribution of major ecosystem types (Hagemann, 2002). Furthermore, the model  
324 simulates clouds using prognostic equations for all water phases (vapour, liquid, and solid), bulk  
325 microphysics, and statistical cloud cover parameterisation (U. Lohmann & Roeckner, 1996;  
326 Tompkins, 2002). The version employed in this study has been expanded to include isotope  
327 tracking capabilities, enabling the simulation of the water's isotopic composition as part of the  
328 hydrological cycle (Werner et al., 2011). The incorporated water isotopologues (i.e.,  $\text{H}_2^{16}\text{O}$ ,  
329  $\text{H}_2^{18}\text{O}$ , and HDO) function as independent tracers that undergo both kinetic and equilibrium  
330 fractionation during phase transitions in the atmosphere. It has been demonstrated that the model  
331 adequately represents the global hydrological cycle and stable isotopic composition (Hagemann  
332 et al., 2006; Werner et al., 2011). In this study, we compare the model's present-day simulations

333 with observed and reanalysis precipitation and near-surface temperature datasets across West  
334 Africa to assess its capability in representing WAM patterns and their seasonality.

### 335 3.2 Model Experiments and Boundary Conditions

336 Previous simulations of Late Cenozoic climate were conducted with different models and  
337 model setups. Varied parameterisation schemes, spatial resolution, and prescribed boundary  
338 conditions complicate the comparison of the regional climates across the considered time  
339 periods. We therefore conducted (paleo)climate simulations for PD, PI, MH, LGM, and MP  
340 boundary conditions using only ECHAM5-wiso, while maintaining the same spatial resolution.  
341 All climate simulation experiments were performed using a high T159 spectral resolution (~80 x  
342 80 km around the equator) and 31 vertical levels up to 10 hPa. The model uses prescribed sea  
343 surface temperature (SST) as the interface between the ocean and atmosphere and, therefore,  
344 requires less time to reach dynamic equilibrium than fully coupled atmosphere-ocean models.  
345 However, the prescribed SSTs disregard oceanic decadal variability, making the simulated  
346 response inevitably biased by the specific SST reconstructions used. The paleoclimate  
347 experiments were run for 18 years with a 6-hour model output and only considered the last 15  
348 years for the analysis. The first 3 years of the model serve as the spin-up period, which is the  
349 time required for the model to reach dynamic equilibrium. Given the study's aim to understand  
350 the WAM response to the diverse paleoenvironmental conditions, the different experimental set-  
351 ups accounting for variations in orbital parameters, greenhouse gases concentration, SSTs, sea  
352 ice concentrations (SICs), and land surface cover (e.g., ice sheet and vegetation) were devised for  
353 the different climates. The prescribed boundary conditions for the experiments are similar to the  
354 Late Cenozoic simulations presented by Mutz et al. (2018) and Botsyun et al. (2022). We build  
355 on those by simulating and analysing the isotopic compositions for all paleoclimates.

356 To validate the model's ability to represent WAM dynamics, we compared the present-  
357 day (PD) simulation conducted by Boateng et al. (2023) with observed and reanalysis  
358 precipitation and near-surface temperature datasets. The PD simulation setup follows the  
359 Atmospheric Model Intercomparison Project (AMIP) protocol, using prescribed annual means of  
360 SST and SIC from 1979 to 2014. The pre-industrial simulation (the reference year 1850) was  
361 also obtained from Boateng et al. (2023). The model was simulated with prescribed SST and SIC  
362 from a transient coupled ocean-atmosphere model (Lorenz & Lohmann, 2004). It used an  
363 atmospheric CO<sub>2</sub> concentration of 280 ppm in accordance with Dietrich et al. (2013), which was  
364 derived from the ice-core record (Etheridge et al., 1996, 1998). Land surface parameters were  
365 taken from Hagemann (2002). The initial isotopic composition of the atmosphere was adopted  
366 from global gridded data of <sup>18</sup>O composition of seawater provided by LeGrande & Schmidt  
367 (2006). In this study, the climate change signals are defined as deviations from the PI estimates.  
368 Therefore, all reported anomalies (e.g., MH-PI) throughout the paper, described as either  
369 "increases" or "decreases", use the simulated PI values as a reference. We also represent the  
370 H<sub>2</sub><sup>18</sup>O composition using the  $\delta$ -notation and calculate it as precipitation-weighted means using  
371 the Vienna Standard Mean Ocean Water (V-SNOW).

372 The SST and SIC boundary conditions prescribed for the MH experiments were derived  
373 from transient MH simulation of a low-resolution ocean-atmosphere coupled model (Etheridge et  
374 al., 1996, 1998)(G. Lohmann et al., 2013; Wei & Lohmann, 2012). The GHG concentrations  
375 (e.g., CO<sub>2</sub> of 280 ppm) are based on ice-core reconstructions (Etheridge et al., 1996, 1998), and  
376 the orbital forcing parameters are taken from Dietrich et al. (2013). On the other hand, the LGM

377 simulation was forced with sea surface variables from reconstructions for the Atlantic, Pacific,  
 378 and Indian oceans based on the GLAMAP (Sarnthein et al., 2003) and CLIMAP (1981) projects.  
 379 Moreover, the GHG concentrations (CO<sub>2</sub> of 185 ppm) and orbital parameters follow Otto-  
 380 Bliesner et al. (2006). The palaeogeography and ice sheet extent and thickness are based on the  
 381 PMIP3 experimental protocol (Abe-Ouchi et al., 2015). The vegetation distribution maps for  
 382 both the LGM and MH are based on the reconstruction of plant functional types from BIOME  
 383 6000 of the paleovegetation mapping project (Bigelow et al., 2003; Harrison et al., 2001; Pickett  
 384 et al., 2004; Prentice et al., 2000). The MP paleoenvironment conditions prescribed in the  
 385 ECHAM5 model were based on the Pliocene Research, Interpretation, and Synoptic Mapping  
 386 (PRISM) project (Dowsett et al., 2010; Haywood et al., 2016). More specifically, GHG  
 387 concentration (e.g., CO<sub>2</sub> of 405 ppm), orbital parameters, land surface variables (e.g.,  
 388 topography, ice cover, and land-sea mask), and sea surface variables (SST, and SIC) were  
 389 derived from PRISM3D. The vegetation distribution map was regenerated with JSBACH plant  
 390 functional types using the PRISM reconstruction (C. Stepanek & Lohmann, 2012). A summary  
 391 of the major boundary conditions used in this study is presented in Table 1.

392 Due to the sparse availability of isotopic composition records for the past climates, all the  
 393 initial conditions of the ocean and the atmosphere were kept the same. The H<sub>2</sub><sup>18</sup>O and HDO  
 394 starting conditions for the ocean were taken from the equilibrium 3000-year run with MPI-OM-  
 395 wiso (Xu et al., 2012), and the atmosphere was initialised with δ<sup>18</sup>O and δD of -10 and -80 ‰,  
 396 respectively, similar to previous studies (e.g., Cauquoin et al., 2019; Werner et al., 2011).

397

398

399

400 **Table 1.** Summary of boundary conditions for the ECHAM5-wiso experiments (this study) and  
 401 the list of PMIP4 models that simulated the coeval climates. e stands for eccentricity, o for  
 402 obliquity, and lop for longitude of perihelion.

403

Experiment name	Greenhouse gas concentrations	Orbital forcing parameters	Surface conditions	PMIP4 models considered
Pre-industrial (PI): year 1850	CO <sub>2</sub> : 280 ppm, CH <sub>4</sub> : 760 ppb, N <sub>2</sub> O: 270 ppb.	e: 0.016804, o: 23.4725, lop: 278.734	The SST and SIC data are taken from a low-resolution coupled ocean-atmosphere simulation by Dietrich et al. (2013) and Lorenz & Lohmann (2004). Vegetation distribution data was adopted from Hagemann (2002).	All models
Mid-Holocene (MH): ~6 ka	CO <sub>2</sub> : 280 ppm, CH <sub>4</sub> : 650 ppb, N <sub>2</sub> O: 270 ppb.	e: 0.018682, o: 24.1048, lop: 180.918	SSTs and SICs are obtained from a transient, low-resolution coupled ocean-atmosphere simulation of the Mid-Holocene (Lohmann et al., 2013; Wei & Lohmann, 2012). Vegetation reconstructions from the BIOME 6000 dataset (Bigelow et al., 2003; Harrison et al., 2001; Pickett et al., 2004;	AWI-ESM-1-1-LR, CESM2, EC-Earth3-LR, GISS-E2-1-G, HadGEM3-GC31-LL, IPSL-CM6A-LR, MIROC-ES2L, NorESM1-F

			Prentice et al., 2000) converted into plant functional types.	
Last Glacial Maximum (LGM): ~21 ka	CO <sub>2</sub> : 185 ppm, CH <sub>4</sub> : 350 ppb, N <sub>2</sub> O: 200 ppb.	e: 0.018994, o: 22.949, lop: 294.42	SSTs and SICs were derived from GLAMAP reconstructions for the Atlantic Ocean (Sarnthein et al., 2003) and CLIMAP reconstructions for the Pacific and Indian Oceans (CLIMAP, 1981). Land-sea distribution, ice sheet extent, and thickness were based on PMIP3 data (Abe-Ouchi et al., 2015). Vegetation patterns were reconstructed using maps of plant functional types from the BIOME 6000 Paleovegetation Mapping Project (Bigelow et al., 2003; Harrison et al., 2001; Pickett et al., 2004; Prentice et al., 2000) and model predictions provided by Arnold et al. (2009).	AWI-ESM-1-1-LR, CESM2-WACCM-FV2, MIROC-ES2L, MPI-ESM1-2-LR, INM-CM4-8
Mid-Pliocene (MP): ~3 Ma	CO <sub>2</sub> : 405 ppm, CH <sub>4</sub> : 760 ppb, N <sub>2</sub> O: 270 ppb.	e: 0.016804, o: 23.4725, lop: 278.734	SSTs, SICs, land-sea mask, topography, and ice cover data were sourced from PRISM3D (Dowsett et al., 2010; Haywood et al., 2010; Sohl et al., 2009). The vegetation boundary condition was established by converting the PRISM vegetation reconstruction into JSBACH plant functional types, following the method outlined by Stepanek and Lohmann (2012).	CESM2, EC-Earth3-LR, GISS-E2-1-G, HadGEM3-GC31-LL, IPSL-CM6A-LR, NorESM1-F

404

### 3.3 Observed and Simulated Data Comparison

405

406 Reanalysis products are used as validation datasets to assess how ECHAM5-wiso  
407 simulates the climatologies and seasonality of precipitation and near-surface temperature across  
408 the WAM region. More specifically, the ERA5 climate reanalysis, produced and maintained by  
409 ECMWF, is compared to the simulated long-term seasonal means of the PD climate. ERA5  
410 consists of globally interpolated observations (e.g., ocean buoys, satellites, aircraft, weather  
411 stations, and other platforms) and numerical simulations using a four-dimensional variational  
412 (4D-var) data assimilation scheme (Hersbach et al., 2020). It has hourly output, an approximately  
413 31 km spatial resolution, and extends back to 1959 (Bell et al., 2021). We only extract the  
414 monthly long-term mean for the period 1979-2014 due to the simulated time range of the PD  
415 experiment. Moreover, the CRU (Climate Research Unit gridded Time series) high-resolution  
416 dataset (i.e., 0.5° x 0.5° over land regions except for Antarctica), maintained at the University of  
417 East Anglia, UK, was used to compare the PD precipitation simulation. CRU relies on the  
418 extensive network of global weather stations, which are interpolated using angular-distance  
419 weighting (ADW). This dataset extends back to 1901 (more details in Harris et al. 2014 and  
2020).

### 420 3.4 Observed and Simulated Data Comparison

421 Simulated model outputs from various climate models that participated in the fourth  
422 phase of the Paleoclimate Model Intercomparison Project (PMIP4), which is a component of the  
423 current Coupled Model Intercomparison Project (CMIP6) (Eyring et al., 2016), were analysed to  
424 further compare our simulated responses to paleoenvironmental conditions with the current state-  
425 of-the-art models. However, we emphasise that our analysis does not constitute a formal inter-  
426 model comparison since different experimental protocols were used for the simulations in this  
427 study. For instance, we rely on a high-resolution atmosphere-only model with prescribed  
428 forcings, in contrast to the fully coupled atmosphere-ocean GCMs used in the PMIP4  
429 experiments. Furthermore, the ECHAM5-wiso simulation time is shorter than that of the PMIP4  
430 models (>100 years) due to the longer period required for fully coupled ocean-atmosphere  
431 models to reach quasi-equilibrium and avoid drifts in climate variables. The boundary conditions  
432 and experimental setup protocols for the PMIP4 models simulating the MH, LGM, and MP are  
433 described in Kageyama et al. (2018) and Otto-Bliesner et al. (2017). We analysed the last 100  
434 years of monthly precipitation amounts for each model, with climate anomalies estimated using  
435 their respective PI control simulations. Moreover, we highlight that the individual PMIP4  
436 models' spatial resolutions were kept for our analysis to disentangle the impact of the model  
437 resolution in representing the WAM dynamics.

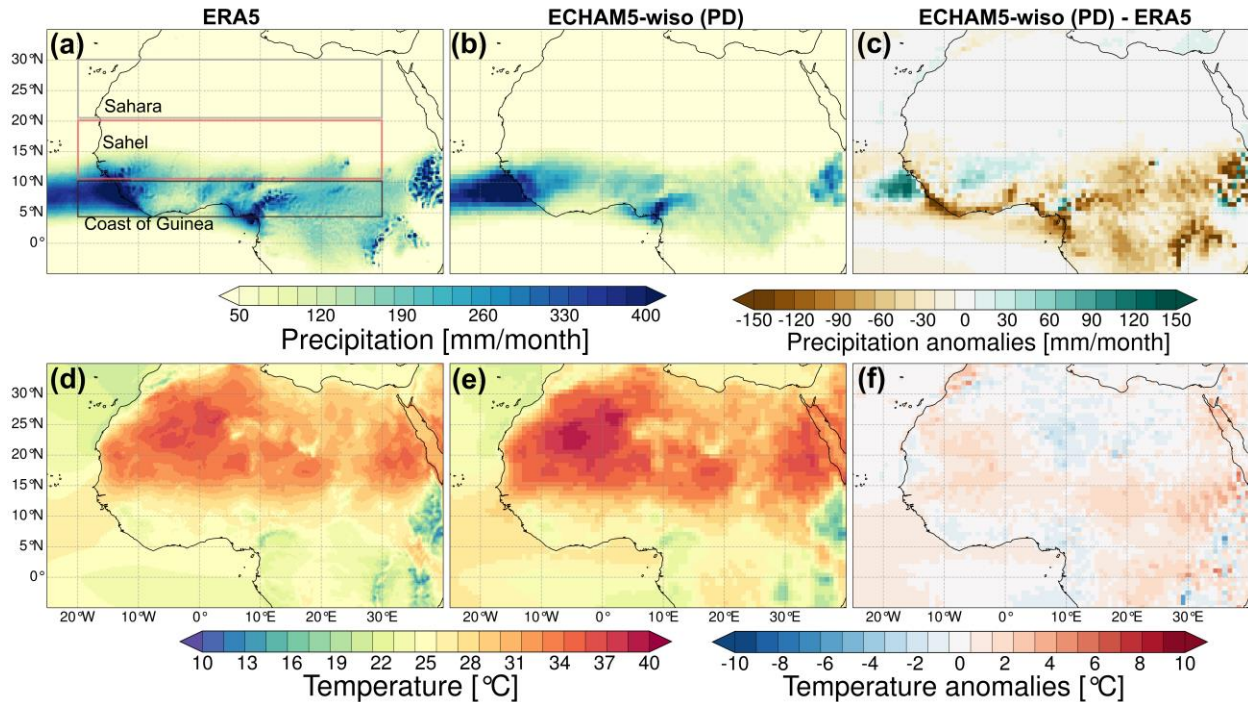
### 438 3.5 West African Monsoon Anomalies and Statistical Test

439 Long-term seasonal means of the WAM months (JJAS) were estimated using the 6-hour  
440 model output from the ECHAM5-wiso experiments and the monthly means from the PMIP4  
441 models. The statistical significance of the long-term anomalies is evaluated using a student t-test  
442 with a confidence interval threshold of 95%. It is important to note that the analysis is based on  
443 uncorrected time, even though orbits were modified in the time slice experiments. However, this  
444 does not influence the analysis since climatological means are considered. As the WAM  
445 seasonality is zonally distributed (Janicot et al., 2011; S. E. Nicholson & Palao, 1993), three  
446 different latitudinal transects were delineated for further analysis. Specifically, zonal averages  
447 over the Sahara (30-20°N, 20°W-30°E), Sahel (20-10°N, 20°W-30°E), and Guinea coast (10-  
448 5°N, 20°W-30°E) were used to understand the meridional variations of the simulated rain belt  
449 across the WAM region.

## 450 4 Results

### 451 4.1 Present-day simulation and comparison to observations

452 Comparisons of the simulated and the observed spatial patterns and seasonality of  
453 precipitation and near-surface temperature revealed that ECHAM5-wiso represents the climate  
454 across the WAM region well. More specifically, the simulated and observed precipitation in the  
455 monsoon season shows a similar rain belt, i.e., a latitudinal band of maximum precipitation of  
456 approximately 400 mm/month across Africa. There are only slight deviations in magnitude  
457 between ECHAM5-wiso and ERA5 (Fig. 1a-c): ERA5 shows a higher magnitude of  
458 precipitation, with ~40 mm/month more than predicted by the simulation. However, comparing  
459 the simulated patterns to the CRU datasets reduces these slight differences in precipitation  
460 patterns and magnitudes (Fig. S1). Moreover, the simulated near-surface temperature indicates  
461 similar spatial patterns with a pronounced meridional gradient, indicating high temperatures of  
462 up to 40 °C across the Sahara region (Fig. 1d-f).

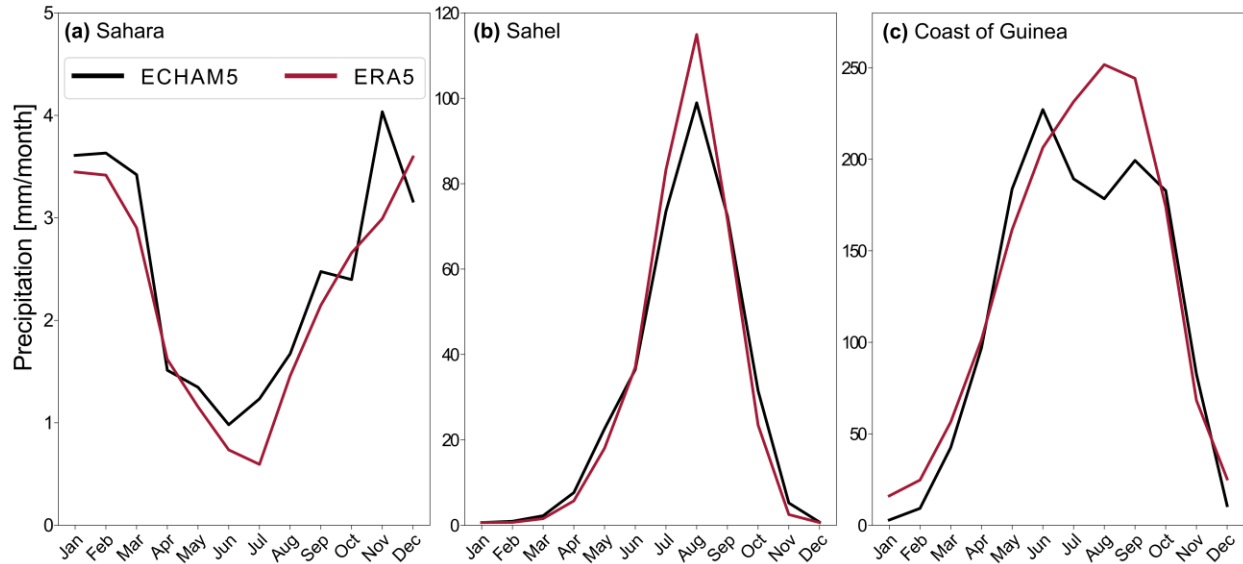


463

464 **Figure 1.** Long-term annual means (1979-2014) of ERA5 and ECHAM5-wiso precipitation (a  
 465 and b) and near-surface temperature (d and e) during the monsoon season (JJAS), and the  
 466 differences in precipitation and near-surface temperature between the datasets (c and f). The  
 467 green colour range in the precipitation difference indicates a wet bias, while the brown colours  
 468 indicate a dry bias in the model. The red colour range also represents a warm bias, and the blue  
 469 colours indicate a cold bias in the model. Overall, the simulated patterns of the rain belt and  
 470 meridional temperature gradient during the monsoon season demonstrate a reasonable model  
 471 performance. The demarcated regions in (a) are used for estimating the regional means.

472

473 The migration of the WAM drives different seasonal precipitation patterns across West  
 474 Africa. Consequently, we analyse the seasonal trends using regional monthly means across the  
 475 Sahara, Sahel, and the coast of Guinea. Overall, the model simulates an accurate seasonal  
 476 distribution and intensity across most of the transects (Fig. 2). Specifically, the observed and the  
 477 modelled seasonal cycle shows a precipitation increase of  $>3$  mm/month during the winter in the  
 478 Sahara region (Fig. 2a). Moreover, the model also simulates a realistic unimodal monthly  
 479 distribution across the Sahel, with maximum precipitation of  $\sim 100$  mm/month in August (Fig.  
 480 2b). However, ECHAM5-wiso predicts the expected bimodal precipitation seasonality across the  
 481 Guinea coast, with peak months in June ( $\sim 225$  mm/month) and September ( $\sim 200$  mm/month),  
 482 while ERA5 indicates wider unimodal patterns of maximum precipitation of  $\sim 250$  mm/month in  
 483 June (Fig. 2c). Despite the adequate precipitation representation of ERA5 over West Africa,  
 484 previous studies have indicated their underestimation over the coast of Guinea (e.g., Quagraine et  
 485 al., 2020). Overall, the present-day simulation results confirm ECHAM5-wiso's ability to  
 486 represent the hydroclimate of the WAM and its associated teleconnections, validating its use for  
 487 paleoclimate simulations.



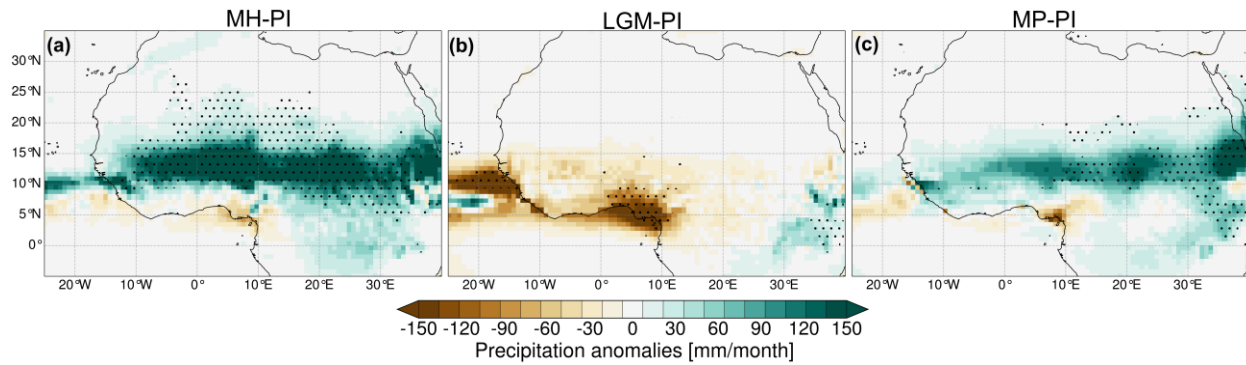
488

489 **Figure 2.** Comparison of ERA5 (red) and ECHAM5-wiso (black) monthly precipitation changes  
 490 across the (a) Sahara (30°–20°N, 20°W–30°E), (b) Sahel (20°–10°N, 20°W–30°E), and (c) Coast of  
 491 Guinea (10°–5°N, 20°W–30°E) (see Fig. 1a). For the Sahara and the Sahel, the modelled evolution  
 492 of the WAM is consistent with ERA5. However, the model produces the expected bimodal  
 493 precipitation seasonality across the Guinea coast, while ERA5 only shows a unimodal pattern.

494

#### 4.2 Simulated changes of the WAM in the late Cenozoic

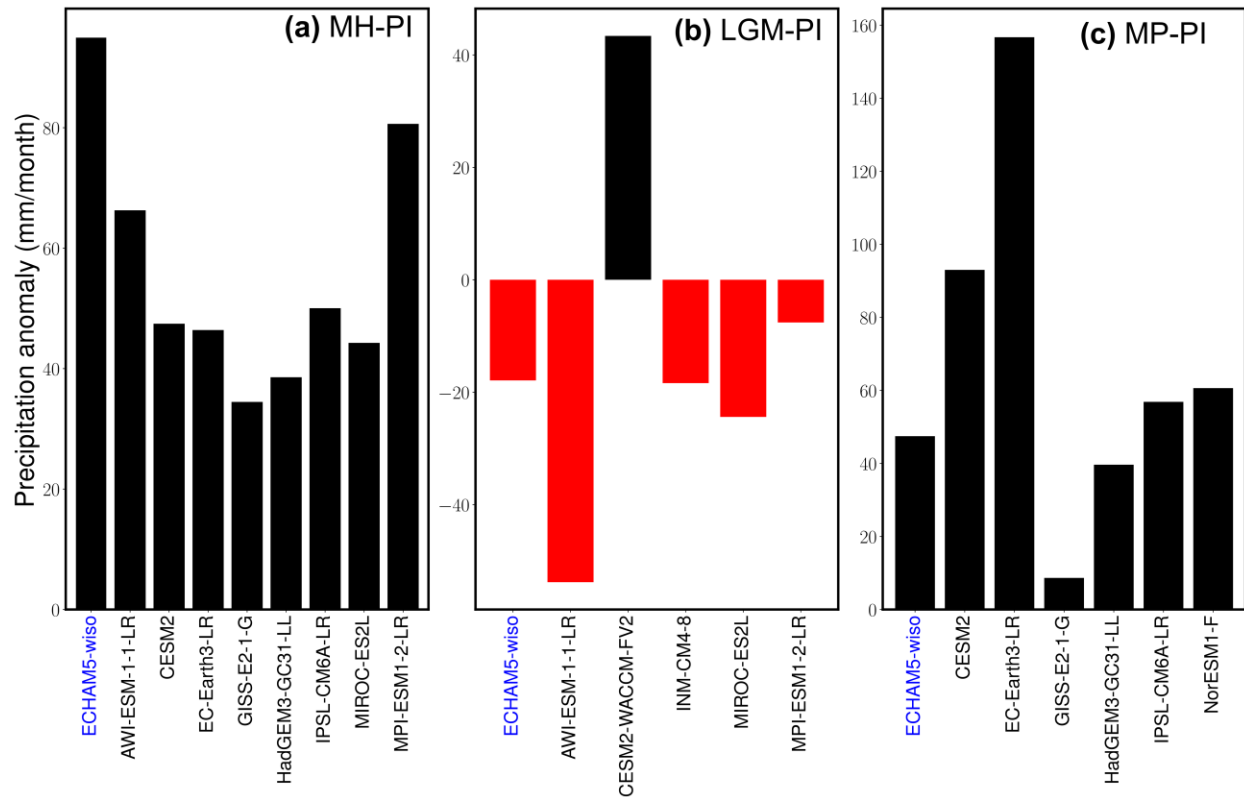
495 The simulated regional patterns of the WAM in the MH, LGM, and MP deviate  
 496 significantly from PI conditions. Overall, the model estimates an intensification of the WAM in  
 497 the MH and MP, with the MH showing a more significant intensification than the MP. On the  
 498 other hand, the model estimates a pattern of extensive dryness during the WAM season in the  
 499 LGM (Fig. 3). The estimated precipitation anomalies during the WAM season in the MH  
 500 indicate bidirectional latitudinal patterns. The MH experiment estimates an increase of ~150  
 501 mm/month from 7°N to 30°N, with statistical significance below 27°N. Conversely, the model  
 502 indicates a decrease of ~30 mm/month towards the coastal regions (2°–6°N) (Fig. 3a). Overall, the  
 503 LGM simulation indicates a precipitation decrease of up to 150 mm/month across the WAM  
 504 region, with significant anomalies along the coastal regions (Fig. 3b). Lastly, MP estimates an  
 505 increase of ~100 mm/month in precipitation anomalies during the WAM season, with patches of  
 506 a slight decrease in precipitation along the coast of Guinea, Nigeria, and Cameroon (Fig. 3c).  
 507 The simulated patterns of precipitation anomalies indicate a higher magnitude of the latitudinal  
 508 extent of the WAM towards the Sahara region in the MH compared to the MP. To assess the  
 509 relative importance and added value of using ECHAM5-wiso to simulate all the studied periods,  
 510 we compare our model estimates to those of other models from the CMIP6-PMIP4 experiments  
 511 (Table 1) that simulate the same periods. We focus our analysis on regional means of  
 512 precipitation anomalies across the Sahel and also evaluate the latitudinal distribution of the  
 513 WAM. The simulated WAM seasonal climatologies of the different climates (i.e., MH, LGM,  
 514 and MP) and their respective control means (PI) are presented in the supplementary material  
 515 (Fig. S2, S3, S4, and S5).



516

517 **Figure 3.** Precipitation anomalies during the WAM season (JJAS) for the (a) Mid-Holocene  
 518 (MH), (b) Last Glacial Maximum (LGM), and (c) Mid-Pliocene (MP), as simulated by  
 519 ECHAM5-wiso. The green colour range represents wetter conditions, while the brown colour  
 520 range represents drier conditions compared to the Pre-Industrial (PI) estimates. The black dot  
 521 stippling indicates regions with statistically significant differences, assuming a confidence  
 522 interval of 95% based on a student t-test analysis. The precipitation anomalies patterns indicate  
 523 the highest intensification of the WAM and its northward reach in the MH despite the enhanced  
 524 hydrological cycle in the MP.

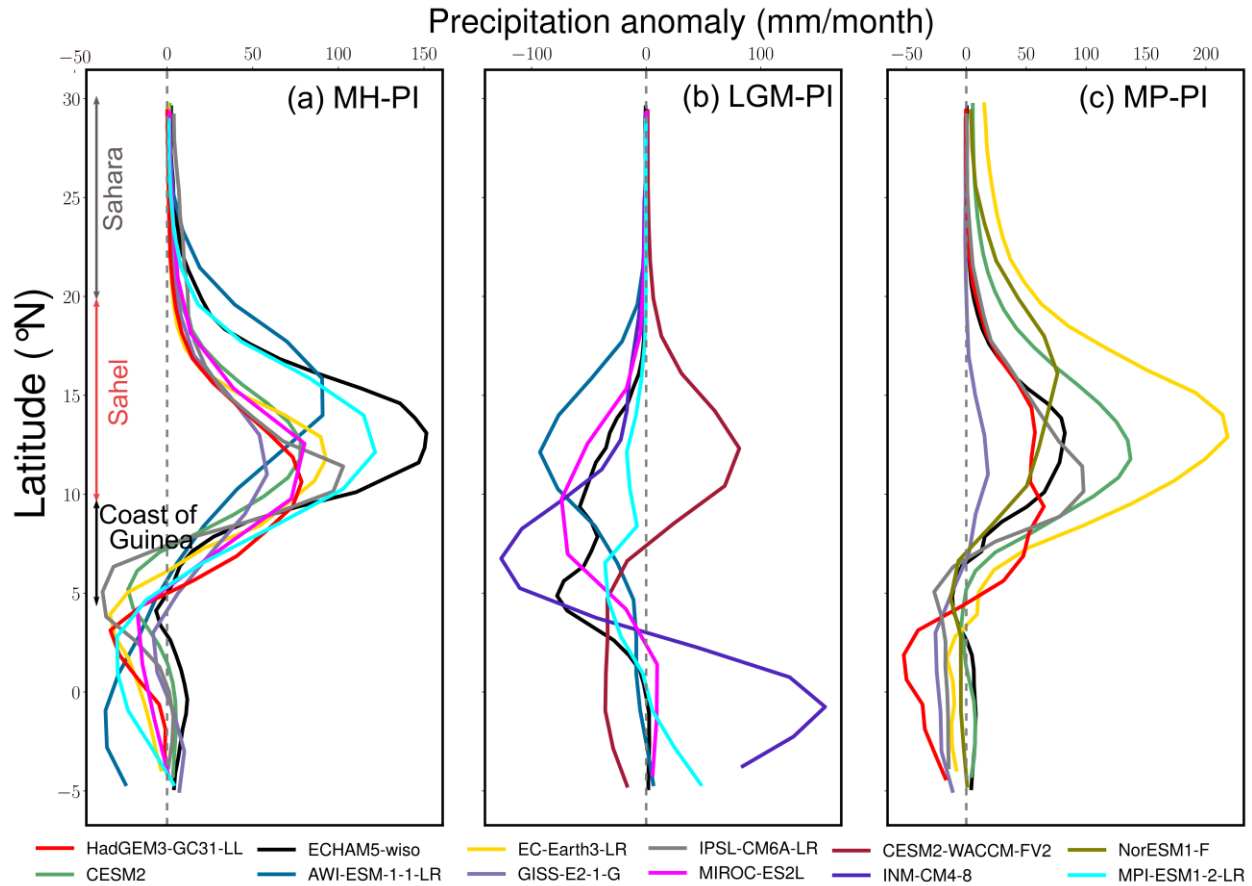
525 Overall, the inter-model comparison reveals consistent estimates in the direction and  
 526 magnitude of change in response to different paleoenvironmental conditions, with the exception  
 527 of CESM2-WCCM-FV2. Surprisingly, this model estimates an increase in precipitation  
 528 anomalies across the Sahel in the LGM. However, Zhu et al. (2021) have indicated that this  
 529 unrealistic sensitivity to colder climates may be attributed to exaggerated shortwave cloud  
 530 feedback or an unrepresented physical mechanism countering such cloud feedback. Specifically,  
 531 ECHAM5-wiso estimates the maximum increase in precipitation anomalies of ~90 mm/month  
 532 across the Sahel in the MH for the WAM season, followed by MPI-ESM1-2-LR (with ~80  
 533 mm/month), while GISS-E2-1-G shows the lowest precipitation anomalies of ~35 mm/month.  
 534 Alternatively, AWI-ESM-1-1-LR estimates a maximum precipitation decrease of 55 mm/month  
 535 across the Sahel in the LGM. The precipitation decreases (~20 mm/month) estimated by  
 536 ECHAM5-wiso is similar to the estimates by the INN-CM4-8 and MIROC-ES2L models. In the  
 537 MP, the WAM response across the Sahel exhibits a wider range of precipitation anomalies, with  
 538 EC-Earth3-LR, indicating the maximum increase of ~160 mm/month and GISS-E2-1-G showing  
 539 the lowest increase of ~10 mm/month. However, ECHAM5-wiso estimates fall within a mid-  
 540 range of ~50 mm/month, which is closer to the estimates by HadGEM3-GC31-LL, IPSL-CM6A-  
 541 LR, and NorESM1-F models. Even though ECHAM5-wiso indicates a maximum intensification  
 542 of the WAM across the Sahel in the MH rather than in the MP, other models (e.g., EC-Earth3-  
 543 LR) suggest the reverse trend. Consequently, the longitudinal regional means of the latitudinal  
 544 distribution of precipitation anomalies during the WAM season are evaluated to compare the  
 545 northward migration of the WAM in response to the different paleoenvironments.



546

547 **Figure 4.** Regional means of precipitation anomalies during the WAM season estimated for the  
 548 Sahel region (see Fig. 1a) using ECHAM5-wiso (labelled in blue) and the PMIP4 models  
 549 considered (Table 1) for the (a) Mid-Holocene (MH), (b) Last Glacial Maximum (LGM), and (c)  
 550 Mid-Pliocene (MP) paleoenvironmental conditions. The individual precipitation anomalies are  
 551 estimated based on their respective pre-industrial (PI) runs.

552 In total, most of the PMIP4 models suggest a higher meridional migration of the WAM in  
 553 the MP than in the MH, while the magnitude of changes in the latitudinal band of maximum  
 554 precipitation varies among the individual models. Specifically, EC-Earth3-LR estimates  
 555 maximum latitudinal precipitation of 200 mm/month with a greater northward extent in MP than  
 556 the ~100 mm/month rain belt in the MH. However, GISS-E2-1-G suggests a higher  
 557 intensification of the WAM with an increase in precipitation by 50 mm/month in the MH, and a  
 558 relatively modest increase of ~10 mm/month in the MP. The ECHAM5-wiso experiments  
 559 suggest a slight northward extent of the WAM in the MH and a higher intensification (~80  
 560 mm/month more) than in the MP. Despite the estimated differences, all the models, including  
 561 ECHAM5-wiso, indicate a similar meridional distribution in the MH and MP. However,  
 562 CESM2-WACCM-FV2 and INM-CM4-8 distinctively suggest an increased distribution of  
 563 meridional precipitation anomalies across the WAM areas and toward the equatorial Atlantic in  
 564 the LGM, respectively, despite the general decreasing trend estimated by the other models.



565

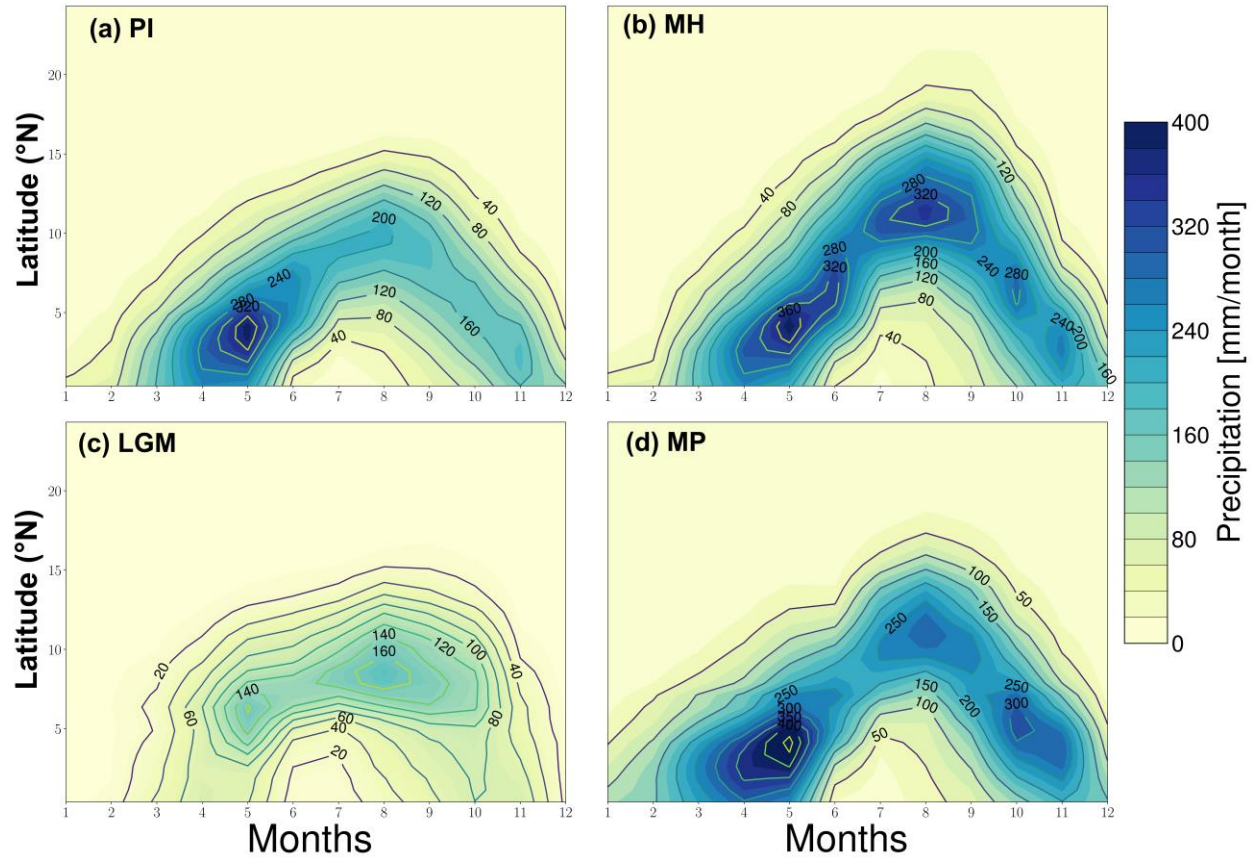
566 **Figure 5.** Latitudinal regional, seasonal means (JJAS) of precipitation anomalies across the  
 567 WAM region (averaged between 20°W and 30°E) estimated for the ECHAM5-wiso and PMIP4  
 568 models for (a) Mid-Holocene (MH), (b) Last Glacial Maximum (LGM), and (c) Mid-Pliocene  
 569 (MP) simulations. ECHAM5-wiso estimates show a latitudinal distribution that is consistent with  
 570 most of the PMIP4 models. ECHAM5-wiso estimates for LGM and MP fall into the PMIP4  
 571 model range, while ECHAM5-wiso estimates for the intensification of the WAM in the MH  
 572 exceed the PMIP4 model range.

573

#### 4.3 Seasonality of the simulated WAM in the late Cenozoic

574

The meridional migration of the WAM is investigated by analysing the evolution of  
 575 latitudinal regional means (Hovmöller diagram) (Fig. 6) and regional means over the coast of  
 576 Guinea, Sahel, and Sahara (Fig. 7). Generally, the seasonal cycle of the WAM progresses from  
 577 two rainy season regimes across the coastal areas to a single rainy event across higher latitudes  
 578 (Fig. 2). The progression of the WAM is classically defined in three phases: (1) the onset period  
 579 (March-May), driven by the low-level south-westerlies moist transport from the South Atlantic  
 580 towards the coastal regions up to 4°N and the abrupt shift of the ITCZ from the quasi-stationary  
 581 zone between 5-8°N to 8-10°N, (2) the high rain period (June-August), which abruptly shifts the  
 582 rain belt up to 10°N (also known as monsoon jump), marking the start of the high rainfall events  
 583 in the Sahel and the end of the first rainy regime across the coast, and (3) the southward retreat  
 584 (September-October), reflecting the last phase of the WAM annual cycle and the second rainfall  
 585 region across the coast (Barbé et al., 2002; Sultan et al., 2003; Sultan & Janicot, 2003).

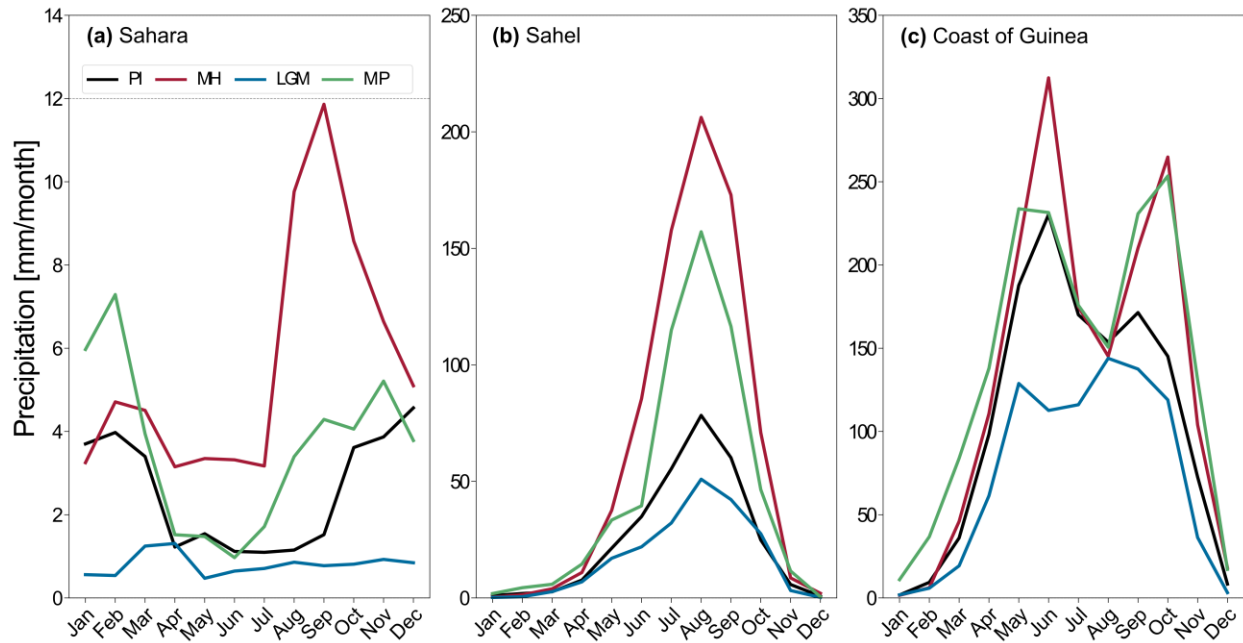


586

587 **Figure 6.** Hovmöller diagram (space-time) showing the latitudinal seasonal migration of  
 588 precipitation across the WAM region (averaged between 20°W and 30°E) for the (a) Pre-  
 589 industrial (PI), (b) Mid-Holocene (MH), (c) Last Glacial Maximum (LGM), and (d) Mid-  
 590 Pliocene (MP) experiments using ECHAM5-wiso. The MH seasonal distribution indicates the  
 591 highest precipitation rate during the high-rainfall period (June-August), while the MP indicates  
 592 more precipitation in the onset (March-May) and southward retreat (September-October)  
 593 periods.

594 The latitudinal evolution of the WAM in the PI indicates maximum precipitation of up to  
 595 320 mm/month during the onset period (from March to May) along the coast, followed by a  
 596 monsoonal jump up to 15°N in the Sahel with  $\leq 40$  mm/month of precipitation (Fig. 6a).  
 597 Moreover, the southward retreat toward the coast at the end of the annual cycle records half of  
 598 the precipitation (i.e.,  $\sim 160$  mm/month) during the onset period. The MH evolution exhibits  
 599 similar phases, but with higher precipitation and a greater northward extent. Specifically, the  
 600 onset period records precipitation of  $\sim 360$  mm/month and a higher northward shift up to  $\sim 25^\circ\text{N}$   
 601 with higher precipitation rates of up to 320 mm/month across the Sahel (Fig. 6b). The southward  
 602 retreat phase in the MH is also characterised by higher precipitation rates of up to 240  
 603 mm/month. Overall, the MP seasonal trend shows an inverted V-shape distribution that is similar  
 604 to the MH pattern, but flatter and with a higher rainfall in the onset and southward retreat phases  
 605 along the coast. The onset and southward retreat phases are characterised by precipitation rates  
 606 of  $\sim 400$  mm/month and 300 mm/month across the coast of Guinea and the equatorial Atlantic,  
 607 respectively (Fig. 6d). However, the high-rainfall period is characterised by less rainfall ( $\sim 250$   
 608 mm/month) across the Sahel and a lower latitudinal extent ( $\leq 18^\circ\text{N}$ ) when compared to MH. On

609 the other hand, the LGM simulations predict drier conditions in all seasons, with a rainfall  
 610 increase of only up to 160 mm/month in the Sahel during the high-rain period (Fig. 6c).



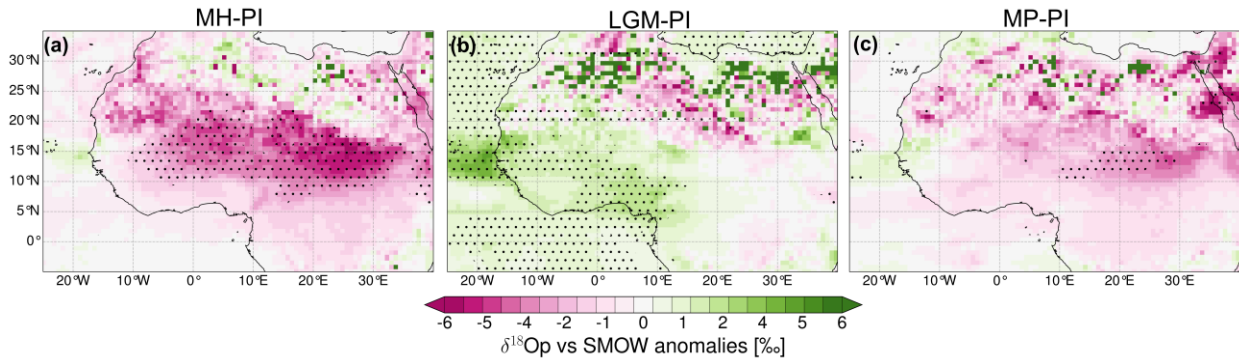
611  
 612 **Figure 7.** Seasonal cycle of precipitation across the (a) Sahara (30-20°N, 20°W-30°E), (b) Sahel  
 613 (20-10°N, 20°W-30°E), and (c) Guinea coast (10-5°N, 20°W-30°E) (See Fig. 1a) estimated for  
 614 the Pre-industrial (PI; black), Mid-Holocene (MH; red), (c) Last Glacial Maximum (LGM; blue),  
 615 and (d) Mid-Pliocene (MP; green) simulation using ECHAM5-wiso. The seasonal distribution of  
 616 precipitation across the Sahara shows different peak months for the different past climates, while  
 617 the Sahel and Coast of Guinea show a more consistent seasonality.

618 The seasonal cycle across the different climate zones is assessed through their regional  
 619 means. The seasonal precipitation cycle exhibits pronounced variations in magnitude, but few  
 620 changes in precipitation distribution. Among those few changes are variations in peak  
 621 precipitation months estimated for the Sahara. While the PI estimates indicate higher  
 622 precipitation (~4 mm/month) in November-February, the MH estimates suggest more  
 623 precipitation from July to October, with peak precipitation rates of 12 mm/month in September.  
 624 Overall, the LGM estimates indicate persistently drier conditions across all seasons in the  
 625 Sahara. The MP also indicates a higher precipitation record in the pre-onset period across the  
 626 Sahara, with a peak month in February (~7 mm/month). Regarding the bimodal monthly  
 627 distribution along the coastal regions, all climates show similar patterns. For the MH, the  
 628 precipitation peaks are highest, i.e. a ~300 mm/month peak in June and a ~260 mm/month peak  
 629 in October. The estimates across the Sahel also exhibit a unimodal distribution and precipitation  
 630 peak in August. The MH simulation produces the highest peak, with an increase of more than  
 631 100% relative to the PI.

#### 632 4.4 Changes of stable oxygen isotopic composition in precipitation associated with late 633 Cenozoic changes in the West African Monsoon

634 In this section, we explore the simulated seasonal climatological anomalies of the  
 635 precipitation-weighted stable oxygen isotopic composition of precipitation ( $\delta^{18}\text{O}_p$ ) during the

636 WAM season. Even though  $\delta^{18}\text{O}_p$  values are closely linked to precipitation due to the "amount  
 637 effect", the simulated spatial patterns of precipitation and  $\delta^{18}\text{O}_p$  values are different. Overall, the  
 638 warmer climates (i.e., MH and MP) estimate a decrease in  $\delta^{18}\text{O}_p$  values across the WAM region  
 639 when compared to the PI patterns during the monsoon season. In contrast, the  $\delta^{18}\text{O}_p$  anomalies  
 640 increase across many parts of the WAM region in response to the colder conditions in the LGM.  
 641 The MH is characterised by a significant decrease of  $\delta^{18}\text{O}_p$  values by  $\sim 5\text{‰}$  between  $10\text{--}20^\circ\text{N}$ ,  
 642 which spatially coincides with the region of the rain belt. The decrease becomes less pronounced  
 643 ( $\sim 1\text{‰}$ ) towards the Sahara region, and shows small areas that experience a slight increase ( $\sim 1$   
 644  $\text{‰}$ ) towards the east. Moreover, the equatorial Atlantic region also experiences a slight  $\delta^{18}\text{O}_p$   
 645 decrease of about  $1\text{‰}$ . The  $\delta^{18}\text{O}_p$  anomalies during the MP also decrease across the continent,  
 646 but show an increase of up to  $-6\text{‰}$  across the Sahara. Furthermore, the decrease of  $\delta^{18}\text{O}_p$  values  
 647 across the Sahel is less significant than the increase in precipitation anomalies in the MP. On the  
 648 other hand, the LGM simulation indicates a significant increase in  $\delta^{18}\text{O}_p$  values of  $\sim 3\text{‰}$  across  
 649 the Atlantic Ocean and the adjacent coastal regions.



650

651 **Figure 8.** Simulated changes in  $\delta^{18}\text{O}_p$  in the WAM season (JJAS) for the (a) Mid-Holocene  
 652 (MH), (b) Last Glacial Maximum (LGM), and (c) Mid-Pliocene (MP). The pink colour range  
 653 represents heavy isotope depletion, and the green colour range represents an enrichment in the  
 654 heavy isotopes in relation to Pre-industrial (PI) values. The black dot stippling indicates regions  
 655 with a statistically significant difference, assuming a confidence interval of 95%, using a student  
 656 t-test analysis.

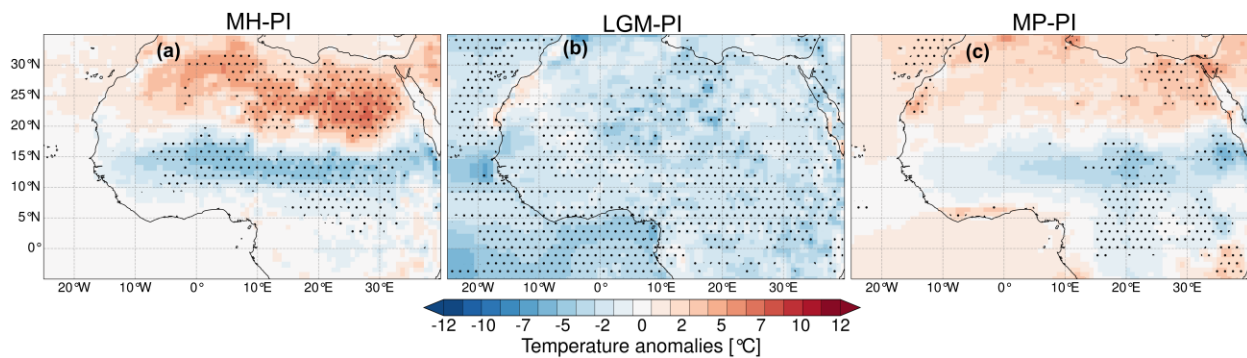
#### 657 4.5 Changes in the atmospheric dynamics behind the simulated WAM changes

658 Here, we analyse the atmospheric dynamics behind the simulated changes in the WAM.  
 659 Specifically, we use near-surface temperature, mean sea level pressure, wind patterns at different  
 660 atmospheric levels, and surface heat fluxes to investigate how these dynamics change in response  
 661 to different late Cenozoic boundary conditions. Due to our current understanding of WAM  
 662 dynamics (section 2.1), we focus on the spatial and intensification changes of the surface  
 663 temperature and pressure gradients, AEJ, TEJ, and the low-level south-westerly winds as the  
 664 dynamic feedback contributing to the simulated changes in the WAM. Additionally, we evaluate  
 665 the changes in the WAM due to land surface conditions (e.g., prescribed vegetation) in the  
 666 experiments through the responses of surface latent and sensible heat fluxes.

##### 667 4.5.1 Changes in near-surface temperature

668 The warmer climate experiments (i.e., MH and MP) produce a north-south near-surface  
 669 temperature gradient with an increase in the Sahara region, a decrease in the Sahel, and smaller

670 regions of increases (MP) or no (MH) changes at the southern coast (Fig. 9). Overall, the MH  
 671 indicates a pronounced meridional gradient with a significant increase in temperature anomaly of  
 672 up to 10 °C across the Sahara and a significant decrease of down to -8 °C towards the Guinea  
 673 coast. The MP anomalies indicate similar patterns, but with less pronounced gradients and  
 674 significant changes only toward Central and East Africa. More specifically, the MP shows an  
 675 increase of up to 5 °C across the Sahara and a decrease of about -3 °C across the Sahel,  
 676 transitioning into a slight increase of up to 2°C in the equatorial Atlantic. This spatial variability  
 677 is consistent with the precipitation patterns. Moreover, the mean sea level pressure patterns also  
 678 indicate the deepening of the low-pressure area across the Sahara in MH compared to the MP  
 679 (Fig. S6). However, comparing the cyclonic flow across the Sahara and the strengthened south-  
 680 westerlies moist transport from the equatorial Atlantic at 850 hPa between the MH and MP  
 681 reveals no noticeable changes (Fig. S6). Contrarily, the temperature anomalies in the LGM  
 682 indicate overall colder conditions across the continent with a significant decrease of up to -5 °C.



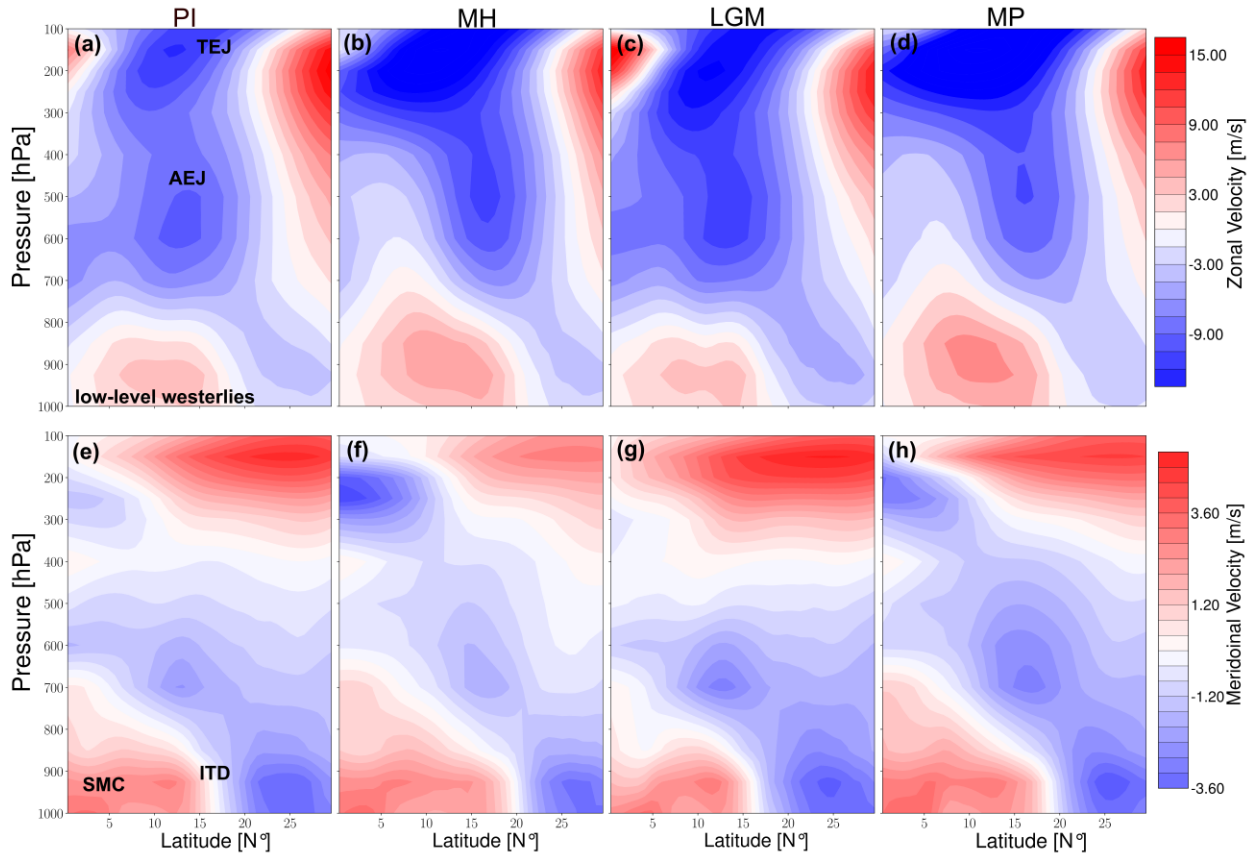
683

684 **Figure 9.** Simulated temperature anomalies of the WAM season (JJAS) estimated in response to  
 685 the (a) Mid-Holocene (MH), (b) Last Glacial Maximum (LGM), and (c) Mid-Pliocene (MP)  
 686 paleoenvironmental conditions using ECHAM5-wiso. The blue colour ranges represent colder  
 687 conditions, and the red colour ranges represent warmer conditions compared to the pre-industrial  
 688 estimates. The black dot stippling indicates regions with a statistically significant difference,  
 689 assuming a confidence interval of 95% using a student t-test analysis.

690

#### 4.5.2 Changes in the vertical structure of zonal and meridional wind speeds

691 We analysed the latitudinal-altitude cross-sections of zonal and meridional wind speeds  
 692 across the WAM region to understand the atmospheric circulation associated with the simulated  
 693 precipitation dynamics. The zonal wind patterns reveal a higher altitudinal reach of the low-level  
 694 southwesterlies and a greater northward propagation in the MH and MP when compared to the PI  
 695 and LGM (Fig. 10). The westerlies reach a latitudinal extent of 17°N and stay below 800 hPa  
 696 atmospheric level in the PI and LGM, while in the MH and MP, the flows extend over 20°N and  
 697 up to the 700 hPa level (Fig. 10 a-d). The MH and MP simulations estimate a higher northward  
 698 reach of the winds, but the latter predicts slightly higher wind shear at the core of the low-level  
 699 flow. Consistently, the AEJ is located between 10-15 °N at approximately 600 hPa in the PI and  
 700 LGM. However, the LGM indicates a more intense AEJ than the PI despite overall drier  
 701 conditions. In the MH and MP, the AEJ experiences a greater northward shift between 15-20 °N,  
 702 and its core shifts to a higher altitude than in the PI. In contrast to the LGM and PI, the AEJ in  
 703 the MH indicates higher intensification than the MP.



704

705 **Figure 10.** Latitudinal vertical cross-sectional for zonal (top panel) patterns, where positive  
 706 (negative) values indicate westerly (easterly) winds, and for meridional patterns (bottom panel),  
 707 where positive (negative) values indicate southerly (northerly) wind speeds estimated for the  
 708 WAM season (JJAS) in response to (a) Pre-industrial (PI), (b) Mid-Holocene (MH), (c) Last  
 709 Glacial Maximum (LGM), and (d) Mid-Pliocene (MP) paleoenvironmental conditions. The  
 710 approximate locations of the African Easterly Jet (AEJ), Tropical Easterly Jet (TEJ), Intertropical  
 711 Discontinuity (ITD), low-level westerlies and Shallow Meridional Cell (SMC) are shown in a  
 712 and e. The low-level westerlies reach the highest latitude and altitude in the MH. The  
 713 strengthened WAM conditions are more associated with the northward position of the Africa  
 714 Easterly Jet (AEJ) than its intensity.

715

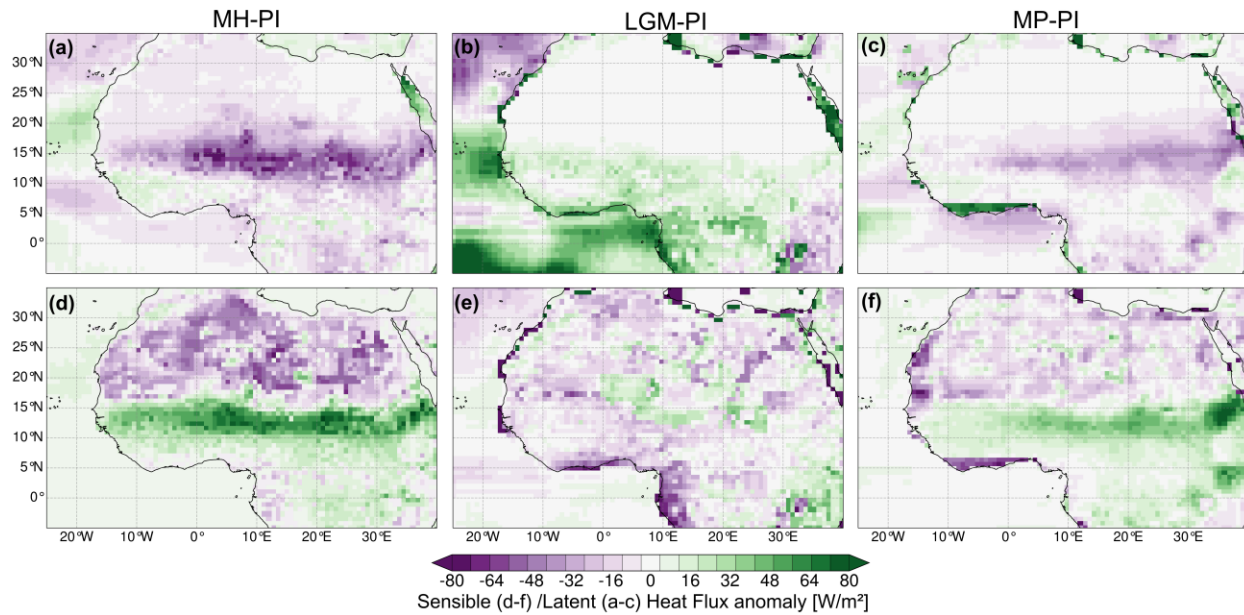
The latitudinal-altitude cross-section of winds also indicates higher vertical wind shear  
 716 (inferred from the transition from the low-level westerlies to the mid-level easterlies) in the MH  
 717 and MP compared to the PI. Stronger southwesterlies (and, therefore, a deeper monsoon depth)  
 718 are also identified in the MH and MP. The monsoon depth defines the altitudinal reach of  
 719 moisture transport from the equatorial Atlantic into the continent. In contrast, the LGM  
 720 experiment estimates a shallow monsoon depth compared to the PI. More specifically, the  
 721 monsoon depth reaches an altitude of 600 hPa in the MH and MP, and only up to 700 hPa in the  
 722 PI and LGM (Fig. 10 e-h). Moreover, the patterns in the MH and MP indicate a more northward  
 723 location of the ITD (i.e., the location where the moist southwesterlies deflect the dry  
 724 northeasterlies from the Sahara) at approximately 20 °N and 19 °N, respectively. For the PI and  
 725 LGM, the ITD is located further south (<17°N). The intensity of the low-level moisture  
 726 transport, TEJ, AEJ, and the location of the ITD coincide with the latitudinal band of negative

727 omega values (wind directions away from the ground; updraft) up to 200 hPa and the associated  
728 subsidence (positive omega values) across the Sahara (Fig. S7). Overall, the tropospheric  
729 structure of the winds reveals stronger southwesterlies moisture transport from the tropical  
730 Atlantic, a higher monsoon depth, the northward position of the AEJ, and the intensification of  
731 the TEJ, consistent with the increased intensity of the WAM and its northward migration in the  
732 MH and MP.

#### 733 4.5.3 Changes in sensible and latent heat fluxes

734 Generally, high vegetation cover yields more water availability through  
735 evapotranspiration, which increases latent heat (LH) flux. Moreover, moisture availability due to  
736 the increased LH flux leads to a rainfall-induced cooling effect, reducing sensible heat (SH) flux  
737 into the atmosphere. Specifically, for the WAM region, the recycling of water vapour through  
738 evaporative fluxes also contributes to the northward extent of precipitation. Therefore, the  
739 response of the WAM to different surface conditions is described here through the analysis of  
740 SH and LH fluxes.

741 The paleoclimate experiments indicate varied responses to the surface heat fluxes (Fig.  
742 11). In the MH experiment, the results indicate pronounced negative LH anomalies (i.e., upward  
743 flux) of up to  $-80 \text{ Wm}^{-2}$  across the Sahel, gradually reducing in magnitude towards the Sahara  
744 (Fig. 11a). Regions with more upward LH fluxes coincide with regions of a significant increase  
745 in precipitation the MH. The LGM reveals overall positive (downward) LH flux anomalies  
746 across the Sahel and coastal regions, with no changes towards the Sahara due to colder and drier  
747 conditions (Fig. 11b). In the MP, the estimated patterns reveal a slight increase in upward fluxes  
748 with negative LH anomalies down to  $-30 \text{ Wm}^{-2}$  across the Sahel, and no changes in the Sahara  
749 (Fig. 11c). Such simulated patterns of releasing LH are consistent with higher enhanced  
750 evaporation over vegetated surfaces through radiative forcing (Fig. S8) in the MH. The SH flux  
751 anomalies also show consistent results with more downward fluxes and colder surface conditions  
752 associated with increased precipitation. The MH experiment estimates negative SH anomalies  
753 down to  $-60 \text{ Wm}^{-2}$  across the Sahara, reaching  $15^\circ\text{N}$  and positive SH anomalies across the Sahel  
754 towards the coastal regions (Fig. 11d). The zonal band of the downward SH anomalies is also  
755 consistent with the simulated rain belt in both the MH and MP. The MP experiment estimates a  
756 similar, albeit less pronounced, north-south gradient of SH. The LGM experiment estimates  
757 negative SH anomalies across most regions on the continent, which is consistent with less  
758 availability of water to evaporate. The simulated SH flux patterns are consistent with the near-  
759 surface temperature anomalies, with a more pronounced meridional gradient in the MH relative  
760 to the MP.



761

762 **Figure 11.** Latent (top panel) and Sensible (bottom panel) heat flux anomalies during the WAM  
 763 months (JJAS) for the (a) Mid-Holocene (MH), (b) Last Glacial Maximum (LGM), and (c) Mid-  
 764 Pliocene (MP). The purple ranges represent net upward fluxes, and the green colour ranges  
 765 represent downward fluxes.

766

## 767 5 Discussion

### 768 5.1 Simulated changes of the WAM in response to the large-scale forcings

#### 769 *Mid-Holocene (~6ka)*

770 Overall, the analysed climate model outputs consistently indicate the intensification and  
 771 expansion of the WAM during the MH, specifically during the boreal summer. These simulated  
 772 patterns align with findings from previous modelling studies (e.g., Bosmans et al., 2012; Gaetani  
 773 et al., 2017; Patricola & Cook, 2007; Zhao & Harrison, 2012) and proxy reconstructions (e.g.,  
 774 Bartlein et al., 2011). The increase in precipitation during the WAM season is not surprising,  
 775 given that the orbital configurations of the MH lead to stronger insolation during the boreal  
 776 summer and autumn, and to weaker insolation during the winter when compared to PI forcings  
 777 (Joussaume et al., 1999; Kutzbach & Liu, 1997). These orbital precision variations with stronger  
 778 seasonal thermal amplitudes also result in more pronounced equator-to-pole and land-sea thermal  
 779 gradients, contributing to moisture redistribution across the continents (Brierley et al., 2020).  
 780 Specifically, the stronger thermal gradients and associated continental warming during the WAM  
 781 season (JJAS) deepen the low-pressure cells over the Sahara. This intensifies the advection of  
 782 moist air masses from the equatorial Atlantic Ocean, thereby amplifying and expanding the  
 783 WAM. Moreover, the redistribution of moisture associated with the seasonal insolation  
 784 distribution can be observed as a weakening of the annual-scale range of precipitation over the  
 785 ocean and a strengthening over the continent, as suggested in previous studies (e.g., Braconnot et  
 786 al., 2004). The MH precipitation anomalies in the inter-annual scale are less pronounced than the  
 787 seasonal changes. These changes reflect that the seasonal variations in insolation primarily drive

788 the MH global climate changes (Kageyama et al., 2013). The ECHAM5-wiso model estimates  
789 global warming of approximately  $\sim 0.3$  °C compared to the PI control run (Fig. S9 in the  
790 supplemental material). The bidirectional precipitation anomalies, with drier conditions toward  
791 the coastal regions, are also consistent with the rainfall dipole patterns of the African Humid  
792 Period (AHP). This phenomenon is explained by the northward shift of the ITCZ during the  
793 boreal summer in response to the insolation in the Northern Hemisphere (Braconnot et al., 2007;  
794 Coe & Harrison, 2002; deMenocal et al., 2000).

795 Compared to the model outputs from the PMIP4-CMIP6 experiments, ECHAM5-wiso  
796 predicts the highest intensification and greatest northward reach of the WAM. The precipitation  
797 anomalies estimated with ECHAM5-wiso indicate a maximum rain belt of approximately 150  
798 mm/month across the Sahel (10-20 °N) and less rainfall reaching 30 °N. Out of all considered  
799 models, ECHAM5-wiso estimates predict the highest regional precipitation means ( $\sim 95$   
800 mm/month), followed by the MPI-ESM-LR, which has a similar atmospheric model component  
801 (i.e., ECHAM6). This also further validates the ability of models in the ECHAM family to  
802 reproduce the atmospheric dynamics and hydrological cycle across the African continent. The  
803 relatively high precipitation rates predicted by our ECHAM5-wiso simulations might be partly  
804 due to the following:

805 (1) The representation of MH vegetation feedbacks. The experimental design for the  
806 PMIP4-CMIP6 MH simulation keeps vegetation from the PI, using prescribed surface conditions  
807 or dynamic vegetation models. However, previous studies have suggested a “Green Sahara”,  
808 characterised by steppe, savanna, and shrub vegetation, and fewer deserts than today (Dallmeyer  
809 et al., 2020; Hoelzmann et al., 1998; Jolly et al., 1998). Such vegetation is required to sustain the  
810 enhancement and northward extent of the WAM during the MH. The simulation with ECHAM5-  
811 wiso used MH vegetation patterns provided by the BIOME6000 vegetation reconstructions  
812 (Bigelow et al., 2003; Harrison et al., 2001; Pickett et al., 2004; Prentice et al., 2000), where the  
813 Sahara desert was drastically reduced, and the Sahelian vegetation belt, consisting of steppe,  
814 tropical dry forest, and xerophytic woods/shrubs, was extended northward (Jolly et al., 1998;  
815 Prentice et al., 2000). Through positive feedback, vegetation has been suggested to increase  
816 orbitally driven precipitation across North Africa due to the warming effect caused by reduced  
817 albedo (Bonfils et al., 2001) and increased evapotranspiration as a result of increased latent heat  
818 fluxes (Levis et al., 2004; Texier et al., 2000). Overall, moisture recycling through  
819 evapotranspiration and induced surface warming increases convection and inland moisture flux  
820 and intensifies the WAM. However, previous studies have also indicated a plausible negative  
821 vegetation feedback on precipitation at the annual scale due to a larger contribution of soil  
822 evaporation than the albedo feedback under wetter conditions (Notaro et al., 2008; Y. Wang et  
823 al., 2008).

824 (2) The lower values of greenhouse gas (GHG) concentrations used for the PMIP4-  
825 CMIP6 MH experiments. Lower  $p\text{CO}_2$  would result in a slightly colder climate than that  
826 produced by the ECHAM5-wiso simulation. This has been shown for the PMIP3-CMIP5 MH  
827 experiments that used GHG concentrations that are similar to those used for our ECHAM5-wiso  
828 experiment. The differences between PMIP4-CMIP6 and PMIP3-CMIP5 were due to the  
829 simulated difference in effective radiative forcing of  $-0.3 \text{ Wm}^{-2}$  (Otto-Bliesner et al., 2017).  
830 Generally, the slightly colder climate would reduce the temperature meridional gradient across  
831 the African continent that drives low-level south-westerly moist air masses from the equatorial  
832 Atlantic Ocean.

833 (3) The use of the high spatial resolution for the ECHAM5-wiso simulation. Several  
834 studies have demonstrated that monsoons are better resolved when resolution is increased, even  
835 though the magnitude changes are more susceptible to the model's parameterisation (e.g., Gao et  
836 al., 2006; Sperber et al., 1994). The higher spatial resolution consequently reproduces the MH  
837 patterns through improved representation of important processes, such as large-scale  
838 condensation, land-sea interaction, and topographic forcings (Boyle & Klein, 2010). Bosmans et  
839 al. (2012) showed that using a high-resolution (T159) for EC-Earth GCM resulted in an  
840 increased intensity and a greater northward reach of the WAM in the MH when compared to the  
841 low-resolution PMIP2 ocean-atmosphere coupled models. The inter-model variabilities can also  
842 be attributed to the differences in complexities and the models' sensitivity to the parameterisation  
843 of clouds, atmospheric dynamics, and the hydrological cycle in general. We highlight that  
844 determining the influence of resolution and model parameterisation is beyond the scope of this  
845 manuscript. Overall, all the models estimate similar latitudinal precipitation patterns across the  
846 WAM region, but the predicted northward reach and regional precipitation amounts are too low  
847 to sustain the plant types that existed during the MH (Braconnot et al., 2007; Jousaume et al.,  
848 1999).

#### 849 *Last Glacial Maximum (~21 ka)*

850 Generally, the global climate during the LGM was characterised by large-scale cooling  
851 due to radiative perturbations linked to the extensive continental ice sheets and lower  
852 atmospheric greenhouse gas (GHG) concentrations (Clark et al., 2009). These large-scale drivers  
853 were further modified by internal feedbacks in the climate system involving factors like sea ice,  
854 snow, and water vapour (e.g., Braconnot et al., 2007). ECHAM5-wiso simulates realistic patterns  
855 of temperature anomalies, indicating maximum cooling of approximately -15 °C across regions  
856 with ice sheets in the Northern Hemisphere, and moderate cooling (-2 to -5 °C) over tropical  
857 areas (Fig. S9). These patterns are similar to the results of PMIP4-CMIP6 experiments and align  
858 with findings from previous modelling studies (e.g., Cao et al., 2019; Kageyama et al., 2021).  
859 The large perturbations in the atmospheric radiative balance due to albedo feedbacks also result  
860 in significant changes in atmospheric circulation patterns, contributing to comprehensive  
861 changes in precipitation patterns (e.g., Liakka et al., 2016; Liakka & Lofverstrom, 2018). Large  
862 ice sheets covering North America and Fennoscandia redirect low-level winds, which strongly  
863 influences moisture transport and regional precipitation. Additionally, the associated  
864 thermodynamics, as indicated through specific humidity, can contribute to regional precipitation  
865 changes (D'Agostino et al., 2019, 2020). Most of the precipitation on land was substantially  
866 decreased due to the large-scale cooling and its associated reduction in evapotranspiration (e.g.,  
867 Braconnot et al., 2007). The lower SSTs led to reduced evaporation over the oceans, which in  
868 turn reduced the surface's moisture flux into the atmosphere. This eventually led to a decreased  
869 inland moisture flux, leading to overall large-scale drying. Apart from surface cooling,  
870 tropospheric cooling also decreased the amount of atmospheric water vapour by limiting its  
871 water-holding capacity through the Clausius-Clapeyron relation. However, in both hemispheres,  
872 other regions across the mid-latitudes experienced an increase in precipitation, mainly in areas  
873 corresponding to the positions of the North Pacific, North Atlantic, and Southern Ocean storm  
874 tracks (Fig. S9). The simulated temperature patterns indicate overall cooling across the African  
875 continent, suggesting that the meridional temperature and pressure gradient that drives northward  
876 moisture flux from the Atlantic Ocean are suppressed, thereby reducing moisture availability  
877 across the WAM areas. Furthermore, the surface cooling over the oceans was more intense than

878 over land, indicating a decrease in the land-sea thermal contrast, which would result in an  
879 additional reduction in inland moisture transport.

880 *Mid-Pliocene (~3 Ma)*

881 Simulating the MP climate provides the opportunity to evaluate the long-term response of  
882 the climate system to currently raised atmospheric GHG concentrations. This period is often  
883 considered an analogue for future climate change (Burke et al., 2018) due to its similarities to  
884 modern palaeogeography and high  $p\text{CO}_2$  (400 ppm). As such, the modelling framework of the  
885 MP helps assess how important climatic components of the Earth system, such as the El Niño-  
886 Southern Oscillation, the global hydrological cycle and monsoon systems, respond to the  
887 ongoing rise in  $\text{CO}_2$  concentrations. The simulated temperature patterns predict a global mean  
888 near-surface temperature increase of approximately 3 °C, primarily due to direct  $\text{CO}_2$  forcing.  
889 The overall warming exhibits polar amplification, with temperature anomalies increasing by  
890 more than 10 °C due to associated changes in albedo at higher latitudes (Chandan & Peltier,  
891 2020; de Nooijer et al., 2020; Samakinwa et al., 2020; Tindall et al., 2022). The simulated global  
892 mean temperature increase predicted by ECHAM5-wiso falls within the range of model  
893 estimates (1.4 to 4.6 °C) from the PlioMIP phase 1 and 2 experiments (Haywood et al., 2013,  
894 2020). The significant warming in high latitudes reduces the meridional temperature gradient,  
895 weakening the tropical atmospheric circulation, specifically the Hadley circulation (Corvec &  
896 Fletcher, 2017; Haywood et al., 2013). Previous studies also indicated a poleward shift of mid-  
897 latitude westerly winds (Li et al., 2015), increased intensity of tropical cyclones (Yan et al.,  
898 2016), and strengthening and poleward extension of the global land monsoon system (Li et al.,  
899 2018). The enhanced hydrological cycle intensifies the East Asian and West African summer  
900 monsoons (R. Zhang et al., 2013, 2016). These changes resemble future climate projections (e.g.,  
901 Erfanian et al., 2016; Seth et al., 2019) and require detailed understanding from a modelling  
902 perspective.

903 Through sensitivity experiments, (Stepanek et al. (2020) determined that MP  
904 palaeogeography contributes to increased rainfall across the WAM areas. The closure of the  
905 Arctic gateway and enhanced topography have also been suggested to strengthen the Atlantic  
906 Meridional Overturning Circulation (AMOC), thereby warming the North Atlantic Ocean (Z.  
907 Zhang et al., 2021), which impacts the WAM (Mulitza et al., 2008). These findings highlight the  
908 importance of other boundary conditions in regulating the WAM. As mentioned earlier, land  
909 surface conditions, such as vegetation, contribute to the variability and spatial extent of the  
910 WAM through evaporative fluxes. Proxy reconstructions from previous studies suggest more  
911 humid conditions across northern Africa, which facilitates an expansion of vegetation. More  
912 specifically, palynological records suggest high tree cover density and broadening of woodlands  
913 and savannas at the expense of deserts across the Sahara (Bonnefille, 2010; Salzmann et al.,  
914 2008). ECHAM5-wiso was set up with converted PRISM3 vegetation reconstructions, which  
915 indicate the expansion of grass and forests across North Africa towards the Mediterranean (Fig.  
916 S10). Such patterns are also consistent with the COSMOS dynamic vegetation results presented  
917 in Stepanek et al. (2020), which estimated an increase in precipitation by 70 mm/month across  
918 the WAM region. The PlioMIP2 models with prescribed MP vegetation also indicate a  
919 strengthened WAM, with an ensemble mean of precipitation showing an increase by ~76 (60 -  
920 120) mm/month (Berntell et al., 2021). The previous modelling inter-comparison project (i.e.,  
921 PlioMIP1) estimates a lower magnitude of increase within a range of 30 to 60 mm/month (R.  
922 Zhang et al., 2016). The PlioMIP1 experimental protocol (Haywood et al., 2010) was similar to

923 the model setup used for the ECHAM5-wiso simulation. These findings suggest that ECHAM5-  
924 wiso simulates a higher magnitude of WAM precipitation in the MP than the PlioMIP1 models.  
925 This may be due to the higher spatial resolution used for ECHAM5-wiso, which improves  
926 representation of land surface conditions (e.g., orography and vegetation) and model  
927 parameterisation. Overall, PlioMIP1 and PlioMIP2 models suggest that the updated MP  
928 boundary conditions from PRISM3 to PRISM4 contribute to the strengthening of the WAM.  
929 Samakinwa et al. (2020) confirm this with a sensitivity experiment using COSMOS, which  
930 indicated that the updated palaeogeography was the main reason for the changes in the large-  
931 scale features between PlioMIP1 and PlioMIP2.

932 The precipitation simulated with ECHAM5-wiso shows an increase of up to 120  
933 mm/month and an intensification towards the east (Fig. 3). However, regional means of  
934 precipitation across the Sahel increase by only ~50 mm/month, which falls within the broader  
935 range of PMIP4-CMIP6 estimates (10-160 mm/month) (Fig. 4). The CESM2 and EC-Earth3-LR  
936 models estimate significant increases of 90 and 160 mm/month, respectively. The HadGEM3-  
937 GC31-LL, IPSL-CM6A-LR, and NorESM1-F estimate a moderate increase of ~50 mm/month,  
938 with GISS-E2-G estimating the lowest increase of only ~10 mm/month. The magnitude of the  
939 precipitation response simulated by the individual models across the WAM is consistent with the  
940 global response. For instance, GISS-E2-1-G indicates a low global response to the MP boundary  
941 conditions and consistently estimates the lowest WAM precipitation anomalies. On the contrary,  
942 models with large land-sea rainfall anomalies (e.g., EC-Earth3-LR and CESM2) also simulate a  
943 strengthened WAM. Even though the updated boundary conditions contributed to the inter-  
944 model variabilities, Haywood et al. (2020) suggested model parameterisation and initial  
945 conditions as the main factors for the varied predictions. Moreover, later model versions tend to  
946 have a higher sensitivity than earlier versions when used with the same boundary and initial  
947 conditions. These findings suggest that using ECHAM6-wiso (Cauquoin et al., 2019) and even  
948 updated PRISM4 reconstructions (Dowsett et al., 2016; Haywood et al., 2016) would increase  
949 the strengthening of the WAM in the model.

## 950 5.2 Control of the precipitation and temperature on stable oxygen isotope in the WAM 951 season in response to the different past climates

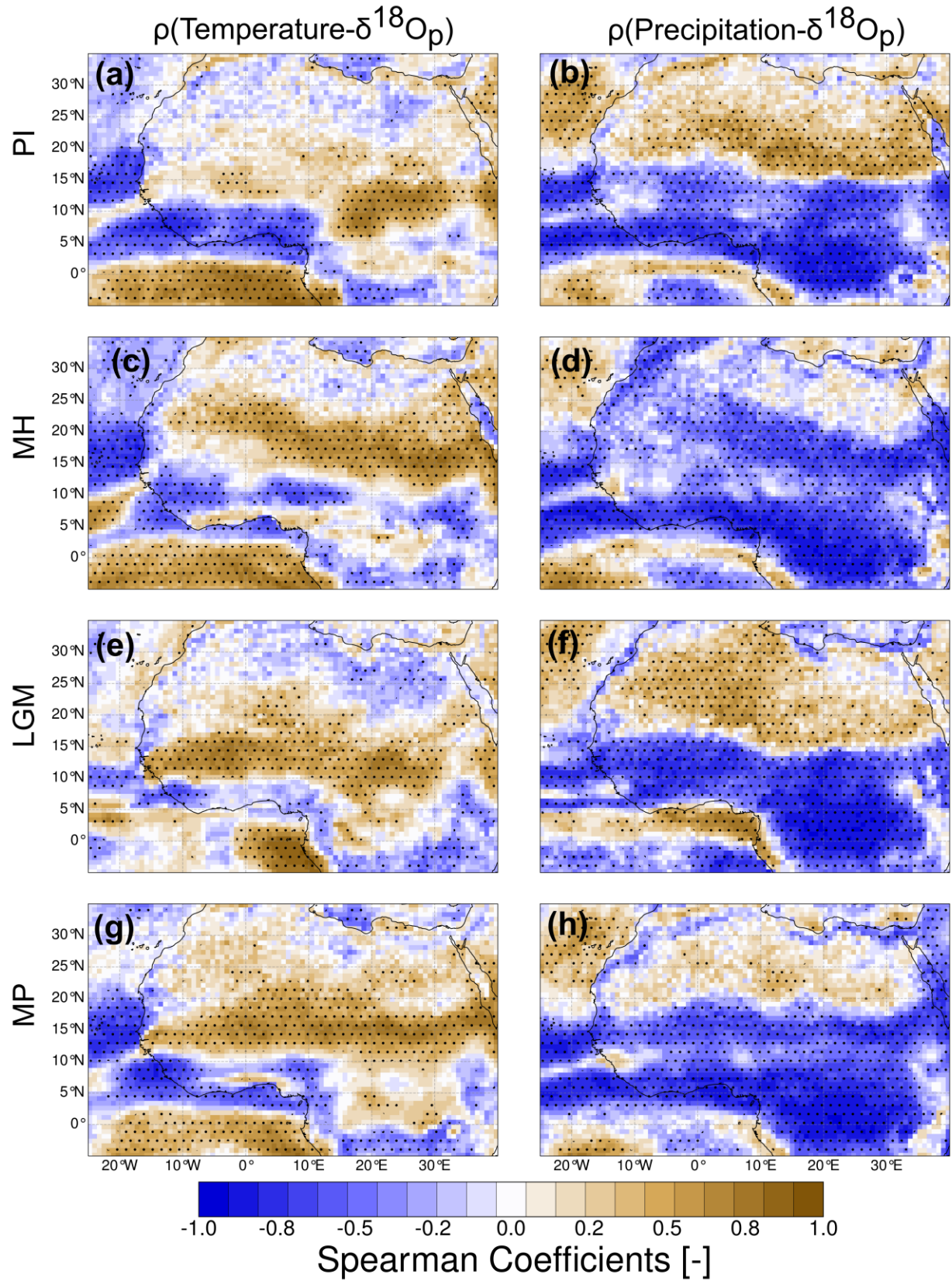
952 The stable oxygen isotopic composition of tropical precipitation provides information  
953 about the hydrological cycle and can be used to reconstruct past tropical climates. Several studies  
954 have employed stable isotopes to understand the intraseasonal water cycle variability in western  
955 Africa (e.g., Risi et al., 2008, 2010). These studies have revealed that the integrated convective  
956 activity in the monsoon season is spatially and temporally reflected in the  $\delta^{18}\text{O}$  values in  
957 precipitation and vapour records. On a broader scale, previous studies have used isotopic patterns  
958 to identify the strengthening of the Northern Hemisphere monsoon in response to warmer  
959 climates, both through modelling (e.g., Cauquoin et al., 2019; Shi et al., 2023; Thompson et al.,  
960 2021) and proxy records (Wang et al., 2008; Bartlein et al., 2011). Simulating the isotopic  
961 composition allows for a direct comparison of model simulations to isotopic archives and  
962 contributes to the understanding of the causal mechanisms behind various proxy archives (Bühler  
963 et al., 2022; Phipps et al., 2013; Risi et al., 2012; Werner et al., 2000). Here, we explore the  
964 response of simulated  $\delta^{18}\text{O}_p$  to varied paleoenvironmental conditions during the WAM season.  
965 The results suggest that meteoric water was more negative in past warmer climates and less  
966 negative in colder climates. Similar patterns have been reported in previous isotope-enabled  
967 GCM modelling studies (e.g., Risi et al., 2010; Cauquoin et al., 2019). Specifically, the oxygen

968 isotopes are most depleted during the MH, indicating the role of seasonal insolation distribution  
969 and associated precipitation dynamics in the isotopic patterns (Thompson et al., 2021).  
970 Importantly, the magnitude and spatial patterns, to some extent, are inconsistent with the  
971 simulated precipitation anomalies despite the expected dependence of the isotopic composition  
972 on convective activity, as suggested in previous studies (e.g., Bony et al., 2008; Lawrence et al.,  
973 2004). These changes reveal the plausibility of additional factors controlling  $\delta^{18}\text{O}_p$  in different  
974 climates. Therefore, we further explore the relative influence of precipitation and temperature on  
975 the simulated  $\delta^{18}\text{O}_p$  patterns to better understand what controls the oxygen isotopes during the  
976 monsoon season.

977 We evaluate the control of precipitation and temperature on  $\delta^{18}\text{O}_p$  values in different time  
978 periods by calculating their linear relationship during the WAM season using Spearman  
979 correlation analysis. The PI simulation yields north-south bidirectional correlation patterns  
980 between precipitation and  $\delta^{18}\text{O}_p$  values, with significant negative correlations ( $\geq -0.8$ ) over the  
981 Guinea Coast up to the Sahel (0-15 °N) and positive correlations ( $\geq 0.7$ ) across the Sahara (Fig.  
982 12). The strong negative relationship along the coastal region towards the Sahel indicates the  
983 amount effect, as is expected based on previous studies (Lawrence et al., 2004; Rozanski et al.,  
984 1993). Convective activity has been well established as the main factor driving the spatial and  
985 temporal patterns of the isotopic composition of precipitation and vapour (Lawrence et al., 2004;  
986 Risi et al., 2008; Bony et al., 2008). The reasons why an increase in precipitation amount results  
987 in the depletion of the heavy oxygen isotope across the WAM might be partially due to the fact  
988 that (1) the increase in rainfall amount moistens the atmosphere, which reduces rainfall re-  
989 evaporation and diffusive fluxes, and ultimately results in lower  $\delta^{18}\text{O}_p$  values in raindrops; (2)  
990 intense convective activity increases vertical mixing in the form of unsaturated downdrafts, so  
991 that the associated depletion of low-level vapour feeds into subsequent convective systems with  
992 lower  $\delta^{18}\text{O}_p$  values (Lawrence et al., 2004; Risi et al., 2008). The change in correlation direction  
993 over the Sahara indicates that the "amount effect" is limited across the Sahel region, where the  
994 maximum rain belt is situated during the monsoon season. These changes are unsurprising, as the  
995 rainout of the moisture transported from the equatorial Atlantic Ocean would deplete the  
996 remaining air masses of heavy oxygen isotopes. However, during the retreat of the WAM,  
997 evaporative recycling provides a moist air mass with relatively enriched heavy oxygen isotopes  
998 that condense to rainfall. These changes suggest the influence of continental recycling on the  
999 isotopic patterns across the Sahel. Surface evaporative fluxes through continental recycling result  
1000 in air masses that are less negative than oceanic fluxes (Risi et al., 2013). Moreover, the warmer  
1001 and drier conditions across the Sahara would contribute to more re-evaporation of falling vapour,  
1002 leading to an enrichment in the heavier isotope in relation to the source (Risi et al., 2008). The  
1003 LGM and MP simulations indicate similar correlation dipole patterns across the WAM, but the  
1004 positive relationship across the Sahara in the MP is less significant (Fig. 12). Nevertheless, the  
1005 correlation patterns in the MH indicate an overall negative link across the whole WAM region,  
1006 suggesting that the amount effect predominantly controls the oxygen isotopic patterns. The  
1007 changes in the correlation structure across different past climates suggest the non-stationarity of  
1008 the controlling mechanism across the WAM areas.

1009 The correlation analyses for  $\delta^{18}\text{O}_p$  and temperature yield fewer regions with significant  
1010 correlation due to the predominant influence of precipitation amount on  $\delta^{18}\text{O}_p$  during the WAM  
1011 season. The analysis indicates positive correlation patterns over the Sahara, which extends  
1012 further northward in the MP. The expanded area of positive correlation in the MP highlights the  
1013 importance of continental recycling during the retreat of the WAM. These patterns also validate

1014 the wider spread of precipitation during the retreat months in the MP (Fig. 6 d), which has also  
1015 been suggested in previous studies (Berntell et al., 2021). Although this analysis is limited to  
1016 empirical evidence that does not consider causal mechanisms, the results clearly indicate that  
1017 proxy reconstructions must efficiently understand the regional climatic influence on various  
1018 proxy records. This would help resolve the inaccuracies in paleoclimate and paleoenvironment  
1019 reconstructions that assume the stationarity of the calibrated transfer function (e.g., Kolstad &  
1020 Screen, 2019; Raible et al., 2014). The comparison of the simulated isotopic values to proxy  
1021 records and the investigation of the causal mechanisms leading to the available proxy records is  
1022 beyond the scope of this study.



1024 **Figure 12.** Spearman correlation coefficients for the relationship between the simulated monthly  
 1025  $\delta^{18}\text{O}_p$  and precipitation amount (right panel) and temperature (left panel) during the WAM  
 1026 months (JJAS). The dot stippling represents the regions with significant correlation coefficients  
 1027 with a 95% confidence interval. The correlations' magnitude and spatial patterns are not  
 1028 stationary in response to the different climates. For example, the bi-directional north-south  
 1029  $\delta^{18}\text{O}_p$ -precipitation relation transitions to an overall negative relationship in the Mid-Holocene  
 1030 (MH).

### 1031 5.3 Atmospheric dynamics driving the simulated WAM changes

1032 Overall, the response of the WAM to GHG forcing, vegetation changes, and orbital  
 1033 forcing is mostly associated with the changing meridional temperature gradient. A more  
 1034 pronounced gradient drives the increased intensity and higher altitude reach of the low-level  
 1035 southwesterlies and a more northward position of the ITD and AEJ. On the other hand, the  
 1036 weakening of the WAM in response to colder conditions can be attributed to the weak or non-  
 1037 existent meridional temperature and pressure gradient. This less pronounced gradient would lead  
 1038 to moisture transport into the continent and into the troposphere to suppress the wind shear of the  
 1039 AEJ. We discuss these simulated dynamics in the context of what has been suggested in previous  
 1040 studies, while also highlighting the new findings.

1041 The pronounced summer meridional temperature and pressure patterns in the MH and  
 1042 MP climates are consistent with the PMIP4 model results (e.g., Bertell et al., 2021; Brierley et  
 1043 al., 2020; Kageyama et al., 2021). These temperature anomalies reflect the patterns of increased  
 1044 precipitation, namely wetter conditions across the Sahel to coastal regions in the MH and MP.  
 1045 The warming over the high latitudes deepened the Sahara Heat Low, inducing low-level moisture  
 1046 convergence and strengthening the south-westerly flow that transports moisture from the  
 1047 equatorial Atlantic into the continent (Lavaysse et al., 2009). In the MH, the warming across the  
 1048 Sahara and the cooling over the Sahel are more intense than in the MP. The increased insolation  
 1049 across the Northern Hemisphere was the main driver of the intense warming across the Sahara.  
 1050 On the other hand, the cooling over the Sahel is partly due to the cloudiness associated with  
 1051 increased precipitation due to enhanced moisture flux into the Sahel areas. Another factor may  
 1052 be the increased evaporative fraction (Fig. S8) and upward latent heat flux (Fig. 11), which  
 1053 moisten the soil and reduce the energy available to heat the near-surface air through sensible heat  
 1054 flux. These mechanisms (a) cool the surface where precipitation increases and (b) further  
 1055 strengthen the north-south gradient to drive moisture advection into the WAM region. This  
 1056 feedback indicates that moisture advection strengthens the WAM more than local recycling does  
 1057 (Marzin & Braconnot, 2009; Y. Zhao et al., 2005). However, the internal feedback reinforces the  
 1058 pressure gradient and determines the northward migration of the WAM through evaporative  
 1059 recycling. In the MP, the seasonal precipitation distribution indicates a delayed WAM retreat  
 1060 with more precipitation during the southward retreat months than in the MH. Such precipitation  
 1061 seasonality highlights the role of internal feedback since the evaporative recycling supplies more  
 1062 moisture during the retreat months. Furthermore, cooling across the Sahel in the MP is more  
 1063 significant toward the east. These patterns coincide with the relative increase in upward latent  
 1064 heat flux toward the east, suggesting more moisture availability through local feedback to  
 1065 strengthen the cooling (Fig. 11). Even though the MP has higher atmospheric  $\text{CO}_2$  with an  
 1066 enhanced hydrological cycle, this study reveals that the orbital forcing and expanded vegetation  
 1067 in the MH produces the highest intensity of the WAM. These imply that GCMs must adequately  
 1068 represent these features to ensure accurate projections of the WAM in response to future climate

1069 change. In the LGM climate, the overall cooling and drying conditions prevent the initiation of a  
1070 meridional pressure gradient to drive moisture into the continent. This resulted in continuous  
1071 wind patterns from the Tropical Atlantic into the North Atlantic Ocean without diverging into the  
1072 continent, as suggested in previous studies (e.g., Jiang et al., 2015; Kageyama et al., 2021; Otto-  
1073 Bliesner et al., 2006). Overall, the strengthening of the meridional temperature and pressure  
1074 gradient determines the intensity of the southwesterlies, northward migration of the WAM, and  
1075 its altitudinal reach, which affects the location of the ITD and AEJ.

1076 The simulated intensity and location of the AEJ and its relationship to the strengthening  
1077 of the WAM suggest a complex causal mechanism. More specifically, the simulated core of the  
1078 AEJ is situated at higher latitudes (15-20°N) and altitudes (600-500 hPa) in summer during the  
1079 MH and MP than in the PI and LGM. These patterns are not surprising since the strengthened  
1080 WAM in these climates is associated with a more northward position of the ITD and deeper  
1081 monsoon depth (Janicot et al., 2011; Nicholson, 2009). Moreover, the surface temperature  
1082 gradient maintains the AEJ, along with two meridional circulations forced by the dry convection  
1083 of the Sahara Heat Low to the north and the moist convection driven by the ITCZ to the south  
1084 (Thorncroft & Blackburn, 1999; Wu et al., 2009). Usually, the monsoonal flow of the low-level  
1085 southwesterlies reaches far into the mid-troposphere to weaken the shear of the AEJ and shift it  
1086 to higher latitudes (Texier et al. 2000; Patricola and Cook 2007). However, the simulated intense  
1087 monsoonal flow due to the pronounced meridional temperature gradient in the MH induces high  
1088 AEJ intensity when compared to the MP. On the other hand, the reduced monsoonal flow  
1089 simulated in the LGM also results in an AEJ intensity that is higher than PI. These causal  
1090 relationship patterns indicate that the weakening of the AEJ is not entirely associated with the  
1091 strengthening of the WAM, especially when orbital forcings mainly control large-scale climatic  
1092 features. Therefore, the atmospheric dynamics response simulated in this study confirms that the  
1093 position of the AEJ is more important in strengthening the WAM than its intensity, as suggested  
1094 in previous studies (Jenkins et al., 2005; Nicholson, 2008; Nicholson & Grist, 2001; Nicholson &  
1095 Webster, 2007). These suggest that the intensity of the AEJ is an effect rather than a cause  
1096 (Newell & Kidson, 1984). The complexity of the causal relationship between AEJ and Sahel  
1097 rainfall and its varied feedback, as reported by some studies, might be due to its sensitivity to  
1098 localised conditions, which is represented differently in GCMs. For instance, Texier et al. 2000  
1099 and Patricola and Cook 2007 reveal that the decrease or even disappearance of the AEJ is  
1100 achieved when the GCM is coupled to a dynamic vegetation model. Contrarily, Texier et al.  
1101 2000 produced an increased AEJ located further north without dynamic vegetation feedback in  
1102 the model.

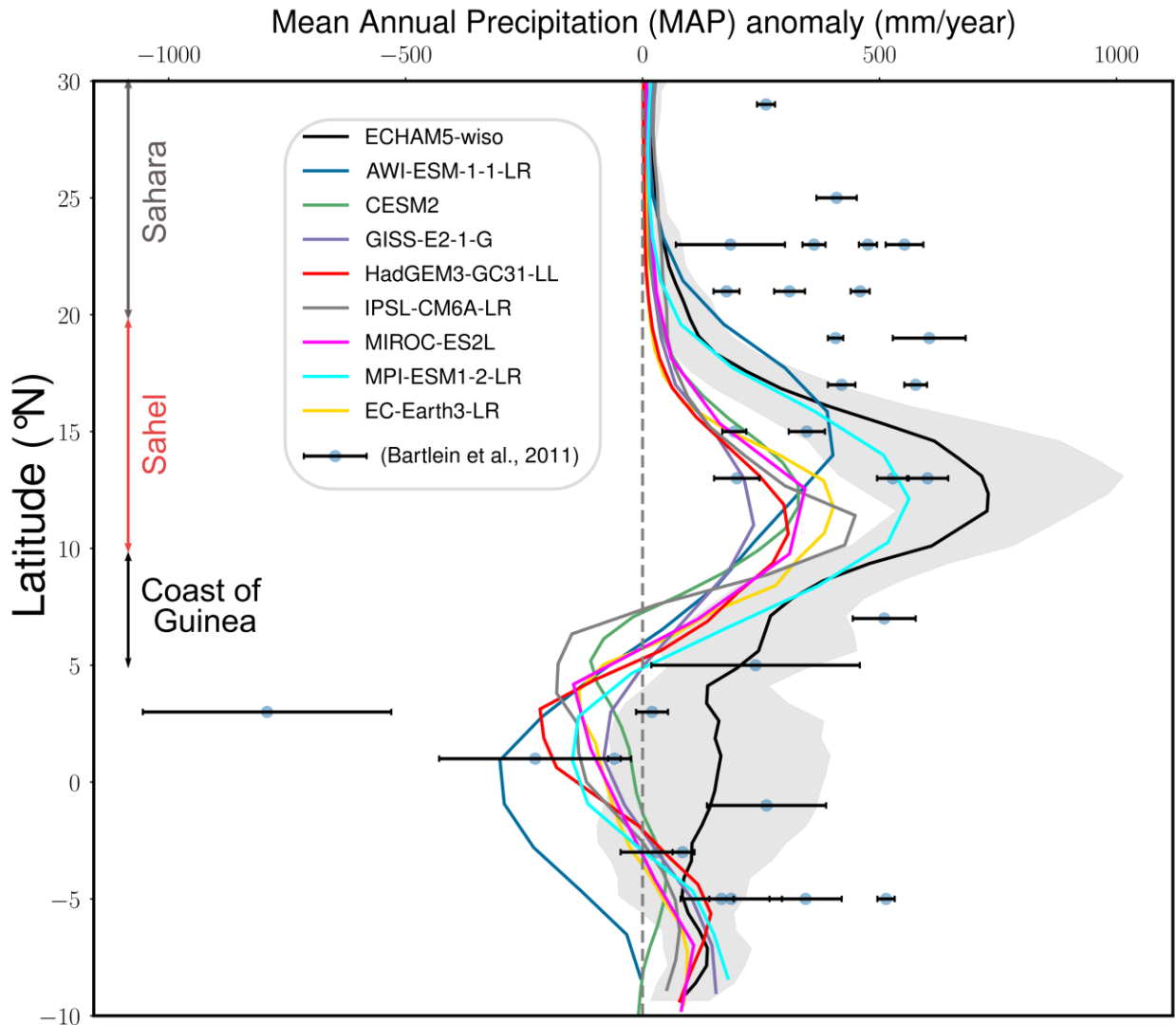
1103 The simulated TEJ intensity shows consistent patterns of increasing shear due to wetter  
1104 conditions, as indicated by previous studies (e.g., Nicholson and Klotter 2021). The simulated  
1105 intensity in the MH and MP revealed no significant changes, but was higher than LGM and PI  
1106 (Fig. 10). The TEJ is mostly driven by large-scale remote features such as convective heating  
1107 over the North Indian Ocean and the Himalayan-Tibetan plateau (Gill, 1980). However,  
1108 Redelsperger et al. (2002) indicate that the latent heat release through convection over the WAM  
1109 can enhance upper-level shear, thereby intensifying the TEJ. The causal mechanisms through  
1110 which the intensified TEJ increases the Sahel rainfall have been proposed in many studies  
1111 (Lemburg et al., 2019). These include upper-level divergence (Nicholson & Grist, 2003), vertical  
1112 and horizontal shear and how it affects dynamic instabilities (Grist, 2002; Nicholson, 2008), and  
1113 the modulation of the equatorial Rossby wave activity (Yang et al., 2018).

1114 The results reveal both the localised and large-scale impacts of vegetation on  
1115 precipitation over the WAM areas in response to different climates. Generally, vegetation  
1116 influences the exchange of mass and energy between the land surface and the atmosphere  
1117 through the modulation of (1) surface albedo, influencing surface radiation, and (2)  
1118 evapotranspiration, influencing the partitioning of net radiation into surface heat fluxes. These  
1119 imply that land cover does not only affect surface climate but also influences atmospheric  
1120 convection and large-scale circulations and moisture fluxes, which create further feedback and  
1121 influence soil moisture and vegetation (Charney et al., 1977; Sylla et al., 2016). In this study, we  
1122 focus on analysing the influence of surface conditions through surface heat flux anomalies.  
1123 Previous modelling studies have highlighted the role of soil moisture and evapotranspiration in  
1124 the vegetation-precipitation feedback due to their effect on low-level moist static energy,  
1125 convective instability, and surface latent heat flux anomalies (Patricola & Cook, 2007;  
1126 Rachmayani et al., 2015). These feedback mechanisms have been shown to strengthen the  
1127 response of the WAM to external forcing in past warmer climates (e.g., Messori et al., 2019).  
1128 The expanded vegetation over the Sahara in the MH resulted in a pronounced upward latent heat  
1129 flux, further strengthening the WAM and the moisture influx through the vegetation-albedo  
1130 feedback (e.g., Bonfils et al., 2001; Levis et al., 2004). The less expanded vegetation in the MP  
1131 also strengthened the WAM and contributed to the increased precipitation in the retreat months  
1132 of the WAM, even though the meridional pressure gradient was weaker than in the MH. Previous  
1133 studies have indicated wetter conditions and a northward migration of the WAM that is driven by  
1134 the cyclonic moisture flux anomaly over North Africa due to expanded vegetation into the  
1135 Sahara region (Chandan & Peltier, 2020; Pausata et al., 2020; Swann et al., 2014). Since the  
1136 various atmospheric dynamics and surface conditions had a unidirectional influence on the  
1137 WAM, isolating the impact of vegetation, a local amplifier forced by other large-scale features  
1138 (e.g., Klein et al., 2017; Messori et al., 2019), would require further sensitivity experiments.

#### 1139 5.4 Comparison of model estimates to proxies

1140 Comparing modelled paleoclimate to proxy reconstructions over Africa is often  
1141 challenging, because of the varying representation of relevant atmospheric processes in different  
1142 GCMs, and high spatial variability of proxy signals (e.g., deMenocal et al., 2000; Harrison et al.,  
1143 2014; Pausata et al., 2016; Tierney et al., 2017; Hopcroft and Valdes, 2019). Moreover, the  
1144 relatively low availability of paleohydrological records over Africa precludes a robust model-  
1145 data comparison (e.g., Salzmann et al., 2008, 2013). The sparsity of proxies also prevents the  
1146 merited direct comparison of simulated isotopic composition with past isotopic archives. Here,  
1147 we focus on the MH model-data comparison due to the relatively large number of proxy  
1148 reconstructions available and the ongoing debate about the northward migration and  
1149 intensification of the WAM during the African Humid Period (e.g., Pausata et al., 2020). The  
1150 sparse tropical African proxy records for the LGM reported in previous studies have shown  
1151 consistent cooling and drying conditions. It has been suggested that the dryness induced a  
1152 downward elevational shift of broadleaved evergreen or warm mixed forest and the enrichment  
1153 of steppe into regions now occupied by tropical forests (e.g., Elenga et al., 2000). The  
1154 reconstructed proxy records over North Africa during the MP consistently suggested more humid  
1155 conditions. More specifically, palynological data reveals denser tree cover and expanded  
1156 woodland and savanna at the expense of deserts over North Africa (Bonnefille, 2010; Salzmann  
1157 et al., 2008). Such vegetation expansion patterns are consistent with the only dynamic vegetation  
1158 GCM output participating in PlioMIP2 (Stepanek et al., 2020). Moreover, multi-proxy records,

1159 including plant wax and dust from marine sediment cores from offshore West Africa, suggest  
 1160 consistent wetter conditions in the MP (deMenocal, 2004; Kuechler et al., 2018). These  
 1161 reconstructed patterns are consistent with the more humid and dryness simulated for the LGM  
 1162 and MP.



1163  
 1164 **Figure 13.** Comparison of the mean annual precipitation (MAP) anomalies of the latitudinal  
 1165 extent of WAM in the Mid-Holocene for all models (ECHAM5-wiso (black) and PMIP4 models)  
 1166 to proxies reconstruction from Bartlein et al., (2011). The black shadings denote one standard  
 1167 deviation value from the regional means of the ECHAM5-wiso simulation. The error bars of the  
 1168 proxies represent the standard errors of the precipitation reconstructions.

1169 In the remainder of this section, we compare the simulated latitudinal variation of Mean  
 1170 Annual Precipitation (MAP) during the MH to pollen-based reconstructions by Bartlein et al.  
 1171 (2011). Overall, the simulated MAP magnitudes and latitudinal distribution by ECHAM5-wiso  
 1172 are closer to the proxy reconstructions than the PMIP4 models (Fig. 13). More specifically, the  
 1173 ECHAM5-wiso inter-annual means of the WAM's northward extent compare well to the lower  
 1174 latitudes pollen-based estimates over the Sahara with regards to the magnitude of changes and  
 1175 the patterns from the Sahel towards the tropical ocean. However, all models (i.e., PMIP4 models

1176 and ECHAM5-wiso) failed to match the magnitudes of the proxy-based MAP increase over the  
1177 high latitudes of the Sahara. The simulated MAP increase over the Sahara was 100-300 mm/year  
1178 less than the proxy reconstruction. It is important to note that the calculated MAP anomalies used  
1179 present-day CRU observation data as a reference period for the proxies, while the GCMs used  
1180 their PI simulations. Although the different reference periods can contribute slightly to the  
1181 discrepancies, the magnitude of the difference is large enough to acknowledge significant  
1182 deviations and thus potential limitations of either the GCMs or the proxy-based reconstructions.  
1183 The simulated ECHAM5-wiso anomalies during the monsoon season indicated wetter conditions  
1184 up to 25 °N, with increased precipitation anomalies of approximately 700 mm/year (Fig. 3). This  
1185 suggests a potential overestimation of precipitation anomalies from the pollen-based records on  
1186 the annual scale due to their potentially biased representation of the dry seasons across the  
1187 Sahara. In addition to the pollen-based reconstructions, other diverse archives over West Africa  
1188 estimate precipitation differences in the range of 300-500 mm/month, which are within the range  
1189 of our model estimates (Harrison et al., 2014; Kröpelin et al., 2008; Tierney et al., 2017). On the  
1190 other hand, recent reconstructions of leaf wax-alkane records off the coast of northern Africa  
1191 suggest MAP of higher than 700 mm/year as far north as 31°N, implying an expansion of the  
1192 WAM in the MH to 15-20° north of its present-day extent (Sultan & Janicot, 2003; Tierney et  
1193 al., 2017). Sha et al. (2019) interpreted their Moroccan speleothem at 31°N with high negative  
1194  $\delta^{18}\text{O}$  of carbonate records as a high rainfall signal created by the expansion of the WAM during  
1195 the MH. Paleoenvironment reconstructions also reflect wetter conditions in the MH with higher  
1196 lake levels and moisture-demanding biomes across North Africa (Kohfeld & Harrison, 2000;  
1197 Peyron et al., 2006; H. Wu et al., 2007). Vegetation reconstructions suggest a northward shift of  
1198 montane forest and a major extension of the tropical rainforest over North Africa (Jolly et al.  
1199 1998; Prentice et al. 2000).

1200 Overall, the model-proxy comparison reveals that all the adopted GCMs show limited  
1201 skill in reproducing the northward migration of the WAM and associated rainfall increase over  
1202 the Sahara. This suggests that the shortcomings leading to these discrepancies are shared by all  
1203 models and are not GCM-specific. The WAM dynamics are sensitive to the representation of  
1204 climate physics in the GCMs. Their limitations include inaccuracies in representing clouds,  
1205 surface conditions (e.g., lakes and wetlands), energy fluxes, and subgrid-scale convection  
1206 parameterisation. Additionally, the coarse spatial resolution of GCMs weakens their ability to  
1207 reproduce the mesoscale convection systems that are the main driver for the WAM. Previous  
1208 studies have also indicated that fully coupled models exhibit biases in reproducing the tropical  
1209 Atlantic dynamics, leading to elevated sea surface temperatures and a weakened monsoonal  
1210 circulation (Roehring et al., 2013). In this study, the high spatial resolution of the ECHAM5-  
1211 wiso experiment contributed to a better representation of surface conditions, such as orography.  
1212 Furthermore, the model was prescribed MH vegetation reconstruction. Contrarily, the PMIP4  
1213 models are fully coupled (atmosphere-ocean), incorporating ocean variability feedback, and  
1214 some consider dynamic vegetation feedback. Since all models, i.e. both ECHAM5-wiso and the  
1215 PMIP models, exhibit the above-mentioned deviations from proxy reconstructions, we propose  
1216 that the limitations are neither related solely to spatial resolution nor the use of fully coupled  
1217 models. Harrison et al. (2015) suggests the simulated biases of the PI control experiments of the  
1218 PMIP4-CMIP6, which indicate a more equatorward ensemble mean of the global monsoon when  
1219 compared to observations. Previous models have also shown that atmosphere-vegetation  
1220 feedback contributes to the northward extent of the WAM, but still underestimates the higher  
1221 latitude precipitation amount from the leaf wax n-alkanes (Dallmeyer et al., 2020; Pausata et al.,

1222 2016; Thompson et al., 2019). Rachmayani et al. (2015) demonstrated that dynamic vegetation  
1223 enhances the orbitally driven increase in precipitation anomalies over West Africa by 20% when  
1224 compared to models using fixed vegetation. However, their models with terrestrial and ocean  
1225 feedback still did not reach the level of vegetation coverage suggested by proxies.

1226 Recent studies have demonstrated that incorporating dust feedbacks associated with the  
1227 Green Sahara in the MH orbitally driven climate further enhances the northward reach and  
1228 intensification of the WAM (e.g., Thompson et al., 2019; Pausata et al., 2016; Hopcroft and  
1229 Valdes, 2019; Egerer et al., 2018) and better matches the paleoclimate reconstructions. This is  
1230 because the albedo-related feedback causes a reduction of dust concentration and changes in soil  
1231 properties over the vegetated Sahara, which induce an increase in incoming shortwave radiation  
1232 on the land surface, strengthening the warming over the Sahara. This further strengthens the  
1233 meridional temperature gradient and tropical circulation and then intensifies the WAM (Chandan  
1234 and Peltier, 2020; Pausata et al., 2016). Pausata et al. (2016) demonstrated the northward extent  
1235 of the WAM up to 31°N in the MH with a model forced with prescribed vegetation and reduced  
1236 dust concentrations, while the prescribed vegetation only reached ~26°N. These suggest that  
1237 simulating vegetation feedback with interactive dust dynamics on a high spatial resolution grid  
1238 would improve the representation of the MH. However, the state-of-art GCMs would require  
1239 improvement of their physical representation of dust dynamics, since they fail to reproduce dust  
1240 emission and transport (Evan et al., 2014; Kok, 2010; Leung et al., 2023; A. Zhao et al., 2022).  
1241 On the other hand, the plausible non-stationarity of the pollen-precipitation transfer function due  
1242 to changes in past climate dynamics from present conditions can also contribute to the mismatch  
1243 between climate simulation and paleoclimate reconstructions. Therefore, using a multi-proxy  
1244 system with varied causal mechanisms could ensure an accurate representation of the WAM  
1245 complex dynamics.

## 1246 **6 Conclusions**

1247 This study presents new and existing climate model simulations of the WAM and  
1248 associated features in the Late Cenozoic (i.e. the PI, MH, LGM and MP). More specifically, the  
1249 study presents an overview of the hydroclimate changes over West Africa and highlights the  
1250 components of the regional climate system that are important for generating accurate projections  
1251 of future climate. The paleoclimate experiments were conducted using the isotope-tracking  
1252 model (ECHAM5-wiso). The simulated results are similar to the CMIP6-PMIP4 experiments  
1253 and proxy reconstructions over West Africa. However, our simulations also show some  
1254 improvement over previous experiments, and yield new insights. We summarise the key results  
1255 as follows:

1256 1. A comparison between the present-day ECHAM5-wiso simulation and observation-  
1257 based datasets (i.e., ERA5 and CRU precipitation and temperature datasets) demonstrates the  
1258 model's ability to represent the atmospheric dynamics over West Africa reasonably well.

1259 2. The ECHAM5-wiso paleoclimate simulations produce the most intense WAM during  
1260 the MH, despite the MP's more enhanced hydrological cycle. In comparison, some of the  
1261 CMIP6-PMIP4 models suggest the highest intensification of the WAM in the MH (e.g., GISS-  
1262 E2-1-G), while others suggest the MP (e.g., EC-Earth3-LR).

1263 3. The intensification of the WAM is associated with a pronounced meridional gradient,  
1264 northward position of the ITD, northward reach of the core of the AEJ, higher altitudinal reach of

1265 the WAM (deeper monsoon depth), and higher moisture recycling through surface heat fluxes  
1266 due to vegetation across the Sahel-Sahara region. Most importantly, the AEJ is not entirely  
1267 responsible for the strengthening of the WAM, especially when large-scale features are  
1268 predominantly controlled by orbital forcings, as is the case in the MH. This needs to be well-  
1269 represented in GCMs to ensure realistic and accurate future projections.

1270 4. The simulation of the patterns and magnitude of  $\delta^{18}\text{O}_p$  values and associated regional  
1271 climate elements (e.g., temperature and precipitation) during the monsoon season reveal a non-  
1272 stationarity of their relationship throughout the late Cenozoic. Their changing relationships stress  
1273 the need to understand the causal mechanisms for each proxy system and refine their transfer  
1274 function to ensure accurate proxy-based reconstructions.

1275 5. ECHAM5-wiso simulates the higher precipitation rates over the WAM region in the  
1276 MH than the CMIP6-PMIP4 models. Since our model uses a more accurate vegetation  
1277 reconstruction and a higher resolution, we propose that a greater consideration of vegetation  
1278 feedbacks, and sub-grid processes will increase other models' representation of West African  
1279 climate during the MH.

1280 6. All models still underestimate the northward extent of the WAM, as reconstructed with  
1281 proxies. If proxy reconstructions are taken as accurate, this suggests that the representation of  
1282 additional climate processes, such as dust loading, interactive vegetation, and surface conditions,  
1283 such as lakes, will have to be improved to ensure a more realistic prediction of the WAM's  
1284 northward extent.

## 1285 **Acknowledgments**

1286 This research was supported by the German Science Foundation (DFG) grants EH329/19-1 and  
1287 EH329/23-1 (awarded to Todd A. Ehlers), MU4188/3-1 and MU4188/1-1 (awarded to Sebastian  
1288 G. Mutz). We acknowledge the World Climate Research Programme, which, through its  
1289 Working Group on Coupled Modeling, coordinated and promoted CMIP6. We thank the climate  
1290 modelling groups for producing and making their model output available, the Earth System Grid  
1291 Federation (ESGF) for archiving the data and providing access, and the multiple funding  
1292 agencies supporting CMIP and ESGF. Additionally, we thank the European Centre for Medium-  
1293 Range Weather Forecasts for providing ERA5 datasets and the University of East Anglia for  
1294 producing the CRU datasets.

1295

1296

1297

## 1298 **Open Research**

1299 Code availability statement:

1300 The ECHAM model code is available under a version of the MPI-M software license agreement  
1301 (<https://www.mpimet.mpg.de/en/science/models/license/>, last access: 03 January 2024). The  
1302 code of the isotopic version ECHAM5-wiso is available upon request on the Alfred Wegner  
1303 Institute's GitLab repository (<https://gitlab.awi.de/mwerner/mwi-esm-wiso>, last access: 03  
1304 January 2024). The scripts used for postprocessing, analysis, and visualisation are based on a  
1305 Python package (pyClimat) available at <https://doi.org/10.5281/zenodo.7143044> (Boateng, 2022)  
1306 and also on Github: <https://github.com/Dan-Boat/pyClimat> (last access: 03 January 2024)

1307

1308 Data availability statement:

1309 The postprocessed model output variables required to reproduce the figures of this study are  
 1310 available in NetCDF format at <https://doi.org/10.5281/zenodo.10455772> (Boateng, 2024). The  
 1311 CMIP6-PMIP4 (Eyring et al., 2016) models output are available at [https://esgf-](https://esgf-node.llnl.gov/projects/esgf-llnl/)  
 1312 [node.llnl.gov/projects/esgf-llnl/](https://esgf-node.llnl.gov/projects/esgf-llnl/) (last access: 03 January 2024). The Climate Research Unit  
 1313 (CRUv4.01) (Harris et al., 2020) precipitation data were obtained from  
 1314 [https://crudata.uea.ac.uk/cru/data/hrg/cru\\_ts\\_4.01/](https://crudata.uea.ac.uk/cru/data/hrg/cru_ts_4.01/) (last access: 03 January 2024).  
 1315 The ERA5 reanalysis products (Hersbach et al., 2020) were obtained from the Copernicus  
 1316 Climate Data Store at <https://cds.climate.copernicus.eu/cdsapp#!/home> (last access: 03 January  
 1317 2024).

1318

1319 **References**

- 1320 Abe-Ouchi, A., Saito, F., Kageyama, M., Braconnot, P., Harrison, S. P., Lambeck, K., et al. (2015). Ice-sheet  
 1321 configuration in the CMIP5/PMIP3 Last Glacial Maximum experiments. *Geoscientific Model*  
 1322 *Development*, 8(11), 3621–3637. <https://doi.org/10.5194/gmd-8-3621-2015>
- 1323 Adegbe, A. T., Schneider, R. R., Röhl, U., & Wefer, G. (2003). Glacial millennial-scale fluctuations in central  
 1324 African precipitation recorded in terrigenous sediment supply and freshwater signals offshore Cameroon.  
 1325 *Palaeogeography, Palaeoclimatology, Palaeoecology*, 197(3), 323–333. [https://doi.org/10.1016/S0031-](https://doi.org/10.1016/S0031-0182(03)00474-7)  
 1326 [0182\(03\)00474-7](https://doi.org/10.1016/S0031-0182(03)00474-7)
- 1327 Annan, J. D., & Hargreaves, J. C. (2013). A new global reconstruction of temperature changes at the Last Glacial  
 1328 Maximum. *Climate of the Past*, 9(1), 367–376. <https://doi.org/10.5194/cp-9-367-2013>
- 1329 Annan, J. D., & Hargreaves, J. C. (2015). A perspective on model-data surface temperature comparison at the Last  
 1330 Glacial Maximum. *Quaternary Science Reviews*, 107, 1–10.  
 1331 <https://doi.org/10.1016/j.quascirev.2014.09.019>
- 1332 Armitage, S. J., Bristow, C. S., & Drake, N. A. (2015). West African monsoon dynamics inferred from abrupt  
 1333 fluctuations of Lake Mega-Chad. *Proceedings of the National Academy of Sciences*, 112(28), 8543–8548.  
 1334 <https://doi.org/10.1073/pnas.1417655112>
- 1335 Arnold, L., Bréon, F.-M., & Brewer, S. (2009). The Earth as an extrasolar planet: the vegetation spectral signature  
 1336 today and during the last Quaternary climatic extrema. *International Journal of Astrobiology*, 8(2), 81–94.  
 1337 <https://doi.org/10.1017/S1473550409004406>
- 1338 Badger, M. P. S., Schmidt, D. N., Mackensen, A., & Pancost, R. D. (2013). High-resolution alkenone  
 1339 palaeobarometry indicates relatively stable pCO<sub>2</sub> during the Pliocene (3.3–2.8 Ma). *Philosophical*  
 1340 *Transactions of the Royal Society A: Mathematical, Physical and Engineering Sciences*, 371(2001),  
 1341 20130094. <https://doi.org/10.1098/rsta.2013.0094>
- 1342 Baidu, M., Schwendike, J., Marsham, J. H., & Bain, C. (2022). Effects of vertical wind shear on intensities of  
 1343 mesoscale convective systems over West and Central Africa. *Atmospheric Science Letters*, 23(8), e1094.  
 1344 <https://doi.org/10.1002/asl.1094>
- 1345 Barbé, L. L., Lebel, T., & Tapsoba, D. (2002). Rainfall Variability in West Africa during the Years 1950–90.  
 1346 *Journal of Climate*, 15(2), 187–202. [https://doi.org/10.1175/1520-](https://doi.org/10.1175/1520-0442(2002)015<0187:RVIWAD>2.0.CO;2)  
 1347 [0442\(2002\)015<0187:RVIWAD>2.0.CO;2](https://doi.org/10.1175/1520-0442(2002)015<0187:RVIWAD>2.0.CO;2)
- 1348 Bartlein, P. J., Harrison, S. P., Brewer, S., Connor, S., Davis, B. A. S., Gajewski, K., et al. (2011). Pollen-based  
 1349 continental climate reconstructions at 6 and 21 ka: a global synthesis. *Climate Dynamics*, 37(3), 775–802.  
 1350 <https://doi.org/10.1007/s00382-010-0904-1>
- 1351 Bartoli, G., Hönisch, B., & Zeebe, R. E. (2011). Atmospheric CO<sub>2</sub> decline during the Pliocene intensification of  
 1352 Northern Hemisphere glaciations. *Paleoceanography*, 26(4). <https://doi.org/10.1029/2010PA002055>

- 1353 Bell, B., Hersbach, H., Simmons, A., Berrisford, P., Dahlgren, P., Horányi, A., et al. (2021). The ERA5 global  
 1354 reanalysis: Preliminary extension to 1950. *Quarterly Journal of the Royal Meteorological Society*,  
 1355 *147*(741), 4186–4227. <https://doi.org/10.1002/qj.4174>
- 1356 Bereiter, B., Eggleston, S., Schmitt, J., Nehrbass-Ahles, C., Stocker, T. F., Fischer, H., et al. (2015). Revision of the  
 1357 EPICA Dome C CO<sub>2</sub> record from 800 to 600 kyr before present. *Geophysical Research Letters*, *42*(2),  
 1358 542–549. <https://doi.org/10.1002/2014GL061957>
- 1359 Berntell, E., Zhang, Q., Li, Q., Haywood, A. M., Tindall, J. C., Hunter, S. J., et al. (2021). Mid-Pliocene West  
 1360 African Monsoon rainfall as simulated in the PlioMIP2 ensemble. *Climate of the Past*, *17*(4), 1777–1794.  
 1361 <https://doi.org/10.5194/cp-17-1777-2021>
- 1362 Biasutti, M. (2013). Forced Sahel rainfall trends in the CMIP5 archive. *Journal of Geophysical Research:*  
 1363 *Atmospheres*, *118*(4), 1613–1623. <https://doi.org/10.1002/jgrd.50206>
- 1364 Bigelow, N. H., Brubaker, L. B., Edwards, M. E., Harrison, S. P., Prentice, I. C., Anderson, P. M., et al. (2003).  
 1365 Climate change and Arctic ecosystems: 1. Vegetation changes north of 55°N between the last glacial  
 1366 maximum, mid-Holocene, and present. *Journal of Geophysical Research: Atmospheres*, *108*(D19).  
 1367 <https://doi.org/10.1029/2002JD002558>
- 1368 Blunier, T., & Brook, E. J. (2001). Timing of Millennial-Scale Climate Change in Antarctica and Greenland During  
 1369 the Last Glacial Period. *Science*, *291*(5501), 109–112. <https://doi.org/10.1126/science.291.5501.109>
- 1370 Boateng, D., Mutz, S. G., Ballian, A., Meijers, M. J. M., Methner, K., Botsyun, S., et al. (2023). The effects of  
 1371 diachronous surface uplift of the European Alps on regional climate and the oxygen isotopic composition  
 1372 of precipitation. *Earth System Dynamics*, *14*(6), 1183–1210. <https://doi.org/10.5194/esd-14-1183-2023>
- 1373 Bonfils, C., Noblet-Ducoudré, N. de, Braconnot, P., & Joussaume, S. (2001). Hot Desert Albedo and Climate  
 1374 Change: Mid-Holocene Monsoon in North Africa. *Journal of Climate*, *14*(17), 3724–3737.  
 1375 [https://doi.org/10.1175/1520-0442\(2001\)014<3724:HDAACC>2.0.CO;2](https://doi.org/10.1175/1520-0442(2001)014<3724:HDAACC>2.0.CO;2)
- 1376 Bonnefille, R. (2010). Cenozoic vegetation, climate changes and hominid evolution in tropical Africa. *Global and*  
 1377 *Planetary Change*, *72*(4), 390–411. <https://doi.org/10.1016/j.gloplacha.2010.01.015>
- 1378 Bony, S., Risi, C., & Vimeux, F. (2008). Influence of convective processes on the isotopic composition ( $\delta^{18}\text{O}$  and  
 1379  $\delta\text{D}$ ) of precipitation and water vapor in the tropics: 1. Radiative-convective equilibrium and Tropical  
 1380 Ocean–Global Atmosphere–Coupled Ocean–Atmosphere Response Experiment (TOGA-COARE)  
 1381 simulations. *Journal of Geophysical Research: Atmospheres*, *113*(D19).  
 1382 <https://doi.org/10.1029/2008JD009942>
- 1383 Boos, W. R. (2012). Thermodynamic Scaling of the Hydrological Cycle of the Last Glacial Maximum. *Journal of*  
 1384 *Climate*, *25*(3), 992–1006. <https://doi.org/10.1175/JCLI-D-11-00010.1>
- 1385 Bosmans, J. H. C., Drijfhout, S. S., Tuenter, E., Lourens, L. J., Hilgen, F. J., & Weber, S. L. (2012). Monsoonal  
 1386 response to mid-holocene orbital forcing in a high resolution GCM. *Climate of the Past*, *8*(2), 723–740.
- 1387 Botsyun, S., Mutz, S. G., Ehlers, T. A., Koptev, A., Wang, X., Schmidt, B., et al. (2022). Influence of Large-Scale  
 1388 Atmospheric Dynamics on Precipitation Seasonality of the Tibetan Plateau and Central Asia in Cold and  
 1389 Warm Climates During the Late Cenozoic. *Journal of Geophysical Research: Atmospheres*, *127*(12),  
 1390 e2021JD035810. <https://doi.org/10.1029/2021JD035810>
- 1391 Boyle, J., & Klein, S. A. (2010). Impact of horizontal resolution on climate model forecasts of tropical precipitation  
 1392 and diabatic heating for the TWP-ICE period. *Journal of Geophysical Research: Atmospheres*, *115*(D23).  
 1393 <https://doi.org/10.1029/2010JD014262>
- 1394 Braconnot, P., Otto-Bliesner, B., Harrison, S., Joussaume, S., Peterchmitt, J.-Y., Abe-Ouchi, A., et al. (2007).  
 1395 Results of PMIP2 coupled simulations of the Mid-Holocene and Last Glacial Maximum &ndash; Part 1:  
 1396 experiments and large-scale features. *Climate of the Past*, *3*(2), 261–277. [https://doi.org/10.5194/cp-3-261-](https://doi.org/10.5194/cp-3-261-2007)  
 1397 2007
- 1398 Braconnot, Pascale, Harrison, S. P., Joussaume, S., Hewitt, C. D., Kitoch, A., Kutzbach, J. E., et al. (2004).  
 1399 Evaluation of PMIP coupled ocean-atmosphere simulations of the Mid-Holocene. In R. W. Battarbee, F.  
 1400 Gasse, & C. E. Stickley (Eds.), *Past Climate Variability through Europe and Africa* (pp. 515–533).  
 1401 Dordrecht: Springer Netherlands. [https://doi.org/10.1007/978-1-4020-2121-3\\_24](https://doi.org/10.1007/978-1-4020-2121-3_24)

- 1402 Braconnot, Pascale, Harrison, S. P., Kageyama, M., Bartlein, P. J., Masson-Delmotte, V., Abe-Ouchi, A., et al.  
 1403 (2012). Evaluation of climate models using palaeoclimatic data. *Nature Climate Change*, 2(6), 417–424.  
 1404 <https://doi.org/10.1038/nclimate1456>
- 1405 Brady, E. C., Otto-Bliesner, B. L., Kay, J. E., & Rosenbloom, N. (2013). Sensitivity to Glacial Forcing in the  
 1406 CCSM4. *Journal of Climate*, 26(6), 1901–1925. <https://doi.org/10.1175/JCLI-D-11-00416.1>
- 1407 Brierley, C. M., Zhao, A., Harrison, S. P., Braconnot, P., Williams, C. J. R., Thornalley, D. J. R., et al. (2020).  
 1408 Large-scale features and evaluation of the PMIP4-CMIP6 *midHolocene* simulations. *Climate of the Past*,  
 1409 16(5), 1847–1872. <https://doi.org/10.5194/cp-16-1847-2020>
- 1410 Bühler, J. C., Axelsson, J., Lechleitner, F. A., Fohlmeister, J., LeGrande, A. N., Midhun, M., et al. (2022).  
 1411 Investigating stable oxygen and carbon isotopic variability in speleothem records over the last millennium  
 1412 using multiple isotope-enabled climate models. *Climate of the Past*, 18(7), 1625–1654.  
 1413 <https://doi.org/10.5194/cp-18-1625-2022>
- 1414 Burke, K. D., Williams, J. W., Chandler, M. A., Haywood, A. M., Lunt, D. J., & Otto-Bliesner, B. L. (2018).  
 1415 Pliocene and Eocene provide best analogs for near-future climates. *Proceedings of the National Academy of*  
 1416 *Sciences*, 115(52), 13288–13293. <https://doi.org/10.1073/pnas.1809600115>
- 1417 Cao, J., Wang, B., & Ma, L. (2019). Attribution of Global Monsoon Response to the Last Glacial Maximum  
 1418 Forcings. *Journal of Climate*, 32(19), 6589–6605. <https://doi.org/10.1175/JCLI-D-18-0871.1>
- 1419 Cauquoin, A., Werner, M., & Lohmann, G. (2019). Water isotopes – climate relationships for the mid-Holocene and  
 1420 preindustrial period simulated with an isotope-enabled version of MPI-ESM. *Climate of the Past*, 15(6),  
 1421 1913–1937. <https://doi.org/10.5194/cp-15-1913-2019>
- 1422 Chandan, D., & Peltier, W. R. (2020). African Humid Period Precipitation Sustained by Robust Vegetation, Soil,  
 1423 and Lake Feedbacks. *Geophysical Research Letters*, 47(21), e2020GL088728.  
 1424 <https://doi.org/10.1029/2020GL088728>
- 1425 Charney, J., Quirk, W. J., Chow, S., & Kornfield, J. (1977). A comparative study of the effects of albedo change on  
 1426 drought in semi-arid regions. *Journal of the Atmospheric Sciences*, 34(9), 1366–1385.  
 1427 [https://doi.org/10.1175/1520-0469\(1977\)034<1366:ACSOTE>2.0.CO;2](https://doi.org/10.1175/1520-0469(1977)034<1366:ACSOTE>2.0.CO;2)
- 1428 Clark, P. U., Dyke, A. S., Shakun, J. D., Carlson, A. E., Clark, J., Wohlfarth, B., et al. (2009). The Last Glacial  
 1429 Maximum. *Science*, 325(5941), 710–714. <https://doi.org/10.1126/science.1172873>
- 1430 Claussen, M., Kubatzki, C., Brovkin, V., Ganopolski, A., Hoelzmann, P., & Pachur, H.-J. (1999). Simulation of an  
 1431 abrupt change in Saharan vegetation in the Mid-Holocene. *Geophysical Research Letters*, 26(14), 2037–  
 1432 2040. <https://doi.org/10.1029/1999GL900494>
- 1433 CLIMAP, P. (1981). *Seasonal reconstructions of the Earth's surface at the last glacial maximum*. Geological  
 1434 Society of America.
- 1435 Coe, M., & Harrison, S. (2002). The water balance of northern Africa during the mid-Holocene: an evaluation of the  
 1436 6 ka BP PMIP simulations. *Climate Dynamics*, 19(2), 155–166. <https://doi.org/10.1007/s00382-001-0219-3>
- 1437 Cook, K. H. (2008). The mysteries of Sahel droughts. *Nature Geoscience*, 1(10), 647–648.  
 1438 <https://doi.org/10.1038/ngeo320>
- 1439 Corvec, S., & Fletcher, C. G. (2017). Changes to the tropical circulation in the mid-Pliocene and their implications  
 1440 for future climate. *Climate of the Past*, 13(2), 135–147. <https://doi.org/10.5194/cp-13-135-2017>
- 1441 Craig, H., & Gordon, L. I. (1965). Deuterium and oxygen 18 variations in the ocean and the marine atmosphere.
- 1442 Cremaschi, M., & Di Lernia, S. (1999). Holocene Climatic Changes and Cultural Dynamics in the Libyan Sahara.  
 1443 *African Archaeological Review*, 16(4), 211–238. <https://doi.org/10.1023/A:1021609623737>
- 1444 Crook, J., Klein, C., Folwell, S., Taylor, C. M., Parker, D. J., Stratton, R., & Stein, T. (2019). Assessment of the  
 1445 Representation of West African Storm Lifecycles in Convection-Permitting Simulations. *Earth and Space*  
 1446 *Science*, 6(5), 818–835. <https://doi.org/10.1029/2018EA000491>
- 1447 D'Agostino, R., Bader, J., Bordoni, S., Ferreira, D., & Jungclaus, J. (2019). Northern Hemisphere Monsoon  
 1448 Response to Mid-Holocene Orbital Forcing and Greenhouse Gas-Induced Global Warming. *Geophysical*  
 1449 *Research Letters*, 46(3), 1591–1601. <https://doi.org/10.1029/2018GL081589>

- 1450 D'Agostino, R., Brown, J. R., Moise, A., Nguyen, H., Dias, P. L. S., & Jungclaus, J. (2020). Contrasting Southern  
1451 Hemisphere Monsoon Response: MidHolocene Orbital Forcing versus Future Greenhouse Gas–Induced  
1452 Global Warming. *Journal of Climate*, *33*(22), 9595–9613. <https://doi.org/10.1175/JCLI-D-19-0672.1>
- 1453 Dallmeyer, A., Claussen, M., Lorenz, S. J., & Shanahan, T. (2020). The end of the African humid period as seen by  
1454 a transient comprehensive Earth system model simulation of the last 8000&thinsp;years. *Climate of the*  
1455 *Past*, *16*(1), 117–140. <https://doi.org/10.5194/cp-16-117-2020>
- 1456 Dansgaard, W., Johnsen, S. J., Clausen, H. B., Dahl-Jensen, D., Gundestrup, N. S., Hammer, C. U., et al. (1993).  
1457 Evidence for general instability of past climate from a 250-kyr ice-core record. *Nature*, *364*(6434), 218–  
1458 220. <https://doi.org/10.1038/364218a0>
- 1459 deMenocal, P., Ortiz, J., Guilderson, T., Adkins, J., Sarnthein, M., Baker, L., & Yarusinsky, M. (2000). Abrupt  
1460 onset and termination of the African Humid Period:: rapid climate responses to gradual insolation forcing.  
1461 *Quaternary Science Reviews*, *19*(1), 347–361. [https://doi.org/10.1016/S0277-3791\(99\)00081-5](https://doi.org/10.1016/S0277-3791(99)00081-5)
- 1462 deMenocal, P. B. (2004). African climate change and faunal evolution during the Pliocene–Pleistocene. *Earth and*  
1463 *Planetary Science Letters*, *220*(1), 3–24. [https://doi.org/10.1016/S0012-821X\(04\)00003-2](https://doi.org/10.1016/S0012-821X(04)00003-2)
- 1464 Dietrich, S., Werner, M., Spanghel, T., & Lohmann, G. (2013). Influence of orbital forcing and solar activity on  
1465 water isotopes in precipitation during the mid- and late Holocene. *Climate of the Past*, *9*(1), 13–26.  
1466 <https://doi.org/10.5194/cp-9-13-2013>
- 1467 Dowsett, H., Robinson, M., Haywood, A. M., Salzmann, U., Hill, D., Sohl, L. E., et al. (2010). The PRISM3D  
1468 paleoenvironmental reconstruction. *Stratigraphy*.
- 1469 Dowsett, Harry, Dolan, A., Rowley, D., Moucha, R., Forte, A. M., Mitrovica, J. X., et al. (2016). The PRISM4 (mid-  
1470 Piacenzian) paleoenvironmental reconstruction. *Climate of the Past*, *12*(7), 1519–1538.  
1471 <https://doi.org/10.5194/cp-12-1519-2016>
- 1472 Dunne, J., Evershed, R. P., Salque, M., Cramp, L., Bruni, S., Ryan, K., et al. (2012). First dairying in green Saharan  
1473 Africa in the fifth millennium BC. *Nature*, *486*(7403), 390–394. <https://doi.org/10.1038/nature11186>
- 1474 Egerer, S., Claussen, M., & Reick, C. (2018). Rapid increase in simulated North Atlantic dust deposition due to fast  
1475 change of northwest African landscape during the Holocene. *Climate of the Past*, *14*(7), 1051–1066.  
1476 <https://doi.org/10.5194/cp-14-1051-2018>
- 1477 Erfanian, A., Wang, G., Yu, M., & Anyah, R. (2016). Multimodel ensemble simulations of present and future  
1478 climates over West Africa: Impacts of vegetation dynamics. *Journal of Advances in Modeling Earth*  
1479 *Systems*, *8*(3), 1411–1431. <https://doi.org/10.1002/2016MS000660>
- 1480 Etheridge, D. M., Steele, L. P., Langenfelds, R. L., Francey, R. J., Barnola, J.-M., & Morgan, V. I. (1996). Natural  
1481 and anthropogenic changes in atmospheric CO<sub>2</sub> over the last 1000 years from air in Antarctic ice and firn.  
1482 *Journal of Geophysical Research: Atmospheres*, *101*(D2), 4115–4128. <https://doi.org/10.1029/95JD03410>
- 1483 Etheridge, D. M., Steele, L. P., Francey, R. J., & Langenfelds, R. L. (1998). Atmospheric methane between 1000  
1484 A.D. and present: Evidence of anthropogenic emissions and climatic variability. *Journal of Geophysical*  
1485 *Research: Atmospheres*, *103*(D13), 15979–15993. <https://doi.org/10.1029/98JD00923>
- 1486 Evan, A. T., Flamant, C., Fiedler, S., & Doherty, O. (2014). An analysis of aeolian dust in climate models.  
1487 *Geophysical Research Letters*, *41*(16), 5996–6001. <https://doi.org/10.1002/2014GL060545>
- 1488 Eyring, V., Bony, S., Meehl, G. A., Senior, C. A., Stevens, B., Stouffer, R. J., & Taylor, K. E. (2016). Overview of  
1489 the Coupled Model Intercomparison Project Phase 6 (CMIP6) experimental design and organization.  
1490 *Geoscientific Model Development*, *9*(5), 1937–1958. <https://doi.org/10.5194/gmd-9-1937-2016>
- 1491 Friedrich, T., Timmermann, A., Tigchelaar, M., Elison Timm, O., & Ganopolski, A. (2016). Nonlinear climate  
1492 sensitivity and its implications for future greenhouse warming. *Science Advances*, *2*(11), e1501923.  
1493 <https://doi.org/10.1126/sciadv.1501923>
- 1494 Gabriel, B. (1987). Palaeoecological evidence from neolithic fireplaces in the Sahara. *African Archaeological*  
1495 *Review*, *5*(1), 93–103. <https://doi.org/10.1007/BF01117085>
- 1496 Gaetani, M., Messori, G., Zhang, Q., Flamant, C., & Pausata, F. S. R. (2017). Understanding the Mechanisms  
1497 behind the Northward Extension of the West African Monsoon during the Mid-Holocene. *Journal of*  
1498 *Climate*, *30*(19), 7621–7642. <https://doi.org/10.1175/JCLI-D-16-0299.1>

- 1499 Gao, X., Xu, Y., Zhao, Z., Pal, J. S., & Giorgi, F. (2006). On the role of resolution and topography in the simulation  
1500 of East Asia precipitation. *Theoretical and Applied Climatology*, 86(1), 173–185.  
1501 <https://doi.org/10.1007/s00704-005-0214-4>
- 1502 Gill, A. E. (1980). Some simple solutions for heat-induced tropical circulation. *Quarterly Journal of the Royal*  
1503 *Meteorological Society*, 106(449), 447–462. <https://doi.org/10.1002/qj.49710644905>
- 1504 Grist, J. P. (2002). Easterly Waves over Africa. Part I: The Seasonal Cycle and Contrasts between Wet and Dry  
1505 Years. *Monthly Weather Review*, 130(2), 197–211. [https://doi.org/10.1175/1520-0493\(2002\)130<0197:EWOAPI>2.0.CO;2](https://doi.org/10.1175/1520-0493(2002)130<0197:EWOAPI>2.0.CO;2)
- 1507 Hagemann, S. (2002). Validierung des Niederschlags in globalen Klimamodellen. 5. *Workshop Zur Hydrologischen*  
1508 *Modellierung: Möglichkeiten Und Grenzen Für Den Einsatz Hydrologischer Modelle in Politik, Wirtschaft*  
1509 *Und Klimafolgenforschung*, 115-127 (2002).
- 1510 Hagemann, S., Arpe, K., & Roeckner, E. (2006). Evaluation of the Hydrological Cycle in the ECHAM5 Model.  
1511 *Journal of Climate*, 19(16), 3810–3827. <https://doi.org/10.1175/JCLI3831.1>
- 1512 Harris, I., Jones, P. d., Osborn, T. j., & Lister, D. h. (2014). Updated high-resolution grids of monthly climatic  
1513 observations – the CRU TS3.10 Dataset. *International Journal of Climatology*, 34(3), 623–642.  
1514 <https://doi.org/10.1002/joc.3711>
- 1515 Harris, Ian, Osborn, T. J., Jones, P., & Lister, D. (2020). Version 4 of the CRU TS monthly high-resolution gridded  
1516 multivariate climate dataset. *Scientific Data*, 7(1), 109. <https://doi.org/10.1038/s41597-020-0453-3>
- 1517 Harrison, S. P., Yu, G., Takahara, H., & Prentice, I. C. (2001). Diversity of temperate plants in east Asia. *Nature*,  
1518 413(6852), 129–130. <https://doi.org/10.1038/35093166>
- 1519 Harrison, S. P., Bartlein, P. J., Brewer, S., Prentice, I. C., Boyd, M., Hessler, I., et al. (2014). Climate model  
1520 benchmarking with glacial and mid-Holocene climates. *Climate Dynamics*, 43(3), 671–688.  
1521 <https://doi.org/10.1007/s00382-013-1922-6>
- 1522 Harrison, S. P., Bartlein, P. J., Izumi, K., Li, G., Annan, J., Hargreaves, J., et al. (2015). Evaluation of CMIP5  
1523 palaeo-simulations to improve climate projections. *Nature Climate Change*, 5(8), 735–743.  
1524 <https://doi.org/10.1038/nclimate2649>
- 1525 Haywood, A. M., Dowsett, H. J., Otto-Bliesner, B., Chandler, M. A., Dolan, A. M., Hill, D. J., et al. (2010).  
1526 Pliocene Model Intercomparison Project (PlioMIP): experimental design and boundary conditions  
1527 (Experiment 1). *Geoscientific Model Development*, 3(1), 227–242. <https://doi.org/10.5194/gmd-3-227-2010>
- 1528 Haywood, A. M., Hill, D. J., Dolan, A. M., Otto-Bliesner, B. L., Bragg, F., Chan, W.-L., et al. (2013). Large-scale  
1529 features of Pliocene climate: results from the Pliocene Model Intercomparison Project. *Climate of the Past*,  
1530 9(1), 191–209. <https://doi.org/10.5194/cp-9-191-2013>
- 1531 Haywood, Alan M., Dowsett, H. J., Dolan, A. M., Rowley, D., Abe-Ouchi, A., Otto-Bliesner, B., et al. (2016). The  
1532 Pliocene Model Intercomparison Project (PlioMIP) Phase 2: scientific objectives and experimental design.  
1533 *Climate of the Past*, 12(3), 663–675. <https://doi.org/10.5194/cp-12-663-2016>
- 1534 Haywood, Alan M., Tindall, J. C., Dowsett, H. J., Dolan, A. M., Foley, K. M., Hunter, S. J., et al. (2020). The  
1535 Pliocene Model Intercomparison Project Phase 2: large-scale climate features and climate sensitivity.  
1536 *Climate of the Past*, 16(6), 2095–2123. <https://doi.org/10.5194/cp-16-2095-2020>
- 1537 Hersbach, H., Bell, B., Berrisford, P., Hirahara, S., Horányi, A., Muñoz-Sabater, J., et al. (2020). The ERA5 global  
1538 reanalysis. *Quarterly Journal of the Royal Meteorological Society*, 146(730), 1999–2049.  
1539 <https://doi.org/10.1002/qj.3803>
- 1540 Hoelzmann, P., Jolly, D., Harrison, S. P., Laarif, F., Bonnefille, R., & Pachur, H.-J. (1998). Mid-Holocene land-  
1541 surface conditions in northern Africa and the Arabian Peninsula: A data set for the analysis of  
1542 biogeophysical feedbacks in the climate system. *Global Biogeochemical Cycles*, 12(1), 35–51.  
1543 <https://doi.org/10.1029/97GB02733>
- 1544 Hoelzmann, Philipp, Keding, B., Berke, H., Kröpelin, S., & Kruse, H.-J. (2001). Environmental change and  
1545 archaeology: lake evolution and human occupation in the Eastern Sahara during the Holocene.  
1546 *Palaeogeography, Palaeoclimatology, Palaeoecology*, 169(3), 193–217. [https://doi.org/10.1016/S0031-0182\(01\)00211-5](https://doi.org/10.1016/S0031-0182(01)00211-5)
- 1547

- 1548 Holmes, J. A. (2008). How the Sahara Became Dry. *Science*, 320(5877), 752–753.  
 1549 <https://doi.org/10.1126/science.1158105>
- 1550 Hopcroft, P. O., & Valdes, P. J. (2019). On the Role of Dust-Climate Feedbacks During the Mid-Holocene.  
 1551 *Geophysical Research Letters*, 46(3), 1612–1621. <https://doi.org/10.1029/2018GL080483>
- 1552 Janicot, S., Caniaux, G., Chauvin, F., de Coëtlogon, G., Fontaine, B., Hall, N., et al. (2011). Intraseasonal variability  
 1553 of the West African monsoon. *Atmospheric Science Letters*, 12(1), 58–66. <https://doi.org/10.1002/asl.280>
- 1554 Jenkins, G. S., Gaye, A. T., & Sylla, B. (2005). Late 20th century attribution of drying trends in the Sahel from the  
 1555 Regional Climate Model (RegCM3). *Geophysical Research Letters*, 32(22).  
 1556 <https://doi.org/10.1029/2005GL024225>
- 1557 Jiang, D., Wang, H., Ding, Z., Lang, X., & Drange, H. (2005). Modeling the middle Pliocene climate with a global  
 1558 atmospheric general circulation model. *Journal of Geophysical Research: Atmospheres*, 110(D14).  
 1559 <https://doi.org/10.1029/2004JD005639>
- 1560 Jiang, D., Tian, Z., Lang, X., Kageyama, M., & Ramstein, G. (2015). The concept of global monsoon applied to the  
 1561 last glacial maximum: A multi-model analysis. *Quaternary Science Reviews*, 126, 126–139.  
 1562 <https://doi.org/10.1016/j.quascirev.2015.08.033>
- 1563 Jolly, D., Prentice, I. C., Bonnefille, R., Ballouche, A., Bengo, M., Brenac, P., et al. (1998). Biome reconstruction  
 1564 from pollen and plant macrofossil data for Africa and the Arabian peninsula at 0 and 6000 years. *Journal of*  
 1565 *Biogeography*, 25(6), 1007–1027. <https://doi.org/10.1046/j.1365-2699.1998.00238.x>
- 1566 Joussaume, S., Taylor, K. E., Braconnot, P., Mitchell, J. F. B., Kutzbach, J. E., Harrison, S. P., et al. (1999).  
 1567 Monsoon changes for 6000 years ago: Results of 18 simulations from the Paleoclimate Modeling  
 1568 Intercomparison Project (PMIP). *Geophysical Research Letters*, 26(7), 859–862.  
 1569 <https://doi.org/10.1029/1999GL900126>
- 1570 Jungandreas, L., Hohenegger, C., & Claussen, M. (2021). Influence of the representation of convection on the mid-  
 1571 Holocene West African Monsoon. *Climate of the Past*, 17(4), 1665–1684. <https://doi.org/10.5194/cp-17-1665-2021>
- 1573 Kageyama, M., Braconnot, P., Bopp, L., Caubel, A., Foujols, M.-A., Guilyardi, E., et al. (2013). Mid-Holocene and  
 1574 Last Glacial Maximum climate simulations with the IPSL model—part I: comparing IPSL\_CM5A to  
 1575 IPSL\_CM4. *Climate Dynamics*, 40(9), 2447–2468. <https://doi.org/10.1007/s00382-012-1488-8>
- 1576 Kageyama, M., Braconnot, P., Harrison, S. P., Haywood, A. M., Jungclaus, J. H., Otto-Bliesner, B. L., et al. (2018).  
 1577 The PMIP4 contribution to CMIP6 – Part 1: Overview and over-arching analysis plan. *Geoscientific Model*  
 1578 *Development*, 11(3), 1033–1057. <https://doi.org/10.5194/gmd-11-1033-2018>
- 1579 Kageyama, M., Harrison, S. P., Kapsch, M.-L., Lofverstrom, M., Lora, J. M., Mikolajewicz, U., et al. (2021). The  
 1580 PMIP4 Last Glacial Maximum experiments: preliminary results and comparison with the PMIP3  
 1581 simulations. *Climate of the Past*, 17(3), 1065–1089. <https://doi.org/10.5194/cp-17-1065-2021>
- 1582 Kim, S.-J., Crowley, T. J., Erickson, D. J., Govindasamy, B., Duffy, P. B., & Lee, B. Y. (2008). High-resolution  
 1583 climate simulation of the last glacial maximum. *Climate Dynamics*, 31(1), 1–16.  
 1584 <https://doi.org/10.1007/s00382-007-0332-z>
- 1585 Klein, C., Bliefernicht, J., Heinzeller, D., Gessner, U., Klein, I., & Kunstmann, H. (2017). Feedback of observed  
 1586 interannual vegetation change: a regional climate model analysis for the West African monsoon. *Climate*  
 1587 *Dynamics*, 48(9), 2837–2858. <https://doi.org/10.1007/s00382-016-3237-x>
- 1588 Kohfeld, K. E., & Harrison, S. P. (2000). How well can we simulate past climates? Evaluating the models using  
 1589 global palaeoenvironmental datasets. *Quaternary Science Reviews*, 19(1), 321–346.  
 1590 [https://doi.org/10.1016/S0277-3791\(99\)00068-2](https://doi.org/10.1016/S0277-3791(99)00068-2)
- 1591 Kok, J. F. (2010). An improved parameterization of wind-blown sand flux on Mars that includes the effect of  
 1592 hysteresis. *Geophysical Research Letters*, 37(12). <https://doi.org/10.1029/2010GL043646>
- 1593 Kolstad, E. W., & Screen, J. A. (2019). Nonstationary Relationship Between Autumn Arctic Sea Ice and the Winter  
 1594 North Atlantic Oscillation. *Geophysical Research Letters*, 46(13), 7583–7591.  
 1595 <https://doi.org/10.1029/2019GL083059>

- 1596 Kröpelin, S., Verschuren, D., Lézine, A.-M., Eggermont, H., Cocquyt, C., Francus, P., et al. (2008). Climate-Driven  
 1597 Ecosystem Succession in the Sahara: The Past 6000 Years. *Science*, *320*(5877), 765–768.  
 1598 <https://doi.org/10.1126/science.1154913>
- 1599 Kuechler, R. R., Dupont, L. M., & Schefuß, E. (2018). Hybrid insolation forcing of Pliocene monsoon dynamics in  
 1600 West Africa. *Climate of the Past*, *14*(1), 73–84. <https://doi.org/10.5194/cp-14-73-2018>
- 1601 Kutzbach, J. E., & Liu, Z. (1997). Response of the African Monsoon to Orbital Forcing and Ocean Feedbacks in the  
 1602 Middle Holocene. *Science*, *278*(5337), 440–443. <https://doi.org/10.1126/science.278.5337.440>
- 1603 Lambeck, K., Rouby, H., Purcell, A., Sun, Y., & Sambridge, M. (2014). Sea level and global ice volumes from the  
 1604 Last Glacial Maximum to the Holocene. *Proceedings of the National Academy of Sciences*, *111*(43),  
 1605 15296–15303. <https://doi.org/10.1073/pnas.1411762111>
- 1606 Lavaysse, C., Flamant, C., Janicot, S., Parker, D. J., Lafore, J.-P., Sultan, B., & Pelon, J. (2009). Seasonal evolution  
 1607 of the West African heat low: a climatological perspective. *Climate Dynamics*, *33*(2), 313–330.  
 1608 <https://doi.org/10.1007/s00382-009-0553-4>
- 1609 Lawrence, J. R., Gedzelman, S. D., Dexheimer, D., Cho, H.-K., Carrie, G. D., Gasparini, R., et al. (2004). Stable  
 1610 isotopic composition of water vapor in the tropics. *Journal of Geophysical Research: Atmospheres*,  
 1611 *109*(D6). <https://doi.org/10.1029/2003JD004046>
- 1612 LeGrande, A. N., & Schmidt, G. A. (2006). Global gridded data set of the oxygen isotopic composition in seawater.  
 1613 *Geophysical Research Letters*, *33*(12). <https://doi.org/10.1029/2006GL026011>
- 1614 Lemburg, A., Bader, J., & Claussen, M. (2019). Sahel Rainfall–Tropical Easterly Jet Relationship on Synoptic to  
 1615 Intraseasonal Time Scales. *Monthly Weather Review*, *147*(5), 1733–1752. [https://doi.org/10.1175/MWR-D-](https://doi.org/10.1175/MWR-D-18-0254.1)  
 1616 [18-0254.1](https://doi.org/10.1175/MWR-D-18-0254.1)
- 1617 Leung, D. M., Kok, J. F., Li, L., Okin, G. S., Prigent, C., Klose, M., et al. (2023). A new process-based and scale-  
 1618 aware desert dust emission scheme for global climate models – Part I: Description and evaluation against  
 1619 inverse modeling emissions. *Atmospheric Chemistry and Physics*, *23*(11), 6487–6523.  
 1620 <https://doi.org/10.5194/acp-23-6487-2023>
- 1621 Levis, S., Bonan, G. B., & Bonfils, C. (2004). Soil feedback drives the mid-Holocene North African monsoon  
 1622 northward in fully coupled CCSM2 simulations with a dynamic vegetation model. *Climate Dynamics*,  
 1623 *23*(7), 791–802. <https://doi.org/10.1007/s00382-004-0477-y>
- 1624 Li, X., Jiang, D., Zhang, Z., Zhang, R., Tian, Z., & Yan, Q. (2015). Mid-Pliocene westerlies from PlioMIP  
 1625 simulations. *Advances in Atmospheric Sciences*, *32*(7), 909–923. [https://doi.org/10.1007/s00376-014-4171-](https://doi.org/10.1007/s00376-014-4171-7)  
 1626 [7](https://doi.org/10.1007/s00376-014-4171-7)
- 1627 Li, X., Jiang, D., Tian, Z., & Yang, Y. (2018). Mid-Pliocene global land monsoon from PlioMIP1 simulations.  
 1628 *Palaeogeography, Palaeoclimatology, Palaeoecology*, *512*, 56–70.  
 1629 <https://doi.org/10.1016/j.palaeo.2018.06.027>
- 1630 Liakka, J., & Lofverstrom, M. (2018). Arctic warming induced by the Laurentide Ice Sheet topography. *Climate of*  
 1631 *the Past*, *14*(6), 887–900. <https://doi.org/10.5194/cp-14-887-2018>
- 1632 Liakka, J., Löfverström, M., & Colleoni, F. (2016). The impact of the North American glacial topography on the  
 1633 evolution of the Eurasian ice sheet over the last glacial cycle. *Climate of the Past*, *12*(5), 1225–1241.  
 1634 <https://doi.org/10.5194/cp-12-1225-2016>
- 1635 Lohmann, G., Pfeiffer, M., Laepple, T., Leduc, G., & Kim, J.-H. (2013). A model–data comparison of the  
 1636 Holocene global sea surface temperature evolution. *Climate of the Past*, *9*(4), 1807–1839.  
 1637 <https://doi.org/10.5194/cp-9-1807-2013>
- 1638 Lohmann, U., & Roeckner, E. (1996). Design and performance of a new cloud microphysics scheme developed for  
 1639 the ECHAM general circulation model. *Climate Dynamics*, *12*(8), 557–572.  
 1640 <https://doi.org/10.1007/BF00207939>
- 1641 Lora, J. M. (2018). Components and Mechanisms of Hydrologic Cycle Changes over North America at the Last  
 1642 Glacial Maximum. *Journal of Climate*, *31*(17), 7035–7051. <https://doi.org/10.1175/JCLI-D-17-0544.1>

- 1643 Lorenz, S. J., & Lohmann, G. (2004). Acceleration technique for Milankovitch type forcing in a coupled  
 1644 atmosphere-ocean circulation model: method and application for the Holocene. *Climate Dynamics*, 23(7–  
 1645 8), 727–743. <https://doi.org/10.1007/s00382-004-0469-y>
- 1646 Manning, K., & Timpson, A. (2014). The demographic response to Holocene climate change in the Sahara.  
 1647 *Quaternary Science Reviews*, 101, 28–35. <https://doi.org/10.1016/j.quascirev.2014.07.003>
- 1648 Marsham, J. H., Dixon, N. S., Garcia-Carreras, L., Lister, G. M. S., Parker, D. J., Knippertz, P., & Birch, C. E.  
 1649 (2013). The role of moist convection in the West African monsoon system: Insights from continental-scale  
 1650 convection-permitting simulations. *Geophysical Research Letters*, 40(9), 1843–1849.  
 1651 <https://doi.org/10.1002/grl.50347>
- 1652 Marzin, C., & Braconnot, P. (2009). Variations of Indian and African monsoons induced by insolation changes at 6  
 1653 and 9.5 kyr BP. *Climate Dynamics*, 33(2), 215–231. <https://doi.org/10.1007/s00382-009-0538-3>
- 1654 McManus, J. F., Francois, R., Gherardi, J.-M., Keigwin, L. D., & Brown-Leger, S. (2004). Collapse and rapid  
 1655 resumption of Atlantic meridional circulation linked to deglacial climate changes. *Nature*, 428(6985), 834–  
 1656 837. <https://doi.org/10.1038/nature02494>
- 1657 Messori, G., Gaetani, M., Zhang, Q., Zhang, Q., & Pausata, F. S. R. (2019). The water cycle of the mid-Holocene  
 1658 West African monsoon: The role of vegetation and dust emission changes. *International Journal of*  
 1659 *Climatology*, 39(4), 1927–1939. <https://doi.org/10.1002/joc.5924>
- 1660 Mulitza, S., Prange, M., Stuut, J.-B., Zabel, M., von Dobeneck, T., Itambi, A. C., et al. (2008). Sahel megadroughts  
 1661 triggered by glacial slowdowns of Atlantic meridional overturning. *Paleoceanography*, 23(4).  
 1662 <https://doi.org/10.1029/2008PA001637>
- 1663 Mutz, S. G., Ehlers, T. A., Werner, M., Lohmann, G., Stepanek, C., & Li, J. (2018). Estimates of late Cenozoic  
 1664 climate change relevant to Earth surface processes in tectonically active orogens. *Earth Surface Dynamics*,  
 1665 6(2), 271–301. <https://doi.org/10.5194/esurf-6-271-2018>
- 1666 Newell, R. E., & Kidson, J. W. (1984). African mean wind changes between sahelian wet and dry periods. *Journal*  
 1667 *of Climatology*, 4(1), 27–33. <https://doi.org/10.1002/joc.3370040103>
- 1668 Nicholson, S. E. (2008). The intensity, location and structure of the tropical rainbelt over west Africa as factors in  
 1669 interannual variability. *International Journal of Climatology*, 28(13), 1775–1785.  
 1670 <https://doi.org/10.1002/joc.1507>
- 1671 Nicholson, S. e., & Grist, J. p. (2001). A conceptual model for understanding rainfall variability in the West African  
 1672 Sahel on interannual and interdecadal timescales. *International Journal of Climatology*, 21(14), 1733–  
 1673 1757. <https://doi.org/10.1002/joc.648>
- 1674 Nicholson, S. E., & Grist, J. P. (2003). The Seasonal Evolution of the Atmospheric Circulation over West Africa and  
 1675 Equatorial Africa. *Journal of Climate*, 16(7), 1013–1030. [https://doi.org/10.1175/1520-0442\(2003\)016<1013:TSEOTA>2.0.CO;2](https://doi.org/10.1175/1520-0442(2003)016<1013:TSEOTA>2.0.CO;2)
- 1676 Nicholson, S. E., & Palao, I. M. (1993). A re-evaluation of rainfall variability in the sahel. Part I. Characteristics of  
 1677 rainfall fluctuations. *International Journal of Climatology*, 13(4), 371–389.  
 1678 <https://doi.org/10.1002/joc.3370130403>
- 1679 Nicholson, S. E., & Webster, P. J. (2007). A physical basis for the interannual variability of rainfall in the Sahel.  
 1680 *Quarterly Journal of the Royal Meteorological Society*, 133(629), 2065–2084.  
 1681 <https://doi.org/10.1002/qj.104>
- 1682 de Nooijer, W., Zhang, Q., Li, Q., Zhang, Q., Li, X., Zhang, Z., et al. (2020). Evaluation of Arctic warming in mid-  
 1683 Pliocene climate simulations. *Climate of the Past*, 16(6), 2325–2341. <https://doi.org/10.5194/cp-16-2325-2020>
- 1684 Notaro, M., Wang, Y., Liu, Z., Gallimore, R., & Levis, S. (2008). Combined statistical and dynamical assessment of  
 1685 simulated vegetation–rainfall interactions in North Africa during the mid-Holocene1. *Global Change*  
 1686 *Biology*, 14(2), 347–368. <https://doi.org/10.1111/j.1365-2486.2007.01495.x>
- 1687 Otto-Bliesner, B. L., Brady, E. C., Clauzet, G., Tomas, R., Levis, S., & Kothavala, Z. (2006). Last Glacial  
 1688 Maximum and Holocene Climate in CCSM3. *Journal of Climate*, 19(11), 2526–2544.  
 1689 <https://doi.org/10.1175/JCLI3748.1>

- 1692 Otto-Bliesner, B. L., Braconnot, P., Harrison, S. P., Lunt, D. J., Abe-Ouchi, A., Albani, S., et al. (2017). The PMIP4  
 1693 contribution to CMIP6 – Part 2: Two interglacials, scientific objective and experimental design for  
 1694 Holocene and Last Interglacial simulations. *Geoscientific Model Development*, *10*(11), 3979–4003.  
 1695 <https://doi.org/10.5194/gmd-10-3979-2017>
- 1696 Patricola, C. M., & Cook, K. H. (2007). Dynamics of the West African Monsoon under Mid-Holocene Precessional  
 1697 Forcing: Regional Climate Model Simulations. *Journal of Climate*, *20*(4), 694–716.  
 1698 <https://doi.org/10.1175/JCLI4013.1>
- 1699 Pausata, F. S. R., Messori, G., & Zhang, Q. (2016). Impacts of dust reduction on the northward expansion of the  
 1700 African monsoon during the Green Sahara period. *Earth and Planetary Science Letters*, *434*, 298–307.  
 1701 <https://doi.org/10.1016/j.epsl.2015.11.049>
- 1702 Pausata, F. S. R., Gaetani, M., Messori, G., Berg, A., Maia de Souza, D., Sage, R. F., & deMenocal, P. B. (2020).  
 1703 The Greening of the Sahara: Past Changes and Future Implications. *One Earth*, *2*(3), 235–250.  
 1704 <https://doi.org/10.1016/j.oneear.2020.03.002>
- 1705 Peltier, W. R., & Fairbanks, R. G. (2006). Global glacial ice volume and Last Glacial Maximum duration from an  
 1706 extended Barbados sea level record. *Quaternary Science Reviews*, *25*(23), 3322–3337.  
 1707 <https://doi.org/10.1016/j.quascirev.2006.04.010>
- 1708 Perez-Sanz, A., Li, G., González-Sampériz, P., & Harrison, S. P. (2014). Evaluation of modern and mid-Holocene  
 1709 seasonal precipitation of the Mediterranean and northern Africa in the CMIP5 simulations. *Climate of the  
 1710 Past*, *10*(2), 551–568. <https://doi.org/10.5194/cp-10-551-2014>
- 1711 Peyron, O., Jolly, D., Braconnot, P., Bonnefille, R., Guiot, J., Wirmann, D., & Chalié, F. (2006). Quantitative  
 1712 reconstructions of annual rainfall in Africa 6000 years ago: Model-data comparison. *Journal of  
 1713 Geophysical Research: Atmospheres*, *111*(D24). <https://doi.org/10.1029/2006JD007396>
- 1714 Phipps, S. J., McGregor, H. V., Gergis, J., Gallant, A. J. E., Neukom, R., Stevenson, S., et al. (2013). Paleoclimate  
 1715 Data–Model Comparison and the Role of Climate Forcings over the Past 1500 Years. *Journal of Climate*,  
 1716 *26*(18), 6915–6936. <https://doi.org/10.1175/JCLI-D-12-00108.1>
- 1717 Pickett, E. J., Harrison, S. P., Hope, G., Harle, K., Dodson, J. R., Peter Kershaw, A., et al. (2004). Pollen-based  
 1718 reconstructions of biome distributions for Australia, Southeast Asia and the Pacific (SEAPAC region) at 0,  
 1719 6000 and 18,000 14C yr BP. *Journal of Biogeography*, *31*(9), 1381–1444. <https://doi.org/10.1111/j.1365-2699.2004.01001.x>
- 1720
- 1721 Prentice, I. C., Jolly, D., & Participants, B. 6000. (2000). Mid-Holocene and glacial-maximum vegetation geography  
 1722 of the northern continents and Africa. *Journal of Biogeography*, *27*(3), 507–519.  
 1723 <https://doi.org/10.1046/j.1365-2699.2000.00425.x>
- 1724 Quagraine, K. A., Nkrumah, F., Klein, C., Klutse, N. A. B., & Quagraine, K. T. (2020). West African Summer  
 1725 Monsoon Precipitation Variability as Represented by Reanalysis Datasets. *Climate*, *8*(10), 111.  
 1726 <https://doi.org/10.3390/cli8100111>
- 1727 Rachmayani, R., Prange, M., & Schulz, M. (2015). North African vegetation–precipitation feedback in early and  
 1728 mid-Holocene climate simulations with CCSM3-DGVM. *Climate of the Past*, *11*(2), 175–185.  
 1729 <https://doi.org/10.5194/cp-11-175-2015>
- 1730 Raible, C. C., Lehner, F., González-Rouco, J. F., & Fernández-Donado, L. (2014). Changing correlation structures  
 1731 of the Northern Hemisphere atmospheric circulation from 1000 to 2100 AD. *Climate of the Past*, *10*(2),  
 1732 537–550. <https://doi.org/10.5194/cp-10-537-2014>
- 1733 Redelsperger, J.-L., Parsons, D. B., & Guichard, F. (2002). Recovery Processes and Factors Limiting Cloud-Top  
 1734 Height following the Arrival of a Dry Intrusion Observed during TOGA COARE. *Journal of the  
 1735 Atmospheric Sciences*, *59*(16), 2438–2457. [https://doi.org/10.1175/1520-0469\(2002\)059<2438:RPAFLC>2.0.CO;2](https://doi.org/10.1175/1520-0469(2002)059<2438:RPAFLC>2.0.CO;2)
- 1736
- 1737 Risi, C., Bony, S., Vimeux, F., Descroix, L., Ibrahim, B., Lebreton, E., et al. (2008). What controls the isotopic  
 1738 composition of the African monsoon precipitation? Insights from event-based precipitation collected during  
 1739 the 2006 AMMA field campaign. *Geophysical Research Letters*, *35*(24).  
 1740 <https://doi.org/10.1029/2008GL035920>

- 1741 Risi, C., Bony, S., Vimeux, F., Frankenberg, C., Noone, D., & Worden, J. (2010). Understanding the Sahelian water  
 1742 budget through the isotopic composition of water vapor and precipitation. *Journal of Geophysical*  
 1743 *Research: Atmospheres*, *115*(D24). <https://doi.org/10.1029/2010JD014690>
- 1744 Risi, C., Noone, D., Worden, J., Frankenberg, C., Stiller, G., Kiefer, M., et al. (2012). Process-evaluation of  
 1745 tropospheric humidity simulated by general circulation models using water vapor isotopologues: 1.  
 1746 Comparison between models and observations. *Journal of Geophysical Research: Atmospheres*, *117*(D5).  
 1747 <https://doi.org/10.1029/2011JD016621>
- 1748 Risi, C., Noone, D., Frankenberg, C., & Worden, J. (2013). Role of continental recycling in intraseasonal variations  
 1749 of continental moisture as deduced from model simulations and water vapor isotopic measurements:  
 1750 Continental Recycling and Water Isotopes. *Water Resources Research*, *49*(7), 4136–4156.  
 1751 <https://doi.org/10.1002/wrcr.20312>
- 1752 Roeckner, E., Bäuml, G., Bonaventura, L., Brokopf, R., Esch, M., Giorgetta, M., et al. (2003). The atmospheric  
 1753 general circulation model ECHAM 5. PART I: Model description. <https://doi.org/10.17617/2.995269>
- 1754 Roehrig, R., Bouniol, D., Guichard, F., Hourdin, F., & Redelsperger, J.-L. (2013). The Present and Future of the  
 1755 West African Monsoon: A Process-Oriented Assessment of CMIP5 Simulations along the AMMA  
 1756 Transect. *Journal of Climate*, *26*(17), 6471–6505. <https://doi.org/10.1175/JCLI-D-12-00505.1>
- 1757 Rozanski, K., Araguás-Araguás, L., & Gonfiantini, R. (1993). Climate change in continental isotopic records.  
 1758 Retrieved from [https://scholar.google.com/scholar\\_lookup?hl=en&publication\\_year=1993&pages=1-](https://scholar.google.com/scholar_lookup?hl=en&publication_year=1993&pages=1-36&author=K.+Rozanski&author=L.+Aragu%C3%A1s&author=R.+Gonfiantini&title=Climate+Change+in+Continental+Isotopic+Records)  
 1759 [36&author=K.+Rozanski&author=L.+Aragu%C3%A1s&author=R.+Gonfiantini&title=Climate+Change+in+Continental+Isotopic+Records](https://scholar.google.com/scholar_lookup?hl=en&publication_year=1993&pages=1-36&author=K.+Rozanski&author=L.+Aragu%C3%A1s&author=R.+Gonfiantini&title=Climate+Change+in+Continental+Isotopic+Records)
- 1760 Salzmann, U., Haywood, A. M., Lunt, D. J., Valdes, P. J., & Hill, D. J. (2008). A new global biome reconstruction  
 1761 and data-model comparison for the Middle Pliocene. *Global Ecology and Biogeography*, *17*(3), 432–447.  
 1762 <https://doi.org/10.1111/j.1466-8238.2008.00381.x>
- 1763 Salzmann, Ulrich, Dolan, A. M., Haywood, A. M., Chan, W.-L., Voss, J., Hill, D. J., et al. (2013). Challenges in  
 1764 quantifying Pliocene terrestrial warming revealed by data–model discord. *Nature Climate Change*, *3*(11),  
 1765 969–974. <https://doi.org/10.1038/nclimate2008>
- 1766 Samakinwa, E., Stepanek, C., & Lohmann, G. (2020). Sensitivity of mid-Pliocene climate to changes in orbital  
 1767 forcing and PlioMIP’s boundary conditions. *Climate of the Past*, *16*(4), 1643–1665.  
 1768 <https://doi.org/10.5194/cp-16-1643-2020>
- 1769 Sarnthein, M., Gersonde, R., Niebler, S., Pflaumann, U., Spielhagen, R., Thiede, J., et al. (2003). Overview of  
 1770 Glacial Atlantic Ocean Mapping (GLAMAP 2000). *Paleoceanography*, *18*(2).  
 1771 <https://doi.org/10.1029/2002PA000769>
- 1772 Scheff, J., & Frierson, D. M. W. (2012). Robust future precipitation declines in CMIP5 largely reflect the poleward  
 1773 expansion of model subtropical dry zones. *Geophysical Research Letters*, *39*(18).  
 1774 <https://doi.org/10.1029/2012GL052910>
- 1775 Sereno, P. C., Garcea, E. A. A., Jousse, H., Stojanowski, C. M., Saliège, J.-F., Maga, A., et al. (2008). Lakeside  
 1776 Cemeteries in the Sahara: 5000 Years of Holocene Population and Environmental Change. *PLOS ONE*,  
 1777 *3*(8), e2995. <https://doi.org/10.1371/journal.pone.0002995>
- 1778 Seth, A., Giannini, A., Rojas, M., Rauscher, S. A., Bordoni, S., Singh, D., & Camargo, S. J. (2019). Monsoon  
 1779 Responses to Climate Changes—Connecting Past, Present and Future. *Current Climate Change Reports*,  
 1780 *5*(2), 63–79. <https://doi.org/10.1007/s40641-019-00125-y>
- 1781 Sha, L., Ait Brahim, Y., Wassenburg, J. A., Yin, J., Peros, M., Cruz, F. W., et al. (2019). How Far North Did the  
 1782 African Monsoon Fringe Expand During the African Humid Period? Insights From Southwest Moroccan  
 1783 Speleothems. *Geophysical Research Letters*, *46*(23), 14093–14102. <https://doi.org/10.1029/2019GL084879>
- 1784 Shi, X., Lohmann, G., Sidorenko, D., & Yang, H. (2020). Early-Holocene simulations using different forcings and  
 1785 resolutions in AWI-ESM. *The Holocene*, *30*(7), 996–1015. <https://doi.org/10.1177/0959683620908634>
- 1786 Shi, X., Cauquoin, A., Lohmann, G., Jonkers, L., Wang, Q., Yang, H., et al. (2023). Simulated stable water isotopes  
 1787 during the mid-Holocene and pre-industrial using AWI-ESM-2.1-wiso. *Geoscientific Model Development*  
 1788 *Discussions*, 1–39. <https://doi.org/10.5194/gmd-2023-68>
- 1789

- 1790 Simmons, A. J., Burridge, D. M., Jarraud, M., Girard, C., & Wergen, W. (1989). The ECMWF medium-range  
 1791 prediction models development of the numerical formulations and the impact of increased resolution.  
 1792 *Meteorology and Atmospheric Physics*, 40(1), 28–60. <https://doi.org/10.1007/BF01027467>
- 1793 Sohl, L. E., Chandler, M. A., Schmunk, R. B., Mankoff, K., Jonas, J. A., Foley, K. M., & Dowsett, H. J. (2009).  
 1794 *PRISM3/GISS Topographic Reconstruction* (No. 419). *Data Series*. U.S. Geological Survey.  
 1795 <https://doi.org/10.3133/ds419>
- 1796 Sperber, K. R., Hameed, S., Potter, G. L., & Boyle, J. S. (1994). Simulation of the Northern Summer Monsoon in  
 1797 the ECMWF Model: Sensitivity to Horizontal Resolution. *Monthly Weather Review*, 122(11), 2461–2481.  
 1798 [https://doi.org/10.1175/1520-0493\(1994\)122<2461:SOTNSM>2.0.CO;2](https://doi.org/10.1175/1520-0493(1994)122<2461:SOTNSM>2.0.CO;2)
- 1799 Stager, J. C., Mayewski, P. A., & Meeker, L. D. (2002). Cooling cycles, Heinrich event 1, and the desiccation of  
 1800 Lake Victoria. *Palaeogeography, Palaeoclimatology, Palaeoecology*, 183(1), 169–178.  
 1801 [https://doi.org/10.1016/S0031-0182\(01\)00468-0](https://doi.org/10.1016/S0031-0182(01)00468-0)
- 1802 Stager, J. C., Ryves, D. B., Chase, B. M., & Pausata, F. S. R. (2011). Catastrophic Drought in the Afro-Asian  
 1803 Monsoon Region During Heinrich Event 1. *Science*, 331(6022), 1299–1302.  
 1804 <https://doi.org/10.1126/science.1198322>
- 1805 Stepanek, C., & Lohmann, G. (2012). Modelling mid-Pliocene climate with COSMOS. *Geoscientific Model*  
 1806 *Development*, 5(5), 1221–1243. <https://doi.org/10.5194/gmd-5-1221-2012>
- 1807 Stepanek, Christian, Samakinwa, E., Knorr, G., & Lohmann, G. (2020). Contribution of the coupled atmosphere–  
 1808 ocean–sea ice–vegetation model COSMOS to the PlioMIP2. *Climate of the Past*, 16(6), 2275–2323.  
 1809 <https://doi.org/10.5194/cp-16-2275-2020>
- 1810 Su, H., & Neelin, J. D. (2005). Dynamical mechanisms for African monsoon changes during the mid-Holocene.  
 1811 *Journal of Geophysical Research: Atmospheres*, 110(D19). <https://doi.org/10.1029/2005JD005806>
- 1812 Sultan, B., & Janicot, S. (2003). The West African monsoon dynamics. Part II: The “preonset” and “onset” of the  
 1813 summer monsoon. *Journal of Climate*, 16(21), 3407–3427.
- 1814 Sultan, B., Janicot, S., & Diedhiou, A. (2003). The West African monsoon dynamics. Part I: Documentation of  
 1815 intraseasonal variability. *Journal of Climate*, 16(21), 3389–3406.
- 1816 Sultan, B., Baron, C., Dingkuhn, M., Sarr, B., & Janicot, S. (2005). Agricultural impacts of large-scale variability of  
 1817 the West African monsoon. *Agricultural and Forest Meteorology*, 128(1), 93–110.  
 1818 <https://doi.org/10.1016/j.agrformet.2004.08.005>
- 1819 Swann, A. L. S., Fung, I. Y., Liu, Y., & Chiang, J. C. H. (2014). Remote Vegetation Feedbacks and the Mid-  
 1820 Holocene Green Sahara. *Journal of Climate*, 27(13), 4857–4870. <https://doi.org/10.1175/JCLI-D-13-00690.1>
- 1821
- 1822 Sylla, M. B., Nikiema, P. M., Gibba, P., Kebe, I., & Klutse, N. A. B. (2016). Climate Change over West Africa:  
 1823 Recent Trends and Future Projections. In J. A. Yaro & J. Hesselberg (Eds.), *Adaptation to Climate Change*  
 1824 *and Variability in Rural West Africa* (pp. 25–40). Cham: Springer International Publishing.  
 1825 [https://doi.org/10.1007/978-3-319-31499-0\\_3](https://doi.org/10.1007/978-3-319-31499-0_3)
- 1826 Texier, D., Noblet, N. de, & Braconnot, P. (2000). Sensitivity of the African and Asian Monsoons to Mid-Holocene  
 1827 Insolation and Data-Inferred Surface Changes. *Journal of Climate*, 13(1), 164–181.  
 1828 [https://doi.org/10.1175/1520-0442\(2000\)013<0164:SOTAAA>2.0.CO;2](https://doi.org/10.1175/1520-0442(2000)013<0164:SOTAAA>2.0.CO;2)
- 1829 Thompson, A. J., Skinner, C. B., Poulsen, C. J., & Zhu, J. (2019). Modulation of Mid-Holocene African Rainfall by  
 1830 Dust Aerosol Direct and Indirect Effects. *Geophysical Research Letters*, 46(7), 3917–3926.  
 1831 <https://doi.org/10.1029/2018GL081225>
- 1832 Thompson, A. J., Tabor, C. R., Poulsen, C. J., & Skinner, C. B. (2021). Water isotopic constraints on the  
 1833 enhancement of the mid-Holocene West African monsoon. *Earth and Planetary Science Letters*, 554,  
 1834 116677. <https://doi.org/10.1016/j.epsl.2020.116677>
- 1835 Thorncroft, C. D., & Blackburn, M. (1999). Maintenance of the African easterly jet. *Quarterly Journal of the Royal*  
 1836 *Meteorological Society*, 125(555), 763–786. <https://doi.org/10.1002/qj.49712555502>
- 1837 Tierney, J. E., Pausata, F. S. R., & deMenocal, P. B. (2017). Rainfall regimes of the Green Sahara. *Science*  
 1838 *Advances*, 3(1), e1601503. <https://doi.org/10.1126/sciadv.1601503>

- 1839 Tindall, J. C., Haywood, A. M., Salzmann, U., Dolan, A. M., & Fletcher, T. (2022). The warm winter paradox in the  
 1840 Pliocene northern high latitudes. *Climate of the Past*, 18(6), 1385–1405. [https://doi.org/10.5194/cp-18-](https://doi.org/10.5194/cp-18-1385-2022)  
 1841 1385-2022
- 1842 Tompkins, A. M. (2002). A Prognostic Parameterization for the Subgrid-Scale Variability of Water Vapor and  
 1843 Clouds in Large-Scale Models and Its Use to Diagnose Cloud Cover. *Journal of the Atmospheric Sciences*,  
 1844 59(12), 1917–1942. [https://doi.org/10.1175/1520-0469\(2002\)059<1917:APPFTS>2.0.CO;2](https://doi.org/10.1175/1520-0469(2002)059<1917:APPFTS>2.0.CO;2)
- 1845 de la Vega, E., Chalk, T. B., Wilson, P. A., Bysani, R. P., & Foster, G. L. (2020). Atmospheric CO<sub>2</sub> during the Mid-  
 1846 Piacenzian Warm Period and the M2 glaciation. *Scientific Reports*, 10(1), 11002.  
 1847 <https://doi.org/10.1038/s41598-020-67154-8>
- 1848 Wang, Y., Notaro, M., Liu, Z., Gallimore, R., Levis, S., & Kutzbach, J. E. (2008). Detecting vegetation-precipitation  
 1849 feedbacks in mid-Holocene North Africa from two climate models. *Climate of the Past*, 4(1), 59–67.  
 1850 <https://doi.org/10.5194/cp-4-59-2008>
- 1851 Wang, Y. J., Cheng, H., Edwards, R. L., An, Z. S., Wu, J. Y., Shen, C.-C., & Dorale, J. A. (2001). A High-  
 1852 Resolution Absolute-Dated Late Pleistocene Monsoon Record from Hulu Cave, China. *Science*, 294(5550),  
 1853 2345–2348. <https://doi.org/10.1126/science.1064618>
- 1854 Wei, W., & Lohmann, G. (2012). Simulated Atlantic Multidecadal Oscillation during the Holocene. *Journal of*  
 1855 *Climate*, 25(20), 6989–7002. <https://doi.org/10.1175/JCLI-D-11-00667.1>
- 1856 Weldeab, S., Frank, M., Stichel, T., Haley, B., & Sangen, M. (2011). Spatio-temporal evolution of the West African  
 1857 monsoon during the last deglaciation. *Geophysical Research Letters*, 38(13).  
 1858 <https://doi.org/10.1029/2011GL047805>
- 1859 Werner, M., Mikolajewicz, U., Heimann, M., & Hoffmann, G. (2000). Borehole versus isotope temperatures on  
 1860 Greenland: Seasonality does matter. *Geophysical Research Letters*, 27(5), 723–726.  
 1861 <https://doi.org/10.1029/1999GL006075>
- 1862 Werner, M., Langebroek, P. M., Carlsen, T., Herold, M., & Lohmann, G. (2011). Stable water isotopes in the  
 1863 ECHAM5 general circulation model: Toward high-resolution isotope modeling on a global scale. *Journal*  
 1864 *of Geophysical Research*, 116(D15), D15109. <https://doi.org/10.1029/2011JD015681>
- 1865 Werner, M., Jouzel, J., Masson-Delmotte, V., & Lohmann, G. (2018). Reconciling glacial Antarctic water stable  
 1866 isotopes with ice sheet topography and the isotopic paleothermometer. *Nature Communications*, 9(1), 3537.  
 1867 <https://doi.org/10.1038/s41467-018-05430-y>
- 1868 Wu, H., Guiot, J., Brewer, S., & Guo, Z. (2007). Climatic changes in Eurasia and Africa at the last glacial maximum  
 1869 and mid-Holocene: reconstruction from pollen data using inverse vegetation modelling. *Climate Dynamics*,  
 1870 29(2), 211–229. <https://doi.org/10.1007/s00382-007-0231-3>
- 1871 Wu, M.-L. C., Reale, O., Schubert, S. D., Suarez, M. J., Koster, R. D., & Pegion, P. J. (2009). African Easterly Jet:  
 1872 Structure and Maintenance. *Journal of Climate*, 22(17), 4459–4480.  
 1873 <https://doi.org/10.1175/2009JCLI2584.1>
- 1874 Xu, X., Werner, M., Butzin, M., & Lohmann, G. (2012). Water isotope variations in the global ocean model MPI-  
 1875 OM. *Geoscientific Model Development*, 5(3), 809–818. <https://doi.org/10.5194/gmd-5-809-2012>
- 1876 Yan, Q., Wei, T., Korty, R. L., Kossin, J. P., Zhang, Z., & Wang, H. (2016). Enhanced intensity of global tropical  
 1877 cyclones during the mid-Pliocene warm period. *Proceedings of the National Academy of Sciences*, 113(46),  
 1878 12963–12967. <https://doi.org/10.1073/pnas.1608950113>
- 1879 Yang, G.-Y., Methven, J., Woolnough, S., Hodges, K., & Hoskins, B. (2018). Linking African Easterly Wave  
 1880 Activity with Equatorial Waves and the Influence of Rossby Waves from the Southern Hemisphere.  
 1881 *Journal of the Atmospheric Sciences*, 75(6), 1783–1809. <https://doi.org/10.1175/JAS-D-17-0184.1>
- 1882 Yoshimori, M., Yokohata, T., & Abe-Ouchi, A. (2009). A Comparison of Climate Feedback Strength between CO<sub>2</sub>  
 1883 Doubling and LGM Experiments. *Journal of Climate*, 22(12), 3374–3395.  
 1884 <https://doi.org/10.1175/2009JCLI2801.1>
- 1885 Zhang, R., Yan, Q., Zhang, Z. S., Jiang, D., Otto-Bliesner, B. L., Haywood, A. M., et al. (2013). Mid-Pliocene East  
 1886 Asian monsoon climate simulated in the PlioMIP. *Climate of the Past*, 9(5), 2085–2099.  
 1887 <https://doi.org/10.5194/cp-9-2085-2013>

- 1888 Zhang, Ran, Zhang, Z., Jiang, D., Yan, Q., Zhou, X., & Cheng, Z. (2016). Strengthened African summer monsoon in  
1889 the mid-Piacenzian. *Advances in Atmospheric Sciences*, 33(9), 1061–1070. <https://doi.org/10.1007/s00376->  
1890 016-5215-y
- 1891 Zhang, Z., Li, X., Guo, C., Otterå, O. H., Nisancioglu, K. H., Tan, N., et al. (2021). Mid-Pliocene Atlantic  
1892 Meridional Overturning Circulation simulated in PlioMIP2. *Climate of the Past*, 17(1), 529–543.  
1893 <https://doi.org/10.5194/cp-17-529-2021>
- 1894 Zhao, A., Ryder, C. L., & Wilcox, L. J. (2022). How well do the CMIP6 models simulate dust aerosols?  
1895 *Atmospheric Chemistry and Physics*, 22(3), 2095–2119. <https://doi.org/10.5194/acp-22-2095-2022>
- 1896 Zhao, Y., & Harrison, S. P. (2012). Mid-Holocene monsoons: a multi-model analysis of the inter-hemispheric  
1897 differences in the responses to orbital forcing and ocean feedbacks. *Climate Dynamics*, 39(6), 1457–1487.  
1898 <https://doi.org/10.1007/s00382-011-1193-z>
- 1899 Zhao, Y., Braconnot, P., Marti, O., Harrison, S. P., Hewitt, C., Kitoh, A., et al. (2005). A multi-model analysis of the  
1900 role of the ocean on the African and Indian monsoon during the mid-Holocene. *Climate Dynamics*, 25(7),  
1901 777–800. <https://doi.org/10.1007/s00382-005-0075-7>
- 1902 Zheng, W., & Braconnot, P. (2013). Characterization of Model Spread in PMIP2 Mid-Holocene Simulations of the  
1903 African Monsoon. *Journal of Climate*, 26(4), 1192–1210. <https://doi.org/10.1175/JCLI-D-12-00071.1>
- 1904 Zhu, J., Otto-Bliesner, B. L., Brady, E. C., Poulsen, C. J., Tierney, J. E., Lofverstrom, M., & DiNezio, P. (2021).  
1905 Assessment of Equilibrium Climate Sensitivity of the Community Earth System Model Version 2 Through  
1906 Simulation of the Last Glacial Maximum. *Geophysical Research Letters*, 48(3), e2020GL091220.  
1907 <https://doi.org/10.1029/2020GL091220>  
1908  
1909

*Journal of Geophysical Research: Atmospheres*

Supporting Information for

**West African Monsoon dynamics and its control on stable oxygen isotopic composition of precipitation in the Late Cenozoic**

Daniel Boateng<sup>1\*</sup>, Jeffrey N. A. Aryee<sup>2</sup>, Michael Baidu<sup>3</sup>, Frank Arthur<sup>4</sup>, Sebastian G. Mutz<sup>5</sup>

<sup>1</sup>Department of Geosciences, University of Tübingen, Tübingen, Germany

<sup>2</sup>Department of Meteorology and Climate Science, Kwame Nkrumah University of Science and Technology, Kumasi, Ghana

<sup>3</sup>Institute for Climate and Atmospheric Science, School of Earth and Environment, University of Leeds, UK

<sup>4</sup>Department of Natural Sciences and Environmental Health, University of South-Eastern Norway, Bo, Norway

<sup>5</sup>School of Geographical and Earth Sciences, University of Glasgow, Scotland, UK

Corresponding author: Daniel Boateng ([daniel.boateng@uni-tuebingen.de](mailto:daniel.boateng@uni-tuebingen.de))

**Contents of this file**

Figures S1 to S10

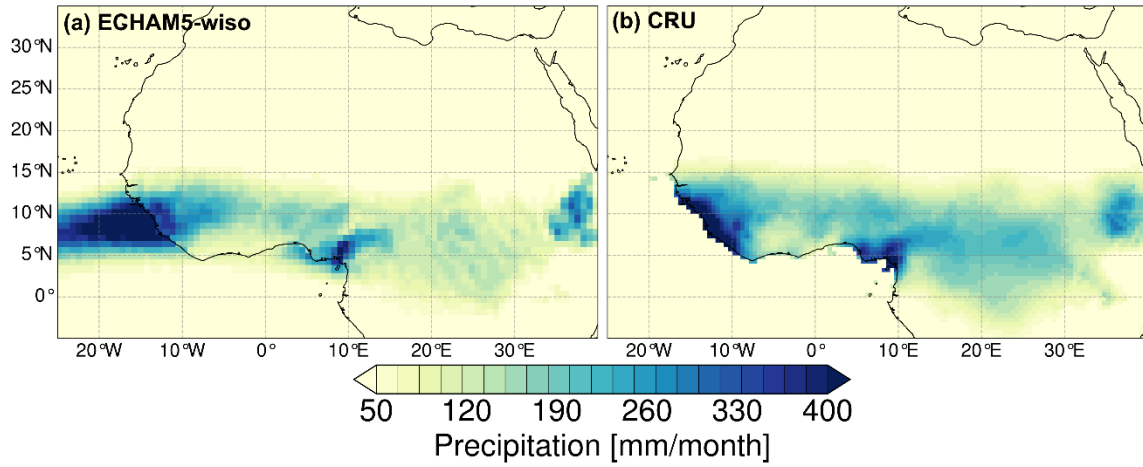


**Figure S1.** Comparison of ECHAM5-wiso simulated long-term (1979-2014) seasonal means for WAM months with the CRU interpolated gridded dataset from weather stations. The simulated patterns indicate that ECHAM5-wiso reasonably represents a latitudinal belt of maximum precipitation (i.e., a rainbelt) during the West African Monsoon (WAM) season.

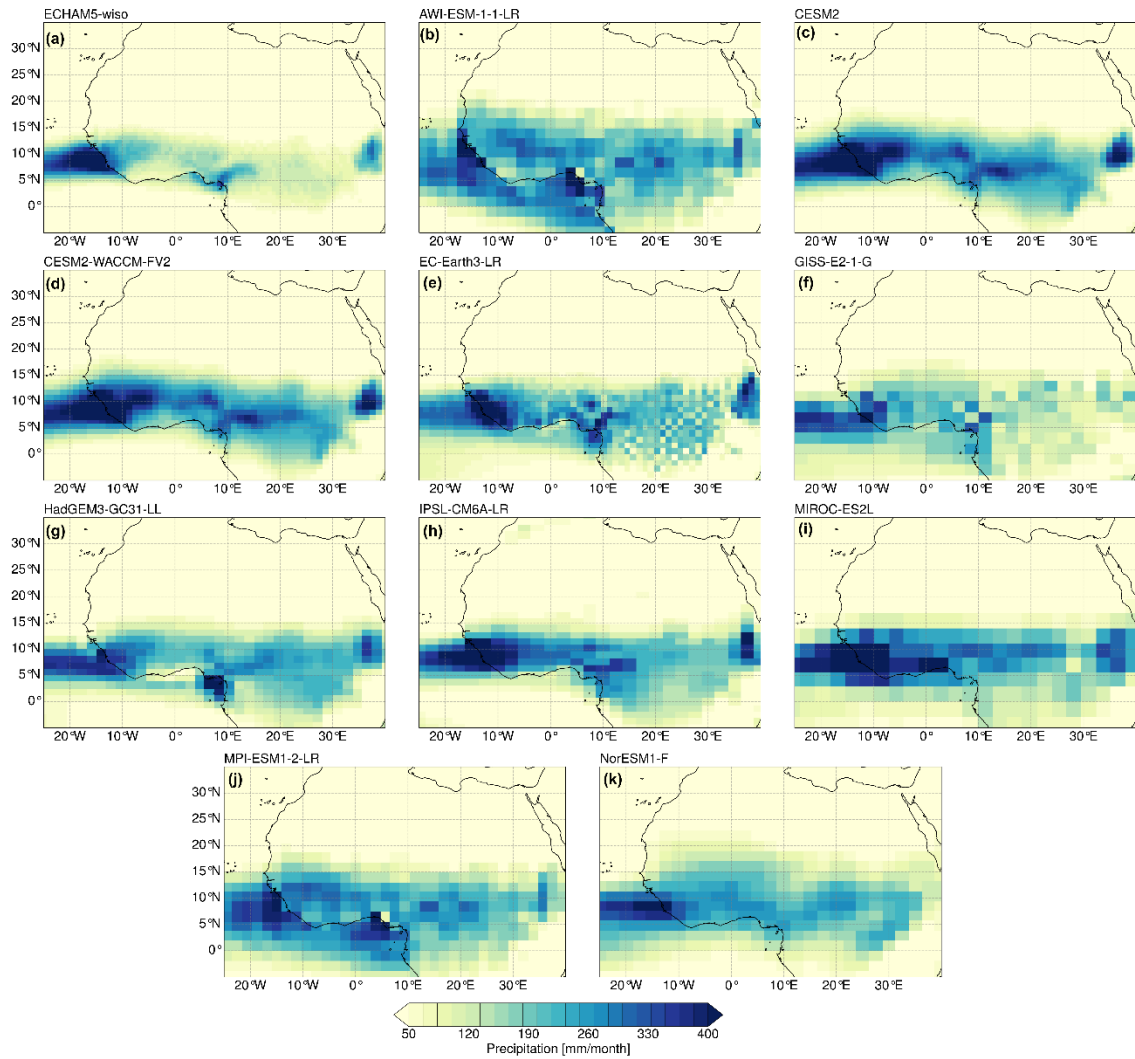


**Figure S2.** Seasonal (JJAS) long-term means of simulated precipitation by ECHAM5-wiso (a) and individual CMIP6-PMIP4 models (b-k) in response to the Pre-Industrial (PI) paleoenvironmental conditions used to estimate the respective precipitation anomalies in different past climates.

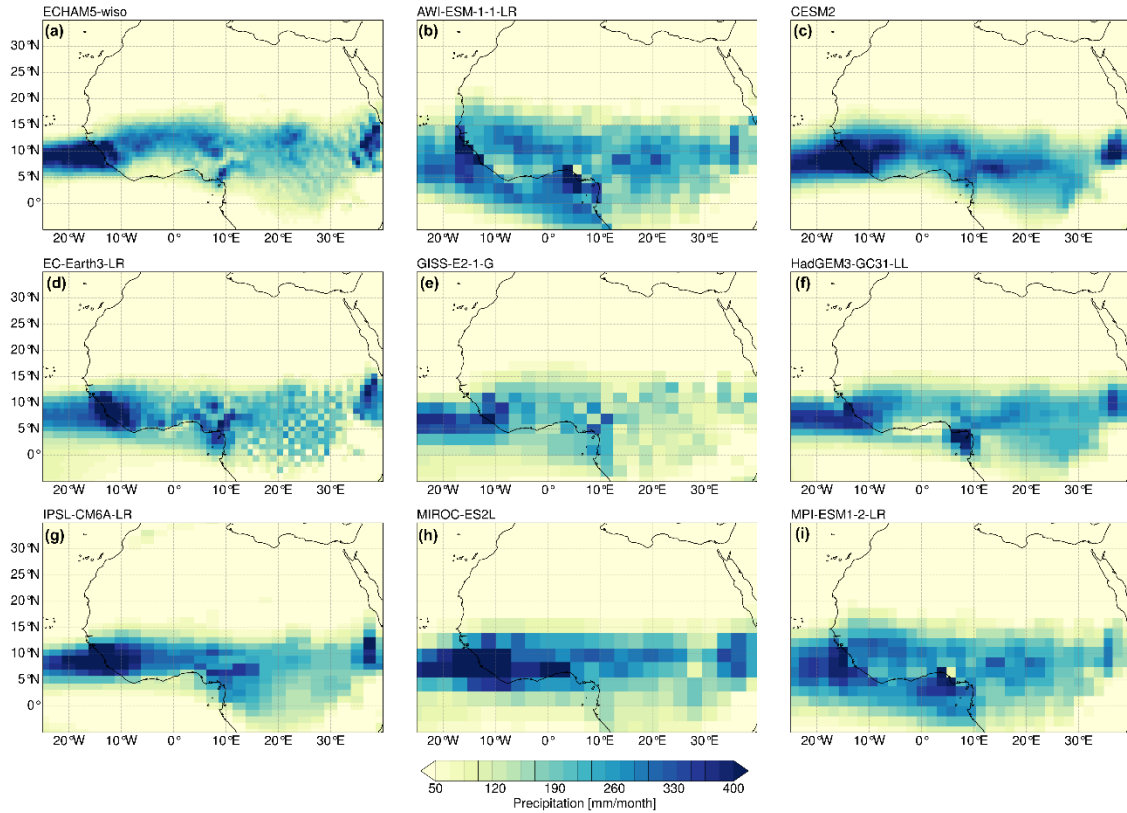


**Figure S3.** Seasonal (JJAS) long-term means of simulated precipitation by ECHAM5-wiso (a) and individual CMIP6-PMIP4 models (b-k) in response to the Mid-Holocene (MH) paleoenvironmental conditions. AWI-ESM-1-1-LR, MPI-ESM-2-LR, and ECHAM5-wiso show relatively more precipitation above 15 °N. However, the Pre-Industrial precipitation estimates reach higher latitudes in AWI-ESM-1-1-LR and MPI-ESM-2-LR compared to ECHAM5-wiso.

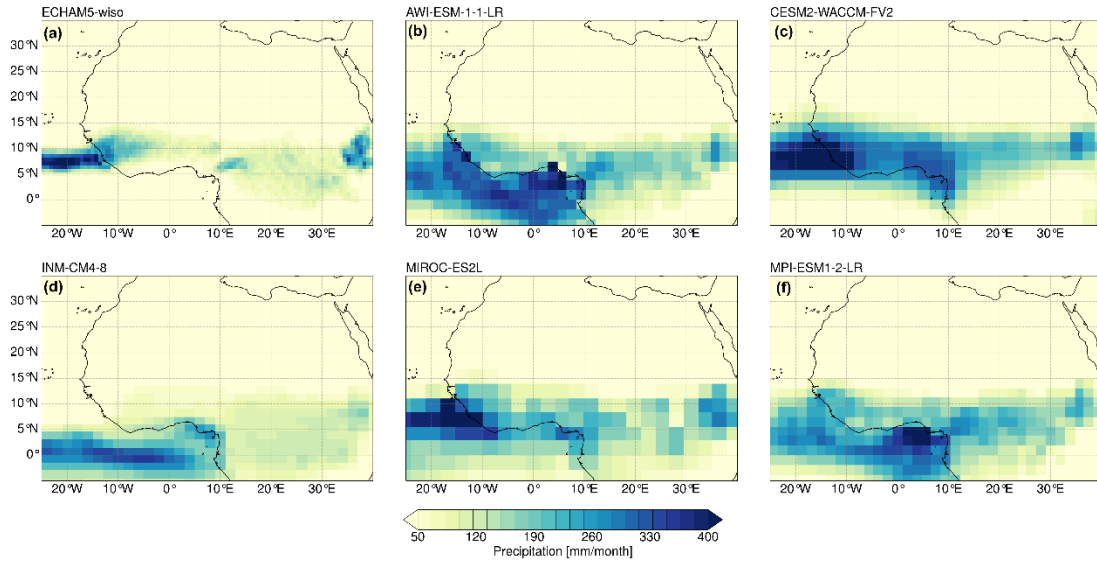


**Figure S4.** Seasonal (JJAS) long-term means of simulated precipitation by ECHAM5-wiso (a) and individual CMIP6-PMIP4 models (b-f) in response to the Last Glacial Maximum (LGM) paleoenvironmental conditions. Overall, ECHAM5-wiso indicates the lowest precipitation across the WAM region.

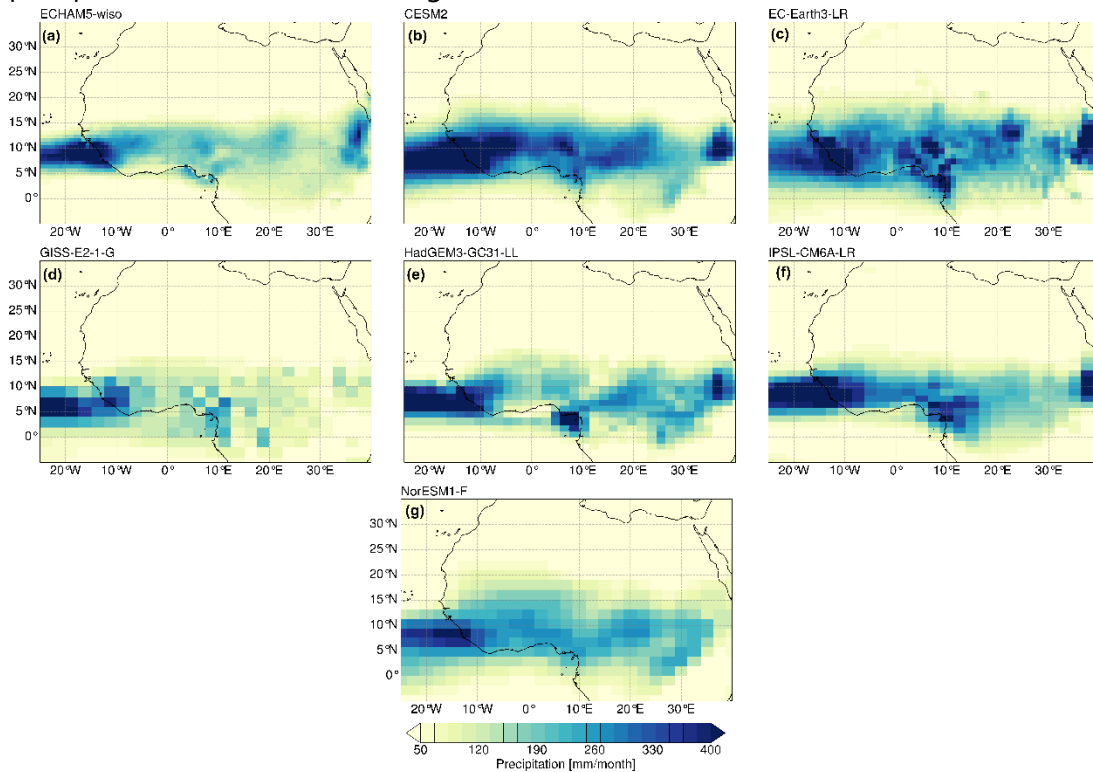


**Figure S5.** Seasonal (JJAS) long-term means of simulated precipitation by ECHAM5-wiso (a) and individual CMIP6-PMIP4 models (b-f) in response to the Mid-Pliocene (mPlio) paleoenvironmental conditions.

paleoenvironmental conditions. Overall, CESM2 and EC-Earth3-LR indicate >30% more precipitation over the WAM region than the other climate models.

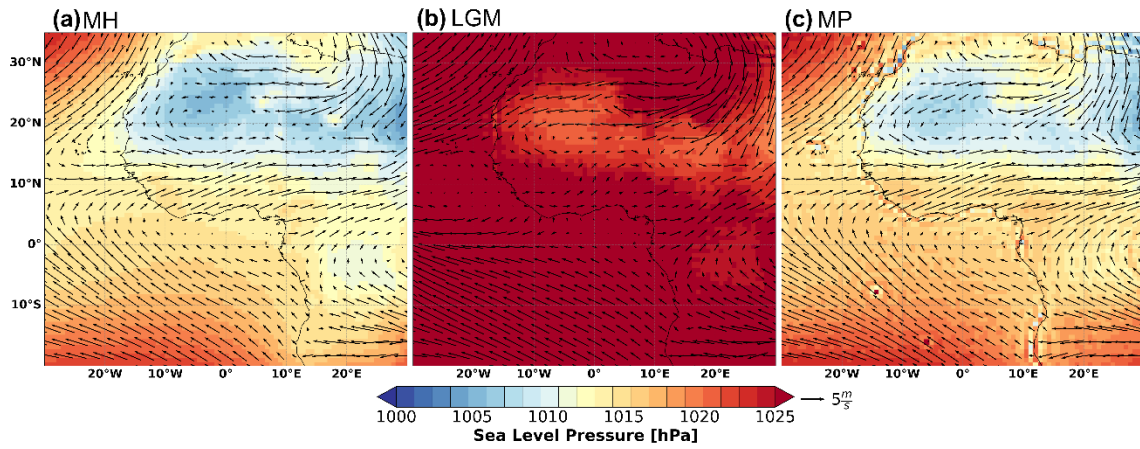


**Figure S6.** Mean sea level pressure (background colour) and wind patterns (arrows) at the 850 hPa pressure level estimated for the WAM season in response to paleoenvironmental conditions (a) MH, (b) LGM, and (c) mPlio using ECHAM5-wiso.

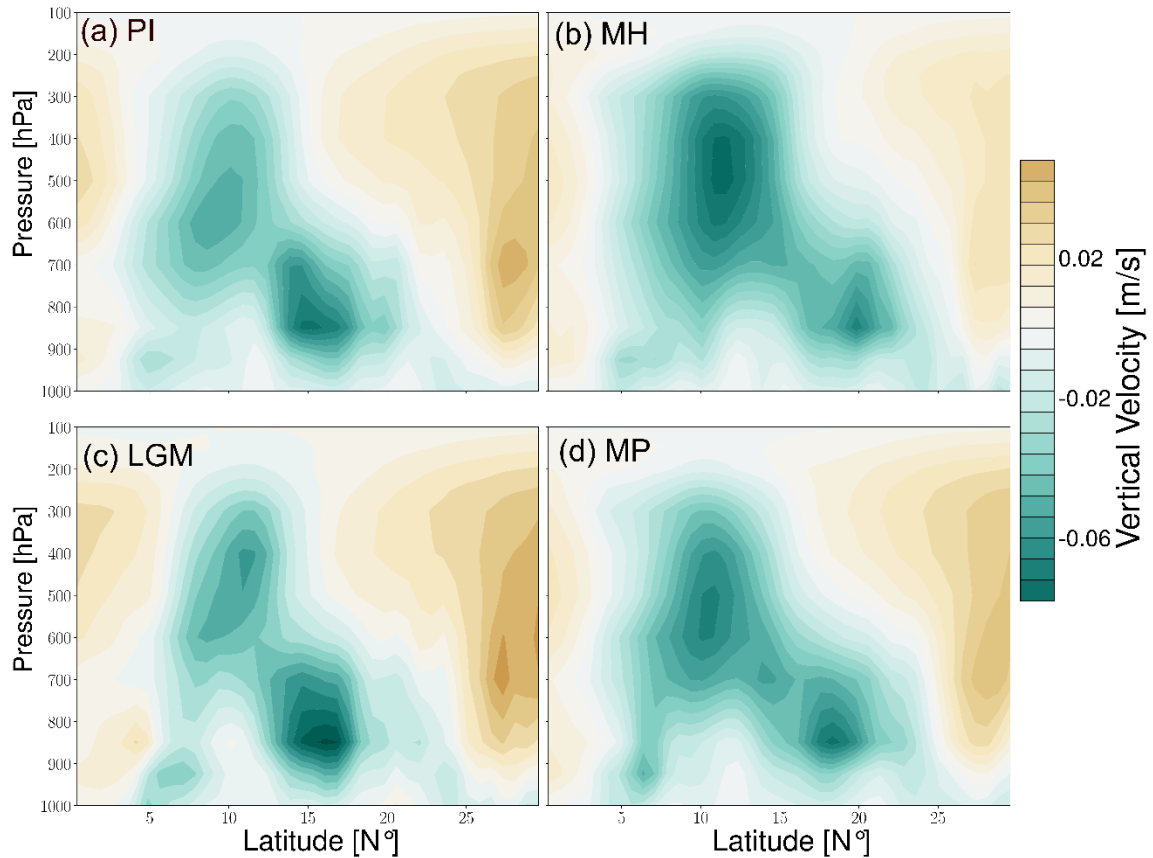


**Figure S7.** Latitudinal vertical (pressure levels) cross-sectional patterns of seasonal (JJAS) means of vertical wind velocity (omega) in response to (a) PI, (b) MH, (c) LGM, and (d) mPlio paleoenvironmental conditions using ECHAM5-wiso. The omega values represent the speed of air motion in the upward or downward direction. Since vertical pressure decreases with height, negative values indicate upward, or ascent velocity, and positive values indicate downward or subsidence velocity.

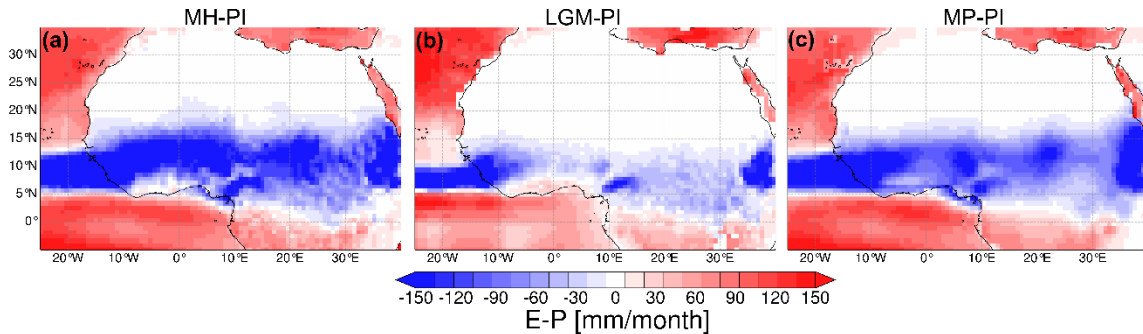


**Figure S8.** Evaporation - Precipitation anomalies during the WAM season (JJAS) estimated in response to the (a) MH, (b) LGM, and (c) mPlio paleoenvironmental conditions using ECHAM5-wiso. The positive values (red colour ranges) indicate more evaporation than precipitation, and vice versa for the negative values (blue colour ranges). The relatively higher evaporation in the MH than in mPlio suggests the role of surface fluxes in contributing to the intensification of the WAM.

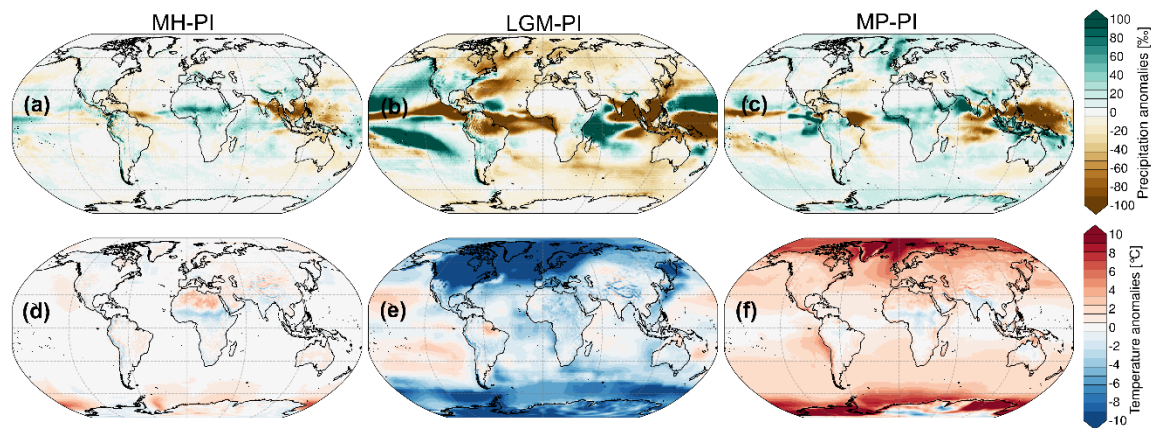


**Figure S9.** Long-term annual means of precipitation (top panel) and near-surface temperature anomalies (bottom panel) estimated in response to the MH (a, d), LGM (b, e), and mPlio (c, f) paleoenvironmental conditions.

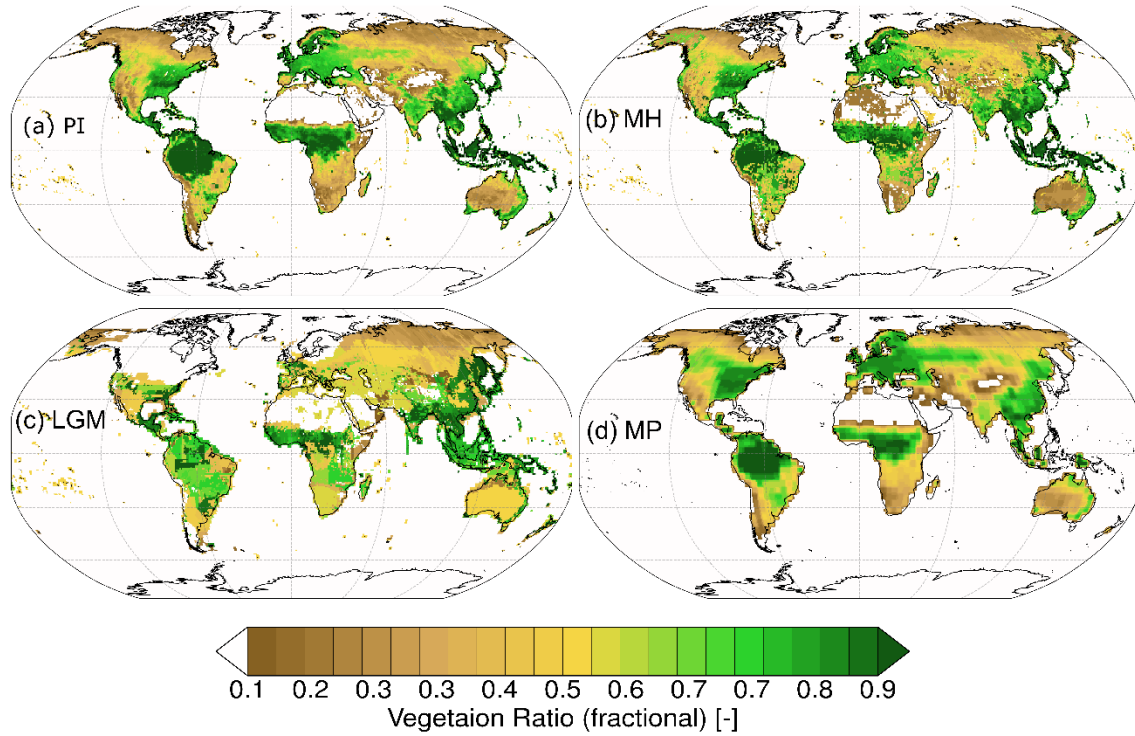


**Figure S10.** Vegetation fractional (i.e., the density of vegetation cover via the maximum vegetation fraction of a grid cell) prescribed as boundary conditions for the different past climate experiments. The values range from 0 to 1, with higher values indicating more vegetation cover.